WASM: Minerals, Energy and Chemical Engineering

Nitrogen Doped Graphene Basal Nanocarbon Materials for Catalytic Decomposition of Persistent Organic Pollutants

Jian Kang

This thesis is presented for the Degree of

Doctor of Philosophy

of

Curtin University

September 2019

Declaration

To the best of my knowledge and belief this thesis contains no material previously published by any other person except where due acknowledgement has been made. This thesis contains no material which has been accepted for the award of any other degree or diploma in any university.

Signature: _____ (Jian Kang)

Date: _____

Acknowledgement

I would like to express my most enthusiastic gratitude to my principal supervisor, Professor Shaobin Wang, who has not only aroused my interest in research and sublimed the tedious research work into fun and satisfaction, but also modelled me by his rigorous scientific approach, optimistic attitude towards life and a kind heart. I believe his influence on me will be lifetime and his edification and guidance will profoundly benefit my future in every aspect. Without him, it would be impossible that my research has been done smoothly and my thesis has been completed on time.

Equally, I am deeply grateful to my co-supervisor, Professor Hongqi Sun, for his inspiration and continuous encouragement. It was Professor Sun who passed me the key to the research kingdom when I firstly started my PhD in 2016. In our first meeting, Professor Sun detailly explained what my research topic was about and listed a series of papers for me to read. Professor Sun is more like a friend, always ready to put aside his work for discussion with me on my research work, and even personal problems. My sincere gratitude also goes to Prof Shaomin Liu for all the kind suggestions for the benefits of my research and career.

I only wish I could thank Xiaoguang Duan enough for his encouragement and selfless support. Dr Duan is of many characters to me, and he is a trusted friend, a patient teacher and a beloved brother. During those countless hours we have spent in laboratory, he taught me how to design and conduct experiment, to utilise laboratory equipment, to analyse results and of course to think critically and learn from failures. I also would like to thank Ping Liang, Xiaochen Guo, and Huayang Zhang for electron microscopes support, and for not showing even a slight impatience especially when the work took consecutive hours. I also thank Chen Wang, my dear colleague who had very similar scope of the work as mine, instead being reserved. Chen has absolutely showed me the spirit of scientific research, including lending me her notebook and sharing her failures and mistakes.

My sincere gratitude also goes to Curtin laboratory technicians, Roshanak, Yu, Jimmy, Andrew, Guanliang, Anja, Jason, Araya, and Karen. Thanks you all for helping prepare the chemicals and training me how to use the equipment and software.

I would like to thank BHP Billiton for generously supporting my PhD scholarship.

Last but not least, I would like to express my deepest love and gratitude to my family, my parents, Yi and Ying, my wife Rebecca and my children Grace and Kathleen. I truly thank you for your unconditional love and tremendous supports. If there is any trivial achievement and pride in my research work, the credit should be yours. With your love, tolerance and caring, I overcame the difficulties and depression, and go further.

Abstract

A wide range of organic compounds is detected in industrial and municipal wastewater, which poses severe problems in the environment due to their resistance to biodegradation and traditional filtration processes. Advanced oxidation processes (AOPs) are favourable technologies that can generate radicals such as hydroxyl and sulfate radicals for toxicants degradation in water due to the high degradation efficiency, complete mineralization capability and eco-friendly nature. In comparison with other hydroxyl based AOPs such as Fenton reactions and ozonation, AOPs employing sulfate radicals for decomposition of organic contaminants have been proven to be more cost-effective. The aim of this research is focused on the development of various carbon based catalysts with heteroatom doping and transition metal encapsulation, and the employment of these catalysts for degradation of aqueous organic pollutants by sulfate radicals based AOPs (SR-AOPs). Various characterization techniques were utilized to investigate the structures and morphologies of these as-synthesized nanomaterials as well as their intrinsic active sites. It was found that the carbon and metal ratio, pyrolysis temperature and time imposed great influences on the catalytic SR-AOPs for organic degradation. With the optimised carbon/metal ratio and nitrogen doping degree, the catalytic activity of the carbon materials can be significantly improved. In addition, the kinetic study indicates that varying reaction temperature, catalyst loading, and pH value play significant roles in catalytic oxidation of pharmaceuticals and personal care products. Moreover, The mechanisms of PMS/PS activation by N-doped nanocarbon catalysts with metal encapsulation were investigated by electronic paramagnetic resonance and quenching tests, showing that the synergistic effect of both radical and nonradical oxidation paths could be responsible for the robust oxidation of organic pollutants.

Publications by the author:

1. **J. Kang**, L. Zhou, X. Duan, H. Sun, Z. Ao, S. Wang, Degradation of Cosmetic Microplastics via Functionalized Carbon Nanosprings, Matter, 1 (2019) 745-758.

2. **J. Kang**, H. Zhang, X. Duan, H. Sun, X. Tan, S. Wang, Nickel in hierarchically structured nitrogen-doped graphene for robust and promoted degradation of antibiotics, Journal of Cleaner Production, 218 (2019) 202-211.

3. **J. Kang**, H. Zhang, X. Duan, H. Sun, X. Tan, S. Liu, S. Wang, Magnetic Ni-Co alloy encapsulated N-doped carbon nanotubes for catalytic membrane degradation of emerging contaminants, Chemical Engineering Journal, 362 (2019) 251-261.

4. **J. Kang**, L. Zhou, X. Duan, H. Sun, S. Wang, Catalytic degradation of antibiotics by metal-free catalysis over nitrogen-doped graphene, Catalysis Today, (2018), DOI: https://doi.org/10.1016/j.cattod.2018.12.002.

5. **J. Kang**, X. Duan, C. Wang, H. Sun, X. Tan, M.O. Tade, S. Wang, Nitrogen-doped bamboo-like carbon nanotubes with Ni encapsulation for persulfate activation to remove emerging contaminants with excellent catalytic stability, Chemical Engineering Journal, 332 (2018) 398-408.

6. **J. Kang**, X. Duan, L. Zhou, H. Sun, M.O. Tadé, S. Wang, Carbocatalytic activation of persulfate for removal of antibiotics in water solutions, Chemical Engineering Journal, 288 (2016) 399-405.

7. S. Zhu, X. Li, **J. Kang**, X. Duan, S. Wang, Persulfate Activation on Crystallographic Manganese Oxides: Mechanism of Singlet Oxygen Evolution for Nonradical Selective Degradation of Aqueous Contaminants, Environmental Science & Technology, 53 (2019) 307-315.

8. X. Duan, W. Li, Z. Ao, **J. Kang**, W. Tian, H. Zhang, S.-H. Ho, H. Sun, S. Wang, Origins of boron catalysis in peroxymonosulfate activation and advanced oxidation, Journal of Materials Chemistry A, (2019), 10.1039/ DOI: 10.1039/C9TA04885E .

9. X. Duan, **J. Kang**, W. Tian, H. Zhang, S.-H. Ho, Y.-A. Zhu, Z. Ao, H. Sun, S. Wang, Interfacial-engineered cobalt@carbon hybrids for synergistically boosted evolution of sulfate radicals toward green oxidation, Applied Catalysis B: Environmental, 256 (2019) 117795.

10. X. Duan, S. Indrawirawan, **J. Kang**, W. Tian, H. Zhang, H. Sun, S. Wang, Temperature-dependent evolution of hydroxyl radicals from peroxymonosulfate activation over nitrogen-modified carbon nanotubes, Sustainable Materials and Technologies, 18 (2018) e00082.

11. Y. Chu, X. Tan, Z. Shen, P. Liu, N. Han, **J. Kang**, X. Duan, S. Wang, L. Liu, S. Liu, Efficient removal of organic and bacterial pollutants by Ag-$La_{0.8}Ca_{0.2}Fe_{0.94}O_{3-\delta}$ perovskite via catalytic peroxymonosulfate activation, Journal of Hazardous Materials, 356 (2018) 53-60.

12. H. Ye, G. Ma, **J. Kang**, H. Sun, S. Wang, Pt-Free microengines at extremely low peroxide levels, Chemical Communications, 54 (2018) 4653-4656.

13. P. Liang, Q. Wang, **J. Kang**, W. Tian, H. Sun, S. Wang, Dual-metal zeolitic imidazolate frameworks and their derived nanoporous carbons for multiple environmental and electrochemical applications, Chemical Engineering Journal, 351 (2018) 641-649.

14. H. Ye, **J. Kang**, G. Ma, H. Sun, S. Wang, High-speed graphene@Ag-MnO_2 micromotors at low peroxide levels, Journal of Colloid and Interface Science, 528 (2018) 271-280.

15. D. Li, X. Duan, H. Sun, **J. Kang**, H. Zhang, M.O. Tade, S. Wang, Facile synthesis of nitrogen-doped graphene via low-temperature pyrolysis: The effects of precursors and annealing ambience on metal-free catalytic oxidation, Carbon, 115 (2017) 649-658.

16. C. Wang, **J. Kang**, P. Liang, H. Zhang, H. Sun, M.O. Tadé, S. Wang, Ferric carbide nanocrystals encapsulated in nitrogen-doped carbon nanotubes as an outstanding environmental catalyst, Environmental Science: Nano, 4 (2017) 170-179.

17. J. Song, **J. Kang**, X. Tan, B. Meng, S. Liu, Proton conducting perovskite hollow fibre membranes with surface catalytic modification for enhanced hydrogen separation, Journal of the European Ceramic Society, 36 (2016) 1669-1677.

18. C. Wang, **J. Kang**, H. Sun, H.M. Ang, M.O. Tadé, S. Wang, One-pot synthesis of N-doped graphene for metal-free advanced oxidation processes, Carbon, 102 (2016) 279-287.

19. X. Duan, H. Sun, Y. Wang, **J. Kang**, S. Wang, N-Doping-Induced Nonradical Reaction on Single-Walled Carbon Nanotubes for Catalytic Phenol Oxidation, ACS Catalysis, 5 (2015) 553-559.

20. X. Duan, Z. Ao, H. Sun, S. Indrawirawan, Y. Wang, **J. Kang**, F. Liang, Z.H. Zhu, S. Wang, Nitrogen-Doped Graphene for Generation and Evolution of Reactive Radicals by Metal-Free Catalysis, ACS Applied Materials & Interfaces, 7 (2015) 4169-4178.

21. X. Duan, H. Sun, **J. Kang**, Y. Wang, S. Indrawirawan, S. Wang, Insights into Heterogeneous Catalysis of Persulfate Activation on Dimensional-Structured Nanocarbons, ACS Catalysis, 5 (2015) 4629-4636.

Contents

Chapter 1. Introduction

1.1 Background of wastewater treatment

Many of the major problems that humanity is facing in the 21st century are originating from the world's thirst for water. Water contamination adds immensely to existing problems of water scarcity by polluting large volumes of available water and making it unsuitable for use[1]. These problems are going to be more aggravated in the future via rapid population growth, industrialisation development and climate change. Conventionally, water pollution derives from numerous sources such as pathogens, organic matter, chemical pollution and salinity[2]. During the past few decades, the impact of chemical pollution has focused mostly on the common "priority" pollutants, particularly those acutely toxic, carcinogenic pesticides and industrial intermediates displaying persistence in the environment[2]. Recently, another emerging group of aquatic chemical pollutants, named pharmaceutical and personal care products (PPCPs) have been receiving increasing attention, including not just prescription drugs and biologics, but also diagnostic agents, "nutraceuticals," fragrances, sunscreen agents, and numerous others[3, 4]. These compounds and their bioactive metabolites can be continually introduced to the aquatic environment by both untreated and treated sewage. Many PPCPs are highly bioactive, water soluble, optically active and all usually occur at trace concentrations in the aquatic environment. However, the continuous introduction of PPCPs into the environment would lead to high, long-term concentrations and promote continual but unnoticed adverse effects on aquatic and terrestrial organisms. More recently, microplastics (< 5 mm) have aroused increasing concern due to their tremendous threats to aquatic species and human beings[5-8]. They not only contribute to accumulation of plastics in the environment, but also act as vectors to spread of micropollutants in the environment[6].

Worldwide, researchers have been accelerating the development of advanced technologies to provide clean drinking water for households and to deal with the contaminated waterbodies.

These water treatment strategies include pressure-driven membrane-based methods, ultrafiltration and microfiltration, biological treatment, oxidation treatment using ozone or chlorine, and treatment with UV radiation. Among these oxidation methods, advanced oxidation processes (AOPs) have been showing outstanding performance for the removal of a wide range of organic pollutants from wastewater attributing to the complete destruction and low selectivity of organic pollutants[3, 9]. Typically, AOPs are involving oxidants and superoxides such as ozone, oxygen, hydroperoxide, and various radicals that are capable of destroying target organics to harmless species such as water and carbon dioxide. Hydroxyl radicals (•OH) have been frequently observed in AOPs, for instance Fenton reaction, UV oxidation and ozonation owing to their superior oxidation ability towards organic pollutants with almost no selectivity[10, 11]. However, the downsides of many •OH related Fenton-like reactions, such as excess sludge production, narrow pH (∼3) requirement and metal leaching, are the bottleneck limits for their further development[12]. More recently, as a promising alternative to •OH, strongly oxidizing sulfate radicals (SO_4 $^{\bullet-}$) have attracted much more attentions for water treatment because they can overcome the drawbacks brought by hydroxyl radical-based systems through the activation of (peroxymonosulfate) PMS or (persulfate) PS[13-15]. Many measures for PMS/PS activation haven been reported such as heating, UV-light irradiation, and catalysis by transition-metal ions, metallic oxides, or carbon-based materials. Among the catalysts used in sulfate radical based AOPs (SR-AOPs), carbon-based nanomaterials stand out owing to the exceptional adsorption capacity, catalysis ability and environmentally friendly nature[16, 17]. More recently, Wang et al. discovered that the heteroatom doping with N, S, P or B into a carbon honeycomb network offers an effective strategy to boost the catalytic activity and stability of pristine carbon materials. Inspired by Wang's work, a recent study reported a one-pot preparation of N doped graphene with a porous structure and transition metal (Ni) encapsulation, and its outstanding performance in adsorptive and

oxidative removal of PPCPs in catalytic SR-AOPs[18-20]. This unique modification of carbon materials with heteroatom doping and metal insertion has be brought not only the improvement in catalysis and stability, but also magnetic properties, which are favourable for magnetic separation and recycling of the carbocatalysts[21].

Our group has carried out several research projects on applying modified nanocarbon catalysts for superoxide activation, which would open up a new prospect for metal free and sustainable wastewater remediation. Despite the great improvements demonstrated within the past few years in our group, there are still undiscovered areas and opportunities to be pursued and these areas indeed inspire the research objectives of this thesis.

1.2 Research objectives

The present study aims to develop the basic knowledge of preparation of robust nanocarbon catalysts with well-designed and controlled morphologies, structure and magnetism for heterogeneous activation of peroxymonosulfate and persulfate to decompose hydrocarbons, pharmaceutical and personal care products, and microplastics in aqueous solution. In the meantime, this research also dedicates to the insight into the intrinsic mechanisms of superoxides (PMS and PS) activation and sulfate radical evolution in nanocarbon catalysis. To this end, the following studies were carried out.

The specific objectives of this research include：

a. Synthesizing high-quality heteroatom (N) doped graphene and single/multi-walled carbon nanotubes in a large scale via facile one-pot green synthesis method.
b. Synthesizing high-quality heteroatom (N) doped graphene and single/multi-walled carbon nanotubes with encapsulated transition metal nanoparticles via facile one-pot green synthesis method.

c. Investigating the catalytic and stability performance for superoxides activation on the synthesized N doped nanocarbon material with transition metal encapsulation for PPCPs degradation in water.
d. Investigating the heteroatom doping effects on nanocarbon catalysts for PMS activation with deliberate materials design and theoretical calculations.
e. Probing the effect of various transition metal precursors on nanocarbon catalysts in terms of morphology, porosity and catalysis.
f. Probing the mechanism unveiling the intrinsic active sites of the carbocatalysis for heterogeneous PMS and PS activations.
g. Investigating the transport and fate of microplastics pollution and the remediation method via a metal-N-nanocarbon catalyst and PMS based AOPs.
h. Determining the effects of reaction parameters, such as catalyst loading, and reaction temperature on the efficiency of degradation.
i. Identifying emerging carbocatalysis and novel oxidation pathways on modified nanocarbon with mechanistic studies.
j. Identifying the degradation intermediates and possible oxidation pathways of emerging aquatic organic pollutants.
k. Identifying the responsible active radicals for organic pollutants degradation in SR-AOPs via quenching experiment and EPR analysis.

1.3 Thesis Outline

According to the specific objectives as listed above, this thesis consists of eight chapters. Each chapter in this thesis is outlined below:

Chapter 1: Introduction

This chapter outlines current wastewater problems and associated solutions, showing how carbon nanomaterials have been applied to address these problems. Objectives and thesis organization are also presented in this chapter.

Chapter 2: Literature review

This chapter provides a comprehensive review and understanding of the reported advanced oxidation processes (AOPs) for wastewater treatment in previous studies, and searches out a reliable strategy to further design new robust nanocarbon materials with optimised catalytic performance. Moreover, this literature review will feature such primary guidelines and relate them to the state of the art in the field.

Chapter 3: Carbocatalytic activation of persulfate for removal of antibiotics in water solutions

This chapter describes a facile method for preparation of nitrogen doped reduced graphene oxide (N-rGO) using urea as a nitrogen precursor. The prepared metal-free N-rGO is able to efficiently activate persulfate (PS) to produce reactive radicals for degradation of an antibiotic, sulfachloropyridazine (SCP). This study suggests a green remediation for removal of the antibiotics in wastewater without producing any heavy metal leaching as the secondary contamination.

Chapter 4: Nitrogen-doped bamboo-like carbon nanotubes with Ni encapsulation for persulfate activation to remove emerging contaminants with excellent catalytic stability

This chapter reports that nitrogen-doped bamboo-like carbon nanotubes encapsulated with nickel nanoparticles (Ni@NCNTs) were fabricated by a one-pot pyrolysis route. In addition, it demonstrated the application of Ni@NCNTs as both adsorbents and catalysts in antibiotic pollutant removal. The nitrogen modification and Ni nanoparticle encapsulation enhanced both adsorption capacity and catalytic ability of Ni@NCNTs and proved to be a promising alternative to metal oxides and other carbon catalysts.

Chapter 5: Catalytic degradation of antibiotics by metal-free catalysis over nitrogen doped Graphene

This chapter describes the direct degradation of antibiotic SCP, one of sulfonamides, by PMS with high efficiency. A comprehensive investigation by in situ EPR, selective radical quenching, and PMS decomposition was performed, revealing the direct and nonradical reactions between PMS and SCP in PMS-based and non-catalytic system without producing free radicals such as $^{\bullet}OH$ and $SO_4^{\bullet-}$. The findings show that the direct oxidation of SCP with

PMS can be used to selectively convert the toxic antibiotics to less or non-toxic organic substances whereas the robust carbocatalysis would contribute to the practical wastewater remediation by metal-free AOPs.

Chapter 6: Magnetic Ni-Co alloy encapsulated N-doped carbon nanotubes for catalytic membrane degradation of emerging contaminants

This chapter describes a facile method for preparation of nitrogen-doped carbon nanotubes encapsulated with Ni-Co alloy nanoparticles (NiCo@NCNTs) by using Ni/Co salts with dicyandiamide as metal and carbon precursors, respectively. The synergistic effect of nitrogen doping and metal alloy encapsulation significantly enhanced the catalytic activity and stability of NCNTs in catalytic activation of PMS for purification of an emerging pollutant, ibuprofen.

Chapter 7: Catalytic degradation of microplastics by sulfate radicals over magnetic carbon nanosprings

This section contributes to a pioneering investigation by integrating carbocatalytic oxidation and hydrothermal hydrolysis for synergistic degradation of microplastics (MPs) over nanocarbon catalysts. Spring-like carbon nanotubes were successfully fabricated bearing high-level nitrogen doping and transition metal anchoring. The novel and robust nanocarbon exhibited an outstanding catalytic performance in activation of PMS to generate sulfate radical for MPs degradation and the spiral-shape architecture guaranteed its superb stability in a hydrothermal environment.

Chapter 8: Conclusions and perspectives

This chapter highlights the meaningful findings in this study and proposes suggestions for further research in the field.

1.4 References

1. Schwarzenbach, R. P.; Egli, T.; Hofstetter, T. B.; Gunten, U. v.; Wehrli, B., Global Water Pollution and Human Health. Annual Review of Environment and Resources 2010, 35, (1), 109-136.

2. Vörösmarty, C. J.; McIntyre, P. B.; Gessner, M. O.; Dudgeon, D.; Prusevich, A.; Green, P.; Glidden, S.; Bunn, S. E.; Sullivan, C. A.; Liermann, C. R.; Davies, P. M., Global threats to human water security and river biodiversity. Nature 2010, 467, (7315), 555-561.

3. Andreozzi, R.; Caprio, V.; Insola, A.; Marotta, R., Advanced oxidation processes (AOP) for water purification and recovery. Catalysis Today 1999, 53, (1), 51-59.

4. Vilhunen, S.; Sillanpää, M., Recent developments in photochemical and chemical AOPs in water treatment: a mini-review. Reviews in Environmental Science and Bio/Technology 2010, 9, (4), 323-330.

5. Andrady, A. L., Microplastics in the marine environment. Marine Pollution Bulletin 2011, 62, (8), 1596-1605.

6. Cole, M.; Lindeque, P.; Halsband, C.; Galloway, T. S., Microplastics as contaminants in the marine environment: A review. Marine Pollution Bulletin 2011, 62, (12), 2588-2597.

7. Sussarellu, R.; Suquet, M.; Thomas, Y.; Lambert, C.; Fabioux, C.; Pernet, M. E. J.; Goïc, N. L.; Quillien, V.; Mingant, C.; Epelboin, Y.; Corporeau, C.; Guyomarch, J.; Robbens, J.; Paul-Pont, I.; Soudant, P.; Huvet, A., Oyster reproduction is affected by exposure to polystyrene microplastics. Proceedings of the National Academy of Sciences of the United States of America 2016, 113, (9), 2430-2435.

8. Li, H.-X.; Ma, L.-S.; Lin, L.; Ni, Z.-X.; Xu, X.-R.; Shi, H.-H.; Yan, Y.; Zheng, G.-M.; Rittschof, D., Microplastics in oysters Saccostrea cucullata along the Pearl River Estuary, China. Environmental Pollution 2018, 236, 619-625.

9. Klavarioti, M.; Mantzavinos, D.; Kassinos, D., Removal of residual pharmaceuticals from aqueous systems by advanced oxidation processes. Environment International 2009, 35, (2), 402-417.

10. Oturan, M. A.; Aaron, J.-J., Advanced Oxidation Processes in Water/Wastewater Treatment: Principles and Applications. A Review. Critical Reviews in Environmental Science and Technology 2014, 44, (23), 2577-2641.

11. Neyens, E.; Baeyens, J., A review of classic Fenton's peroxidation as an advanced oxidation technique. Journal of Hazardous Materials 2003, 98, (1), 33-50.

12. Wang, N.; Zheng, T.; Zhang, G.; Wang, P., A review on Fenton-like processes for organic wastewater treatment. Journal of Environmental Chemical Engineering 2016, 4, (1), 762-787.

13. Anipsitakis, G. P.; Dionysiou, D. D., Degradation of Organic Contaminants in Water with Sulfate Radicals Generated by the Conjunction of Peroxymonosulfate with Cobalt. Environmental Science & Technology 2003, 37, (20), 4790-4797.

14. Ji, Y.; Fan, Y.; Liu, K.; Kong, D.; Lu, J., Thermo activated persulfate oxidation of antibiotic sulfamethoxazole and structurally related compounds. Water Research 2015, 87, 1-9.

15. Lee, H.; Lee, H.-J.; Jeong, J.; Lee, J.; Park, N.-B.; Lee, C., Activation of persulfates by carbon nanotubes: Oxidation of organic compounds by nonradical mechanism. Chemical Engineering Journal 2015, 266, 28-33.
16. Zhang, J.; Su, D.; Zhang, A.; Wang, D.; Schlögl, R.; Hébert, C., Nanocarbon as robust catalyst: Mechanistic insight into carbon-mediated catalysis. Angewandte Chemie - International Edition 2007, 46, (38), 7319-7323.
17. Indrawirawan, S.; Sun, H.; Duan, X.; Wang, S., Nanocarbons in different structural dimensions (0–3D) for phenol adsorption and metal-free catalytic oxidation. Applied Catalysis B: Environmental 2015, 179, 352-362.
18. Duan, X.; Sun, H.; Wang, Y.; Kang, J.; Wang, S., N-Doping-Induced Nonradical Reaction on Single-Walled Carbon Nanotubes for Catalytic Phenol Oxidation. ACS Catalysis 2015, 5, (2), 553-559.
19. Tian, W.; Zhang, H.; Duan, X.; Sun, H.; Tade, M. O.; Ang, H. M.; Wang, S., Nitrogen- and Sulfur-Codoped Hierarchically Porous Carbon for Adsorptive and Oxidative Removal of Pharmaceutical Contaminants. ACS Applied Materials & Interfaces 2016, 8, (11), 7184-7193.
20. Kang, J.; Zhou, L.; Duan, X.; Sun, H.; Wang, S., Catalytic degradation of antibiotics by metal-free catalysis over nitrogen-doped graphene. Catalysis Today 2018.
21. Wang, S.; Sun, H.; Ang, H. M.; Tadé, M. O., Adsorptive remediation of environmental pollutants using novel graphene-based nanomaterials. Chemical Engineering Journal 2013, 226, 336-347.

Chapter 2 Literature Review

2.1 Introduction

Water, as one of the most fundamental resources for life, is precious for all human civilization. In recent years, globally fresh water shortage has become increasingly intense due the extensive water pollutions that occurred as a critical challenge worldwide[1, 2]. Due to the fast-paced development of pharmaceuticals and personal care products (PPCPs), many newly emerged organic pollutants have attracted tremendous attention[3]. Unlike traditional pollutants, some of these PPCPs, such as antibiotics, hormones, antimicrobial agents, etc., are extremely reluctant to be removed from water due to their intrinsic properties such as high water solubility, recalcitrant to natural biodegradation and trace concentration[4, 5]. Substantial studies have confirmed the detection of various worrying PPCPs, for example antibiotics and anti-inflammatory drugs in a wide range of aqueous environment[4]. Regardless their low concentration, a continuous and long-term exposure to these toxic organics could accelerate the process of bio-accumulation and lead to severe adverse effects on both wildlife animals and humans. Being exposed in antibiotics contaminated situation, for instance, could accelerate the persistence or emergence of antibiotic resistance genes (ARGs), which poses a potential harm to the ecosystem. Liu et al. reported that a common PPCPs "sulfonamides", which have been widely discovered in both wastewater plants and natural waters, can cause detrimental damages to the ecosystem if entering into the local food chain, such as endocrine disruption, development of antibiotic-resistance and potential enhanced toxicity of chemical mixture[6].

A large variety of water remediation strategies, such as physical, biological and chemical means, have been developed to remove the pollutants from water[7, 8]. Physical methods like filtration and flotation that can be useful for heterogeneous pollution, but when it comes to homogeneous water pollution, the processes merely transfer soluble substances like PPCPs from one media to another without degradation[5, 9]. Biological methods are believed to be an

eco-friendly and effective way to decompose a wide variety of pollutants into harmless or less hazardous compounds without expensive inputs of chemicals and energy. However, the role of biodegradation in many PPCPs removal is much hindered due the high toxicity and drug resistance. Recently, advanced oxidative processes (AOPs) that involve the in-situ production of highly reactive oxidant species such as hydroxyl and sulfate radicals have been developed as an increasingly important type of technology[9, 10]. The optimised AOPs shows great potentials in decomposing organic molecules regardless of the strength of the chemical bonding and intermolecular force, therefore, the complete mineralization of a wide variety of recalcitrant organic pollutants in wastewater that reluctantly to be removed by physical and biological means now can be readily achieved[11-13].

Ozonation has long been applied as one of the most effective chemical oxidation strategies. Recently various ozone originated AOPs that utilize hydroxyl radicals have attracted many attentions due to its ability to degrade organic pollutants such as pesticides[14]. It is reported that the direct reaction between ozone and organics is much less significant when comparing with the indirect reaction where the degradation of organics was achieved by the decomposition and formation of hydroxyl radicals[9, 15]. Hydroxyl radicals are often regarded as powerful nonselective oxidants that have high redox potential and less influence from the target organic molecules[16]. Ozone can be decomposed to form hydroxyl radicals regardless of the solution pH value, nonetheless the ozone derived AOPs are significantly faster at a higher pH, which attributes to a faster hydroxyl radical production to be triggered at a higher pH, therefore an increased hydroxyl radial exposure[17]. It is worth to notice that its dependence on solution pH and high operating cost (ozone generation mainly) are often believed to undermine the wide application and future development[18, 19]. To overcome the pH restriction, H_2O_2, a relatively inexpensive, highly soluble and readily available chemical, is often added at lower pH solution

at an O_3/H_2O_2 ratio of 2:1 to ozonation to accelerate the decomposition of ozone and to boost the formation of hydroxyl radicals[11].

Photooxidation without an oxidant such as ozone and H_2O_2 has very limited application to degrade organics because they are mostly sensitive to the light between the wavelength of 200 and 300 nm. It is usually practical for degrading a single target organic with specific light preference at a mild mineralization level. In many cases, the traditional ozone and hydrogen peroxide oxidation of organic pollutants hardly undergo complete oxidation with only carbon dioxide and water as final products. Many degradation intermediate products would often remain in the solution, which could be as toxic as or more toxic than the mother compounds. By supplementing the reaction with ultraviolet (UV) assistance, complete oxidation on both initial organics and their intermediates as well as compounds that are immune to ozone or H_2O_2 oxidation can be largely achieved. It is reported that the UV radiation (254nm) accelerates the decomposition of ozone and hydroperoxide molecules, where the hydroxyl production from ozone is about twenty times faster than the formation of hydroxyl radicals from H_2O_2[20]. In practice, the combination of O_3, H_2O_2 and UV has showed to be the best in terms of hydroxyl radical production rate and economical energy input[21, 22].

Fenton reaction was first discovered more than a century ago, however, its wide application on wastewater treatment had only started to attract attention in recent years[22, 23]. Because the hydroperoxide molecules cannot efficiently absorb light in a range of 200-300 nm and are inactive to the wavelength over 300 nm, the application of H_2O_2/UV system is very limited for dealing pollutants with high UV absorbance or at high concentration[23, 24]. Typically, Fenton reactions applying H_2O_2 as an oxidant and ferrous salt as a homogeneous catalyst to generate hydroxyl radicals can be used to degrade a wide range of contaminants. However, there are some innate problems in the application of Fenton's reagent, for example, the addition of iron salts can cause the precipitation of iron hydroxide at neutralisation[25]. The production of sludge

may contain organic substances and heavy metals as byproducts of the organic decomposition process and has to be deposited or treated at high costs. In addition, Fenton reaction suffers from strict environmental requirements, such as low pH (pH≈3) and low recovery efficiency of the catalyst. In some cases, external activation methods are required, such as electrolytic stimulation and UV radiation, in order to enhance the activation of hydroperoxide[26].

More recently, as a promising substitute to hydroxyl radical-based AOPs, sulfate radical originated advanced oxidative processes (SR-AOPs) have attracted extensive attention, attributing to its outstanding oxidative properties. Sulfate radicals have a greater oxidation potential (2.5 - 3.1 V) than •OH (1.8 - 2.7 V) and are hence highly effective for recalcitrant organic pollutants destruction[27, 28]. The generation of sulfate radicals can be mainly achieved by the activation of two oxidants, persulfate (PS) or/and peroxymonosulfate (PMS), which are cheaper, more ecofriendly and lower requirement for storage[29]. Analogously, the activation strategies of PMS/PS can be various, including UV-light irradiation, heating, homogenous and heterogeneous catalysts[30]. Moreover, sulfate radicals can maintain high oxidative efficiency in a wider range of pH environment, which makes it more applicable for real life situations[18, 31].

In recent years, amongst the catalysts applied in SR-AOPs, carbon-based nanomaterials, such as graphene, carbon nanotubes and nanodiamonds, have won more favours than their metal counterparts have, attributing to the unique adsorption capacity, large theoretical surface area, catalysis ability and environment-benign nature[32-34]. By applying a carbon-based catalyst on SR-AOPs can fundamentally avoid metal leaching and other associated secondary contamination[35].

However, it is worth to notice that pristine carbocatalysts often suffer from mediocre catalytic activity and substandard catalytic stability in heterogeneous activation reaction. To tackle such problems, Wang et al. have found that by doping heteroatoms such as nitrogen, sulfur, phosphorous and boron into carbon honeycomb networks could largely boost the stability of

carbon catalysts[20, 35, 36]. Since many nanocarbon materials such as graphene and carbon nanotubes are perfect scaffolds for molecular engineering of the heteroatom (e.g., N, B, and P) active sites and introducing new properties attributing to their excellent conductivity, high surface, and honeycomb lattice. In addition, a wide range of researchers have proved that anchoring transition metal nanoparticles on carbon catalysts can further improve the catalytic activity, due to the fact that metals are enriched with electrons to endow the carbons with high electron conductivity and electron-transfer capacity[37]. However, the current researches on metal decoration were still mostly dedicated to nanocarbon catalysts with brief introduction on the derived materials and the lack of environmental consideration needs to be further addressed. Moreover, the rapid development of modified carbon catalysts has promoted the creation of newer materials with intriguing properties during the past several years. Herein, we critically reviewed recent advances in the fabrication of modified nanostructures based on heteroatom doping and metal anchoring, dedicating to providing insights into the structure optimisation strategies for carbon-derived catalysts. Nanocarbon materials with unique structure properties and environmental-friendly nature show great potential in a wide variety of fields, thus the promising outlook and challenges are presaged. In this literature review, the similarity or overlapping with other available reviews is greatly avoided.

2.2 Advance oxidation processes

Wide-ranging organic compounds have been discovered in industrial and urban wastewaters. Many of these discharged compounds can irretrievably pose serious problems in the biological treatment systems because of their resistance to biodegradation or toxic effects on microbial processes, including artificial organic chemicals and naturally occurring substances etc. Consequently, it is urgent to find and employ substitute treatment technologies which are sophisticated on oxidizing or transforming recalcitrant organic molecules into less or no toxic substances for further biodegradation. Among these wastewater treatments, advanced

oxidation processes have been widely applied for the treatment of wastewater containing refractory organic compounds such as insecticides, surfactants, dyes, pharmaceuticals and endocrine disrupting chemicals. In addition, advanced oxidation processes have been showing promising effectiveness as pretreatment methods for minimizing the concentrations of toxic organic compounds that could inhibit biological wastewater treatment processes. For that reason, advance oxidation processes are considered to constitute significant, promising, competent, and ecofriendly techniques to be established to primarily eliminate toxic organic pollutants from both natural water systems and wastewaters. Typically, advanced oxidation processes are founded on the *in situ* production of a variety of powerful oxidizing agents, such as hydroxyl radicals ($^{\bullet}OH$)[16], singlet oxygen ($^1O_2$)[38, 39] and sulfate radicals ($SO_4^{\bullet-}$)[19], attained at an adequate concentration to efficiently purify waters[12]. The *in situ* formation of these radicals can be realized by various measures, including chemical, photochemical, sono-chemical, and electrochemical reactions. In this part, a detailed and inclusive description of the recent literatures regarding the main categories of AOPs would be presented[16]. Moreover, the mechanisms, performances, advantages, downsides, and applications of various advanced oxidation processes to the purification treatment of wastewater and natural water bodies have also been discussed and compared.

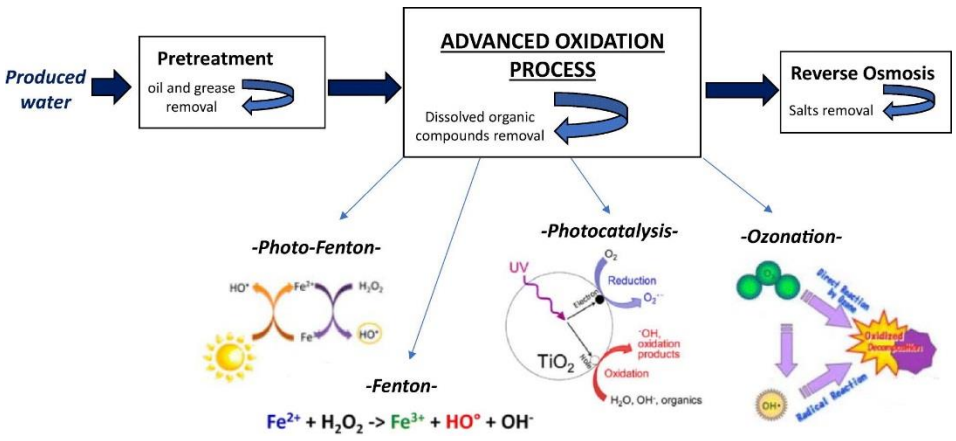

Figure 2.1. Flowchart of advanced oxidation processes[40].

2.2.1 Fenton and Fenton derived advanced oxidation processes (AOPs)

Fenton and Fenton derived reactions, as typical AOPs have been studied as an efficient organic wastewater treatment technique that are relied on the *in situ* production of hydroxyl radicals (•OH), which present a powerful oxidation capability with redox potential of 2.81 V comparing to standard hydrogen electrode. In Fenton treatment, as shown in Figure 2.1, a refractory organic compound can be oxidized by •OH to either sub-molecular organics or to carbon dioxide (CO_2) and water (H_2O) when complete mineralization occurs[12, 16].

Conventionally, Fenton reaction requires the catalyst, ferrous ions (Fe^{2+}), to activate the oxidant, hydrogen peroxide (H_2O_2), to generate •OH, because the mediocre oxidative potential of H_2O_2 (1.2 V) itself can hardly degrade most of the refractory organic pollutants. In the H_2O_2 activation process by ferrous ions, the •OH is produced through a number of complex reactions, as shown in Eqs 2.1 and 2.2.[16].

$Fe^{2+} + H_2O_2 \rightarrow Fe^{3+} + {}^{\bullet}HO + OH^{-}$ Eq. (2.1)

$Fe^{3+} + H_2O_2 \rightarrow Fe^{2+} + HO_2^{\bullet} + H^{+}$ Eq. (2.2)

It is noteworthy that only a low concentration of Fe^{2+} catalyst is required because this dyadic ion can be reproduced from the Fenton-like reaction, Eq. 1, between ferric iron ions and peroxide. It was reported that $HO_2^{\bullet}$ was proved to have a much lower redox potential and considerably less reactive towards POPs than •HO. However, the reproduction of Fe^{2+} can be promoted by the reduction of ferric iron ions with $HO_2^{\bullet}$, consequently improving the POPs degradation efficiency. In addition, several features, for example temperature, solution pH and hydroperoxide and catalyst concentrations, can dramatically influence the Fenton's oxidizing performance. Haber *et al.* reported that the Fenton process can be effectively employed by the catalytic behavior of the Fe^{3+}/Fe^{2+} pair given the optimal pH value of the contaminated water medium is about 3[41]. Due to the transient lifetime of hydroxyl radicals, it can only be *in situ* generated via a number of methods, for instance, peroxonation (a combination of H_2O_2 and

O_3), photolysis and sonochemical, catalysts and photo-catalysts (such as Fe^{2+} and Fe^{2+}/UV), and electrochemical are widely used approaches to yield hydroxyl radicals. In the following paragraphs, a summarized description of major AOPs for wastewater treatment based on the mechanisms of hydroxyl radical production have been in detail presented[26].

2.2.1.1 Peroxonation

The amalgamation of ozone and H_2O_2 (peroxonation) can boost the generation process of oxidizing radicals. Santana *et al.* reported that the peroxonation could be more effective than ozonation and H_2O_2 along due to the effect of accelerating the disintegration rate of ozone in aqueous solution, which generates abundant amount of hydroxyl radicals[11]. The mechanism is shown in Eq.2.3 and this rapid reaction happened between peroxide, which is in ionized form (HO_2^-, pK_a = 11.6), and ozone resulting in the production of $^{\bullet}OH$. Additionally, the hydroxyl radicals can also be produced by the reaction of $^{\bullet}OH$ with $HO_2^{\bullet}$. It is worth to notice that the optimum experimental conditions of peroxonation are pH=7.6 and H_2O_2:O_3 ratio=0.5, which is a more neutral and closer to real life situation[42]. The ratio between peroxide and ozone was suggested to be kept constant during the reaction and the H_2O_2 residual concentration should be kept below 0.5 mg L^{-1} in the treated solution.

$O_3 + HO^-_2 \rightarrow O_2 + {}^{\bullet}OH + O2^{-\bullet}$ Eq. (2.3)

The peroxonation process has been extensively used to the elimination of micropollutants and toxic organic compounds, pharmaceuticals and personal care products (PPCPs) found in various water systems. The oxidation system involved peroxide and ozone can be introduced between a filtration on sand and active carbon in a reactor through running water. The principal highlights of peroxonation reactions include that it is easy to operate and that it has good bactericide activity. For example, Ikehata *et al.* reported that peroxonation can successfully applied to eliminate several pesticides, such as phenlyureas, organochlororines, and trianzines, from wastewater plants[43]. However, the limitations of peroxonation in practical application

should also be noticed, which are the low water solubility of O_3, the significant energy consumption, and the high sensitivity to some factors such as pH, temperature, and the possible side reaction which are also depriving oxidizing radicals[43].

2.2.1.2 Photo-Fenton

Photochemical technologies are considered to be simple, environmental friendly, comparatively economical and more competent in the general than chemical AOPs. Typically, UV radiations have been equipped with strong oxidants, including hydroperoxide and ozone. In some research, catalysts such as Fe^{3+} and TiO_2 have also been applied to degrade and destroy pollutants[25]. There are three main reactions occurred during the degradation process, , excitation upon UV irradiation and degradation of toxic organic molecules, oxidation by direct reaction with H_2O_2 and O_3, and oxidation by photocatalysis[25].

To avoid the troublesome sludge caused by Fe^{3+} and other environmental issues, acidic condition requirement is associated with conventional Fenton reaction. Hydrogen peroxide has been photolysised by UV radiations at particular wavelengths ranging from 200 to 300 nm, generating the hemolytic abscission of the double oxygen bond of the peroxide molecule and resulting in the generation $^{\bullet}OH$ radicals which can further facilitate the decomposition of $^{\bullet}OH$ by subordinate reactions. A series of successive reaction steps can take place, Eqs. 2.4 - 2.10[24, 25, 44].

$H_2O_2 + h\nu \rightarrow 2^{\bullet}OH$ Eq. (2.4)

$^{\bullet}OH + H_2O_2 \rightarrow H_2O + HO^{\bullet}_2$ Eq. (2.5)

$HO_2^{\bullet} + H_2O_2 \rightarrow {}^{\bullet}OH + H_2O + O_2$ Eq. (2.6)

$^{\bullet}OH + HO^{-}_2 \rightarrow HO^{\bullet}_2 + OH^{-}$ Eq. (2.7)

$2HO_2^{\bullet} \rightarrow H_2O_2 + O_2$ Eq. (2.8)

$^{\bullet}OH + HO^{\bullet}_2 \rightarrow H_2O + O_2$ Eq. (2.9)

$2^{\bullet}OH \rightarrow H_2O_2$ Eq. (2.10)

Unlike classic Fenton, photo Fenton reaction is optimized in basic solution at pH greater than 10, which is due to the production of $HO^{\bullet}_2$, and this H_2O_2 ionization process can efficiently absorb UV radiations and produce reactive oxygen species. It is worthwhile to notice that a major drawback of the photo Fenton is the molar absorption coefficient of peroxide is comparatively low in the UV wavelength range, as a result, it is often required high dosage of H_2O_2 for an effective degradation of toxic organic contaminants. Many studies have examined the efficiency of H_2O_2/UV for the degradation of organic contaminants like benzene, trichloroethylene, tetrachloroethylene, etc. Alaton *et al.* have investigated and reported the degradation efficiency of the H_2O_2/UV process is much higher than that of conventional AOPs such as peroxonation and TiO_2/UV for the degradation of a combination of monochlorotriazine-type dyes and numerous coloring supplementary chemicals. [13]

In another study, researchers investigated employment of the photo derived Fenton oxidation systems to the treatment of contaminated marine wastewater with hydrocarbons, as shown in Figure 2.2a. In their study, the photo derived Fenton process utilized a typical Fenton system with the assistance of UV radiation. Firstly, the classic Fenton reaction (Eq. 2.1) is carried on and then followed by UV irritation on peroxide as shown in Eq.2.11, in which the ferric ions (Fe^{3+}) and hydroxyl radicals produced in the thermal Fenton reaction are photocatalytically transformed back to ferrous ions. As shown in Figure 2.2b, the photoFenton reaction has demonstrated to be an highly effective process for the oxidation of organic contaminants in water solution, where the organic (in this case, commercial gasoline) reached complete removal in just three to five hours. At the end of the reaction, the lowest performance of oxidation for the sequences of experiments was 80% of removal. Furthermore, in an optimized oxidation condition, the photo-degradation successfully achieved almost complete mineralization. Later on, the experiment was done with the presence of a moderate pressure mercury lamp in a borosilicate glass photochemical reactor and the results revealed that such a system could take

advantage of solar energy as the source of photons in the oxidation process of toxic organic contaminated wastewaters.

$Fe^{3+} + H_2O\ (h\nu) \rightarrow Fe^{2+} + H^+ + HO^{\bullet}$ Eq. (2.11)

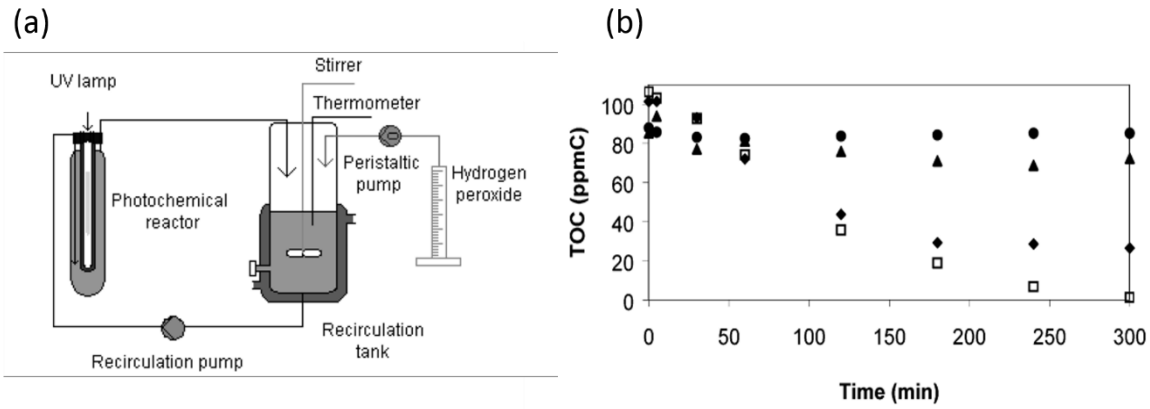

Figure 2.2. (a) Scheme of the photochemical reactor, (b) Influence of UV radiation, sodium chloride concentration, and Fenton reagents on the commercial gasoline photocatalyzed degradation in water at 30 °C; photo-Fenton process(solid rhombus); photo-Fenton process(hollow square); thermal Fenton reaction (solid triangle), and b photolysis(solid circle).

However, there are some technological issues: it is important to mention the photo-Fenton process also has its drawbacks. Firstly, the stability of metal-based catalyst is directly associated to the metal leaching, which sequentially is affected by the operating perimeters engaged, especially the effect of solution pH[25, 44]. It is commonly known that the leaching process of active metal species can not be simply understood as a dissolution reaction that only correlated to the acidic condition of the reaction solution. Nevertheless, it is more likely to be triggered by a more sophisticated mechanism in which the ratio of peroxide and active species within the course of the catalytic run plays an crucial role. For this reason, various methods have been practiced to address the low catalytic stability and the corresponding metal leaching issues, which will be further explained in later chapters. Another problem is the use of visible radiation. The ultraviolet band occupied only 3-5% of the solar light energy that reaches our

planet and artificial ultraviolet apparatus often consume large quantities of electrical power, which greatly limits the large-scale industrial application. Therefore, it is of significance to develop catalysts to be used in the sunlight or visible light irradiation rather than using the ultraviolet as the only source for heterogeneous photo-Fenton process in wastewater treatment. In a recent study, Chen *et al*. fabricated an iron-pillared montmorillonite catalyst, which was proved predominantly efficient under visible light radiation where the wavelength is greater than 420 nm. The capability of such a material was believed to be attributed to the substantial absorption in long wavelength region up to 600 nm, as showed by the UV-Vis diffuse reflectance spectrum of the catalyst [45].

Moreover, another non-negligible feature deserves to be considered is the environmental implication of the treatment process, for example, the toxicity of the degradation intermediates. The purpose of AOPs is to remove harmful compounds from water bodies, thus the degradation intermediates should be non-toxic or at least less toxic than the parent compound. Some studies have reported, the target compound is not obstinate in natural waters, however, the daughter byproducts generated during the degradation process may lengthen or even increase the detrimentally toxic effect of contaminants[46]. Consequently, performing microtoxicity tests is a simple way to evaluate the plausibility of photo-Fenton AOPs, which involves testing the inhabitation of some microorganisms, such as algae and bacteria.

2.2.1.3 Electro-Fenton/sono-Fenton

The combination of electrochemical processes and Fenton-like processes is considered as an effective way to improve the oxidation reaction during wastewater treatment. Many studies have investigated electro-Fenton (EF) processes and suggested the oxidation capacity of electro-Fenton processes are closely related to the scission of (OH)-O-center on the anode surface and in the medium where Fenton reaction takes place. They proved that electrochemical

process has many technical advantages such as environmental compatibility, flexibility, high efficiency, amenability of automation and safety because they are operated at moderate conditions[47, 48].

Brillas *et al.* reported that the application of electro-Fenton on elimination of industrial chemicals. In his work, the possible effect of experimental conditions, the decomposition kinetics of target organic pollutants, and the matching degradation byproducts were discussed[23]. In electro-Fenton processes, the sources of the oxidant and catalyst can be various. As shown in Eq. 2.12, for both homogeneous and heterogeneous oxidation processes, hydroperoxide can be produced *in situ* through a typical electrochemical process where the dissolved O_2 molecules are reduced by a double electron reduction and the reaction is predominantly taking place on the cathode surface.

$O_2 + 2H^+ + 2e^- \rightarrow H_2O_2$ Eq. (2.12)

There are several benefits of the *in situ* H_2O_2 production by electrochemical processes, such as the improvement in the removal rate of organic pollutants, a reduction in the cost, and a decrease in the risks related with transportation. Moreover, during the electro-Fenton processes, the produced H_2O_2 can be consumed prior to the decomposition to water and oxygen. In addition, the homogeneous metal catalysts, M^{n+}, such as Fe^{2+}, Cu^{2+}, Mn^{2+}, and Co^{2+}, can be supplied in various routes such as by leaching out the matching metal anode directly and reproduced on the surface of cathode after external addition of metal ion, Eq.2.13. Due to these advantages, an extensive variety of approaches have been established for homogeneous EF processes that can be categorized by differentiating the H_2O_2 source and the catalyst.

$M^{(n+1)} + e^- \rightarrow M^{n+}$ Eq. (2.13)

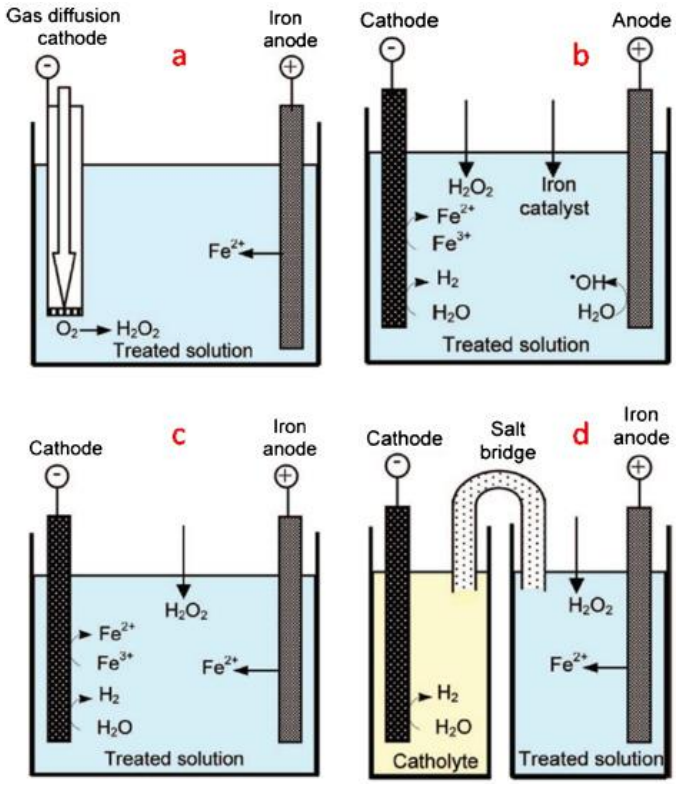

Figure 2.3. Scheme of the typical electro-Fenton system.[17]

One drawback of EF process is the requirement of acidic reaction environment, and this is because the homogeneous metal ions can easily precipitate in alkaline and even neutral conditions, which would lead to the retardation or termination of the oxidation reaction. To tackle such a problem, Liu *et al*. synthesized a metal oxide and graphite hybrid to overcome the dependence on low pH environment, and their study showed that the degradation of organic pollutants could be achieved within a wide pH range[49].

2.2.2 Sulfate radical based AOPs

Recently, advanced oxidation processes associated with sulfate radicals, SR-AOPs, have demonstrated a superior oxidation ability towards organics to conventional Fenton and Fenton-like AOPs owing to a series of advantages. Firstly, sulfate radicals present a comparable or even higher oxidation potential (2.5V to 3.1V vs. NHE) than hydroxyl radicals (2.8 V). In addition, sulfate radicals possess a wider selectivity that can more effectively achieve complete

degradation through electron transfer with organic complexes that contain unsaturated bonds or aromatic π electrons. Meanwhile, hydroxyl radicals could also react with different background constitutes by hydrogen abstraction or electrophilic addition at high reaction rates. [50] Moreover, sulfate radicals as a dominant oxidizing species, is able to oxidize organics efficiently over a wide pH range (2-8), which can adapt better than hydroxyl radicals in neutral and alkaline environment. Moreover, the half-life period of sulfate radicals is reported to be 30-40 μs, as a result enabling $SO_4^{\bullet-}$ to have sufficient time for mass transfer and better interact with target organics than $^{\bullet}OH$ [50-52].

Typically, $SO_4^{\bullet-}$ can be generated from peroxymonosulfate (PMS, HSO_5^-) or persulfate (PDS, $S_2O_8^{2-}$) activation reaction. Oxone, a commercial name of potassium peroxymonosulfate ($2KHSO_5 \cdot KHSO_4 \cdot K_2SO_4$), is a multipurpose and ecofriendly oxidant that has been widely utilized for bleaching, cleaning and disinfection and more importantly as a favourable source of PMS[53, 54]. In terms of PMS and PDS activation reaction, a large variety of activation approaches have been reported, such as chemical, thermal, photochemical, sono-chemical and electrochemical processes. Due to the fact that most of these methods are very familiar to Fenton and Fenton-like processes, which have been explained in aforementioned text, in this part, we tend to emphasis on the catalyst induced activation processes.

2.2.2.1 Thermal activation

Thermal activation could initiate persulfate degradation to generate sulfate radicals that can further undergo radical interconversion to produce hydroxyl radicals in basic environment. The radicals ($SO_4^{\bullet-}$ / $^{\bullet}OH$) can be present either individually or simultaneously in the persulfate thermal activation system, Eqs 2.14 and 2.15.

$$S_2O_8^{2-} \xrightarrow{\Delta} 2SO_4^{\bullet-} \quad (E^o\ (SO_4^{2-}/\ SO_4^{\bullet-}) = 2.4V) \qquad \text{Eq. (2.14)}$$

$$SO_4^{\bullet-} + H_2O \rightarrow OH^{\bullet} + SO_4^{2-} + H^+ \qquad \text{Eq. (2.15)}$$

In our recent study, during the PDS thermal activation experiment, the decomposition reaction rates increased dramatically with the raised temperatures from 5 to 75 ^{o}C[31]. The activation energy was shown to be 50 kJ/mol with a high coefficient of determination (R^2) of 0.99. This can be attributed to production of hydroxyl radicals via the water oxidation, which has been demonstrated by both radical capture and theoretical predictions. In addition, the radical evolution study indicates that both hydroxyl and sulfate radicals were detected in the solution, and the production of hydroxyl radicals (Figure 2.4) is responsible for the improved mineralization of the target organic and its degradation intermediates.

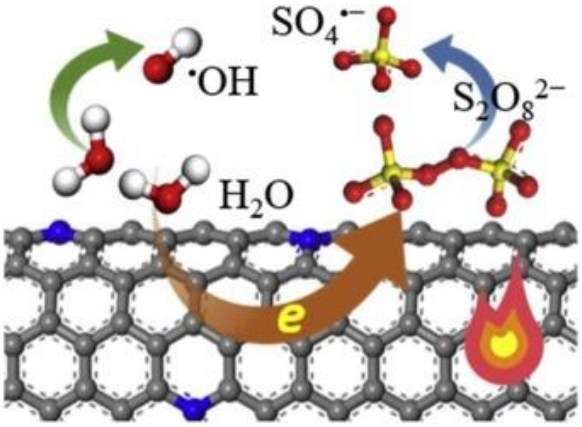

Figure 2.4. A mechanistic illustration for radical evolution by heat assisted PDS activation over nitrogen doped carbon nanotubes[31].

2.2.2.2 Radiation activation

Photochemical degradation of persistent organic contaminants in water solution by use of persulfate ion have been widely studied. Photolysis of PMS or PDS generates highly oxidative sulfate radical anions $SO_4^{\bullet-}$, which can be effectively applied to decompose organics, Eq. 2.16 and 2.17. PMS activated by UV was reported to produce both sulfate and hydroxyl radicals though the cleavage of the double oxygen bond. The generation of sulfate radicals from PMS irradiated by a pulsed laser at λ=248 nm and at λ=248 nm accessible in the form of HSO_5^- were 19 $M^{-1}cm^{-1}$ and 12.5 or 14 $M^{-1}cm^{-1}$, accordingly. Ying *et al.* reported that the generation of

both sulfate and hydroxyl radicals in the UV/PMS system was able to efficiently degrade a refractory organic, benzoic acid[55]. The degradation of benzoic acid was proved to be improved largely as the pH increased from 8 to 11, therefore, the UV/PMS system could be more appropriate for the application to enhance the degradation of organic pollutants under alkaline condition. In addition, Xue and Armah investigated the removal of cylindrospermopsin (CYN) by UV-254 nm mediated advanced oxidation processes and compared the degradation efficiency among UV/PDS, UV/PMS and UV/H_2O_2. The results showed that the UV/PDS presented the highest CYN degradation rate, followed by UV/PMS, given the same molar concentration of the oxidants. It was also proposed that certain radical quenchers, such as natural organic matter and chlorides in the tap water or in wastewaters could pose more inhabitation of the oxidation of CYN on the UV/H_2O_2 than the other two SR-AOPs systems. The results suggested the wider application of UV initialised sulfate AOPs than UV/Fenton like system.

$HSO_5^-/SO_5^{2-} + h\nu \rightarrow SO_4^{\bullet-} + {}^{\bullet}OH$ Eq. (2.16)

$S_2O_8^{2-} + h\nu \rightarrow 2SO_4^{\bullet-}$ Eq. (2.17)

Other radiation methods such as gamma ray have also been proved to be able to activate oxidants, PDS and PMS, however fewer investigations have been conducted. For instance, in the "γ" irradiation process, γ-ray with high energy shows great potential to activate PDS and PMS by the fission of double oxygen bond in the structure of PDS and PMS[4]. Moreover, reactive oxygen species such as hydroxyl radicals, hydrated electrons and hydrogen atom can also be generated. These reactive oxygen species not only can attack the target organics through hydroxyl radical oxidation or the reduction of hydrated electrons, but also can contribute to the PDS and PMS activation[56].

2.3 Catalytic activation of sulfate radical based AOPs

Recently, $SO_4^{\bullet-}$ has attracted tremendous attention in wastewater treatment field as a substitute to hydroxyl radical for the decomposition of refractory organic contaminants. In spite of the physical activation method of PMS and PDS such as thermal, UV and ultrasonication, researchers have found that catalytic activation process is a more promising technique to efficiently produce sulfate radicals in terms of higher catalytic activity, low energy inputs and simpler operation.

2.3.1 Homogeneous catalysts

In the early age of peroxymonosulfate (PMS) and persulfate activation (PDS), a wide variety of metal ions have been extensively applied to decompose peroxymonosulfate. In 1956, Donald and John first investigated the catalytic decay of peroxymonosulfate using transition metal (Co) species, which proceeded through a radical oxidation mechanism[57]. Since then, there have been numerous researches examining the kinetic and the mechanisms of this effective oxidising system, and investigating the PMS activation initiated by transition metals for the elimination of organic contaminants [58-61]. In comparison with a series of homogenous metal ions and metal oxides, silver ion (Ag^+) demonstrated the highest catalytic activity for PDS activation, whereas cobalt ion ($Co^{2+)}$ displayed the highest activated activity for activating PMS. However, due to the toxic effect of silver and cobalt ions, iron ions (II and III) were the most widely studied metals due to the fact that they have lest negative impact on the environment and are cost-effective when comparing to other transition metals [62]. Anipsitakis *et al.* showed a robust PMS activation scheme by cobalt ions to produce sulfate radicals for the oxidation of PPCPs such as atrazine, 2,4-dichlorophenol, and naphthalene. Ding and Anipsitakis have reported the activation of PMS by Ce^{3+} and Cu^{2+}, respectively, and found that the reaction is not thermodynamically favourable. As a result, when these metal ions were applied as electron acceptors for PMS activation, the hydrogen and oxygen bond in the structure of PMS is

cleaved. Moreover, in another study, Liang compared the metal activation efficiency on PMS and PDS, which indicated that the metal/PDS systems represented a slower reaction rate is attributing to the different molecular structures of PDS and PMS. The activation mechanism of PDS and PMS by metal species is presented in Figure 2.5, which shows that the content of metal is directly linked to the activation capacity.

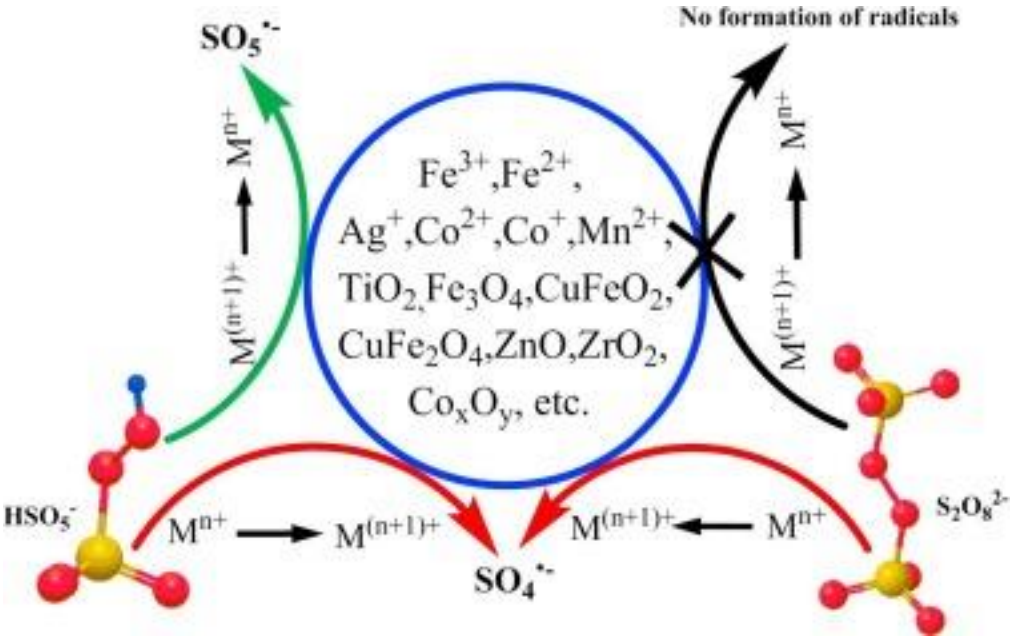

Figure 2.5. Activation mechanism of metal ions and metal oxide for PDS and PMS. Red line represents the formation of $SO_4^{\bullet-}$; Green line represents the formation of $SO_5^{\bullet-}$; Black line represents no formation of oxidative species; Cross-represents no formation of radicals[13].

$HSO_5^- + Co^{2+} \rightarrow Co^{3+} + OH^- + SO_4^{\bullet-}$ Eq. (2.18)

$S_2O_8^{2-} + Fe^{2+} \rightarrow Fe^{3+} + SO_4^{2-} + SO_4^{\bullet-}$ Eq. (2.19)

$SO_4^{\bullet-} + Fe^{2+} \rightarrow Fe^{3+} + SO_4^{2-}$ Eq. (2.20)

$HSO_5^- + Fe^{2+} \rightarrow Fe^{3+} + OH^- + SO_4^{\bullet-}$ Eq. (2.21)

$HSO_5^- + Fe^{2+} \rightarrow Fe^{3+} + OH^{\bullet} + SO_4^{2-}$ Eq. (2.22)

Furthermore, Rodriduez *et al.* have reported the degradation Orange G by PDS activation with iron. It was found that both ferrous and ferric ions could achieve complete Orange G degradation within 30 min via Eqs. 2.18-2.22, and the quinone byproducts produced in the

process of pollutant degradation could contribute to the electron transfer, which facilitates the reduction of ferric to ferrous ions in the reduction–oxidation reaction cycling of the metal ions. However, in another study, Jing and Jun reported that the transformation between ferric ions to ferrous ions, the inferior degradation efficiency for obstinate organic pollutants and the accumulation of ferric oxide are intrinsic drawback in the PMS activation process that limit its widespread application[60]. It is reported that in homogenous systems, the dissolved metal ions are able to freely react with PDS and PMS, which leads to minor mass transfer effect on the activation of PDS and PMS. Nevertheless, there are numerous drawbacks for the homogenous metal/ (PMS or PDS) systems. Firstly, it is almost impossible to completely recapture the metal ions regardless the different levels of toxicity of metal ions. This situation can be further deteriorated especially when the wastewater containing great concentration of organic contaminants, where large quantities of metal ions are necessary and could result in the presence of abundant of metal species in the municipal and industrial sewage. Additionally, the pH value and the composition of water can highly affect the species of transition metals. Metal ions may undergo precipitation reaction at alkaline condition or turn into hydrated species at low pH environment, which can dramatically deteriorate the catalytic activity of metal ions towards PMS and PDS. Moreover, the existence of organic compounds, for example organic matter (humic acid), can react with the metal species, which also affects the activation of PDS and PMS.

2.3.2 Heterogeneous catalysts

In general, sulfate radical production through homogeneous activation of PMS and PDS with transition metal species is efficient and can readily decompose water pollutants. However, the health concerns related to the adverse effect of dissolved metal species such as cobalt and nickel in water need to be tackled. Many researchers have found their solution in heterogeneous

catalyst, for instance metal oxide and metal-free carbon catalysts. In this section, various heterogeneous catalysts for PMS and PDS activation are reviewed.

2.3.2.1 Metal oxides

Unlike their homogenous counterpart, to efficiently generate sulfate radicals from PMS and PDS activation, one major issue that a heterogeneous metal oxide catalyst (Co, Mn, Fe, etc.) needs to be addressed is the relatively small contact surface. It is essential for PMS to be in direct interact with the reduction–oxidation reaction active sites of the catalyst to allow superficial PMS-catalyst interactions to take place. Many methods have been employed to synthesize metal oxide catalysts such as polymer combustion, thermal decomposition, hydrothermal treatment, and sol-gel synthesis. For instance, one facile and efficient way to generate a metal oxide is to allow inorganic or organometallic metal precursors to undergo direct thermal decomposition, for instance, cobalt nitrate ($Co(NO_3)_2 \cdot 6H_2O$), cobalt sulphate ($CoSO_4 \cdot 7H_2O$), cobalt acetate ($Co(CH_3COO)_2 \cdot 4H_2O$) and cobalt oxalate ($CoC_2O_4 \cdot 2H_2O$) [63-66]. In recent years, other simple methods have been developed to fabricate metal oxides catalysts. Yang *et al.* have reported a facile and economical mechanochemical process[67]. In their study, a cobalt oxide precursor ($Co_2(OH)_2CO_3$) can be acquired on a large scale via a solid-state displacement chemical reaction by milling $Co(NO_3)_2 \cdot 6H_2O$ and NH_4HCO_3 in an agate mortar[68]. Such preparation process, molten salt synthesis (MSS) is an accessible and ecofriendly approach to synthesize one-dimensional metal oxides without containing high-energy input and surfactants. In another study, Wang *et al.* have prepared and evaluated the shape-controlled 3D MnO_2 via the catalytic activities in activation of PMS for pharmaceutical contaminant degradation. It is reported that the corolla-like δ-MnO_2 with sub-blocks of nanosheets, and urchin-shaped δ-MnO_2 with sub-blocks of nanorods were fabricated via a

simple hydrothermal method. It was proved that the fabrication temperature largely affected the crystal structure, morphology and textural structure of the synthesized three-dimensional (3D) MnO_2 catalysts. The catalytic performances of these three samples fabricated at various temperature (60, 100 and 110 ◦C, denoted as Mn-60, -100 and -110, respectively) were investigated by PMS activation initiated phenol decomposition. The results showed that the 3D sea urchin-like δ-MnO_2 not only presented a high catalytic activity, it also possessed a strong catalytic stability, which could achieve 100% phenol removal even after the third run. It was proposed that MnO_2 firstly activated PMS to generated $SO_4^{\bullet-}$ and $^{\bullet}OH$ simultaneously (Eqs. 2.23-2.25), then a large proportion of the produced sulfate radicals were depleted by reacting with phenol and some of sulfate radicals were used to generate hydroxyl radicals. Meanwhile, the reduced Mn (III) can also react with PMS to produce $^{\bullet}OH$.

$Mn(IV) + HSO_5^- \rightarrow Mn(III) + SO_4^{\bullet-} + OH^-$ Eq. (2.23)

$Mn(IV) + HSO_5^- \rightarrow Mn(III) + SO_4^{2-} + {}^{\bullet}OH$ Eq. (2.24)

$Mn(III) + HSO_5^- \rightarrow Mn(IV) + SO_5^{\bullet-} + H^+$ Eq. (2.25)

More recently, the magnetic properties of zero valent iron (ZVI), magnetic Fe_3O_4 and maghemite (γ -Fe_2O_3) have attracted increasing interests on sulfate radical induced AOPs, due to the reasons that iron's abundance and poses no harsh threat to organism's health and the environment, and its good catalytic stability and activity. It is often considered that iron can be an excellent alternative to cobalt and other transition metal catalysts due to their toxicity even at trace amounts. The commonly used iron derived heterogeneous catalysts are ZVI, Fe_2O_3 and Fe_3O_4 and the mechanism of PMS activation are shown in Eqs. 2.20-2.22. Fei *et al.* reported the decolorization of Rhodamine B(RhB) in porous iron oxide catalyst activation of PMS[69]. The catalytic reaction process involved a comparatively high loading of Fe_2O_3, which mainly contains of bulk of Fe^{3+} species. The activation processes were suggested to be comparable to those of CuO and Fe^{3+} on the surface that necessary to be reduced to Fe^{2+} prior to the $SO_4^{\bullet-}$

production from PMS. The hematite functionalized by dipicolinic acid has been applied as a catalyst for PMS activation to degrade bisphenol A. Moreover, magnetic Fe_3O_4, a different form of iron oxides, has similarly shown efficient catalytic activity on PMS/PDS activation[44]. A nano-scaled magnetic (Fe_3O_4), with an inverse spinel crystal structure, has been used as a heterogeneous catalyst for PDS activation and the removal of aqueous contaminants. In Fe_3O_4/PMS system, the absorbed or lattice Fe^{2+} of Fe_3O_4 provides electrons to O_2 to generate $O_2^{-\bullet}/HO_2^{\bullet}$ radicals. The $O_2^{-\bullet}/HO_2^{\bullet}$ radicals would activate the PDS to trigger a more efficient $SO_4^{-\bullet}$ production rate, following by reaction with H_2O to generate H_2O_2. It was found that the Fe_3O_4/PMS system is suitable for drinking water treatment due to the fact that it exhibited the best acetaminophen degradation under a neutral condition.

2.3.2.2 Poly-metallic oxide catalysts

Many studies have found that by mixing two or multiple different metals together to form a polymetallic oxides could bring numerous improvments, such as enhanced stability, versatility, magnetic property, higher reduction–oxidation activity and boosted catalytic activity [70-74]. As mentioned above, despite of the good catalytic ability of metal oxides like Co_3O_4, the nonappearance of practical and effective methods to recapture the leached metal ion is a blockage for its wastewater treatment because it may cause secondary environmental problems[75]. Qiujing *et al.* fabricated a Fe-Co mixed oxide derived from ferric nitrate nonahydrate and cobalt(II) nitrate hexahydrate by pyrolysis in air at 300-700^{o}C , which was proved to be a productive way to achieve efficient catalysts for PMS activation. It is worth to mention that the metal discharge from the Fe/Co catalysts can be largely optimized due to the strong interactions between metals during the thermal process. Moreover, the problematic reusability of metal oxide catalysts during SR-AOPs was also alleviated since the achieved $CoFe_2O_4$ can be facilely recaptured via the magnetic-based collection owing to its ferromagnetic properties. Regarding to its catalytic activity on PMS activation, attributing to

the role of intimate Fe-Co interactions, $CoFe_2O_4$ presented better catalytic performance than both individual iron oxide and cobalt oxide, and their mixture[76]. In 2018, Liwei and others synthesized cobalt and iron bimetallic oxides catalyst and showed excellent catalytic activity towards PMS activation, shown in Figure2.6.

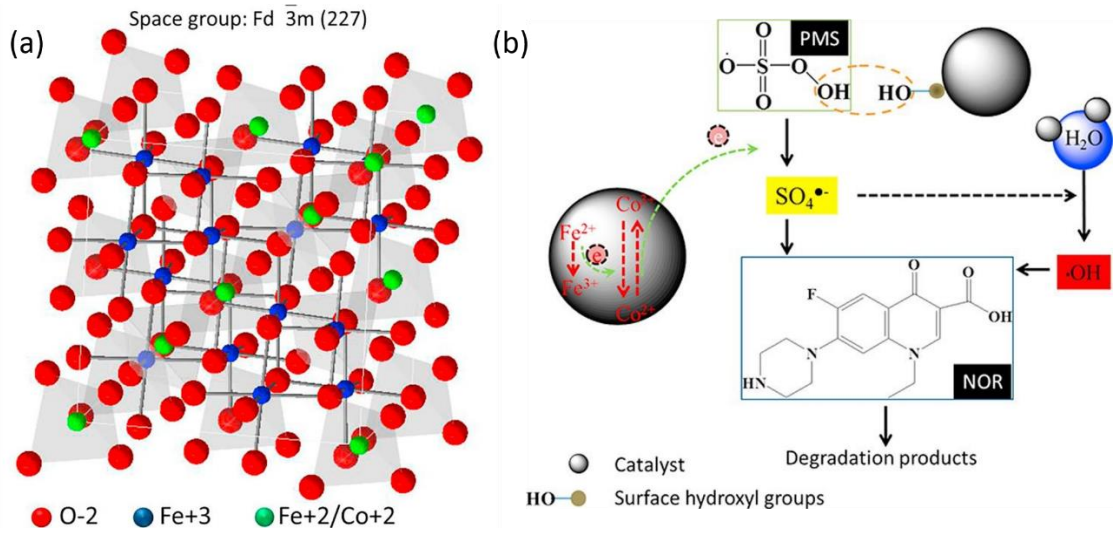

Figure 2.6. (a) Crystalline structures of the spinel Co/Fe bimetallic oxides. (b) $CoFe_2O_4$ induced peroxymonosulfate activation to degrade norfloxacin[79].

Interestingly, they focused on investigating the effect of various stoichiometric iron to cobalt ratios for the heterogeneous activation of PMS to produce sulfate radicals. It shows that the bimetallic oxides reached its highest catalytic efficiency at the Fe/Co ratio 1:1.65 other than the ratios such as 1:1 and 1:2. In addition, the metal leaching tests showed that the Co concentration was much lower than Co_3O_4, which confirmed that such a bimetallic oxide could evidently lower cobalt leaching attributed to the sturdy Fe-Co interactions[77]. In a parallel research, Yuxian *et al.* prepared $CoMn_2O_4$ catalyst derived from cobalt (II) acetate tetrahydrate and manganese(II) acetate tetrahydrate by hydrothermal reaction at 200 ^oC for 20 h, which was revealed to be effective and ecofriendly for the heterogeneous activation of PMS. The stability and reusability investigation showed that $CoMn_2O_4$ could reach 87% of rhodamine B degradation even after five successive oxidation cycles. According to their XPS analysis and other experimental, the results indicated that the great catalytic activity and stability of

$CoMn_2O_4$ was due to the synergistic effect of Co(II)/ Co(III), Mn(II)/ Mn(III) and Mn(III)/ Mn(IV) redox pairs. However, $CoMn_2O_4$ did not show much catalytic activity to PDS and H_2O_2, which indicated that the unsymmetrical character of PMS made it easy to be activated[54]. To investigate the optimum metal pair, Yueming prepared different magnetic ferrospinel MFe_2O_4 (M = Co, Cu, Mn, and Zn) in a sol-gel process and applied them as a catalyst to produce robust reactive radicals from PMS activation process for obstinate dinbutyl phthalate (DBP) degradation in water (Figure 2.7). In their study, they prepared various ferrospinel by mixing different transition metal nitrates pairs and fresh egg white and followed by calcination at 400 ^oC for 5 h, and later on compared their catalytic activity accordingly. The parallel

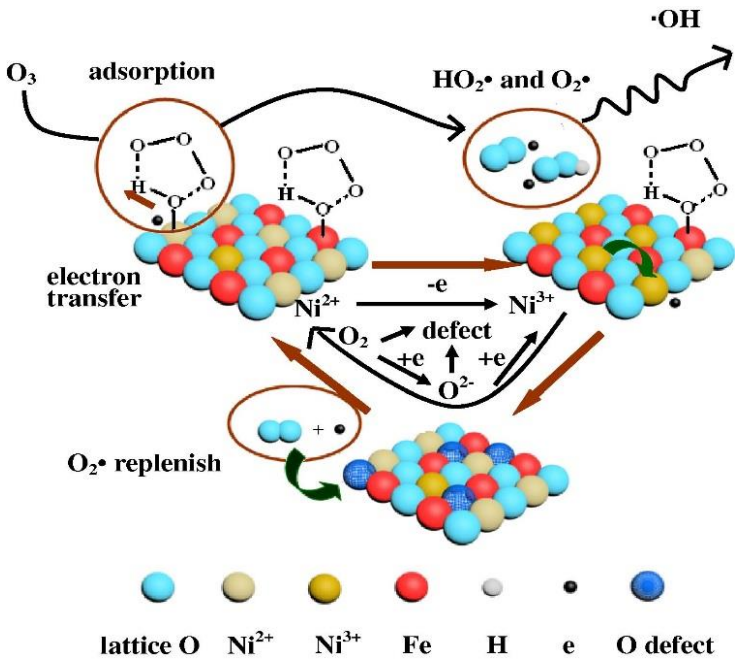

experiments results showed that the catalytic activation by these metal hybrids on PMS for DBP oxidation can be ranged in an order of $CoFe_2O_4 > CuFe_2O_4 > MnFe_2O_4 > ZnFe_2O_4$. It is then estimated that Co and Fe bimetallic oxides have the optimum synergistic effect on DBP degradation in the PMS solution.

Figure 2.7. Proposed recyclable surface processes during catalytic ozonation over $NiFe_2O_4$ catalyst[80].

Moreover, some studies have found their solutions in polymetallic derived catalysts to improve the persulfate activation on organic pollutant removal in water. Kong *et al*. have successfully prepared Cu_2FeSnS_4 (CFTS) derived from $CuCl_2{\cdot}2H_2O$, $FeCl_3{\cdot}6H_2O$, $SnCl_4{\cdot}5H_2O$ and NH_2CSNH_2 by hydrothermal reaction at 220 ^oC for 18 h. The as-synthesized CFTS presented a rose-like morphology and showed high activity and stability in catalytic activation of PDS for bisphenol in model industrial wastewater. The bisphenol degradation experiments showed that the Cu_2FeSnS_4 was more effective than monometallic Cn, Fe and Sn sulfides in a wider range of pH condition, which can be due to two main reasons. Firstly, the synergetic effect of Cu(I) and Fe(III) on the surface of CFTS is beneficial for interfacial electron transfer, which can accelerate the PDS activation process and generate radicals such as sulfate and hydroxyl radicals in a faster rate. In addition, the Fe(II)* played an significant role in the tandem synergistic effect in the CFTS/PDS system, which induced the formation of S→M σ-bonds (M = Cu, Fe, and Sn) that further promoted the electron transfer, Eq.2.26-2.34. Moreover, the tandem synergistic effect of Cu/Fe/Sn has been proved to impede the metal ions leaching by improving the cycle between M^{n+} and $M^{(n+1)}$.

$Cu(I) + S_2O_8^{2-} \rightarrow Cu(II) + SO_4^{\bullet-} + SO_4^{2-}$ Eq. (2.26)

$Cu(II) + S_2O_8^{2-} \rightarrow Cu(III) + SO_4^{\bullet-} + SO_4^{2-}$ Eq. (2.27)

$Cu(III) + H_2O \rightarrow Cu(II) + H^+ + OH$ Eq. (2.28)

$SO_4^{\bullet-} + H_2O \rightarrow SO_4^{2-} + H^+ + {}^{\bullet}OH$ Eq. (2.29)

$Fe(II) + S_2O_8^{2-} \rightarrow Fe(III) + SO_4^{\bullet-} + SO_4^{2-}$ Eq. (2.30)

$Cu(I) + Fe(III) \rightarrow Cu(II) + Fe(II)$ Eq. (2.31)

$Fe(II) + \rightarrow Fe(II)^*$ Eq. (2.32)

$2Fe(II)^* + Sn(IV) \rightarrow 2Fe(III) + Sn(II)$ Eq. (2.33)

$Sn(II) + 2S_2O_8^{2-} \rightarrow Sn(IV) + 2SO_4^{\bullet-} + 2SO_4^{2-}$ Eq. (2.34)

2.3.2.3 Metal free pristine carbon catalysts

Metal-free nanostructured carbons and carbon based composites have showed an excellent alternate solution to traditional metal based catalysts in many areas, such as dehydrogenation of aromatic hydrocarbons and advanced oxidation reaction[33]. It is believed that carbon catalyst can present many advantages over the metal-based materials due to the distinctive modification of its surface acidity/basicity and π electron density through surface functionalization[33, 78]. In a recent study on catalytic AOPs, nanocarbon catalysts, such as graphene oxide (GO) and carbon nanotubes (CNTs) with enormous specific surface area (SSA), unique carrier mobility, high thermal conductivity, one or two dimensional structure and sp^2-hybridized carbon configuration, have exhibited to be effective in sulfate radical derived heterogeneous advanced oxidation processes[78]. It was demonstrated that the catalytic performance and the defect degree are directly correlated to the exceptional properties of graphene, such as the oxygen content and the defects loadings. Additionally, by using the theoretical modeling data, it showed that the key active sites of graphene are more likely to be the edge sites and carbon frame vacancies than the honeycomb like basal plane to activate persulfates[15, 79]. Duan *et al.* reported that manifold oxidative mechanisms upon PMS activation by carbocatalysis were established, which the graphene with abundant defects initiated a nonradical degradation process where radical quenchers (to rapidly scavenge out radicals) hardly retarded the oxidative effectiveness. It is then believe that, in a typical nonradical oxidation reaction, firstly PMS molecules are adhered on the nanocarbon surface, and then a reactive intermediate is generated by the temperate electron transfer from the catalyst surface to PMS without instantaneous production of free radicals. Secondly, the adsorbed organic pollutants with abundant electron would be attracted by the partially activated PMS via a rapid electron abstraction. Interestingly, the nanocarbon and PDS system is more complex and involved direct attack to the organic pollutants in a nonradical process where the conductive nanocarbon matrix acted as a charged

vehicle between the adsorbed organic pollutants, acting as an electron contributor, and PDS, acting as an electron receiver. By comparing various pristine nanocarbon materials, the adsorption capacity towards organics like phenolic was discovered to be closely interrelated with the molecular arrangement and SSA, which was in the order 0D < 1D < 2D < 3D[80]. Nevertheless, the catalytic activity to PMS/PDS activation is not essentially correlated to the dimensional effect, however it might be attributed to the active-sites and carbon-arrangement-dependent[79]. For instance, Stacey *et al.* found that the sp^2-hybridized carbon nanotubes and graphene oxide showed a much better catalytic performance than sp^2/sp^3 fullerene and sp^3 diamond nanocrystals for PMS- or PDS-based degradation systems. Moreover, their study implied that the delocalized π electrons is advantageous for creating electron-enriched edge/ vacancy defects and ketonic oxygen functional groups at the grain boundaries to facilitate redox processes.

On the other hand, proposed by Wang's group that activated carbon showing great catalytic potential to activate PMS merely at a temperate level and pristine GO did not show any activity toward PMS activation[81]. The bluntness of pristine carbon on PMS activation was later proved to be the consequence of insufficient active sites and low absorptivity on organic pollutants. Therefore, proper modification of pristine carbon could be done in order to bring promotion to the adsorptive and catalytic oxidation performance for eliminating organic pollutants[82]. Depending on the catalytic performance of pristine nanocarbons, wide varieties of strategies have been established to boost both the adsorption capacity and catalytic activity. For example, chemical and thermal activation have been commonly employed to concurrently modify the crystalline, porous structures and optimize the loading and category of oxygen groups.

2.3.3 Modification methodologies for promoted carbonaceous catalysis

2.3.3.1 CO_2 activation

Employing nanocarbon as a powerful catalyst without metal leaching and other inherent pollution for catalytic induced degradation of aqueous toxic organic contaminants has attracted much attention for a promising purification of contaminated water. It was previously reported that the characteristics of nanocarbon materials such as SSA, adsorption capacity, conductivity and supercapacitance could be improved through activation by potassium hydroxide (KOH). Although it has been proved as an effective method to enhance nanocarbon material in terms of surface area and catalytic ability, the process is complicated and would introduce foreign chemicals into natural water, which can cause acute pH change and is also difficult to be removed. In another study, Peng *et al.* reported that greatly porous reduced graphene oxide (rGO) can be fabricated by an facile and ecofriendly activation process applying carbon dioxide at high temperature. By doing so, the SSA of rGO was significantly enlarged from 200 to approximately 1200 m^2/g, and the catalytic performance was also largely improved [83]. In a comparative experiment, 100% methyl blue degradation was accomplished in 4 h by unmodified rGO, and the time was shortened to 1 h on the CO_2 activated reduced graphene oxide.

2.3.3.2 Chemical reduction

Emerging nancarbons as a catalyst demonstrated outstanding merits in nontoxicity, large surface area, higher activity and better catalytic stability than bulk carbon allotropes[33]. For wastewater remediation, the chief use of graphene (oxide) is the adsorption of dyes or heavy metal, meanwhile the efficiency of nanocarbon based catalysts showed inferior performance on PMS activation. Sun *et al.* discovered a new method to modify GO by a hydrothermal reduction process under alkaline ammonia solution at 453 K for 18 h. In the hydrothermal reduction process, the surface acidity/ alkalinity was adjusted by removing the oxygen containing groups in ammonia solution and the catalytic performance of graphene in PMS

activation was then improved. In their study, a comparative experiment showed that the catalytic activity of chemical reduced GO was surprisingly superior to some supported cobalt catalysts. By characterizing the morphology, crystalline phase and defective structure of graphene before and after reaction, it was found that no obvious changes and the deactivation of rGO during reusability tests might be attributed to the coverage of degradation intermediates. In a perfect graphene basal plane where the sp^2-hyridaized carbon atoms are situated in a six-carbon-rings as a π conjugated system and the edge defects and curvature at stacked graphene layers produce nonsix-membered carbon rings. The study revealed two types of edges, which are zigzag and armchair, are produced depending on the orientation of the broken σ bonds between carbon atoms, and the localized state at zigzag edge makes their π electrons not to be limited by the border carbons, leading to a greater chemical activity that is considered to be the active sites. In addition, the chemically reduced graphene oxide would retain some oxygen containing groups such as -OH, C=O and -COOH, which are abundant in electrons and possess high intrinsic activity and higher redox potential than those dismissing the flat (001) surface. The reaction mechanism is shown in Figure 2.8. In addition, Eq. 2.35-2.36 indicate that two categories of radicals, $SO_4^{\bullet-}$ and $SO_5^{\bullet-}$, were produced through the PMS activation reaction by graphene, and $SO_4^{\bullet-}$ presents a higher oxidative potential than $SO_5^{\bullet-}$ which is playing a more important role in degradation of organics.

$HSO_5^- + e^- \rightarrow SO_4^{\bullet-} + HO^-$ Eq. (2.35)

$HSO_5^- + h^+ \rightarrow SO_5^{\bullet-} + H^+$ Eq. (2.36)

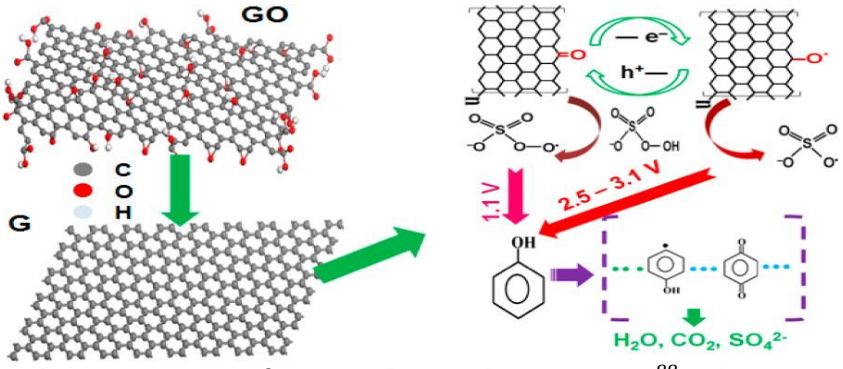

Figure 2.8. Graphene activation of PMS and its probing reaction[88].

2.3.3.3 Heteroatom doping

It was found that the structural modification of nanocarbon materials was efficient for promoting the catalysis performance in advanced oxidation reactions. It was widely suggested that chemical doping of different atoms could provide an effective method to modify the electron states of nanocarbon such as graphene and bring about new properties such as selective sensitivity for adsorbents and electrochemical catalytic activity. It was also reported that the doping effect might be caused by electron transferring from nanocarbon surface to PMS/PDS generated by the reaction, such as endoperoxides, hydroperoxides, and charge-transfer complexes, adhered on the graphene plane[84].

Many theoretic and empirical researches have proved that by deliberate incorporation of monoheteroatoms such as nitrogen, phosphorous, boron and sulfur into the one dimensional carbon structure could efficiently modify its chemical and electronic properties.

Many nitrogen doping methodologies have been reported including nitrogen plasma process, chemical vapour deposition (CVD), hydrothermal, and thermal annealing approach by ammonia gas, which are often complex, expensive and involving organic pollutants. In one study, Sun and his colleagues suggested a single step synthesis of nitrogen doped rGO using GO and ammonium nitrate as carbon and nitrogen precursors.The as-synthesized catalyst presented superior catalytic performance for activating PMS, comparable to nanosized cobalt

oxide and manganese oxide. The XPS study (Figure 2.9) showed that three types of N species were doped into graphene basal plane, such as nitrogen atoms doped into a graphene basal plane (quaternary or graphitic N at *ca.* 401.8 eV), N in a six-carbon ring (pyridinic at *ca*. 398.3 eV), and a five-carbon ring (pyrrolic N at *ca*. 399.8 eV). The effect of N doping on the catalytic activity of graphene was studied by activation of PMS for catalytic degradation of pharmaceutical solution, in which N-rGO presented the best catalytic performance over GO, rGO and carbon nanotubes. Interestingly, the SSA of N-rGO (60 m^2/g) is four times less than rGO (300 m^2/g), which indicated that the enhanced catalytic activity of N-rGO was attributed to the N doping. As aforementioned, the sp^2 carbon of graphene would be responsible for the activation of PMS, as a result the carbon network has plentiful free moving π electron that can be activated by combing with the long-pair electrons from the doped nitrogen species, thus leading to a higher catalytic performance.

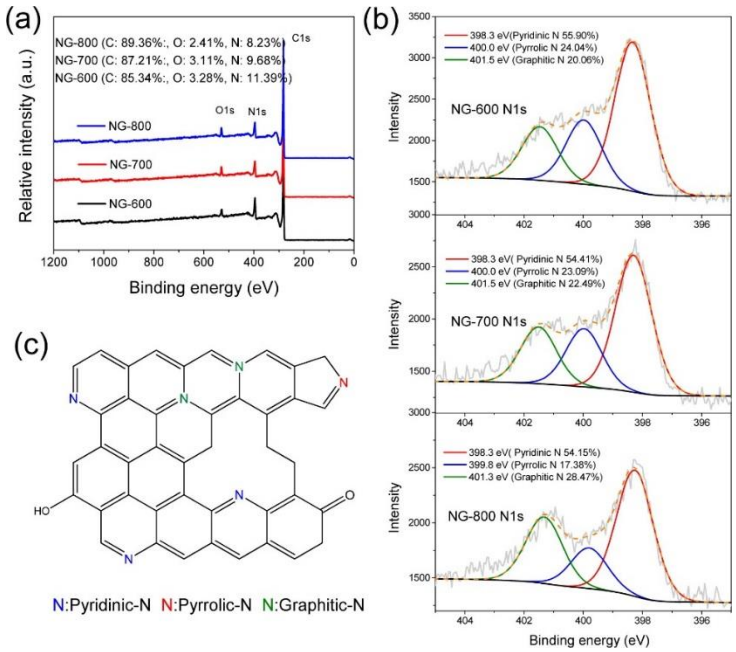

Figure 2.9. (a) XPS survey of NG-600, NG-700, and NG-800. (b) N 1s scan of NG-600, NG-700, and NG-800. (c) Different types of N-doping[90].

In an extended study, the N modified graphene (NG) was prepared from graphite oxide and melamine (nitrogen precursor) by a direct annealing process in nitrogen gas atmosphere at 600-

800^{o}C[85]. Duan and his team investigated the catalytic activities of NG in catalytic activation of PMS for phenol oxidation in water solution. Despite the improved catalytic activity of NG compared with pristine graphene, the effect of reaction temperature on target organic oxidation was found to be marginal due to the N-doping modification. It is believed that the introduction of nitrogen atoms could considerably stimulate the sp^2 carbon framework and lower the activation energy for electron transfer from nanocarbon surface to PMS molecules, as a result, exerting a more important influence on PMS activation processes. Moreover, the study suggested that the specific nitrogen species (graphitic N), with a smaller covalent radius and higher electronegativity than C atom, could induce electron transfer from adjacent carbon atoms to nitrogen, consequently disturbing the chemical inertness of the sp^2 carbon layer and promoting the catalytic activity of graphene. Other studies proposed that the pyridinic N with a two lone electrons can effectively modify the valence band of carbon basal plane and promote the pi statuses of Fermi level and the quaternary N could act as the active sites for catalytic degradation of organics[86, 87]. Also in Duan's study, they applied electron paramagnetic resonance (EPR) spectra to show that hydroxyl radicals were efficiently produced in the first minute and the generation rate slowed down while the sulfate radical was showing a similar trend but slower rate, as shown in Figure 2.10. It was suggested that the drop of hydroxyl radical generation rate was attributed to the depletion by organic oxidation and the interconversion between sulfate radicals, and this leaded to the conclusion that the robust oxidation process could be attributed to the co-effect of $SO_4^{\bullet-}$ and $OH^{\bullet}$, Eqs 2.37-2.41. Similarly, Kang *et al.* introduced a single-step facile hydrothermal fabricaton of N-rGO using urea as a nitrogen precursor. The nitrogen-modified nanocarbon not only presented a larger SSA but also showed an improved catalytic activity in catalytic PDS activation over pristine graphene and metal oxide (Co_3O_4) for degradation of sulfachloropyridazine, a common pharmaceutical contaminant[88]. Kinetic studies suggested that the catalytic performance of N-

rGO on PDS activation was closely related to the catalyst dosage, PDS concentration and reaction temperature, and confirmed the assumption from the previous study that both $SO_4^{\bullet-}$ and $OH^{\bullet}$ were accountable for SCP oxidation.

$HSO_5^- + e^- \rightarrow SO_4^{\bullet-} + OH^-$ Eq. (2.37)

$HSO_5^- + e^- \rightarrow SO_4^{2-} + OH^{\bullet}$ Eq. (2.38)

$HSO_5^- - e^- \rightarrow SO_5^{\bullet-} + H^+$ Eq. (2.39)

$SO_4^{2-} + OH^{\bullet} \rightarrow SO_4^{\bullet-} + OH^-$ Eq. (2.40)

$SO_4^{\bullet-} + OH^- \rightarrow SO_4^{2-} + OH^{\bullet}$ Eq. (2.41)

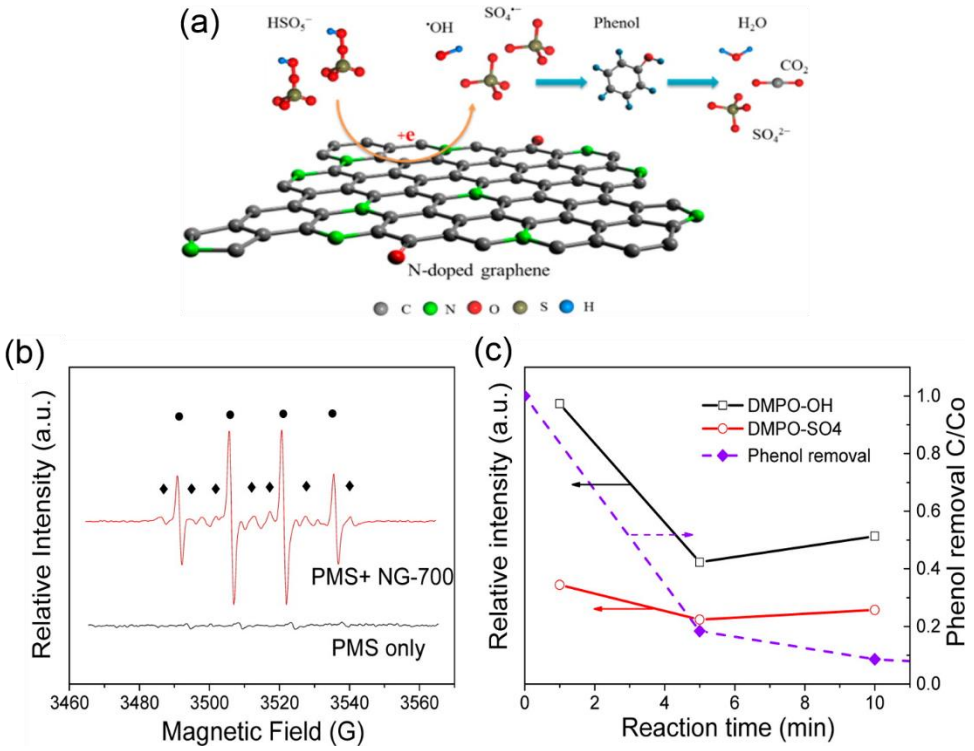

Figure 2.10. (a) Proposed Mechanism of PMS Activation and Phenol Oxidation on N-Doped Graphene. (b) EPR spectra of DMPO adducts under different conditions (●, DMPO–OH; ◆, DMPO–SO4). (c) Intensity changes of DMPO adducts. Reproduced with permission from American Chemical Society[90].

Modifying the electronic arrangement of graphene by inserting heteroelements that have lower electronegativity than carbon, for example sulfur, is an applied approach for generating greatly promoted carbon catalysts for the oxygen-reduction reaction (ORR) and AOPs. Zhi *et al.* studied the catalytic performance alternation of graphene when doped with element that has

very similar electronegativity (Sulfur: 2.58 vs Carbon: 2.55). A sulfur doped graphene was prepared from GO and benzyl disulfide by a direct annealing in argon at 600-1000 ^{o}C. It was speculated that the development of carbon sulfur bond could be triggered by the reaction between oxygen functional groups in graphene oxide, such as carbonyl, carboxylic, and lactone groups. The catalytic ability of sulfur and carbon bond was superior to that of pristine graphene, and the experimental results approved that the S-doped graphene has a higher electrocatalytic activity than the corresponding untreated graphene. It is believed that S doping played an important role in the catalytic promotion of graphene, and that it is mainly due to the creation of the edge plane active site and disorder of basal plane after the S-doping, subsequently promoting the catalytic activity. In a parallel study, Hwee *et al.* proposed an environmental friendly and economical technique to synthesize sulfur modified graphene, which is derived from graphene, SO_2, and H_2S by a direct pyrolysis at 1000 ^{o}C. In the ζ-potential and conductivity testing, sulfur-doped graphene showed greater (absolute value) ζ-potentials than the pristine counterparts. It was discovered that the degree of heteroatom doping could be largely affected by the type of graphite oxide used rather than the type of sulfur-containing gas used during exfoliation, as shown in Figure 2.11. Additionally, there is also a close relationship between the doping level of sulfur and the improvement of catalytic activity, where the lowest sulfur doping level in sulfur doped graphene corresponded the least catalytic performance[89].

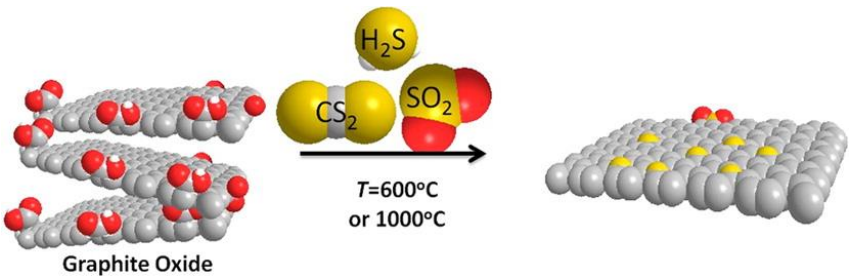

Figure 2.11. Sulfur-doped graphene via thermal exfoliation of graphite oxide[95].

2.3.3.4 Polyatomic doping

It has been widely proved that the substitutional doping with adventitious elements into the carbon network can modify the catalytic activity, such as creating extra active sites, and largely improve the catalytic activity of nanocarbon catalysts. By taking the next step, many studies have proposed that co-doping by two or more types of atoms with various electronegativity can further bring enhancement to a novel electron distribution and result in a synergistic effect. Yu *et al.* prepared a bromine and nitrogen co-doped carbon nanotubes via a CVD growth treatment. Their study proved that the essential role of the doping heteroatoms on nanocarbon's catalytic performance, which is crucial in scheming and optimizing advanced nanocarbon catalysts[90]. The results in their study suggested that the method to transform sp^2 carbon hybrids into metal-free catalysts deduced from the mono-doped cases is applicable for the multi-doped situations. In order to distinguish the recompense effect between the p- and n-type dopants, which is corresponding to distinct electronic structures and different conjugation effects with the carbon π system, two types of B and N co-doped CNT were prepared[91]. In one sample, B and N atoms are separated while they are bonded in another sample. Interestingly, the B/N bonded sample presented deterioration in catalysis as the B/N ratio is increased, meantime, the separated case showed an improvement with increasing B and N concentration. It was suggested that a neutralization happens between the newly released electron from N and the vacant orbital from B for the attached case, resulting in opposed chemisorption of O_2 on the co-doped CNTs[92]. In addition, the bonded case can barely disrupt the inertness of CNTs, while the separated case can modify CNTs into exceptional catalysts, indicating the significant role of the doping microstructure in catalytic performance[90]. Zheng *et al.* also studied the enhancement in catalytic performance of co-doping N and B into a carbon framework, however they incorporated B atoms into prepared N-doped graphene. It was revealed that the heteroatom dopants, bromine in this case, were able to boost the chemical activity of pyridinic N to a large

extent through a B-C-N bridge, as a result, it realized the synergistic coupling between the dopants (B and N).

Many studied have also approached the modification of nanocarbon materials by another common polyatomic doping combination, sulfur and nitrogen. Ji *et al.* designed a facile fabrication of nitrogen, sulfur dual-doped graphene (denoted as NSG), and investigated the synergistic effects creating from dual element doping. NSG demonstrated a higher catalytic stability over single atom doped catalyst, N-G and S-G, which could be ascribed to the strongly bonded heteroatoms in NSG and the enhanced chemical and mechanical stability of the mesoporous graphene. In Figure 2.12, it shows the graphene frameworks doped by nitrogen and/or sulfur atoms with diverse relative positions have been constructed for computational simulation, where S and N are instantaneously combined into graphene to form dual-doped N-SG. The results showed that the maximum spin density is considerably raised to 0.43 (C1 in Figure 2.12) indicating significant elevation of catalytic performance. In addition, a great amount of active carbon atoms have been discovered (S and C1-C5 as shown in Figure 2.13) and this can be attributed to that the multi-element doping of S and N creates irregular spin and charge density. The simulation investigation unveiled that the charge/spin densities of NSG sample with various relative positions of sulfur and nitrogen atoms can be augmented to a particular level. The results suggest that the co-doping of sulfur and nitrogen atoms into carbon network could directly cause the redistribution of spin and charge densities, and such a synergistic effect would create more active sites, thus dramatically enhance the catalytic activity. A large porosity and high specific surface area is often believed to be a key characteristic of metal-free catalysts for water remediation. A multi-element N and S-co-doped porous carbons (NSPCs) with large surface and hierarchically spongy structures were effectively fabricated through direct pyrolysis of a mixture of carbon precursors (glucose), sodium bicarbonate, and (N/S precursor) thiourea[93]. The synthesized NSPCs present not only

outstanding adsorption ability towards target organic pollutant, but also high efficiency for PDS activation when applied as catalysts for oxidative degradation of sulfachloropyridazine solutions.

Tian *et al.* attributed the outstanding catalytic activity of nitrogen and sulfur codoped carbon catalyst to several features. Firstly, its great specific surface area and well-defined pore structure allow additional active sites to be uncovered. In addition, the high surface area accelerates the superficial reactions where PDS activation takes place. In the PDS activation process, as soon as the SCPs and PDS were adhered on the surface of carbon catalyst, the SCPs will be degraded directly, and then an adsorption–decomposition cycle was followed until full SCP removal was reached. Consequently, the large adsorption capacity of NSPC2 was advantageous for promoting the oxidation reaction rate. Secondly, the enhanced catalytic activity is suggested to be linked with N- and S multi-atom doping species and their doping quantities, which can be further studied by employing density functional theory (DFT). As it was mentioned earlier, the electronegativity of nitrogen atoms (3.04) is higher than carbon atoms (2.55), as a result, particularly, pyridinic and graphitic nitrogen are able to generate a net positive charge on the neighboring carbon atoms. In addition, the electronegativity of S atoms (2.58) is similar to the electronegativity of C atoms, which can lower the energy difference amongst vacant carbon molecular orbitals. Therefore, they deduced that suitable amounts of N and S doping are able to stimulate and break the chemical inertness of carbon and exert a synergistic effect on the improvement of the catalytic activity due to the redistribution of spin and charge densities and creation of more active sites. However, their calculation results indicate that over doping of N or S might cause disturbance to the charge balance of the covalent carbon electron system, resulting in the charge redistribution, and thus deteriorate the synergistic effect.

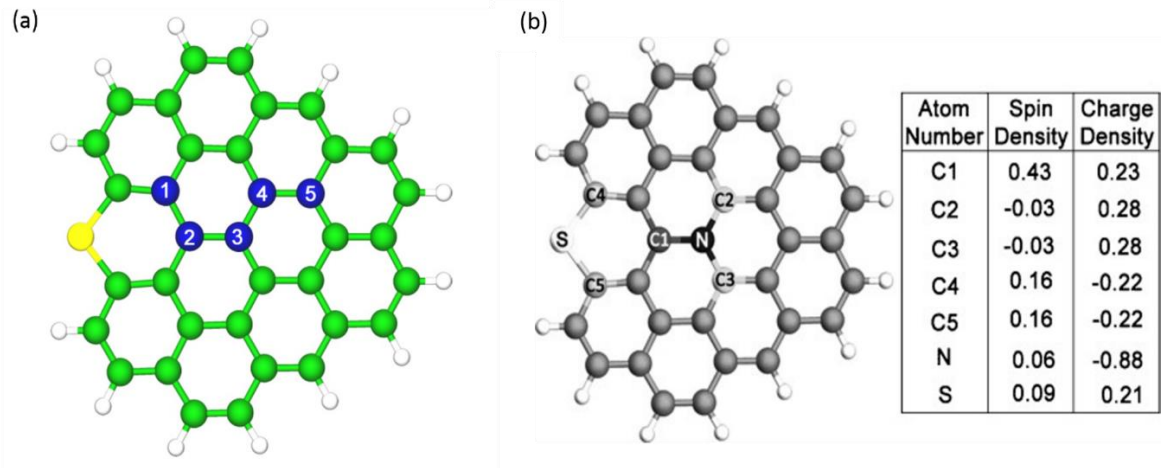

Atom Number	Spin Density	Charge Density
C1	0.43	0.23
C2	-0.03	0.28
C3	-0.03	0.28
C4	0.16	-0.22
C5	0.16	-0.22
N	0.06	-0.88
S	0.09	0.21

Figure 2.12. Spin and charge density of graphene network (gray) dual-doped by N (black) and S (white). C1 has very high spin density, C2 and C3 have high positive charge density, and C4 and C5 have moderately high positive spin densities[101].

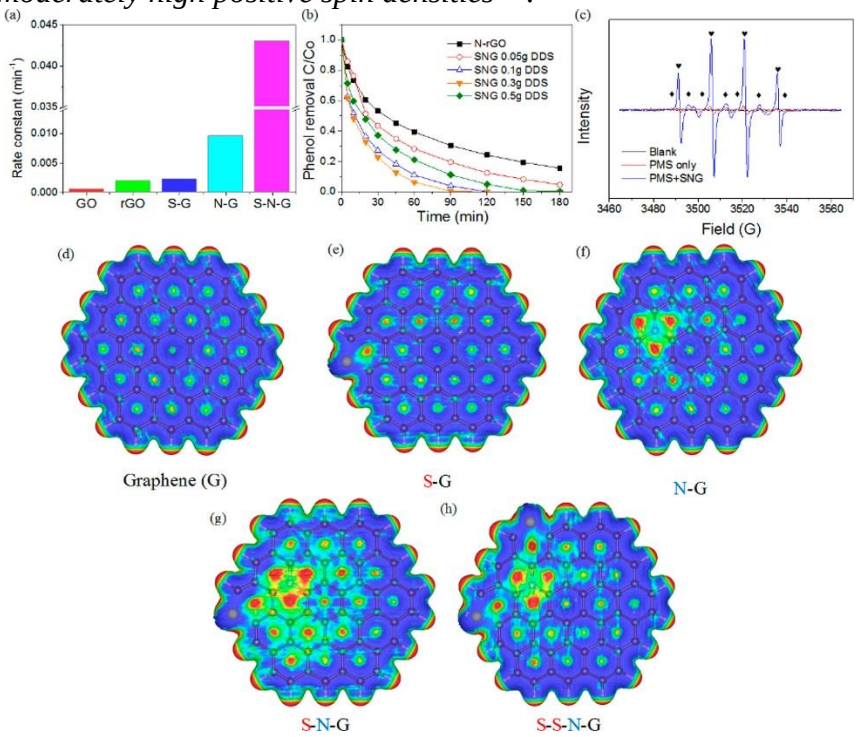

Figure 2.13. (a) Reaction rate for phenol degradation on various nanocarbons. (b) The effect of sulfur loading on phenol degradation rate. (c) Radical formation studies on SNG/PMS system. (d–h) Electrostatic potential distributions of various nanocarbons[99].

2.3.3.5 Nanocarbon hybrids

Both 2D (graphene) and 3D (carbon nanotube) carbon materials have shown excellent catalytic activity on sulfate radical based AOPs. However, both of them have drawbacks due to their unique morphology and surface characteristics. For example, graphene, a typical 2 dimensional material, can easily cause aggregation when repeated used during SR-AOPs[88, 94]. Meanwhile,

carbon nanotube often presents relatively inferior catalytic activity than graphene due to the insufficient surface area.

Recently, many studies have reported that construction of nanohybrids from different primary nanocarbon with distinct morphological characteristics could avoid the shortcomings and carry forward their good points such as increasing the amount of catalytic sites and tailoring the catalytic centers. For instance, it was found that unmodified bulk nanodiamonds (NDs) with untainted sp^3 hybridization were discovered not active in PMS/PDS-based degradation reaction, while graphitized nanodiamonds (GNDs) show outstanding catalytic activity to start the PMS and PDS activation[27, 95]. Duan *et al.* firstly reported that thermal annealing of diamond nanocrystals could bring about a typical core/shell structure attributing to the collapse and re-synthesis of the surface of nanodiamonds, which is denoted as sp^3-hybridized carbon, into a confined graphene basal plane, denoted as sp^2-hybridized carbon. As a result, the graphitized nanodiamonds (G-NDs) was enabled to pass on the physicochemical characteristics of one dimensional nanocarbon-based catalysts while the diamond core instills the curled basal plane with novel features. Consequently, the sp^2/sp^3-hybridized architecture has exhibited new properties for nanocarbon catalysis. Sun *et al.* demonstrated a facile preparation method of a carbon nanosphere and carbon nitride (C_3N_4) hybrid (CN-CS) which is derived from glucose and carbon nitride by a hydrothermal treatment at 180 ^oC for 3 hours. The synthesized CN-CS presented nearly 5 times more powerful catalytic activity than pristine carbon nanosphere in phenol oxidation under artificial sunlight irradiations. It was suggested that the structural modifications improved the separation rate of carriers, and the reformed surface morphology could bring about a synergistic effect for contributing to the enhanced catalytic activity of modified nanocarbon. In addition, with an increased hydrothermal temperature (180 °C), a noteworthy amount of carbon spheres were generated, resulting in the reduced band gap energy and significant improvement of carrier separation. As a result, CN-CS showed the most

outstanding catalytic activity in degradation of pharmaceutical organics. It also showed the importance of hydrothermal duration to the catalytic activity of CN-NS. The reduced catalytic activities of the samples in a pyrolysis process for shorter period were possibly attributing to excessively loading of carbon spheres and larger particle size, which blocks the light absorption. It was further confirmed by the specific surface area and porosity characterization, showing that the shorter hydrothermal treatment could induce the carbon hybrid to have less surface area and reduced photocatalytic activity in the oxidation process of phenol.

In another study, Qian *et al.* reported the synthesis and application of graphene and single-walled carbon nanotube hybrid complex, which presented large surface area and better specific capacitance than both graphene and CNTs, Figure 2.14.

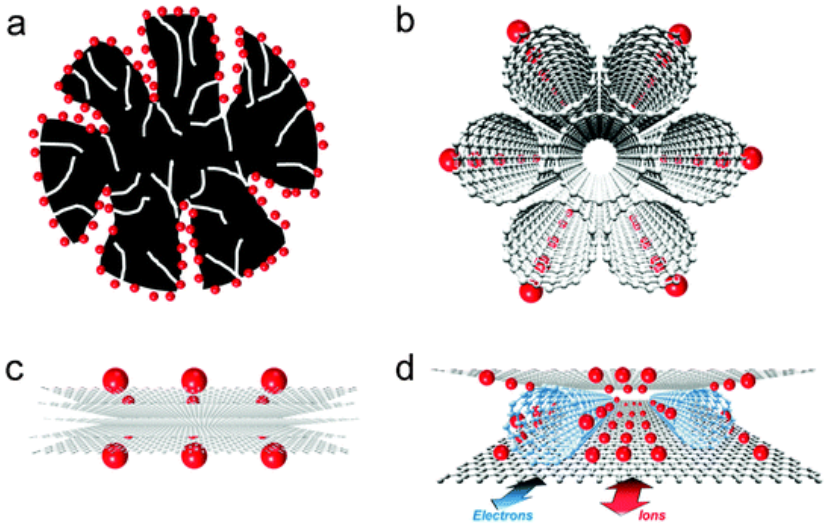

Figure. 2.14 Illustration of different nanocarbons. (a) Activated carbon. (b) Single-walled carbon nanotube (SWCNT). (c) Pristine graphene. (d) Graphene/CNT hybrids[32].

Although both graphene and carbon nanotubes have shown outstanding catalytic and mechanical properties, and have been employed in a wide range of fields, meanwhile, their limitations should not be ignored and deserve further development[81, 88, 96]. For example, only the outer surface part of the pristine CNTs is able to participate in the reactions such as AOPs and energy performance and the internal carbon atoms are all unexploited, leading to an inferior catalytic performance. On the other hand, the main issue of pristine graphene is that it can

produce permanent agglomerates or cause the basal planes to collapse to reform graphite due to the dispersion interactions during the drying process. As a result, the ions could only access and gather on the upper and the lower surfaces of the stacked graphene sheets (graphite) which could further cause a lower catalytic ability[27, 32]. In Qian's study, there are some new favorable properties that the graphene/CNTs hybrid has shown. Firstly, the good water dispersibility of graphene could benefit to disperse the CNTs in water to produce a homogenous solution that can provide higher ion adsorption, shown in Figure 2.15. Also, in the graphene/CNT complex, one dimensional graphene nano-sheets provide a supreme nanostructure for ion adsorption. Furthermore, in the graphene/CNTs hybrid, SWCNTs is acting as a separator between the graphene basal planes to efficiently improve the rapid diffusion paths for the electrons, leading to boost the electrical conduction of electrons.

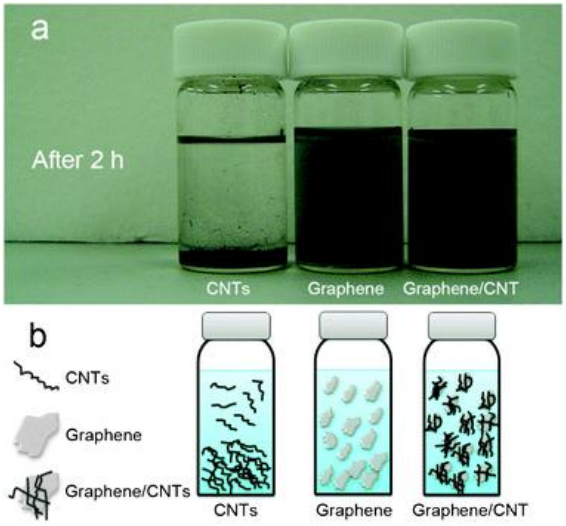

Figure 2.15. Hybrids of graphene and carbon nanotubes. (a) Dispensability of different nanocarbon materials in water for 2 hours after sonication. (b) Schematic illustration of the respective structures in suspension[32].

2.3.3.6 Transition metal anchorage on nanocarbon catalysts

Many researchers have reported that transition metals, such as nickel and cobalt, are often used as catalysts to synthesize carbon precursors into a well-defined low dimensional graphitic complex, for example graphene or carbon nanotubes. By embedding the metal nano-particles

underneath the carbon sheets, this hybrid structure can provide an intriguing scheme for large-scale production of nanocarbon catalysts[15]. Bao *et al.* reported that iron nanoparticles were encapsulated into the partitions of pea-pod like carbon nanotubes (CNTs) via a facile synthesis at 350 ^{o}C in nitrogen atmosphere using ferrocene and sodium azide as catalyst and carbon precursors, respectively. In their oxygen reduction reaction experiment, the iron encapsulated CNT showed excellent catalytic performance. It was believed that the exceptional structure of such a complex provides a well-defined low dimensional nanocarbon material for investigating the nature of transition metal (iron)-induced catalyst, in which the direct interaction of metal particles with harsh environment including acid/basic medium, oxygen, and sulfur contaminations is avoided. In addition the DFT calculation suggested that the catalytic activity was largely enhanced due to the electron transfer from the metal particles to the carbon network which can further lead to a decrease on local work function on the carbon surface[97]. In a similar study, Hong *et al.* report a simplistic method for the synthesis of porous iron and nitrogen modified graphene carbon matrix with Fe_3N encapsulated in graphitic layers. The synthesized hybrid showed good catalytic performance and chemical stability owing to the encapsulation of Fe_3N and the protection of graphitic layers, respectively.

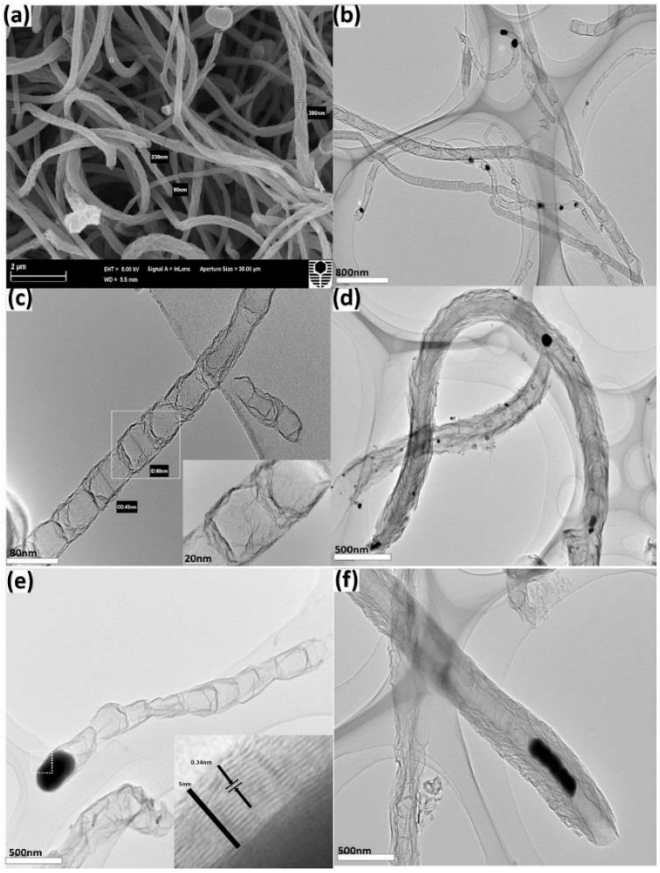

Figure 2.16. Electron Microscope images of the N-doped carbon nanotube with Ni encapsulated. (a) Ni@NCNT fabricated at 800°C. (b) Pea-pod like Ni particle encapsulation . (c) Bamboo like CNT structure with compartments. (d) Ni@NCNT without acid treatment. (e) Ni@NCNT with tip Ni encapsulation. (f) TEM image of Ni@NCNT with worm like Ni particle accumulation at the tube end[35].

Inspired by aforementioned works, in one of recent works of Wang's group, we have feasibly fabricated N modified bamboo-like carbon nanotube embedded with nickel nanoparticles (Ni@NCNTs) by a one-step fabrication route[35]. Ni@NCNTs were not only engaged as adsorbents due to its large surface area, but also applied as catalysts for activating PDS to eliminate an pharmaceutical organic, antibiotic sulfachloropyridazine (SCP). Ni@NCNTs showed a better catalytic activity on PDS activation over other classic carbon based catalysts such as graphene oxide and carbon nanotubes, ascribed to the collaborated effect of heteroatom doping and transition metal insertion. It is then suggested that the exceptional nanotube structure (Figure 2.16) and the heteroatom doping are working as active sites for both the SCP adsorption and PDS activation. Furthermore, with the assistance of Ni insertion the mediocre

catalytic stability of carbon nanotubes was dramatically enhanced. It is worth to mention that the EPR investigation and the quenching tests indicated the radical activation process of Ni@NCNTs/PDS system differs from pristine carbon catalyst. Unlike pristine carbon nanotubes, Ni@NCNTs exhibited a trivial effect from radical quenching agents (ethanol and TBA), which suggested a non-radical pathway was comprised in the PDS activation process. As Figure 2.17 shown, the oxidant (PDS) was suggested to be first attached with the sp^2-hybridizaion complex and then attach the adsorbed SCP molecules, in which the greatly covalent π electrons could activate the double oxygen bond in PDS. In addition, the heteroatom dopants (especially for the quaternary N) would continue to activate the neighboring carbons and largely improve the catalysis.

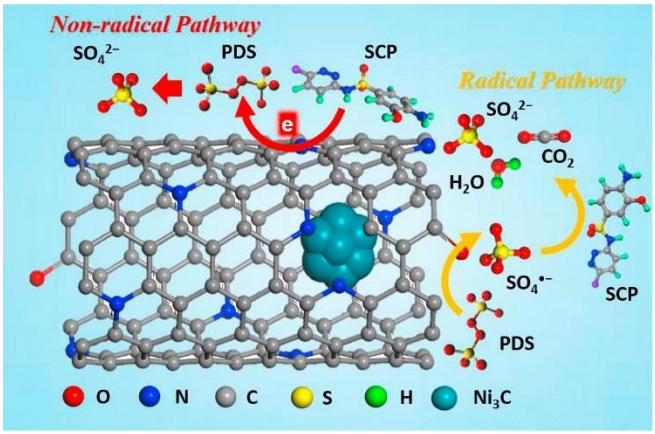

Figure 2.17. Reaction mechanism for organic SCP oxidation by the Ni@NCNTs/PDS system[35].

It is believed that by embedding various transition metals into a carbon framework can considerably influence the structures and catalytic activity of the nanocarbon materials. Yao et al. employed a series of transition metals, such as iron, cobalt and nickel, to fabricate carbon nanotubes with different metal nanocrystals encapsulation for PMS activation. The graphitization degree of different metal encapsulated CNTs was investigated by Raman spectra and the results showed that the graphitization degree increased in an order of Co@CNTs >Ni@CNTs >Fe@CNTs, which could directly affect the catalytic activity in PMS activation process[98]. In another study, unique spring-like CNTs were prepared by using manganese via a one pot pyrolysis. In their study, Mn encapsulated CNTs (Mn@CNTs) demonstrated robust catalytic ability on PMS activation and applied on polymer

degradation under hydrothermal conditions. Comparing the other metal decorated nanocarbon catalysts, Mn@NCNTs showed both enhanced catalytic activity and catalytic stability due to its chemical and mechanical properties, respectively. In addition, the catalytic properties of CNT could further strengthened by taking the advantage of the synergistic effect of two or more metal types. In a recent study, nitrogen-doped carbon nanotubes embedded with Ni/Co bimetallic nanoparticles (NiCo@NCNTs) were prepared by pyrolysis of Ni/Co chlorides with carbon precursor (dicyandiamide). It proved that the hybrid carbon catalyst generated a faster activation efficiency for SR-AOPs, which was 20 and 5 times greater than monometallic embedded CNTs. Moreover, the kinetic study showed that the Ni and Co molar ratio and pyrolysis temperature could significantly affect the catalytic performance, in which Ni/Co-1:1 and 800 ^{o}C demonstrated the most outstanding activity for organic pollutant degradation than other ratios such as 1:2 or 2:1 and 700 or 900 ^{o}C, respectively[29].

2.4. Microplastics pollution

Microplastics treatment is a new research area that Wang' started in late 2018, and it is a later topic of PhD study, in which various AOPs techniques and carbon nano-catalysts have been applied on MPs decomposition for the first time.

In modern society, plastic has been playing a significant role, with widespread commercial, industrialized, pharmaceutical and metropolitan applications, thus the demand of plastic is tremendous that the yearly plastic manufacture has been boosted from 1.5 million tons to almost 300 million tons in the past half of century[99]. A large proportion of these plastics litter has accumulated in the nature at an overwhelming rate via accidental release and indiscriminate discards, and eventually end up in oceans. In recent years, a new type of plastic waste , referred to here as 'microplastics', have attracted extensive attention due to its inconspicuous appearance and detrimental effects on the environment. According to the National Oceanic and Atmospheric Administration, microplastics (MPs) are defined as less than 5 mm in size, which

is an omnipresent constituent of sea debris. MPs can be further categorized into primary and secondary MPs (Figure 2.18), which are purposefully manufactured to be of microscopic size and derived from the fragmentation of microplastics items, respectively[100].

In the past several decades, MPs have been largely accumulating in oceans globally. Studies showed that MPs have been detected on beaches, in surface waters, throughout the water column and within the benthos, surprisingly, microplastics have pervaded and even found its way to the most remote marine environments[101].

2.4.1. Occurrence of MPs

Microplastics can originate from two main sources, land and ocean[102]. The ocean-based MPs sources only contribute approximately one fifth of the total plastic debris in marine environment, which is consisted of commercial fishing, containers and other activities[103]. Meanwhile, the rest 80% of microplastics are attributed to the terrestrial sources, which include airblasting process, pharmaceutical and cosmetic products, inappropriately disposed plastics and discharges from garbage station. It was reported that, when the terrestrial derived MPs are discharged into the water systems in nature, a large proportion of them would be eventually end up in oceans via rivers while the residual MPs would exist in fresh water systems, even in some isolated water systems such as distant highland lakes[100].

Much of efforts have been done on the research of microplastics occurrence in oceans, where merely less than 4% of MPs occurrence studies were done and reported associated with freshwaters. Despite the limited research on MPs distribution in freshwater, the available information discovered that the large quantity of MPs in freshwaters is equivalent to that of marine environment and the distribution is greatly heterogeneous. Eerkes *et al*. reported that the mean values of MPs abundance in freshwater systems can be greatly varied, where zero detection of MPs in some areas while millions of MPs pieces per cubic meter in other places.

The noteworthy MPs distribution variation can be attributed to factors like sampling locations, human activities, inherent natural conditions and sampling means. Among all the terrestrial MPs sources, wastewater treatment is considered to be the dominant one. In one recent study, Mika *et al*. revealed that, although wastewater treatment plants (WWTPs) functioned based on the traditional activated sludge process can remove up to 95% of MPs and the tertiary treatment can remove 90% of MPs with size larger than 10 μm, there are still considerable amount of MPs released into natural waters via WWTPs.

Regarding the direct transfer of MPs in to oceans, seaside tourism, recreational and commercial fishing, marine containers and marine businesses, such as aquaculture and oilrigs, are the dominant sources[100, 104]. Tourism and entertaining activities make up a vast amount of plastics rubbish and discharged along beaches and coastal resorts, though it is significant to realize that plastic pieces observed on beaches will also accumulate via the beaching of materials carried on in-shore and ocean currents[105]. In addition, fishing gears are commonly detected MPs, such as plastic monofilament line and nylon netting that are neutrally buoyant, as a result they can drift at different depths within the oceans. Lozano *et al*. suggested that these fishing gear plastic wastes known as "ghost fishing" with an inherent capacity is particularly problematic, often causing entanglement of marine biota[100]. Moreover, marine vessels are believed to be an important contributor to marine MPs source. A study estimated that more than 23,000 tons of plastic packaging rubbish have been discharge into oceans by commercial fishing companies during the 1970s along, and this number has been continuously increased since then[106]. Even though an international agreement was implemented forbidding marine vessels from dumping plastic waste in oceans in 1988, shipping still account for a leading contributor of plastic in the marine environment due to the lack of enforcement and education[104]. More recently, it was reported that the extensively used rinse-off personal care products contain plentiful primary MPs exfoliators such as ''microbeads'' or ''micro exfoliates,'' which are irresponsibly flushed

into sewage and are almost impossible to eliminate by water treatment plants[107]. In the early 1990s, these primary MPs were first reported and considered as a minor source of plastic pollution, and they were often existing in PPCPs such as facial cleansers and rarely used by mass consumers[108]. However, in recent years microplastics have now largely substituted natural exfoliating materials such as oatmeal, pumice, apricot or walnut husks in PPCPs, the mass customers now commonly are using microplastic-containing products on a day-to-day basis. It was reported that the majority of facial cleansers in New Zealand supermarkets discovered that polyethylene as common ingredient presenting in diverse forms and described as "micro-beads" and "micro exfoliates"[108].

When these MPs containing produces are used, the microplastics would travel through city wastewater treatment plants. However, due to their small size (< 5 mm), they are easily to escape the preliminary treatment screens on wastewater systems and enter the oceans[109].

Figure 2.18 Types of MPs, primary MPs and secondary MPs[118].

2.4.2. Impact of MPs on the environment

The broad occurrence of MPs in the natural waters has aroused the concerns of potential harmful impacts on the natural environment. Researchers have catalogued the MPs impacts into three classes: physical, chemical and biological impacts. Although these finds are mainly

based on oceanic environment, it was suggested that they could be employed for freshwater bodies as well[110].

Physical impacts of MPs mostly contain entanglement and ingestion satiety, in which the entanglement of marine lives happened more frequently than ingestion; however, entanglement caused by microplastics predominantly occurs to relatively large marine organism. While, ingestion of MPs can be detected throughout nearly all the trophic levels, such as zooplankton taxa, marine lugworm, mussel, oyster, fish, sea turtles, dolphins, whales and seabirds.

One frequent question is that: what happens if MPs are swallowed by water organisms? In early reports, it was believed that the ingestion did not directly execute lethal damage on organisms, however, the chromic effects was an important issue. With the intention of mimic the biological behavior of ingested plastics on water birds, researchers conducted an investigation on the possible impacts of plastic ingestion on domestic chickens. The results later showed that the more plastic was fed to the chicken the less food consumption was observed, which indicated that the ingested plastic debris (MPs) could directly impair seabirds' digestion system. Additionally, Daniel *et al*. provide insight into MPs in oysters along the Pearl River in China (Figure 2.19)[111]. It was reviewed that the highest microplastics detection was found in oysters near urban areas because of the impacts of vast human activities. Great amount of small polymer fibers were detected in the oysters and the accumulation of MPs in oysters' digestion system may lead to severe starvation. It was also suggested that the occurrence of MPs in oyster could indicate the MPs pollution in water, which can be used as biomonitor for the MPs in estuarine environment[111].

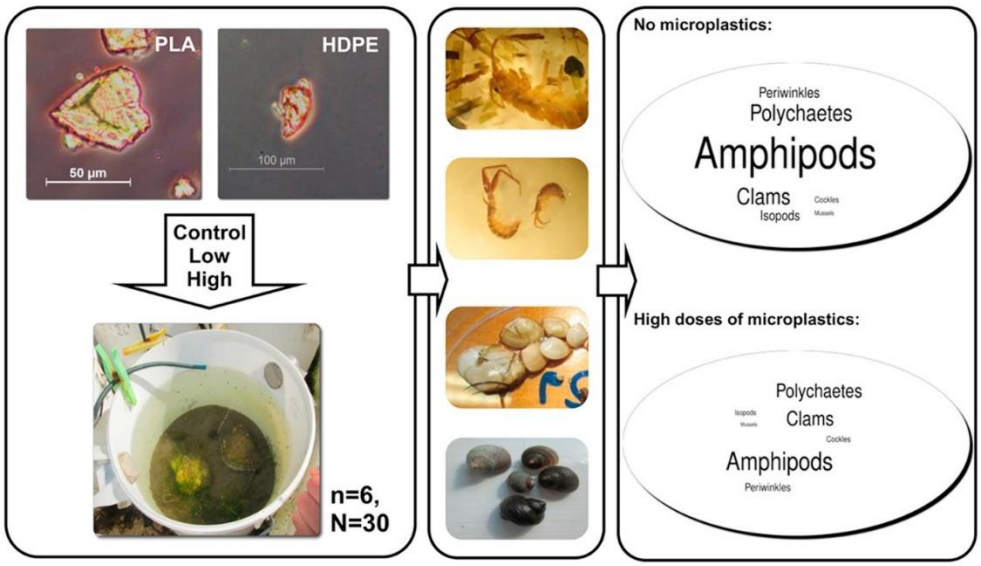

Figure 2.19. MPs plastic are found in oysters[121]. The chemical and biological impacts of MPs on living creatures are more significant. Once the MPs is taking in the digestion system, it can effectively cause poisonous effects to humans and other living organisms via a number of paths and mechanisms. For instance, it is known that MPs are composed of polymer molecules, which can lead to certain health issues. The polymers used in manufacture of plastics and the pigment and additives such as copper ions can be even more toxic. Additionally, MPs often possess large surface area, especially for aged and oxidized MPs, which can be perfect absorbents for toxins in oceans, as the MPs is transported by the ocean current, the absorbed toxic contaminated would be desorbed and also transported to other locations[110]. In addition, for even smaller plastic debris like nano plastics, is resistant to undergo biodegradation that not only accumulate in the stomach of fish and also translocate through blood circulation[110, 112]. Studies reported that shellfishes, after being experienced months of exposure to polystyrene microplastics, showed that the oocyte number was reduced, and the reproductive system was irreversibly damaged[113]. In recent studies, Espinosa *et al.* examined the *in vitro* influences of MPs on various types of fishes. After 24 h of exposure of head-kidney leucocytes with MPs in a rotatory system, the results suggested that the constant exposure of sea creatures to polyvinylchloride and polyethylene microplastics could permanently damage fish immune

systems, and this could be attributing to the oxidative stress secrete in the fish leucocytes[114]. Another study found that MPs could pass in the human food chain either by inhalation or by ingestion, such as shellfish and crustaceans. It was suggested that the small plastic debris are easily absorbed and may accumulate in the organs such as brain, liver and other tissues in aquatic species and other animals, which will pose great potential threat to human central nervous system and the reproductive system if under high exposure level[115]. MPs are also proved to be a perfect vehicle for water based hydrophobic pollutants. In a recent study, Division *et al*. showed that common plastic materials presented high sorption capacities to hydrophobic organic contaminants, and due to the fact that MPs are widespread, they have a crucial role in the fate and transport of hydrophobic organic chemicals in the marine environment[116]. Several other studies suggested that MPs could sorb high amount of polychlorinated biphenyls, lubrication oils and heavy metals from the surrounding seawater in coastal areas[117]. These pollutants are initially adhered on MPs surface and then released when MPs are transferred and ingested by organisms under a preference circumstance such as low pH and high temperature. It is worth to note that the research on the real sorption behavior for water borne pollutants in fresh water on MPs is rather limited and the toxicity of MPs in fresh waters is also lack of research efforts. Yini *et al*. recently have studied the joint toxicity of MPs with a pharmaceutical pollutant (phenanthrene) to algae and the effects of MPs on the environmental fate and bioaccumulation of the pharmaceutical chemical in fresh water. During a fortnight development, the existence of MPs considerably improved bioaccumulation of phenanthrene-derived remains and repressed the degeneracy and transformation of phenanthrene in the medium. The results showed that the smaller size (nano-plastics) of plastic debris would have higher potential ecological risks due to the higher adsorption towards hydrophobic toxic pollutants.

2.4.3. MPs sampling, extraction and identification

Although the research on MPs have been carried on for nearly a decade, the approaches on MPs sampling, sample pretreatment, quantification and identification vary significantly from studies, which makes it difficult to compare. Volume reduced sampling (VRS) and bulk sampling (BS) are the two main types of sampling methodologies that have been most frequently reported. In the VRS, it was found that the volume of sample was decreased during the sampling period while there was no reduction on water volume in the bulk sampling. Typically, a trawl is used along a transect to collect surface water MPs samples due to that the lower density MPs have a tendency to drift on the water surface[118]. Regarding the BS, the volume also varies among studies[119]. For example, a 100 L water sample was used while the 100 mL and 2 L were used in other studies[120]. It was reported that the MPs size distribution and particle compositions were depended on the how the sample was taken. For example, there was a conspicuous difference on polystyrene abundance between the samples collected by manta trawl (96%) and by surface microlayer (0.2%)[110]. Another important factor to sampling is the size of the MPs, as mentioned earlier; the size of MPs can vary from 1 μm to 5 mm. Song *et al*. discovered that MPs with a size less than 50 micrometers were underestimated[121]. Therefore, when larger size meshes (>100 μm) are used to collect samples a big proportion of MPs with sizes smaller than the mesh would be miscounted in the results. For that reason, it is urgent to develop advanced and suitable methods for sampling MPs with various sizes.

After the MPs are sampled, the following step is extraction or purification, where the MPs are segregated from the initial matrix for preparing for later procedures, which are quantification and identification. Frequently, MPs extraction can be achieved by density separation, where saturated salt solution (NaCl, NaI, $ZnCl_2$ and sodium polytungstate etc.) with designed density

is used to suspend MPs with the assistance of stir and shake[122-124]. After a certain time of settling, MPs then float to the top layer of salt solution and other particles with greater density for instance sand and metal would sink to the bottom. Additionally to density separation, other separation techniques were reported. Elutriation has been often applied to isolate MPs from marine sediments, where low-density MPs can be reserved through the upward water or aeration flow in a designed elutriation and floatation equipment, usually columns. Subsequently, purification processes are applied to minimize the interference on analysis from matters like organic compounds and inorganic dusts. Purification is usually done by chemical degradation and enzymatic degradation. Hydrogen peroxide (10 -30%) and mineral acids are commonly used[125].

The final step is to sort the MPs that have been collected. Currently, visual sorting is mostly used, though it does not always provide the accurate information on MPs due to the human misjudgment on other non-plastic particles such as sand and microorganisms. This surely deserve further approaches such as automatic sorting by robots to be more efficient and accurate on MPs identification and quantification.

2.4.4. Removal techniques

Unfortunately, the removal technique of MPs is still in its infant stage, where only a few studies were conducted. There are three dominant removal techniques available, which are physical (filtration), chemical (advance oxidation processes) and biodegradation (marine fungus).

Although a big proportion of MPs can be efficiently removed by conventional wastewater treatment, millions of tons of MPs are discharged into the aquatic environment. Julia *et al*.

examined the elimination of MPs from effluents in a variety of metropolitan wastewater treatment plants applying different newer designed final stage treatment techniques, which includes membrane bioreactor and tertiary treatment. The results showed that the designed advanced final-stage wastewater treatment, such as disc filter, fast sand filtration and dissolved air flotation, could largely increase the MPs removal efficiency, especially on MPs less than 20 µm[126]. After final stages of treatment, MPs with the smallest size fraction (20–200 µm) were found to be the most abundant[8]. In addition, more fiber wad found in the final effluent than in the previous stages, indicating that the fibers could pass filter or membrane through more easily and vertically. For this reason, it is required to develop more advanced final stage treatment method that can be applied to effectively to remove MPs with very small sizes[127]. It is worth to note that MPs removed through backwashing of filters are unavoidably sent back to the early stages of the WWTP. As a result, the MPs captured by final treatment stage might not be eliminated from the WWTP and could lead to the accumulation of MPs in the WWTP[128]

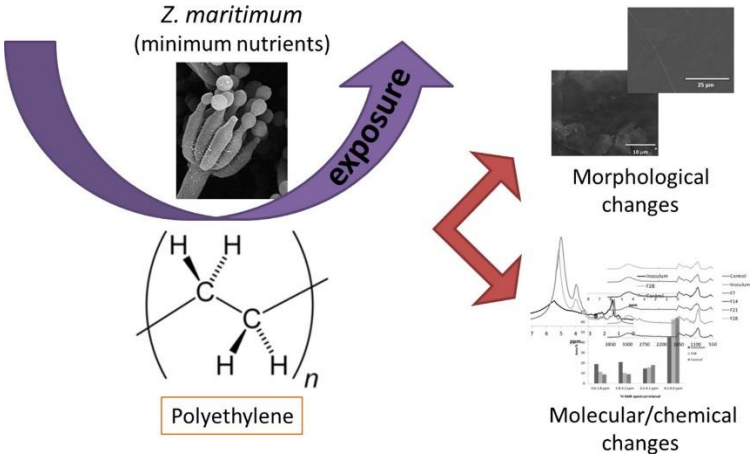

Figure 2.20 Biodegradation of polyethylene microplastics by the marine fungus Zalerion maritimum[139].

It is believed that MPs are subject to biotic degradation mechanism in the environment, where the degradation process is mediated by microorganisms and the MPs are decomposed into less

toxic or nontoxic substances, such as carbon dioxide, water and some inorganic compounds[129]. It was reported that the chemical and physical properties of MPs and natural environmental perimeters such as light, heat, humidity and the presence of other organic chemicals can be dramatically influence the biodegradation processes, Figure 2.20[129]. A number of studies have reported that some particular types of microorganisms have been shown to be capable of using plastics as the only source of food, which were found in solid matrices, such as soil and compost. This provided a potential application of these microorganisms (often are algae) in the biodegradation of MPs. Ana *et al.*, in their recent study, proved the capacity of a type of fungus called Z. maritimum in the marine environment can be applied as a biodegradation mediator of polyethylene, one of the most commonly used polymers. Their study showed that a significant mass decrease of MP was observed after a 14-day exposure to the Z. maritimum, in which a biomass variation of 82% was exhibited.

In our recent study, Wang's team has demonstrated that AOPs could be a powerful technique to remove MPs via deep oxidation. In a typical sulfate radical induced AOPs, catalysts were first scattered into pure water in an autoclave and the MPs were also added into the mixture. The oxidation reaction was initiated by introducing PMS into the solution, shown in Figure 2.21. The autoclave was then placed in an oven at designed temperature, ranging from 100 to 160 ºC. The results showed that polyethylene-based MPs were successfully oxidized by the integrated carbon/HT/persulfate system. This technique is proved great potential for breaking down other plastics such as high-density polyethylene, polyvinyl chloride, and polypropylene. Moreover, in the toxicity evaluation, a common algae (C. vulgaris) was used to evaluate the toxicity of the generated byproducts during MPs oxidation. It is proved that the MPs degradation byproducts from MPs can be used by the microorganisms as nutrient to be transformed to other nontoxic products, such as sugar, protein, biofuels, converting the carbons back to nature in an environmental friendly and sustainable strategy. The results would

encourage the application of ecofriendly carbocatalysis for microplastics elimination and offer an advanced technique for the conversion of microplastics into the carbon cycle of the ecosystem in a sustainable manner[130].

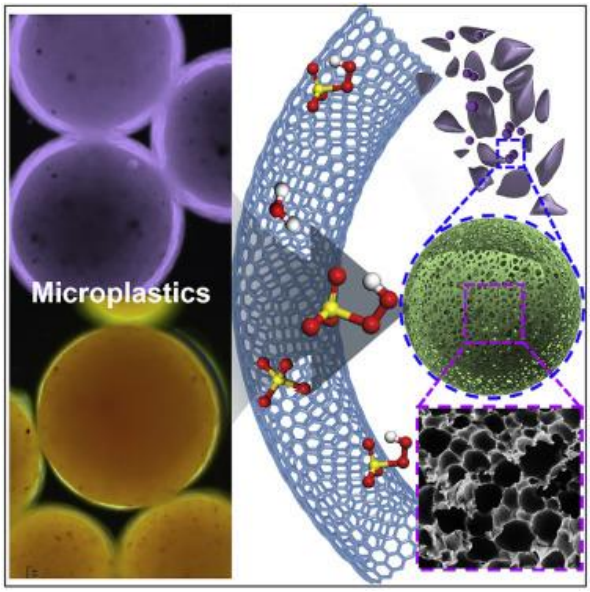

Figure 2.21. Degradation of Cosmetic Microplastics via Functionalized Carbon Nanosprings[30].

.

2.5 Conclusions

Advanced oxidation processes have been extensively studied and showing great potential for the complete degradation of a large variety of organic pollutants such as antibiotics, pesticides, pigments and microplastics to harmless substances in wastewater treatment fields. A number of oxidants are applied, such as hydroperoxide, peroxymonosulfate and ozone for the production of reactive oxygen species, including hydroxyl radical, sulfate radical, singlet oxygen etc. To sufficiently activate these oxidants for deep oxidation, various activation strategies have been approached, which include the early physical activation measures such as ultrasonic, ultraviolet radiation, and electrical energy. Although these primitive physical activation techniques have shown great performance on oxidant activation, the high-energy

consumption has intrinsically limited their further development. Alternately, catalytic activation with little energy input and superior catalytic performance has attracted increasingly scientific attention in recent years. Among these catalysts, metal-free nanocarbon materials such as graphene and nanocarbon tubes have been proved to be superior to metal based catalysts in terms of catalytic activity and stability, and environmental-friendly nature.

Nanocarbons are not without limitations, for example, pristine carbon materials often show inert activity toward oxidants due to the well-arranged carbon frameworks. A large scale of temptation have been established to break the inertness and enhance the stability by either creating more active sites or anchored with transition metals. These modifications include carbon dioxide activation, heteroatom doping and metal encapsulation. Many studies have confirmed the improvement of the nanocarbon catalysts in the AOPs oxidants activation performance by introducing one or a combination of different modification methods. It is worth to mention that a novel carbon modification technique has recently been reported, which involves the synergistic effect between transition metal encapsulation and heteroatom doping. Nanocarbons fabricated in such a method could take the advantage of the transition metals that are with abundant electrons while significantly avoid the metal leaching issue due to the protection from multiple-layer carbon walls. Despite the greatly enhanced catalytic activity of carbon materials, the research of facile synthesis methods with less complicated procedures and minimum energy consumption for metal free catalysts is still greatly underdeveloped and deserves additional efforts in the future.

Moreover, the application of AOPs on microplastics decomposition has recently proved to be feasible, where the long polymer carbon chains can be clipped by reactive oxygen species with the assistance of hydrothermal condition. In addition, the oxidation intermediates and products can be further broken-down into water and carbon dioxide by microorganisms though bio-degradation, which provides a novel method to improve the increasingly serious damage

caused by the microplastics pollution. The study of MPs decomposition by AOPs is still in its infant stage which currently shows some limitations such as the heavy dependence on hydrothermal assistance and the low minimization level, therefore requires a continuous future study.

2.6 References

1. Vörösmarty, C. J.; McIntyre, P. B.; Gessner, M. O.; Dudgeon, D.; Prusevich, A.; Green, P.; Glidden, S.; Bunn, S. E.; Sullivan, C. A.; Liermann, C. R.; Davies, P. M., Global threats to human water security and river biodiversity. *Nature* **2010,** *467*, (7315), 555-561.

2. Schwarzenbach, R. P.; Egli, T.; Hofstetter, T. B.; Gunten, U. v.; Wehrli, B., Global Water Pollution and Human Health. *Annual Review of Environment and Resources* **2010,** *35*, (1), 109-136.

3. Yang, X.; Flowers, R. C.; Weinberg, H. S.; Singer, P. C., Occurrence and removal of pharmaceuticals and personal care products (PPCPs) in an advanced wastewater reclamation plant. *Water Research* **2011,** *45*, (16), 5218-5228.

4. Wang, J.; Chu, L., Irradiation treatment of pharmaceutical and personal care products (PPCPs) in water and wastewater: An overview. *Radiation Physics and Chemistry* **2016,** *125*, 56-64.

5. Matamoros, V.; Arias, C.; Brix, H.; Bayona, J. M., Removal of Pharmaceuticals and Personal Care Products (PPCPs) from Urban Wastewater in a Pilot Vertical Flow Constructed Wetland and a Sand Filter. *Environmental Science & Technology* **2007,** *41*, (23), 8171-8177.

6. Liu, J.-L.; Wong, M.-H., Pharmaceuticals and personal care products (PPCPs): A review on environmental contamination in China. *Environment International* **2013,** *59*, 208-224.

7. Murphy, F.; Ewins, C.; Carbonnier, F.; Quinn, B., Wastewater Treatment Works (WwTW) as a Source of Microplastics in the Aquatic Environment. *Environmental Science & Technology* **2016,** *50*, (11), 5800-5808.

8. Ziajahromi, S.; Neale, P. A.; Rintoul, L.; Leusch, F. D. L., Wastewater treatment plants as a pathway for microplastics: Development of a new approach to sample wastewater-based microplastics. *Water Research* **2017,** *112*, 93-99.

9. Deng, Y.; Zhao, R., Advanced Oxidation Processes (AOPs) in Wastewater Treatment. *Current Pollution Reports* **2015,** *1*, (3), 167-176.

10. Vilhunen, S.; Sillanpää, M., Recent developments in photochemical and chemical AOPs in water treatment: a mini-review. *Reviews in Environmental Science and Bio/Technology* **2010,** *9*, (4), 323-330.

11. Germán, S.-M.; Gabriela, R.-M.; Dora, S.-C.; Rubí, R.; Reyna, N., Advanced Oxidation Processes: Ozonation and Fenton Processes Applied to the Removal of Pharmaceuticals. In *Ecopharmacovigilance: Multidisciplinary Approaches to Environmental Safety of Medicines*, Gómez-Oliván, L. M., Ed. Springer International Publishing: Cham, 2019; pp 119-142.

12. Oturan, M. A.; Aaron, J.-J., Advanced Oxidation Processes in Water/Wastewater Treatment: Principles and Applications. A Review. *Critical Reviews in Environmental Science and Technology* **2014,** *44*, (23), 2577-2641.

13. Alaton, I. A.; Balcioglu, I. A.; Bahnemann, D. W., Advanced oxidation of a reactive dyebath effluent: comparison of O3, H2O2/UV-C and TiO2/UV-A processes. *Water Research* **2002,** *36*, (5), 1143-1154.

14. Pignatello, J. J.; Oliveros, E.; MacKay, A., Advanced Oxidation Processes for Organic Contaminant Destruction Based on the Fenton Reaction and Related Chemistry. *Critical Reviews in Environmental Science and Technology* **2006,** *36*, (1), 1-84.

15. Duan, X.; Sun, H.; Wang, S., Metal-Free Carbocatalysis in Advanced Oxidation Reactions. *Accounts of Chemical Research* **2018,** *51*, (3), 678-687.

16. Neyens, E.; Baeyens, J., A review of classic Fenton's peroxidation as an advanced oxidation technique. *Journal of Hazardous Materials* **2003,** *98*, (1), 33-50.

17. Wang, N.; Zheng, T.; Zhang, G.; Wang, P., A review on Fenton-like processes for organic wastewater treatment. *Journal of Environmental Chemical Engineering* **2016,** *4*, (1), 762-787.

18. Duan, X.; Kang, J.; Tian, W.; Zhang, H.; Ho, S.-H.; Zhu, Y.-A.; Ao, Z.; Sun, H.; Wang, S., Interfacial-engineered cobalt@carbon hybrids for synergistically boosted evolution of sulfate radicals toward green oxidation. *Applied Catalysis B: Environmental* **2019,** *256*, 117795.

19. Deng, Y.; Ezyske, C. M., Sulfate radical-advanced oxidation process (SR-AOP) for simultaneous removal of refractory organic contaminants and ammonia in landfill leachate. *Water Research* **2011,** *45*, (18), 6189-6194.

20. Wang, S., A Comparative study of Fenton and Fenton-like reaction kinetics in decolourisation of wastewater. *Dyes and Pigments* **2008,** *76*, (3), 714-720.

21. Shuai, W.; Gu, C.; Fang, G.; Zhou, D.; Gao, J., Effects of iron (hydr)oxides on the degradation of diethyl phthalate ester in heterogeneous (photo)-Fenton reactions. *Journal of Environmental Sciences* **2019,** *80*, 5-13.

22. Sun, Y.; Yang, Z.; Tian, P.; Sheng, Y.; Xu, J.; Han, Y.-F., Oxidative degradation of nitrobenzene by a Fenton-like reaction with Fe-Cu bimetallic catalysts. *Applied Catalysis B: Environmental* **2019,** *244*, 1-10.

23. Brillas, E., Electro-fenton, UVA photoelectro-Fenton and solar photoelectro-Fenton treatments of organics in waters using a boron-doped diamond anode: A review. *Journal of the Mexican Chemical Society* **2014,** *58*, (3), 239-255.

24. Lucas, M. S.; Peres, J. A., Decolorization of the azo dye Reactive Black 5 by Fenton and photo-Fenton oxidation. *Dyes and Pigments* **2006,** *71*, (3), 236-244.

25. Herney-Ramirez, J.; Vicente, M. A.; Madeira, L. M., Heterogeneous photo-Fenton oxidation with pillared clay-based catalysts for wastewater treatment: A review. *Applied Catalysis B: Environmental* **2010,** *98*, (1), 10-26.

26. Bokare, A. D.; Choi, W., Review of iron-free Fenton-like systems for activating H2O2 in advanced oxidation processes. *Journal of Hazardous Materials* **2014,** *275*, 121-135.

27. Duan, X.; Su, C.; Zhou, L.; Sun, H.; Suvorova, A.; Odedairo, T.; Zhu, Z.; Shao, Z.; Wang, S., Surface controlled generation of reactive radicals from persulfate by carbocatalysis on nanodiamonds. *Applied Catalysis B: Environmental* **2016,** *194*, 7-15.

28. Zhang, T.; Chen, Y.; Wang, Y.; Le Roux, J.; Yang, Y.; Croué, J.-P., Efficient Peroxydisulfate Activation Process Not Relying on Sulfate Radical Generation for Water Pollutant Degradation. *Environmental Science & Technology* **2014,** *48*, (10), 5868-5875.

29. Kang, J.; Zhang, H.; Duan, X.; Sun, H.; Tan, X.; Liu, S.; Wang, S., Magnetic Ni-Co alloy encapsulated N-doped carbon nanotubes for catalytic membrane degradation of emerging contaminants. *Chemical Engineering Journal* **2019,** *362*, 251-261.

30. Kang, J.; Zhou, L.; Duan, X.; Sun, H.; Ao, Z.; Wang, S., Degradation of Cosmetic Microplastics via Functionalized Carbon Nanosprings. *Matter* **2019,** *1*, (3), 745-758.

31. Duan, X.; Indrawirawan, S.; Kang, J.; Tian, W.; Zhang, H.; Duan, X.; Zhou, X.; Sun, H.; Wang, S., Synergy of carbocatalytic and heat activation of persulfate for evolution of reactive radicals toward metal-free oxidation. *Catalysis Today* **2019**.

32. Cheng, Q.; Tang, J.; Ma, J.; Zhang, H.; Shinya, N.; Qin, L.-C., Graphene and carbon nanotube composite electrodes for supercapacitors with ultra-high energy density. *Physical Chemistry Chemical Physics* **2011,** *13*, (39), 17615-17624.

33. Zhang, J.; Su, D.; Zhang, A.; Wang, D.; Schlögl, R.; Hébert, C., Nanocarbon as robust catalyst: Mechanistic insight into carbon-mediated catalysis. *Angewandte Chemie - International Edition* **2007,** *46*, (38), 7319-7323.

34. Zhong, Z.; Chen, H.; Tang, S.; Ding, J.; Lin, J.; Lee Tan, K., Catalytic growth of carbon nanoballs with and without cobalt encapsulation. *Chemical Physics Letters* **2000,** *330*, (1–2), 41-47.

35. Kang, J.; Duan, X.; Wang, C.; Sun, H.; Tan, X.; Tade, M. O.; Wang, S., Nitrogen-doped bamboo-like carbon nanotubes with Ni encapsulation for persulfate activation to remove emerging contaminants with excellent catalytic stability. *Chemical Engineering Journal* **2018,** *332*, 398-408.

36. Saputra, E.; Muhammad, S.; Sun, H.; Ang, H.-M.; Tade, M. O.; Wang, S., Shape-controlled activation of peroxymonosulfate by single crystal alpha-Mn2O3 for catalytic phenol degradation in aqueous solution. *Applied Catalysis B-Environmental* **2014,** *154*, 246-251.

37. Wang, S.; Sun, H.; Ang, H. M.; Tadé, M. O., Adsorptive remediation of environmental pollutants using novel graphene-based nanomaterials. *Chemical Engineering Journal* **2013,** *226*, 336-347.

38. Krieger-Liszkay, A., Singlet oxygen production in photosynthesis. *Journal of Experimental Botany* **2004,** *56*, (411), 337-346.

39. Wang, S. Y.; Jiao, H., Scavenging Capacity of Berry Crops on Superoxide Radicals, Hydrogen Peroxide, Hydroxyl Radicals, and Singlet Oxygen. *Journal of Agricultural and Food Chemistry* **2000,** *48*, (11), 5677-5684.

40. Jiménez, S.; Andreozzi, M.; Micó, M. M.; Álvarez, M. G.; Contreras, S., Produced water treatment by advanced oxidation processes. *Science of The Total Environment* **2019,** *666*, 12-21.

41. Pereira, M. C.; Oliveira, L. C. A.; Murad, E., Iron oxide catalysts: Fenton and Fentonlike reactions – a review. *Clay Minerals* **2012,** *47*, (3), 285-302.

42. Hesse, S.; Kleiser, G.; Frimmel, F. H., Characterization of refractory organic substances (ROS) in water treatment. *Water Science and Technology* **1999,** *40*, (9), 1-7.

43. Ikehata, K.; Gamal El-Din, M., Aqueous Pesticide Degradation by Ozonation and Ozone-Based Advanced Oxidation Processes: A Review (Part II). *Ozone: Science & Engineering* **2005,** *27*, (3), 173-202.

44. Pérez, M.; Torrades, F.; Domènech, X.; Peral, J., Fenton and photo-Fenton oxidation of textile effluents. *Water Research* **2002,** *36*, (11), 2703-2710.

45. Miller, A. J.; Hatton, R. A.; Chen, G. Y.; Silva, S. R. P., Carbon nanotubes grown on In2O3:Sn glass as large area electrodes for organic photovoltaics. *Applied Physics Letters* **2007,** *90*, (2), 023105.

46. Bobu, M.; Yediler, A.; Siminiceanu, I.; Schulte-Hostede, S., Degradation studies of ciprofloxacin on a pillared iron catalyst. *Applied Catalysis B: Environmental* **2008,** *83*, (1-2), 15-23.

47. Martínez-Huitle, C. A.; Brillas, E., Decontamination of wastewaters containing synthetic organic dyes by electrochemical methods: A general review. *Applied Catalysis B: Environmental* **2009,** *87*, (3), 105-145.

48. Brillas, E.; Martínez-Huitle, C. A., Decontamination of wastewaters containing synthetic organic dyes by electrochemical methods. An updated review. *Applied Catalysis B: Environmental* **2015,** *166-167*, 603-643.

49. Liu, S.; Zeng, T. H.; Hofmann, M.; Burcombe, E.; Wei, J.; Jiang, R.; Kong, J.; Chen, Y., Antibacterial Activity of Graphite, Graphite Oxide, Graphene Oxide, and Reduced Graphene Oxide: Membrane and Oxidative Stress. *ACS Nano* **2011,** *5*, (9), 6971-6980.

50. Neta, P.; Huie, R. E.; Ross, A. B., Rate Constants for Reactions of Inorganic Radicals in Aqueous Solution. *Journal of Physical and Chemical Reference Data* **1988,** *17*, (3), 1027-1284.

51. Janzen, E. G.; Kotake, Y.; Randall D, H., Stabilities of hydroxyl radical spin adducts of PBN-type spin traps. *Free Radical Biology and Medicine* **1992,** *12*, (2), 169-173.

52. Olmez-Hanci, T.; Arslan-Alaton, I., Comparison of sulfate and hydroxyl radical based advanced oxidation of phenol. *Chemical Engineering Journal* **2013,** *224*, (1), 10-16.

53. Hu, L.; Yang, X.; Dang, S., An easily recyclable Co/SBA-15 catalyst: Heterogeneous activation of peroxymonosulfate for the degradation of phenol in water. *Applied Catalysis B: Environmental* **2011,** *102*, (1–2), 19-26.

54. Yao, Y.; Cai, Y.; Wu, G.; Wei, F.; Li, X.; Chen, H.; Wang, S., Sulfate radicals induced from peroxymonosulfate by cobalt manganese oxides (CoxMn3−xO4) for Fenton-Like reaction in water. *Journal of Hazardous Materials* **2015,** *296*, 128-137.

55. Guan, Y.-H.; Ma, J.; Li, X.-C.; Fang, J.-Y.; Chen, L.-W., Influence of pH on the Formation of Sulfate and Hydroxyl Radicals in the UV/Peroxymonosulfate System. *Environmental Science & Technology* **2011,** *45*, (21), 9308-9314.

56. Wang, S.; Wang, J.; Sun, Y., Degradation of chlorinated paraben by integrated irradiation and biological treatment process. *Journal of Environmental Management* **2017,** *189*, 29-35.

57. Ball, D. L.; Edwards, J. O., The Kinetics and Mechanism of the Decomposition of Caro's Acid. I. *Journal of the American Chemical Society* **1956,** *78*, (6), 1125-1129.

58. Zou, J.; Ma, J.; Chen, L.; Li, X.; Guan, Y.; Xie, P.; Pan, C., Rapid Acceleration of Ferrous Iron/Peroxymonosulfate Oxidation of Organic Pollutants by Promoting Fe(III)/Fe(II) Cycle with Hydroxylamine. *Environmental Science & Technology* **2013,** *47*, (20), 11685-11691.

59. Rodriguez, S.; Vasquez, L.; Costa, D.; Romero, A.; Santos, A., Oxidation of Orange G by persulfate activated by Fe(II), Fe(III) and zero valent iron (ZVI). *Chemosphere* **2014,** *101*, 86-92.

60. Zou, J.; Ma, J.; Chen, L.; Li, X.; Guan, Y.; Xie, P.; Pan, C., Rapid acceleration of ferrous iron/peroxymonosulfate oxidation of organic pollutants by promoting Fe(III)/Fe(II) cycle with hydroxylamine. *Environmental Science and Technology* **2013,** *47*, (20), 11685-11691.

61. Usman, M.; Faure, P.; Ruby, C.; Hanna, K., Application of magnetite-activated persulfate oxidation for the degradation of PAHs in contaminated soils. *Chemosphere* **2012,** *87*, (3), 234-240.

62. Rastogi, A.; Al-Abed, S. R.; Dionysiou, D. D., Sulfate radical-based ferrous-peroxymonosulfate oxidative system for PCBs degradation in aqueous and sediment systems. *Applied Catalysis B: Environmental* **2009,** *85*, (3-4), 171-179.

63. Kalpanadevi, K.; Sinduja, C. R.; Manimekalai, R., Characterisation of nanostructured Co3O4 synthesised by the thermal decomposition of an inorganic precursor. *Australian Journal of Chemistry* **2014,** *67*, (11), 1671-1674.

64. Małecka, B.; Drozdz-Cieśla, E.; Małecki, A., Non-isothermal studies on mechanism and kinetics of thermal decomposition of cobalt(II) oxalate dihydrate. *Journal of Thermal Analysis and Calorimetry* **2002,** *68*, (3), 819-831.

65. Grimes, R. W.; Fitch, A. N., Thermal decomposition of cobalt(II) acetate tetrahydrate studied with time-resolved neutron diffraction and thermogravimetric analysis. *Journal of Materials Chemistry* **1991,** *1*, (3), 461-468.

66. Straszko, J.; Olszak-Humienik, M.; Mozejko, J., Study of the mechanism and kinetic parameters of the thermal decomposition of cobalt sulphate hexahydrate. *Journal of Thermal Analysis and Calorimetry* **2000,** *59*, (3), 935-942.

67. Yang, H.; Hu, Y.; Zhang, X.; Qiu, G., Mechanochemical synthesis of cobalt oxide nanoparticles. *Materials Letters* **2004,** *58*, (3), 387-389.

68. Ilyas, M.; Saeed, M., Oxidation of Benzyl Alcohol in Liquid Phase Catalyzed by Cobalt Oxide. In *International Journal of Chemical Reactor Engineering*, 2010; Vol. 8.

69. Ji, F.; Li, C.; Wei, X.; Yu, J., Efficient performance of porous Fe2O3 in heterogeneous activation of peroxymonosulfate for decolorization of Rhodamine B. *Chemical Engineering Journal* **2013,** *231*, 434-440.

70. Zinatloo-Ajabshir, S.; Salavati-Niasari, M., Nanocrystalline Pr<inf>6</inf>O<inf>11</inf>: Synthesis, characterization, optical and photocatalytic properties. *New Journal of Chemistry* **2015,** *39*, (5), 3948-3955.

71. Zinatloo-Ajabshir, S.; Salavati-Niasari, M.; Hamadanian, M., Praseodymium oxide nanostructures: Novel solvent-less preparation, characterization and investigation of their optical and photocatalytic properties. *RSC Advances* **2015,** *5*, (43), 33792-33800.

72. Salehi, Z.; Zinatloo-Ajabshir, S.; Salavati-Niasari, M., Novel synthesis of Dy2Ce2O7 nanostructures via a facile combustion route. *RSC Advances* **2016,** *6*, (32), 26895-26901.

73. Zinatloo-Ajabshir, S.; Salavati-Niasari, M.; Zinatloo-Ajabshir, Z., Nd2Zr2O7-Nd2O3 nanocomposites: New facile synthesis, characterization and investigation of photocatalytic behaviour. *Materials Letters* **2016,** *180*, 27-30.

74. Xu, A.; Yang, M.; Qiao, R.; Du, H.; Sun, C., Activity and leaching features of zinc-aluminum ferrites in catalytic wet oxidation of phenol. *Journal of Hazardous Materials* **2007,** *147*, (1-2), 449-456.

75. Griffitt, R. J.; Weil, R.; Hyndman, K. A.; Denslow, N. D.; Powers, K.; Taylor, D.; Barber, D. S., Exposure to copper nanoparticles causes gill injury and acute lethality in zebrafish (Danio rerio). *Environmental Science and Technology* **2007,** *41*, (23), 8178-8186.

76. Yang, Q.; Choi, H.; Al-Abed, S. R.; Dionysiou, D. D., Iron–cobalt mixed oxide nanocatalysts: Heterogeneous peroxymonosulfate activation, cobalt leaching, and ferromagnetic properties for environmental applications. *Applied Catalysis B: Environmental* **2009,** *88*, (3), 462-469.

77. Chen, L.; Zuo, X.; Zhou, L.; Huang, Y.; Yang, S.; Cai, T.; Ding, D., Efficient heterogeneous activation of peroxymonosulfate by facilely prepared Co/Fe bimetallic oxides: Kinetics and mechanism. *Chemical Engineering Journal* **2018,** *345*, 364-374.

78. Pyun, J., Graphene oxide as catalyst: Application of carbon materials beyond nanotechnology. *Angewandte Chemie - International Edition* **2011,** *50*, (1), 46-48.

79. Indrawirawan, S.; Sun, H.; Duan, X.; Wang, S., Nanocarbons in different structural dimensions (0–3D) for phenol adsorption and metal-free catalytic oxidation. *Applied Catalysis B: Environmental* **2015,** *179*, 352-362.

80. Duan, X.; Sun, H.; Kang, J.; Wang, Y.; Indrawirawan, S.; Wang, S., Insights into Heterogeneous Catalysis of Persulfate Activation on Dimensional-Structured Nanocarbons. *ACS Catalysis* **2015,** *5*, (8), 4629-4636.

81. Sun, H.; Liu, S.; Zhou, G.; Ang, H. M.; Tade, M. O.; Wang, S., Reduced graphene oxide for catalytic oxidation of aqueous organic pollutants. *ACS Appl Mater Interfaces* **2012,** *4*, (10), 5466-71.

82. Murali, S.; Potts, J. R.; Stoller, S.; Park, J.; Stoller, M. D.; Zhang, L. L.; Zhu, Y.; Ruoff, R. S., Preparation of activated graphene and effect of activation parameters on electrochemical capacitance. *Carbon* **2012,** *50*, (10), 3482-3485.

83. Peng, W.; Liu, S.; Sun, H.; Yao, Y.; Zhi, L.; Wang, S., Synthesis of porous reduced graphene oxide as metal-free carbon for adsorption and catalytic oxidation of organics in water. *Journal of Materials Chemistry A* **2013,** *1*, (19), 5854-5859.

84. Susi, T.; Kotakoski, J.; Arenal, R.; Kurasch, S.; Jiang, H.; Skakalova, V.; Stephan, O.; Krasheninnikov, A. V.; Kauppinen, E. I.; Kaiser, U.; Meyer, J. C., Atomistic Description of Electron Beam Damage in Nitrogen-Doped Graphene and Single-Walled Carbon Nanotubes. *ACS Nano* **2012,** *6*, (10), 8837-8846.

85. Duan, X.; Ao, Z.; Sun, H.; Indrawirawan, S.; Wang, Y.; Kang, J.; Liang, F.; Zhu, Z. H.; Wang, S., Nitrogen-Doped Graphene for Generation and Evolution of Reactive Radicals by Metal-Free Catalysis. *ACS Applied Materials & Interfaces* **2015,** *7*, (7), 4169-4178.

86. Long, J.; Xie, X.; Xu, J.; Gu, Q.; Chen, L.; Wang, X., Nitrogen-Doped Graphene Nanosheets as Metal-Free Catalysts for Aerobic Selective Oxidation of Benzylic Alcohols. *ACS Catalysis* **2012,** *2*, (4), 622-631.

87. Luo, Z.; Lim, S.; Tian, Z.; Shang, J.; Lai, L.; MacDonald, B.; Fu, C.; Shen, Z.; Yu, T.; Lin, J., Pyridinic N doped graphene: synthesis, electronic structure, and electrocatalytic property. *Journal of Materials Chemistry* **2011,** *21*, (22), 8038-8044.

88. Kang, J.; Duan, X.; Zhou, L.; Sun, H.; Tadé, M. O.; Wang, S., Carbocatalytic activation of persulfate for removal of antibiotics in water solutions. *Chemical Engineering Journal* **2016,** *288*, 399-405.

89. Poh, H. L.; Šimek, P.; Sofer, Z.; Pumera, M., Sulfur-Doped Graphene via Thermal Exfoliation of Graphite Oxide in H2S, SO2, or CS2 Gas. *ACS Nano* **2013,** *7*, (6), 5262-5272.

90. Zhao, Y.; Yang, L.; Chen, S.; Wang, X.; Ma, Y.; Wu, Q.; Jiang, Y.; Qian, W.; Hu, Z., Can Boron and Nitrogen Co-doping Improve Oxygen Reduction Reaction Activity of Carbon Nanotubes? *Journal of the American Chemical Society* **2013,** *135*, (4), 1201-1204.

91. Yang, L.; Jiang, S.; Zhao, Y.; Zhu, L.; Chen, S.; Wang, X.; Wu, Q.; Ma, J.; Ma, Y.; Hu, Z., Boron-Doped Carbon Nanotubes as Metal-Free Electrocatalysts for the Oxygen Reduction Reaction. *Angewandte Chemie International Edition* **2011,** *50*, (31), 7132-7135.

92. Khalfoun, H.; Hermet, P.; Henrard, L.; Latil, S., B and N codoping effect on electronic transport in carbon nanotubes. *Physical Review B* **2010,** *81*, (19), 193411.

93. Tian, W.; Zhang, H.; Duan, X.; Sun, H.; Tade, M. O.; Ang, H. M.; Wang, S., Nitrogen- and Sulfur-Codoped Hierarchically Porous Carbon for Adsorptive and Oxidative Removal of Pharmaceutical Contaminants. *ACS Applied Materials & Interfaces* **2016,** *8*, (11), 7184-7193.

94. Duan, X.; Sun, H.; Wang, Y.; Kang, J.; Wang, S., N-Doping-Induced Nonradical Reaction on Single-Walled Carbon Nanotubes for Catalytic Phenol Oxidation. *ACS Catalysis* **2015,** *5*, (2), 553-559.

95. Duan, X.; Ao, Z.; Zhou, L.; Sun, H.; Wang, G.; Wang, S., Occurrence of radical and nonradical pathways from carbocatalysts for aqueous and nonaqueous catalytic oxidation. *Applied Catalysis B: Environmental* **2016,** *188*, 98-105.

96. Zhu, Y.; Murali, S.; Cai, W.; Li, X.; Suk, J. W.; Potts, J. R.; Ruoff, R. S., Graphene and graphene oxide: synthesis, properties, and applications. *Adv Mater* **2010,** *22*, (35), 3906-24.

97. Deng, D.; Yu, L.; Chen, X.; Wang, G.; Jin, L.; Pan, X.; Deng, J.; Sun, G.; Bao, X., Iron Encapsulated within Pod-like Carbon Nanotubes for Oxygen Reduction Reaction. *Angewandte Chemie International Edition* **2013,** *52*, (1), 371-375.

98. Yao, Y.; Chen, H.; Lian, C.; Wei, F.; Zhang, D.; Wu, G.; Chen, B.; Wang, S., Fe, Co, Ni nanocrystals encapsulated in nitrogen-doped carbon nanotubes as Fenton-like catalysts for organic pollutant removal. *Journal of Hazardous Materials* **2016,** *314*, 129-139.

99. Wright, S. L.; Thompson, R. C.; Galloway, T. S., The physical impacts of microplastics on marine organisms: A review. *Environmental Pollution* **2013,** *178*, 483-492.

100. Cole, M.; Lindeque, P.; Halsband, C.; Galloway, T. S., Microplastics as contaminants in the marine environment: A review. *Marine Pollution Bulletin* **2011,** *62*, (12), 2588-2597.

101. Ivar do Sul, J. A.; Spengler, A.; Costa, M. F., Here, there and everywhere. Small plastic fragments and pellets on beaches of Fernando de Noronha (Equatorial Western Atlantic). *Marine Pollution Bulletin* **2009,** *58*, (8), 1236-1238.

102. Hammer, J.; Kraak, M. H. S.; Parsons, J. R., Plastics in the marine environment: The dark side of a modern gift. In *Reviews of Environmental Contamination and Toxicology*, 2012; Vol. 220, pp 1-44.

103. Andrady, A. L., Microplastics in the marine environment. *Marine Pollution Bulletin* **2011,** *62*, (8), 1596-1605.

104. Derraik, J. G. B., The pollution of the marine environment by plastic debris: A review. *Marine Pollution Bulletin* **2002,** *44*, (9), 842-852.

105. Thompson, R. C., Plastic debris in the marine environment: consequences and solutions. *Marine Nature Conservation in Europe* **2006**, 107-115.

106. Pruter, A. T., Sources, quantities and distribution of persistent plastics in the marine environment. *Marine Pollution Bulletin* **1987,** *18*, (6 SUPPL. B), 305-310.

107. Fendall, L. S.; Sewell, M. A., Contributing to marine pollution by washing your face: Microplastics in facial cleansers. *Marine Pollution Bulletin* **2009,** *58*, (8), 1225-1228.

108. Gregory, M. R., Plastic scrubbers' in hand cleansers: A further (and minor) source for marine pollution identified. *Marine Pollution Bulletin* **1996,** *32*, (12), 867-871.

109. Browne, M. A.; Galloway, T.; Thompson, R., Microplastic--an emerging contaminant of potential concern? *Integrated environmental assessment and management* **2007,** *3*, (4), 559-561.

110. Li, J.; Liu, H.; Paul Chen, J., Microplastics in freshwater systems: A review on occurrence, environmental effects, and methods for microplastics detection. *Water Research* **2018,** *137*, 362-374.

111. Li, H.-X.; Ma, L.-S.; Lin, L.; Ni, Z.-X.; Xu, X.-R.; Shi, H.-H.; Yan, Y.; Zheng, G.-M.; Rittschof, D., Microplastics in oysters Saccostrea cucullata along the Pearl River Estuary, China. *Environmental Pollution* **2018,** *236*, 619-625.

112. Chen, J.; Tan, M.; Nemmar, A.; Song, W.; Dong, M.; Zhang, G.; Li, Y., Quantification of extrapulmonary translocation of intratracheal-instilled particles in vivo in rats: Effect of lipopolysaccharide. *Toxicology* **2006,** *222*, (3), 195-201.

113. Sussarellu, R.; Suquet, M.; Thomas, Y.; Lambert, C.; Fabioux, C.; Pernet, M. E. J.; Goïc, N. L.; Quillien, V.; Mingant, C.; Epelboin, Y.; Corporeau, C.; Guyomarch, J.; Robbens, J.; Paul-Pont, I.; Soudant, P.; Huvet, A., Oyster reproduction is affected by exposure to polystyrene microplastics. *Proceedings of the National Academy of Sciences of the United States of America* **2016,** *113*, (9), 2430-2435.

114. Espinosa, C.; García Beltrán, J. M.; Esteban, M. A.; Cuesta, A., In vitro effects of virgin microplastics on fish head-kidney leucocyte activities. *Environmental Pollution* **2018,** *235*, 30-38.

115. Waring, R. H.; Harris, R. M.; Mitchell, S. C., Plastic contamination of the food chain: A threat to human health? *Maturitas* **2018,** *115*, 64-68.

116. Zhu, L.; Wang, H.; Chen, B.; Sun, X.; Qu, K.; Xia, B., Microplastic ingestion in deep-sea fish from the South China Sea. *Science of The Total Environment* **2019,** *677*, 493-501.

117. Angiolillo, M.; Lorenzo, B. D.; Farcomeni, A.; Bo, M.; Bavestrello, G.; Santangelo, G.; Cau, A.; Mastascusa, V.; Cau, A.; Sacco, F.; Canese, S., Distribution and assessment of marine debris in the deep Tyrrhenian Sea (NW Mediterranean Sea, Italy). *Marine Pollution Bulletin* **2015,** *92*, (1-2), 149-159.

118. Rocha-Santos, T.; Duarte, A. C., A critical overview of the analytical approaches to the occurrence, the fate and the behavior of microplastics in the environment. *TrAC - Trends in Analytical Chemistry* **2015,** *65*, 47-53.

119. Song, Y. K.; Hong, S. H.; Jang, M.; Kang, J. H.; Kwon, O. Y.; Han, G. M.; Shim, W. J., Large accumulation of micro-sized synthetic polymer particles in the sea surface microlayer. *Environmental Science and Technology* **2014,** *48*, (16), 9014-9021.

120. Leslie, H. A.; Brandsma, S. H.; van Velzen, M. J. M.; Vethaak, A. D., Microplastics en route: Field measurements in the Dutch river delta and Amsterdam canals, wastewater treatment plants, North Sea sediments and biota. *Environment International* **2017,** *101*, 133-142.

121. Song, Y. K.; Hong, S. H.; Jang, M.; Han, G. M.; Rani, M.; Lee, J.; Shim, W. J., A comparison of microscopic and spectroscopic identification methods for analysis of microplastics in environmental samples. *Marine Pollution Bulletin* **2015,** *93*, (1-2), 202-209.

122. Stolte, A.; Forster, S.; Gerdts, G.; Schubert, H., Microplastic concentrations in beach sediments along the German Baltic coast. *Marine Pollution Bulletin* **2015,** *99*, (1-2), 216-229.

123. Corcoran, P. L., Benthic plastic debris in marine and fresh water environments. *Environmental Sciences: Processes and Impacts* **2015,** *17*, (8), 1363-1369.

124. Hanvey, J. S.; Lewis, P. J.; Lavers, J. L.; Crosbie, N. D.; Pozo, K.; Clarke, B. O., A review of analytical techniques for quantifying microplastics in sediments. *Analytical Methods* **2017,** *9*, (9), 1369-1383.

125. Zettler, E. R.; Mincer, T. J.; Amaral-Zettler, L. A., Life in the "plastisphere": Microbial communities on plastic marine debris. *Environmental Science and Technology* **2013,** *47*, (13), 7137-7146.

126. Talvitie, J.; Mikola, A.; Koistinen, A.; Setälä, O., Solutions to microplastic pollution – Removal of microplastics from wastewater effluent with advanced wastewater treatment technologies. *Water Research* **2017,** *123*, 401-407.

127. Kotlarz, N.; Upadhyaya, G.; Togna, P.; Raskin, L., Evaluation of electron donors for biological perchlorate removal highlights the importance of diverse perchlorate-reducing populations. *Environmental Science: Water Research & Technology* **2016,** *2*, (6), 1049-1063.

128. Michielssen, M. R.; Michielssen, E. R.; Ni, J.; Duhaime, M. B., Fate of microplastics and other small anthropogenic litter (SAL) in wastewater treatment plants depends on unit processes employed. *Environmental Science: Water Research & Technology* **2016,** *2*, (6), 1064-1073.

129. Paço, A.; Duarte, K.; da Costa, J. P.; Santos, P. S. M.; Pereira, R.; Pereira, M. E.; Freitas, A. C.; Duarte, A. C.; Rocha-Santos, T. A. P., Biodegradation of polyethylene microplastics by the marine fungus Zalerion maritimum. *Science of The Total Environment* **2017,** *586*, 10-15.

130. Kang, J.; Zhou, L.; Duan, X.; Sun, H.; Ao, Z.; Wang, S., Degradation of Cosmetic Microplastics via Functionalized Carbon Nanosprings. *Matter* **2019, 1, 745-758**.

Chapter 3: Catalytic degradation of antibiotics by metal-free catalysis over nitrogen-doped graphene

This chapter has been published on journal "Catalysis Today", DOI: 10.1016/j.cattod.2018.12.002. Every reasonable effort has been made to acknowledge the owners of copyright material. I would be pleased to hear from any copyright owner who has been omitted or incorrectly acknowledged.

Abstract

Emerging pharmaceutical contaminants, for example antibiotics, have raised severe challenges to remediation technologies due to their resistance to biodegradation and the ineffectiveness in adsorptive removal or membrane separation. In this study, we observed the direct degradation of antibiotic sulfachlorpyridazine (SCP), one of sulfonamides, by peroxymonosulfate (PMS) with high efficiency. Nevertheless, SCP could be rapidly decomposed, but the overall mineralization efficiency was rather low. Then, nitrogen-doped reduced graphene oxide (N-rGO), synthesized by a facile hydrothermal route, was employed as a metal-free catalyst to improve the degradation and mineralization of SCP. A comprehensive investigation of in situ electron paramagnetic resonance (EPR), selective radical quenching, and PMS decomposition was performed, revealing the direct and nonradical reactions between PMS and SCP in PMS-based and non-catalytic system without producing free radicals such as $^{\bullet}OH$ and $SO_4^{\bullet -}$. Upon the introduction of N-rGO, the SCP removal rate was similar to the PMS-only reaction, though, an enhanced total organic removal was achieved. This suggests that N-doped nanocarbon materials would achieve a greater extent of mineralization of SCP into inorganic salts, carbon dioxide and water. The findings show that the direct oxidation of SCP with PMS can be used to selectively convert the toxic antibiotics to less or non-toxic organic substances whereas the robust carbocatalysis would

contribute to the practical wastewater remediation by metal-free advanced oxidation processes (AOPs).

3.1 Introduction

Environmental deterioration caused by the rapid industrialization and expanded civilization has posed severe heath issues to both humans and animals. Modern pharmaceuticals, since the discovery of penicillin in 1919, have been significantly contributed to the improved health status for human beings and livestock. For example, veterinary antibiotics have been widely introduced to feeds in livestock farms to improve the growth rate and feed efficiency especially in developing countries. It was reported that 7920 tons of sulfonamides (11 chemicals), one category of antibiotics, were consumed in 2013 in China.[1] Sulfonamide antibiotics are effective antimicrobial agents and have been widely applied in aquaculture, animal husbandry and human medicine for infection control. However, most sulfonamides can only be partially metabolised in the organism, thus their residuals would contaminate ground/underground water and soil.[2, 3]

As a typical sulfonamide, sulfachloropyridazine (SCP, 4-amino-*N*-(6-chloro-3-pyridazinyl) benzenesulfonamide, $C_{10}H_9ClN_4O_2S$), has long been used as a broad spectrum antibiotic for treating Gram-positive and Gram-negative aerobic bacteria. Due to the wide application, it has been extensively detectable in groundwater and soil in natural systems. The accumulation in the food chain and the induced bacterial- or drug-resistance of SCP makes it imperative to purify the antibiotic contaminants from the eco-system.[4] However, due to the antibiotic nature, biodegradation in a traditional wastewater processing unit is not effective. [2] Adsorption can be one option, yet it only accumulates and transfers the pharmaceutical contaminants which still need post-treatment for a complete removal. [5-7] Photochemical and electrochemical degradations have been employed to remove SCP, however, the duration and the treatment

scale would be the bottlenecks of such advanced oxidation processes (AOPs).[3, 8-10] The limited solubility of SCP in acidic condition also leads to unsatisfactory practice of Fenton or Fenton-like reactions, where hydroxyl radicals decompose the organic contaminants in a strict pH range of 3 - 4. Therefore, there is still a high demand in developing an effective SCP remediation technology.

Sulfate radicals can work in a flexible condition, and have become promising alternatives to hydroxyl radicals.[11-14] More recently, a catalytic remediation technology using sulfate radicals by metal-free catalysis was discovered to be able to decompose diverse organic pollutants in water.[15, 16] Nitrogen-doped reduced graphene oxide (N-rGO) demonstrated fantastic performances for activating peroxymonosulfate (PMS) or persulfate (PS) to produce sulfate radicals for catalytic oxidation.[17-20] In this study, such a metal-free process based on N-rGO catalysis is applied for catalytic oxidation of antibiotic SCP. Other than the high-temperature calcination for fabrication of N-rGO, a facile hydrothermal route is developed in this study for the catalyst preparation.

Additionally, some recent studies have reported that PMS could oxidize organic pollutants through spontaneously self-activation to generate of reactive oxygen species (ROS), mainly singlet oxygen ($^1O_2$) and trace of $^{\bullet}OH$ and $SO_4^{\bullet -}$. [21-23] In this study, we found that the PMS had excellent oxidation efficiency towards sulfonamide antibiotics (SAs) through direct reaction, which achieved a complete removal of 5 different SAs in 10 min. Ibuprofen, phenol and other organic pollutants were further tested by the reaction with PMS alone, whereas PMS-only exhibited a selective oxidation capacity to SAs. Moreover, the removal of total organic carbon (TOC) is much lower in PMS-only reaction than in the carbon-driven catalytic systems. This suggests that the SCP was not fully mineralized to water and carbon dioxide by PMS-only,

instead, it might have been partially oxidized or converted to other organics through a direct oxidation by PMS. To verify our hypothesis, EPR, quenching tests and HPLC detection were employed to facilitate insights into the intrinsic reactive species in non-activated PMS oxidation and carbocatalysis.

3.2 Experimental section

3.2.1 Materials and chemicals

Phenol (99%), sulfachloropyridazine (SCP, 99%), sulfathiazole (STZ, 99%), sulfamethazine (SMZ, 99%), sulfadiazine (SDZ, 99%), sulfamerzine (SMR, 99%) p-hydroxybenzoic acid (PHBA, 99%), sodium azide (NaN_3, 99.5%), 5, 5-dimethyl-1-pyrroline (DMPO), 2,2,6,6-tetramethyl-4-piperidinol (TMP, 99%), 4-amino-3-hydroxybenzenesulfonic acid (4-A-3H, 99%), 3-amino-4-hydrocy-6-chloropyridazine (3-A-4H-6C, 99%), potassium peroxylmonosulfate (oxone, >99.0%), potassium peroxydisulfate (PS, >99.0%), sulfuric acid (98%), sodium hydroxide (99%), tert-butanol (TBA, 99.5%), ethanol (99.5%), methanol and acetic acid (HPLC grade) were obtained from Sigma-Aldrich.

3.2.2 Carbon catalyst preparation

Graphene oxide (GO) was prepared by a modified Hummers' method and the details can be found in our previous reports.[15, 20] A novel synthesis was applied to prepare nitrogen doped reduced graphene oxide (N-rGO). Typically, 1 g GO and 1 g urea were added into 70 mL ultrapure water in a 300 mL beaker, followed by an ultrasonic treatment for 20 min. Then the pH value was adjusted by titration using 30% ammonia to pH 10 under magnetically stirring. The mixture was transferred into a Teflon-lined autoclave and heated at 180 °C for 18 h. After the autoclave was cooled down to room temperature, the solid was washed and filtered by

ultrapure water and ethanol for three times. Finally, the N-rGO was dried in an oven at 60 °C. The same procedure without addition of urea produced a reduced graphene oxide (rGO) sample.

3.2.3 Characterization of materials

X-ray diffraction (XRD) was employed to monitor the crystal structure changes. The morphological information was investigated by scanning electron microscopy (FE-SEM, Zeiss Neon 40 EsB). The composition and chemical states were studied by X-ray photoelectron spectroscopy (XPS). The instrumental and operational information can be found in our recent reports.[17-19]

3.2.4 Direct SCP degradation with PMS-only and catalytic oxidation over N-rGO

The experiments were carried out in a thermostatic water bath. Direct SCP degradation was conducted by addition of a certain amount of Oxone ($KHSO_5$•$0.5KHSO_4$•$0.5K_2SO_4$, PMS is the effective component), e.g. 0.5, 1.0 or 2.0 g/L, to 20 ppm SCP solutions. For catalytic oxidation, 0.2 g/L graphene catalyst was suspended in the SCP solutions for activating PMS. During each time interval, 1 mL SCP solution was withdrawn with a syringe and the catalyst was filtered by a 0.45 μm Millipore film, then the solution was injected to a HPLC vial for analysis. For quenching tests only, reagents such as methanol, *t*-butanol and sodium azide were dissolved in SCP solution prior to the addition of PMS.

3.2.5 Analytical methods

The SCP concentrations were monitored on a Thermo Scientific Ultimate 3000 UHPLC under a UV lamp set at 270 nm with a C18 column. The mobile phase was made of 40 wt% methanol

and 60 wt% acetic acid solution (pH=4.2) at a flow rate of 0.2 mL/min. The mineralization rates of organic contaminants were evaluated by a Shimadzu TOC analyzer. The mechanism of PMS activation on N-graphene was investigated by electron paramagnetic resonance (EPR). DMPO was selected as the spin-trapping agent for $SO_4^{\bullet -}$ and $^{\bullet}OH$. TMP was used to capture $^1O_2$ which can oxidize TMP into 2,2,6,6-tetramethyl-4-piperidinol-N-oxyl radical (TMN). The quantitative results were obtained by Spin Fitting from the Bruker Xenon software package. PMS decomposition was investigated by applying a modified iodometric titration method.[24] The titration procedure is listed as follows: 1. the sample solution was diluted by deionized (DI) water to 30 mL. 2. Sodium bicarbonate was added to avoid oxygen-oxidation of iodide. 3. Potassium iodide was added and then allowed standing for 15 min. 4. Several drops of starch indicator was introduced. 5. Acetic acid was added to acidify the solution. 6. Titrate it with the standard thiosulfate. The persulfate anion concentration was calculated by Eq (3.1). [25]

$$KHSO_5\,(mgL^{-1}) = \frac{(A+B)}{2}\,N\,MW\ of\ KHSO_5\ \frac{1}{mL\ sample}\,DF \qquad (Eq.\ 3.1)$$

Where A is the titration volume in mL for sample; B is the titration volume in mL of blank; N is the normality of $KHSO_5$; MW of $K_2S_2O_8$ is 152.2 $\times 10^3$ mg mol^{-1}; DF is the dilution factor. A UV-Vis spectrophotometer (Agilent Cary 100) was applied to detect the absorption spectra of a yellow solution, resulted from the reaction of persulfate and iodide at 352 nm.

3.3 Results and discussion

3.3.1 Characterization of N-rGO

Figure 3.1a shows XRD patterns of the carbonaceous materials. The graphitic peak of graphite powder at around $2\theta = 26^o$ completely disappeared after the oxidation processes of Hummers'

method [26], indicating the successful oxidation of graphite to graphene oxide. It was further confirmed by the newly appeared peak at around 2θ= 9.4°, representing the (002) reflection of GO with a well-ordered and layered structure.[15] After the hydrothermal reduction processes without (rGO) or with urea (N-rGO), the characteristic peak of GO completely disappeared. A broad peak between 21-26° was observed for both rGO and N-rGO. The changes in XRD patterns suggested that the hydrothermal process can effectively remove the surface oxygen groups on GO.[15, 17] Moreover, nitrogen doping would not significantly influence the crystal structure of graphene materials. The morphology of the N-rGO sample is shown in **Figure** 3.1b. Hydrothermal synthesis led to a light aggregation of graphene sheets. However, the advantages of this method in fabrication of rGOs lie in the mild synthesis condition and less toxic or explosive chemical involved, which could achieve a higher yield of carbocatalyst, compared to thermal combustion processes.[20]

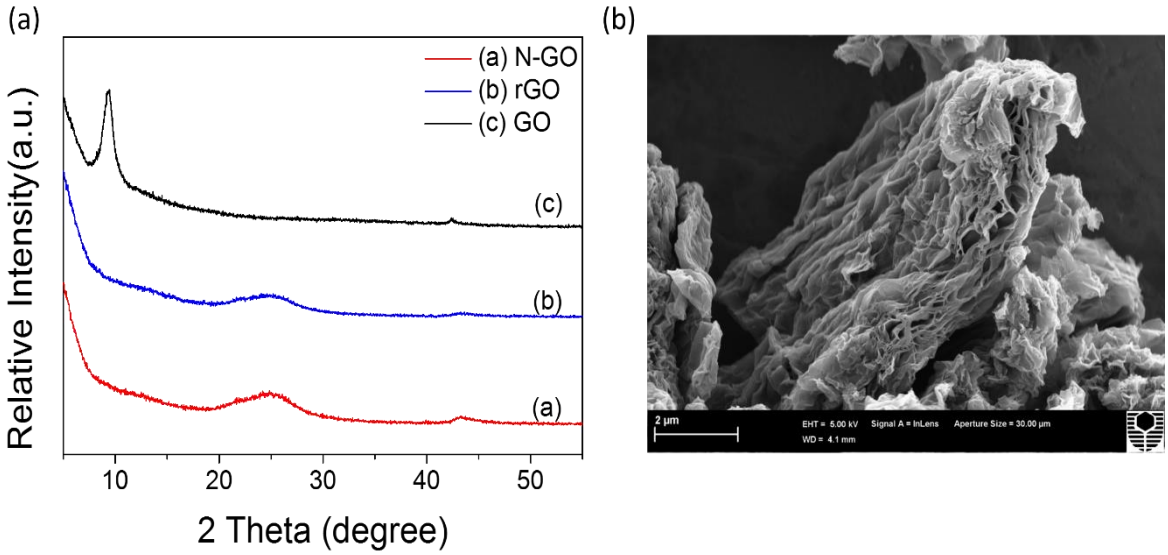

Figure 3.1 (a) XRD patterns of GO, rGO and N-rGO and (b) SEM image of N-rGO.

The nitrogen doping by the hydrothermal route was investigated by XPS spectra. **Figure** 3.2a displays the XPS survey of N-rGO sample. Three main elements, e.g. oxygen, nitrogen, and carbon, were observed with an atomic level of 7.0, 6.2 and 86.8%, respectively. It was reported that the oxygen content can be made up over 45 at.% in graphene oxide [27]. Then the much lower oxygen level further confirmed the successful reduction of GO. It is interesting to find that the nitrogen doping level was 6.2 at.%, which is higher than the nitrogen doping level of 4.4% from NH_3 annealing [28], 5.0% from plasma enhanced CVD [29], and 5.6% from thermal treatment with ammonium nitrate [20]. The XPS results suggested that nitrogen could be successfully implanted into the carbon lattice by the hydrothermal treatment of GO and urea.

Figure 3.2b displays the high-resolution N 1s XPS spectra in a range of 390-410 eV. N signals were fitted into four components: 398.5, 401.1, 403.1 and 406.2 eV, corresponding to pyridinic N (nitrogen in a six-atom heterocyclic ring), pyrrolic N (nitrogen in a five-atom heterocyclic ring), graphitic N (sp^2-hybridized N neighboured with three sp^2-C), and oxidized N (bonded with C and O), respectively. In addition, the atomic percentages of the pyridinic N, pyrrolic N, graphitic N and oxidized N were evaluated to be 49.7%, 35.2%, 9.0% and 5.9%, respectively. According to the literature, the graphitic N and quaternary nitrogen are playing the key role in catalysis because they have higher electronegativity and smaller covalent radius to facilitate the electron transfer from the neighbouring C, giving rise to high asymmetric spin and charge density to the adjacent carbon atoms. [30]

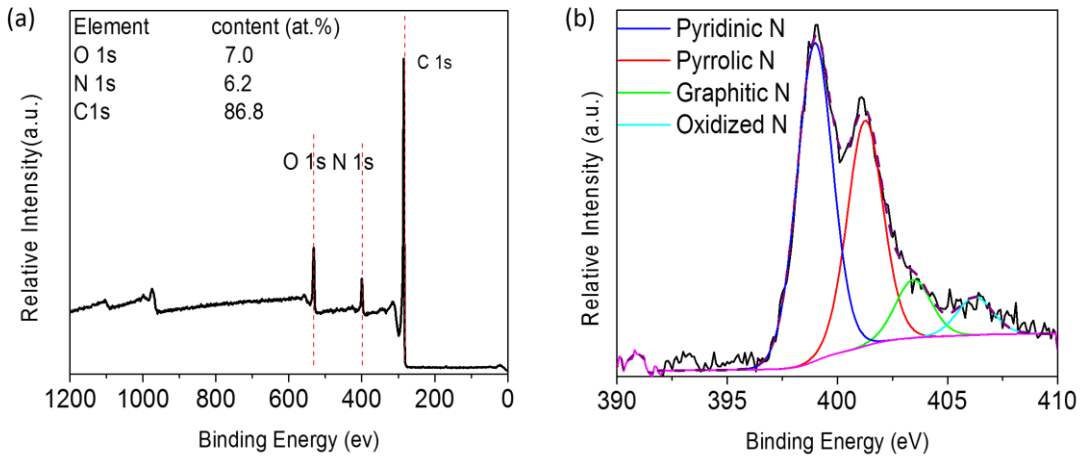

Figure 3.2 (a) XPS survey of N-rGO. (b) N 1s scan of N-rGO.

3.3.2 Catalytic and PMS-only oxidation of SCP

The SCP degradation performances by PMS-only and catalytic activation of PMS by carbon were evaluated in water solution. In our previous studies, we found that PMS could hardly oxidize phenol in the absence of a catalyst or other external activation methods.[15-20, 31, 32] As shown in **Figure** 3.3a, it was intriguing to spot that PMS itself could efficiently degrade SCP. Specifically, at a PMS dose of 2 g/L, 20 ppm SCP was completely degraded in 9 min, which is comparable to other carbon-based catalysts, GO, rGO and N-rGO. For comparison, when the same molar concentration of peroxydisulfate (PDS) was used, the SCP degradation was insignificant with less than 1% removal in 30 min. The intrinsic differences of the two persulfates may lie in the asymmetric structure of PMS ($HO\text{-}SO_4$) which facilitate the direct interaction with SCP without steric hindrance to break the $\text{-}O_2S\text{-}NH\text{-}$ bond.[33] Ji et al. reported that sulfonamides oxidation can be initiated by a nonradical process, which lead to the formation of a transition state complex between PMS molecule and amino functional group of sulfonamides with the assistance of two water molecules.[34]

The graphene catalysts were then introduced for catalytic SCP oxidation. In the catalytic tests, we selected a low PMS loading of 0.5 g/L for evaluating the catalytic performances of graphene catalysts (**Figure** 3.3a). GO demonstrated a reverse effect for SCP degradation, providing a lower efficiency than PMS-only. This was consistent with the observation in phenol degradation, where GO was not effective for PMS activation.[15, 19, 20] rGO and N-rGO were able to increase the SCP degradation efficiencies. Because fast SCP degradation could occur in homogeneous phase by PMS, the enhanced degradation by rGO and N-rGO might be attributed to the catalytic PMS activation which is much faster than PMS self-oxidation.

The mineralization of SCP was also investigated under various conditions (**Figure** 3.3b). It shows that the SCP removal rates were similar under different conditions (except for PS-only), while the corresponding TOC removals were largely different. All the graphene induced PMS activation reactions show a much better TOC removal efficiency than the non-catalytic system. This can be attributed to the fact that the carbocatalysts can greatly promote PMS to generate large amounts of highly reactive oxygen species (ROS) such as $^{\bullet}OH$ and $SO_4^{\bullet -}$, which manifest much higher redox potentials than the parent peroxide of PMS. Hence, the reactive radicals played a significant role in mineralization of SCP, and the trend of radical intensity was in a good agreement with the organic decomposition rate. Among these graphene catalysts, N-rGO represents the highest TOC removal, which mineralized around 60% of SCP. The pristine graphene based materials showed a moderate activity in PMS activation with 40% and 20% of SCP decomposition in 7 hours for rGO and GO, respectively. Duan et al. reported that the introduction of heteroatoms, N and S for instance, into graphene layer would disrupt uniform sp^2–hybridized carbon configurations and modulate the physical, chemical and electrical properties of graphene. As a result, new reactive catalytic sites were created for PMS activation.[19] In addition, theoretical studies revealed that the graphitic N (sp^2-hybridized N

neighboured with three sp^2-C) with a smaller covalent radius and higher electronegativity than carbon atom would induce electron transfer from adjacent carbon atoms to nitrogen to break the chemical inertness of the sp^2 carbon layer and enhance the catalytic activity of graphene. It is noteworthy that the PMS-only shows the most inconsistent results of SCP degradation between the concentration change and the corresponding mineralization. The SCP concentration showed the complete SCP removal was reached in 10 min, whereas the TOC results indicated marginal amount of SCP (7%) was ultimately degraded. Based on the above results, the high SCP removal rate in the PMS-only system suggested a distinct degradation mechanism from the conventional radical processes. Herein, a hypothesis was proposed that, instead of attacking SCP molecules by generated ROS in AOPs, PMS could directly react with SCP by attacking the S-N bond. This is also in line with some recent reports that the PMS can directly react with antibiotics with similar structures via a nonradical pathway.[19, 35, 36] Furthermore, a lowered concentration of SCP (≈1ppm) was evaluated to study the degradation performance in real water matrixes, and the results showed that the trace amount of SCP could be rapidly degraded by PMS-only and N-rGO/PMS systems, while PDS-only yielded around 20% of SCP removal in 10 min. The results indicate that the PMS and N-rGO/PMS systems are applicable to remediate realistic aquatic environment.

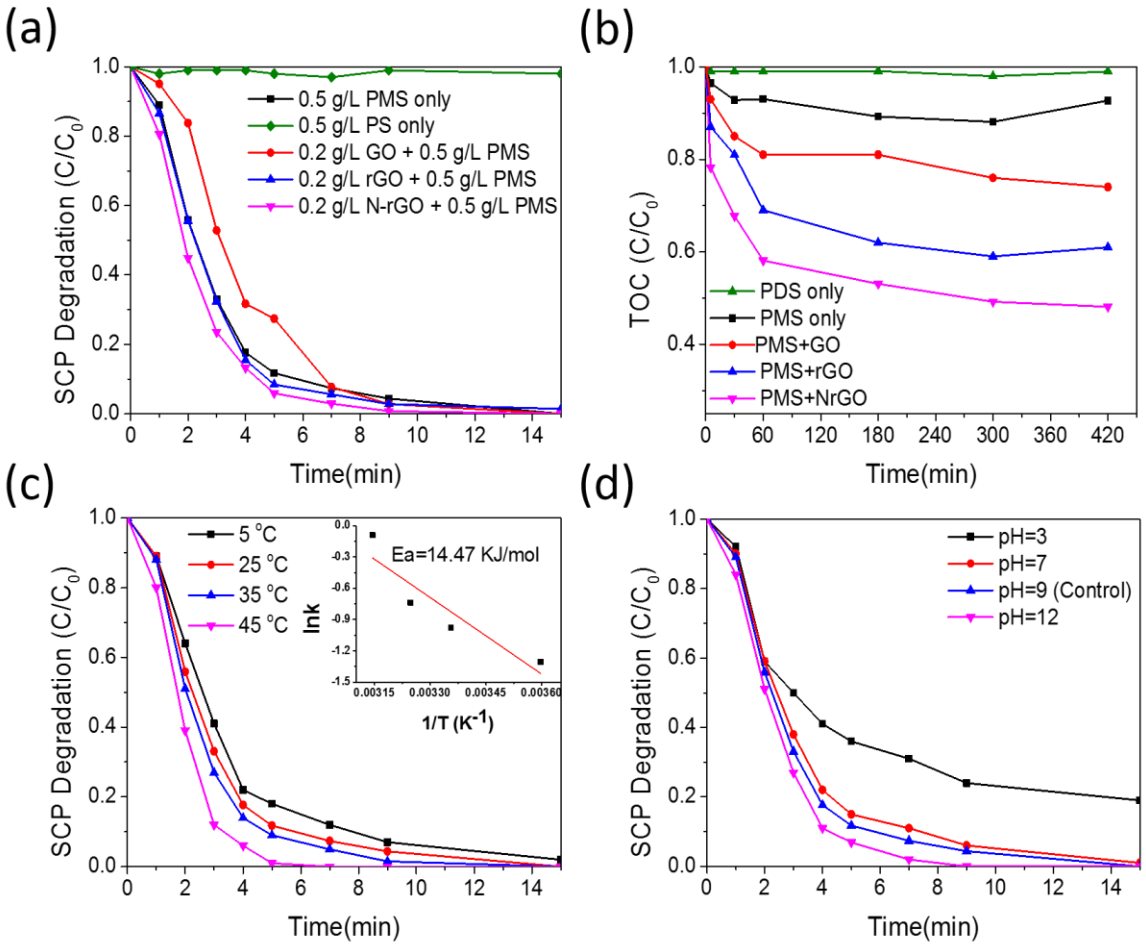

Figure 3.3 (a) SCP oxidative degradation on various oxidants and nanocarbons. (b) Mineralization evaluation of SCP degradation. Effects of (c) reaction temperature (Inset: activation energy of PMS-only on SCP degradation), and (d) solution pH on PMS-only reaction for SCP oxidation. Reaction condition: 25 °C, catalyst loading of 0.2 g/L, SCP concentration of 20 ppm, PMS concentration of 0.5 g/L, PS concentration of 0.5 g/L.

The stability and reusability were evaluated and showed that the fresh catalyst was able to completely decompose SCP in 10 min and 99% and 96% of SCP removals were attained in 15 min for the second and third runs. The results show that the TOC removal in the second and third runs decreased to 20% and 43%, respectively. It could be confirmed that the initial SCP oxidation may be due to the direct oxidation by PMS and the carbocatalysts was slightly

passivated in the oxidative environment. The deactivation of the catalyst could be ascribed to intricate influences of surface chemistry and structural changes, adsorption of intermediates, coverage of surface active sites, changes of pore structures, and dopants re-fabrication in graphene network.[19]

3.3.3 Kinetic study of PMS-only oxidation

Figure 3.3c represents the effect of reaction temperature on SCP degradation by PMS self-decomposition. Not surprisingly, higher temperatures are beneficial for PMS self-activation. The reaction rate at 45 ^{o}C was much accelerated than the low-temperature conditions and the complete SCP removal was reached in only 6 min. In general, the elevated temperature would promote more kinetic energy between molecules, and consequently more SCP molecules would be able to overcome the activation energy barrier. Interestingly, the PMS-only degradation of SCP did not show much abatement in reaction rate even when the temperature was dropped to 5 ^{o}C, indicating the great removal capability of PMS toward SCP. Moreover, the rate constants at different reaction temperatures were calculated and the overall activation energy for PMS-only reaction was fitted. As shown in the inset **of Figure** 3.3c, the activation energy of PMS self-activation oxidation of SCP was calculated to be 14.47 kJ/ mol, which is lower than the reported value of CNT (33.3 kJ/mol), NCNT (39.2 kJ/mol), and graphene (84.0 kJ/mol)[15, 20]. Moreover, the mineralization performance showed a great improvement when the temperature was elevated to 35 °C and 45 °C, which suggests that reaction temperature (above 25 °C) may impact PMS-only system by heat activation, which can simultaneously stimulate PMS to generate $^{\bullet}OH$ and $SO_4^{\bullet -}$ toward a high TOC removal [37].

The effect of reaction solution pH on SCP degradation efficiency is shown in **Figure** 3.3d. The pH conditions presented significant influences on SCP degradation. The initial pH was adjusted

by sulfuric acid and sodium hydroxide ranging from 3 to 12 while the solution pH was undisturbed and monitored during the degradation reaction. Under a lower pH condition, the SCP degradation efficiency was dramatically reduced. When the control test was acidified to pH=3, SCP degradation rate was apparently slowed down with only 80% SCP removal in 15 min. In contrast, in a basic solution (pH=12), the SCP degradation rate was impressively enhanced with 100% SCP degradation in just 9 min. Thus, the oxidation reaction was favored in a basic solution due to partial base activation of PMS. It was reported by Guan et al. that the PMS exists in a mono-anion form (HSO_5^-) in an acidic range and di-anion form (SO_5^{2-}) at pH $\geq$ 11. [38] Assuming the production of SO_5^{2-} by PMS self-decomposition was improved in a basic solution, it was reasonable to infer that the SO_5^{2-} presented a stronger oxidative capacity than the mono-anion and acid forms in SCP oxidation.

For better understanding of the effect of common anions on the SCP oxidation process, chloride ions (NaCl) and carbonate ions (Na_2CO_3) were introduced. The introduction of chloride and carbonate anions in SCP degradation solution demonstrated distinct effects on PMS-only and catalytic systems. Specifically, PMS-only reaction was negligibly affected by the introduced anions while the nanocarbon catalytic SCP degradation reaction was impressively retarded to a decline of over 50% in terms of degradation efficiency. The minor influence of anions on PMS-only reaction indicates that the anions such Cl^- and CO_3^{2-} would not disturb the direct interaction between PMS and SCP. In the catalytic systems, the presence of anions (Cl^- and CO_3^{2-}) dramatically decreased the radical intensity, attributed to the scavenging effect of anions via Eqs 3.2-3.5 [39]. The generated chlorine radical ($Cl^{\bullet}$, 2.4V) and carbonate radical ($CO_3^{\bullet -}$, 2.1V) presented much lower oxidative potentials than $SO_4^{\bullet -}$ (3.1V) and $HO^{\bullet}$ (2.7V) [40-42].

$$Cl^- + SO_4^{\bullet -} \rightarrow SO_4^{2-} + Cl^{\bullet} \quad \text{(Eq. 3.2)}$$

$$Cl^- + OH^{\bullet} \rightarrow ClOH^{\bullet} \quad \text{(Eq. 3.3)}$$

$$HO^{\bullet} + CO_3^{2-} \rightarrow CO_3^{\bullet -} + HO^- \quad \text{(Eq. 3.4)}$$

$SO_4^{\bullet -} + CO_3^{2-} \rightarrow CO_3^{\bullet -} + SO_4^{2-}$ (Eq. 3.5)

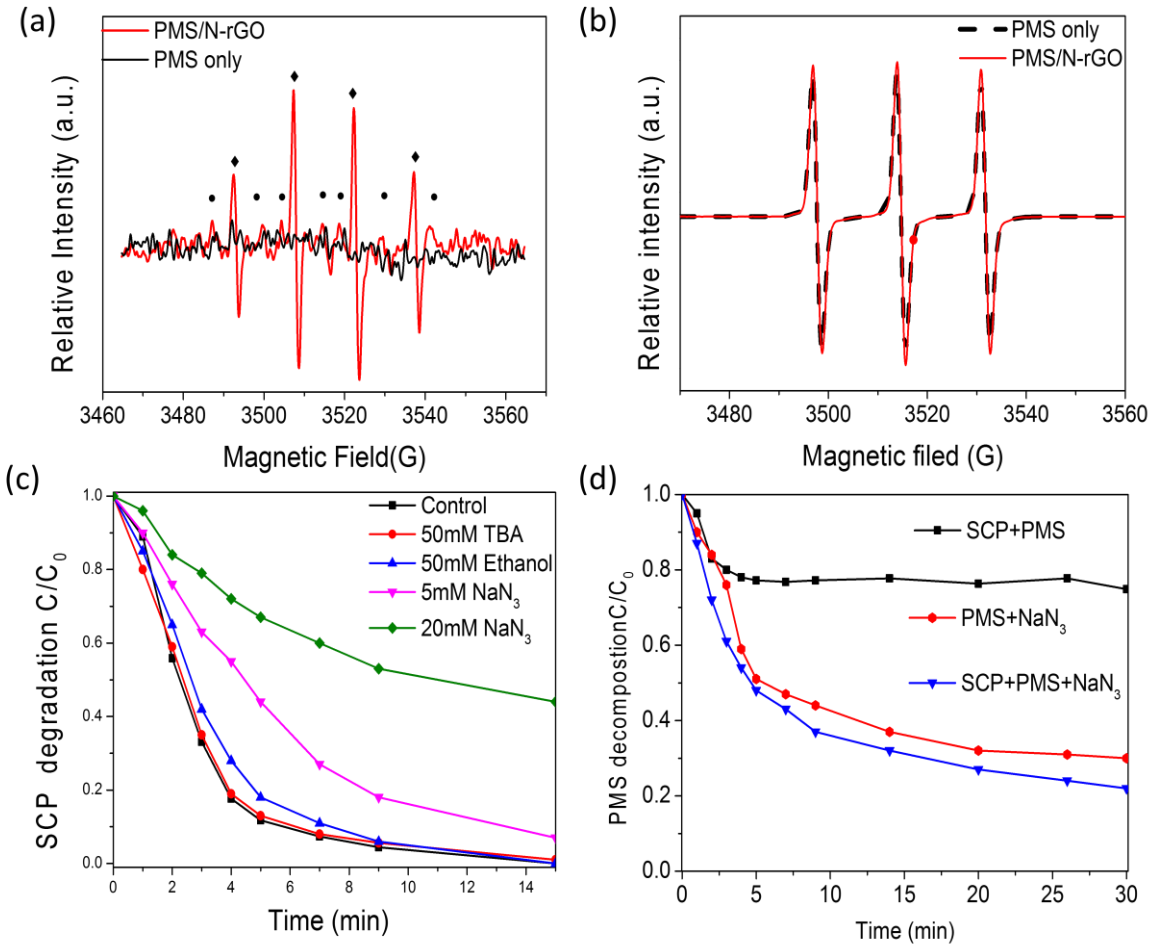

Figure 3.4 (a) EPR spectra of PMS self-activation and N-rGO catalytic activation using DMPO as the trapping agent (◆, DMPO-OH; ●, DMPO-SO_4). (b) EPR spectra of PMS self-activation and N-rGO catalysis activation with TMP as the trapping agent. (c) Impacts of radical quenching agents on SCP degradation in PMS-only system. (Reaction condition: temperature 25 °C, SCP concentration 20 ppm, PMS concentration 0.5 g/L, PS concentration 0.5 g/L.) (d) The effect of $^1O_2$ on SCP degradation in PMS-only system (no catalyst, NaN_3 20 mM).

3.3.4 Mechanism of PMS-only oxidation of SCP

To verify our earlier hypothesis, the evolution of ROS during SCP degradation was investigated by EPR detection and radical quenching tests. In the EPR tests, DMPO is a classical radical trapping agent for both $^{\bullet}OH$ and $SO_4^{\bullet -}$, and TMP can be used for detection of $^1O_2$. The radical generations with/without the presence of N-rGO are shown in **Figure** 3.4. **Figure** 3.4a illustrates that PMS along can hardly produce $^{\bullet}OH$ and $SO_4^{\bullet -}$, which is consistent with the previous study.[43] This suggested the trivial contribution of $^{\bullet}OH$ and $SO_4^{\bullet -}$ to SCP degradation in PMS-only system. When a carbocatalyst (N-rGO) was introduced, conspicuous DMPO-OH and DMPO-SO_4 peaks were observed, suggesting the N-rGO is able to effectively activate PMS to generate substantial $^{\bullet}OH$ and $SO_4^{\bullet -}$. The DMPO-OH showed a much higher peak intensity than DMPO-SO_4, which may be attributed to the reactions between peroxymonosulfate ions (HSO_5^-)/$SO_4^{\bullet -}$ and ^-OH via Eqs 3.6-3.9.

$$HSO_5^- + e^- \rightarrow {}^{\bullet}OH + SO_4^{2-} \qquad \text{(Eq. 3.6)}$$

$$HSO_5^- + e^- \rightarrow {}^-OH + SO_4^{\bullet -} \qquad \text{(Eq. 3.7)}$$

$$SO_4^{\bullet -} + OH^- \rightarrow SO_4^{2-} + {}^{\bullet}OH \qquad \text{(Eq. 3.8)}$$

$$HSO_5^- + SO_5^{2-} \rightarrow HSO_4^- + SO_4^{2-} + {}^1O_2 \qquad \text{(Eq. 3.9)}$$

The singlet oxygen ($^1O_2$) was detected in **Figure** 3.4b, the characteristic triplet signals with equal intensities appeared when PMS was added into SCP alone. The test indicated that either PMS itself may be able to produce minor amount of $^1O_2$ (Eq. 3.4) or direct reaction between PMS and TMP occurred to produce similar signals. However, N-rGO was introduced in SCP/PMS solution, no enhancement in peak intensity was observed, irrelevant to the presence of carbocatalyst. The results suggested that $^1O_2$ did not produced from the carbon/PMS system, therefore did not dominantly contribute to the enhanced SCP decomposition in the metal-free

catalytic system. Yi et al. reported that the high intensity of triplet peaks was likely to represent the association between PMS and TMP rather than TMP-$^1O_2$ adducts. [44] The contribution of $^1O_2$ to organic removal was also found negligible in another report due to the rapid reaction between $^1O_2$ and water. [45]

Competitive radical quenching was performed to investigate the differences between carbocatalysis and PMS-only based SCP oxidation. Owing to the rapid reaction rates with •OH and $SO_4^{\bullet -}$ ($k_{SO4\bullet-}$ = (1.6− 7.8) × 10^7 M^{-1} s^{-1}, $k_{\bullet OH}$ = (1.2−2.8) × 10^9 M^{-1} s^{-1}), ethanol was applied as an effective quencher for the radicals. [14] In typical AOPs, radicals are crucial for organic degradation. Thus, if the oxidative radicals are scavenged by the alcohol quencher, the radical oxidation will be partially hindered or completely terminated. As shown in **Figure** 3.4c, when ethanol presented in PMS-only reaction, the SCP removal rate was marginally stalled, suggesting the reaction between PMS and SCP did not rely on free radicals but via a direct nonradical oxidation. Furthermore, TBA was used to probe the participation of •OH in SCP removal as it can instantaneously react with •OH (3.8-7.6× 10^8 M^{-1} s^{-1}) whereas poses a negligible effect on $SO_4^{\bullet -}$. The addition of 50 mM TBA had almost no effect on the SCP degradation. However, when sodium azide (NaN_3, 5 mM), an effective scavenger for $^1O_2$ (1.2 × 10^8 M^{-1} s^{-1}), was added to the PMS-only system, SCP removal rate was decayed to some degree. A greater dosage of NaN_3 (20 mM) gave rise to a further decline in SCP removal rate. [46]

The variation in PMS concentration was monitored during the SCP degradation by PMS alone. As shown in **Figure** 3.4d, PMS decomposed rapidly at the beginning of the reaction (first 5 min) and slowed down and eventually stopped after 7 min. This result is consistent with the change in SCP degradation rate (**Figure** 3.3a) that most of the PMS decomposition reaction occurred in the first 5 min. However, the total PMS decomposition was merely 20% at the end of the 30 min test, indicating that only a small portion of PMS was consumed in the SCP oxidation. On the other hand, when NaN_3 (5 mM) was added with PMS, more PMS was consumed (60%), suggesting that NaN_3

could directly react with PMS. The PMS decomposition was further increased when the SCP was co-presented. Based on the results, it could be deduced that that the inhibition effect of NaN_3 on SCP degradation was primarily due to the PMS consumption by NaN_3 reduction rather than screening $^1O_2$.

3.3.5 Role of N-doped graphene in PMS activation

Our previous studies have reported that PMS can be activated by nanocarbon catalysts to produce $^{\bullet}OH$ and $SO_4^{\bullet -}$ for phenol degradation, while PMS alone can hardly oxidize phenol without activation. [19] Therefore, phenol was chosen as the target organic to rule out the direct reaction with PMS and to investigate the catalytic processes. **Figure** 3.5 shows the catalytic oxidation of phenol on nanocarbon materials such as GO, rGO and N-rGO with and without a radical quenching agent. As shown in **Figure** 3.5, with and without addition of ethanol, the marginal degradation of phenol confirms that the phenol cannot be oxidized in the presence of PMS alone. In **Figure** 3.5a, 100% phenol removal was achieved in 180 min on N-rGO, meanwhile only 40% and 20% phenol oxidation was attained on rGO and GO accordingly. When ethanol was introduced into the reaction solution at a molar ratio of 200:1 (ethanol:PMS) in **Figure** 3.5b, the phenol degradation efficiency was severely deteriorated for all the carbocatalysts. In GO and rGO induced PMS activation reaction, the phenol degradation was instantly terminated due to the addition of ethanol, indicating the phenol degradation heavily relied on the ROS. Notably, in the N-rGO/PMS system, 60% phenol degradation was still yielded in the presence of ethanol.

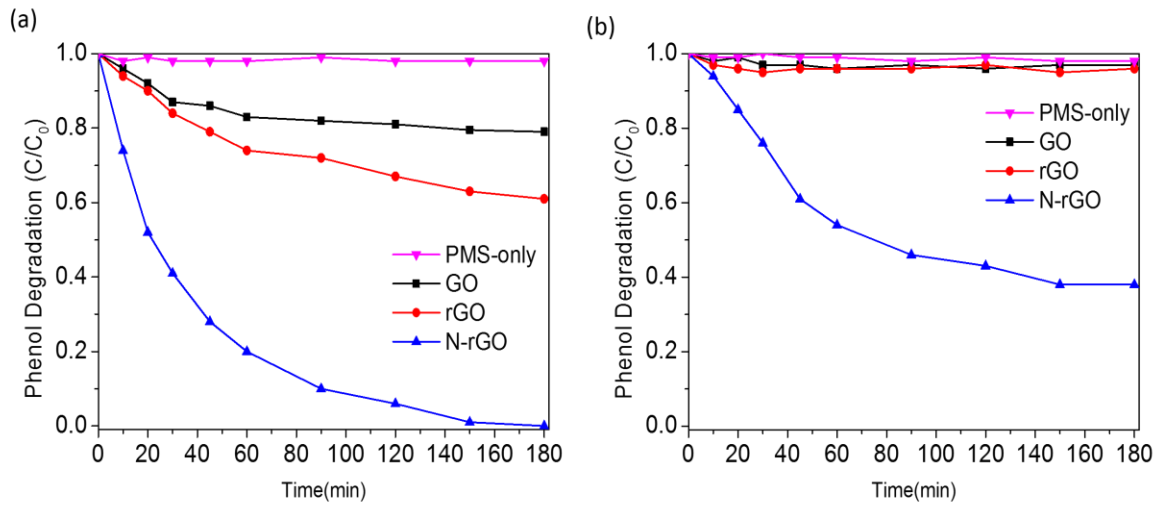

Figure 3.5 (a) Phenol degradation under various catalysts. (b) Effect of ethanol quencher on phenol removal. (Reaction conditions: temperature of 25 °C, catalyst loading of 0.2 g/L, phenol concentration of 20 ppm, PMS concentration of 0.5 g/L, ethanol concentration of 50 mM)

It has been reported that the highly covalent π system of graphitic carbons could activate the O-O bond in PMS and coordinate a redox process to produce free radicals.[47] Moreover, introduction of nitrogen dopants would further activate the adjacent carbon atoms to be positively charged, which would impressively enhance the interactions between carbon and the negatively charged peroxide O-O bond.[19] Due to the formation of strong affinity of PMS onto N-doped region, a more reactive and surface confined ROS was formed as a nonradical species to directly attack the organic substances via electron abstraction through the conductive carbon framework. Therefore, the remaining oxidative capacity in the ethanol/N-rGO/PMS system was originated from the emerging nonradical pathway upon N-doping, which might also exist and contribute to SCP degradation in N-rGO/PMS systems.

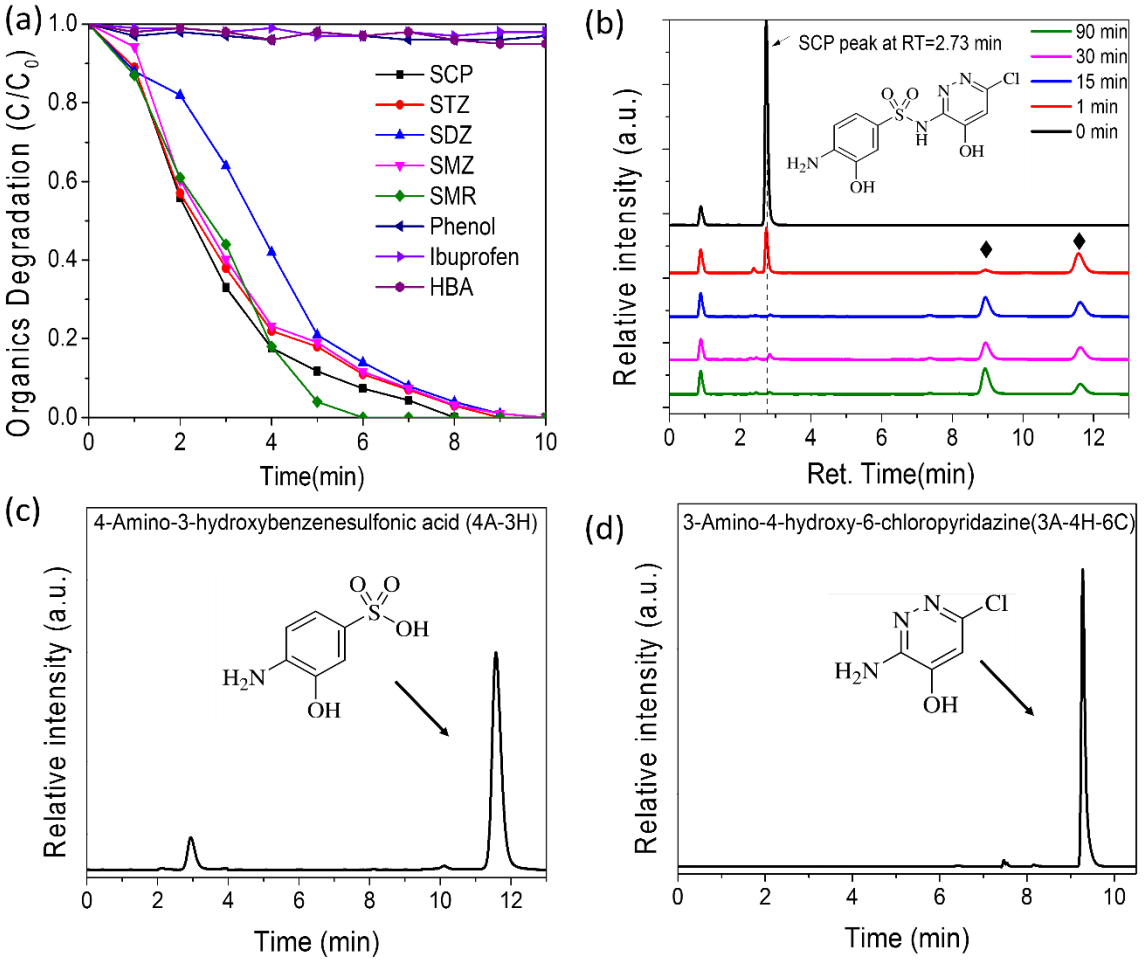

Figure 3.6 (a) Degradation of various organics by PMS only. (b) Degradation of various organic pollutants by PMS-only. (c) SCP degradation intermediate, 4A-3H. (d) SCP degradation intermediates, 3A-4H-6C.

3.3.6 PMS-only selective degradation of different organic pollutants

Inspired by the distinct degradation performances of SCP and phenol with PMS-only, we tested a wide array of organic pollutants to investigate the direct PMS oxidation. As shown in **Figure** 3.6a, phenol, ibuprofen and HBA can be rarely oxidized (< 5%) by PMS only. In contrast, five sulfonamides (SCP, STZ, SDZ SMZ and SMR) could rapidly react with PMS and reached a complete removal in 10 min. The PMS was highly selective to sulfonamide antibiotics. The

HPLC spectra were displayed in **Figure** 3.6b to reveal the SCP degradation process. The SCP peak (2.73 min) decreased rapidly by PMS oxidation and SCP signal completely disappeared after 15 min. Interestingly, the intermediates (marked by black diamonds) emerged at the very beginning (1 min) and did not show any decline in intensity during the whole degradation processes. The intermediates were identified by HPLC in **Figure**s 3.6c and d. The comparison of HPLC retention time of detected intermediates with pure standards of 4A-3H and 3A-4H-6C indicates that the two by-products were produced by the cleavage of the S-N bond in SCP molecules. This supports the assumption that the sulfonamides can be destroyed directly by PMS via breaking-up the S-N bond into smaller organic molecules. Ranyi et al. reported that the N-S bond of sulfonamide families was very vulnerable, which could be readily attacked by PMS. In this process, the abduction of the N atom via electrophilic reaction with PMS was the dominant reaction pathway to form nitroso moiety.[44] Anne et al. also uncovered a similar degradation reaction pathway that the breaking of N-S bond accounted for 70% removal of sulfonamides by photodegradation.[48]

3.4 Conclusions

In summary, nitrogen doped graphene was synthesized via a facile hydrothermal method, which presented an enhanced catalytic activity for PMS activation and SCP degradation compared with the undoped rGO and GO. We observed that PMS can achieve a rapid noncatalytic destruction of SCP by directly attacking the S-N bond. The EPR and quenching experiments further confirmed that SCP oxidation by PMS-only was a nonradical process without generating reactive radicals such as $^{\bullet}OH$ and $SO_4^{\bullet -}$. The PMS-based oxidation is different from the carbocatalytic activation of PMS by N-rGO, which involves both radical and nonradical processes and can achieve a deeper mineralization. Furthermore, PMS-based oxidation was discovered to be effective to the vulnerable S-N bond in sulfonamides (SAs),

whereas inert to phenolics and ibuprofen. The increase of reaction temperature or solution pH were favorable to the PMS-only oxidation. The degradation pathway of selective SCP degradation by PMS was analyzed that SAs was transferred to smaller organic compounds without further mineralization. The study contributes to the insights into the reactive species and mechanisms of carbocatalytic and noncatalytic degradation of SCP with PMS. The feasible application of such a green remediation technique with a manipulated redox capacity and reaction pathways helps achieve a rapid purification of antibiotic contaminants in wastewater.

3.5 References

1. Zhang, Q.-Q.; Ying, G.-G.; Pan, C.-G.; Liu, Y.-S.; Zhao, J.-L., Comprehensive Evaluation of Antibiotics Emission and Fate in the River Basins of China: Source Analysis, Multimedia Modeling, and Linkage to Bacterial Resistance. *Environmental Science & Technology* **2015,** *49*, (11), 6772-6782.

2. Zessel, K.; Mohring, S.; Harnscher, G.; Kietzmann, M.; Stahl, J., Biocompatibility and antibacterial activity of photolytic products of sulfonamides. *Chemosphere* **2014,** *100*, 167-174.

3. Haidar, M.; Dirany, A.; Sires, I.; Oturan, N.; Oturan, M. A., Electrochemical degradation of the antibiotic sulfachloropyridazine by hydroxyl radicals generated at a BDD anode. *Chemosphere* **2013,** *91*, (9), 1304-1309.

4. Baran, W.; Adamek, E.; Sobczak, A.; Sochacka, J., The comparison of photocatalytic activity of Fe-salts, TiO2 and TiO2/FeCl3 during the sulfanilamide degradation process. *Catalysis Communications* **2009,** *10*, (6), 811-814.

5. Ji, L.; Chen, W.; Zheng, S.; Xu, Z.; Zhu, D., Adsorption of Sulfonamide Antibiotics to Multiwalled Carbon Nanotubes. *Langmuir* **2009,** *25*, (19), 11608-11613.

6. Srinivasan, P.; Sarmah, A. K.; Manley-Harris, M., Co-contaminants and factors affecting the sorption behaviour of two sulfonamides in pasture soils. *Environmental Pollution* **2013,** *180*, 165-172.

7. Martucci, A.; Cremonini, M. A.; Blasioli, S.; Gigli, L.; Gatti, G.; Marchese, L.; Braschi, I., Adsorption and reaction of sulfachloropyridazine sulfonamide antibiotic on a high silica mordenite: A structural and spectroscopic combined study. *Microporous and Mesoporous Materials* **2013,** *170*, 274-286.

8. Dirany, A.; Sirés, I.; Oturan, N.; Özcan, A.; Oturan, M. A., Electrochemical Treatment of the Antibiotic Sulfachloropyridazine: Kinetics, Reaction Pathways, and Toxicity Evolution. *Environmental Science & Technology* **2012,** *46*, (7), 4074-4082.

9. Wammer, K. H.; Lapara, T. M.; McNeill, K.; Arnold, W. A.; Swackhamer, D. L., Changes in antibacterial activity of triclosan and sulfa drugs due to photochemical transformations. *Environmental Toxicology and Chemistry* **2006,** *25*, (6), 1480-1486.

10. Boreen, A. L.; Arnold, W. A.; McNeill, K., Triplet-sensitized photodegradation of sulfa drugs containing six-membered heterocyclic groups: Identification of an SO2 extrusion photoproduct. *Environmental Science & Technology* **2005,** *39*, (10), 3630-3638.

11. Guo, W.; Su, S.; Yi, C.; Ma, Z., Degradation of antibiotics amoxicillin by Co3O4-catalyzed peroxymonosulfate system. *Environmental Progress & Sustainable Energy* **2013,** *32*, (2), 193-197.

12. Ahmed, M. M.; Barbati, S.; Doumenq, P.; Chiron, S., Sulfate radical anion oxidation of diclofenac and sulfamethoxazole for water decontamination. *Chemical Engineering Journal* **2012,** *197*, 440-447.

13. Nfodzo, P.; Choi, H., Sulfate Radicals Destroy Pharmaceuticals and Personal Care Products. *Environmental Engineering Science* **2011,** *28*, (8), 605-609.

14. Anipsitakis, G. P.; Dionysiou, D. D., Degradation of Organic Contaminants in Water with Sulfate Radicals Generated by the Conjunction of Peroxymonosulfate with Cobalt. *Environmental Science & Technology* **2003,** *37*, (20), 4790-4797.

15. Sun, H.; Liu, S.; Zhou, G.; Ang, H. M.; Tade, M. O.; Wang, S., Reduced Graphene Oxide for Catalytic Oxidation of Aqueous Organic Pollutants. *Acs Applied Materials & Interfaces* **2012,** *4*, (10), 5466-5471.

16. Sun, H.; Kwan, C.; Suvorova, A.; Ang, H. M.; Tade, M. O.; Wang, S., Catalytic oxidation of organic pollutants on pristine and surface nitrogen-modified carbon nanotubes with sulfate radicals. *Applied Catalysis B-Environmental* **2014,** *154*, 134-141.

17. Duan, X.; Sun, H.; Wang, Y.; Kang, J.; Wang, S., N-Doping-Induced Nonradical Reaction on Single-Walled Carbon Nanotubes for Catalytic Phenol Oxidation. *ACS Catalysis* **2015,** *5*, (2), 553-559.

18. Duan, X.; O'Donnell, K.; Sun, H.; Wang, Y.; Wang, S., Sulfur and Nitrogen Co-Doped Graphene for Metal-Free Catalytic Oxidation Reactions. *Small* **2015,** *11*, (25), 3036-3044.

19. Duan, X.; Ao, Z.; Sun, H.; Indrawirawan, S.; Wang, Y.; Kang, J.; Liang, F.; Zhu, Z. H.; Wang, S., Nitrogen-Doped Graphene for Generation and Evolution of Reactive Radicals by Metal-Free Catalysis. *ACS Applied Materials & Interfaces* **2015,** *7*, (7), 4169-4178.

20. Sun, H.; Wang, Y.; Liu, S.; Ge, L.; Wang, L.; Zhu, Z.; Wang, S., Facile synthesis of nitrogen doped reduced graphene oxide as a superior metal-free catalyst for oxidation. *Chemical Communications* **2013,** *49*, (85), 9914-9916.

21. Z., Y.; Y., N.; P., V. H. A. R., Kinetics of the peracetic acid decomposition: Part II: pH effect and alkaline hydrolysis. *The Canadian Journal of Chemical Engineering* **1997,** *75*, (1), 42-47.

22. Yang, Y.; Banerjee, G.; Brudvig, G. W.; Kim, J.-H.; Pignatello, J. J., Oxidation of Organic Compounds in Water by Unactivated Peroxymonosulfate. *Environmental Science & Technology* **2018,** *52*, (10), 5911-5919.

23. Qi, C.; Liu, X.; Ma, J.; Lin, C.; Li, X.; Zhang, H., Activation of peroxymonosulfate by base: Implications for the degradation of organic pollutants. *Chemosphere* **2016,** *151*, 280-288.

24. Willard, H. H., Volumetric Analysis. By I. M. Kolthoff and V. A. Stenger. *The Journal of Physical Chemistry* **1944,** *48*, (2), 97-97.

25. Liang, C.; Huang, C.-F.; Mohanty, N.; Kurakalva, R. M., A rapid spectrophotometric determination of persulfate anion in ISCO. *Chemosphere* **2008,** *73*, (9), 1540-1543.

26. Hummers, W. S.; Offeman, R. E., Preparation of Graphitic Oxide. *Journal of the American Chemical Society* **1958,** *80*, (6), 1339-1339.

27. Kumar, N. A.; Nolan, H.; McEvoy, N.; Rezvani, E.; Doyle, R. L.; Lyons, M. E. G.; Duesberg, G. S., Plasma-assisted simultaneous reduction and nitrogen doping of graphene oxide nanosheets. *Journal of Materials Chemistry A* **2013,** *1*, (14), 4431-4435.

28. Zheng, Y.; Jiao, Y.; Ge, L.; Jaroniec, M.; Qiao, S. Z., Two-Step Boron and Nitrogen Doping in Graphene for Enhanced Synergistic Catalysis. *Angewandte Chemie-International Edition* **2013,** *52*, (11), 3110-3116.

29. Wang, C.; Zhou, Y.; He, L.; Ng, T.-W.; Hong, G.; Wu, Q.-H.; Gao, F.; Lee, C.-S.; Zhang, W., In situ nitrogen-doped graphene grown from polydimethylsiloxane by plasma enhanced chemical vapor deposition. *Nanoscale* **2013,** *5*, (2), 600-605.

30. Deng, D.; Pan, X.; Yu, L.; Cui, Y.; Jiang, Y.; Qi, J.; Li, W.-X.; Fu, Q.; Ma, X.; Xue, Q.; Sun, G.; Bao, X., Toward N-Doped Graphene via Solvothermal Synthesis. *Chemistry of Materials* **2011,** *23*, (5), 1188-1193.

31. Saputra, E.; Muhammad, S.; Sun, H.; Ang, H.-M.; Tade, M. O.; Wang, S., Manganese oxides at different oxidation states for heterogeneous activation of peroxymonosulfate for

phenol degradation in aqueous solutions. *Applied Catalysis B-Environmental* **2013,** *142*, 729-735.

32. Saputra, E.; Muhammad, S.; Sun, H.; Ang, H. M.; Tadé, M. O.; Wang, S., Different Crystallographic One-dimensional MnO2 Nanomaterials and Their Superior Performance in Catalytic Phenol Degradation. *Environmental Science & Technology* **2013,** *47*, (11), 5882-5887.

33. Zhang, B.-T.; Zhang, Y.; Teng, Y.; Fan, M., Sulfate Radical and Its Application in Decontamination Technologies. *Critical Reviews in Environmental Science and Technology* **2015,** *45*, (16), 1756-1800.

34. Ji, Y.; Lu, J.; Wang, L.; Jiang, M.; Yang, Y.; Yang, P.; Zhou, L.; Ferronato, C.; Chovelon, J.-M., Non-activated peroxymonosulfate oxidation of sulfonamide antibiotics in water: Kinetics, mechanisms, and implications for water treatment. *Water Research* **2018,** *147*, 82-90.

35. Duan, X. G.; Sun, H. Q.; Ao, Z. M.; Zhou, L.; Wang, G. X.; Wang, S. B., Unveiling the active sites of graphene-catalyzed peroxymonosulfate activation. *Carbon* **2016,** *107*, 371-378.

36. Kang, J.; Duan, X. G.; Zhou, L.; Sun, H. Q.; Tade, M. O.; Wang, S. B., Carbocatalytic activation of persulfate for removal of antibiotics in water solutions. *Chemical Engineering Journal* **2016,** *288*, 399-405.

37. Ji, Y.; Dong, C.; Kong, D.; Lu, J.; Zhou, Q., Heat-activated persulfate oxidation of atrazine: Implications for remediation of groundwater contaminated by herbicides. *Chemical Engineering Journal* **2015,** *263*, 45-54.

38. Guan, Y.-H.; Ma, J.; Li, X.-C.; Fang, J.-Y.; Chen, L.-W., Influence of pH on the Formation of Sulfate and Hydroxyl Radicals in the UV/Peroxymonosulfate System. *Environmental Science & Technology* **2011,** *45*, (21), 9308-9314.

39. Lian, L.; Yao, B.; Hou, S.; Fang, J.; Yan, S.; Song, W., Kinetic Study of Hydroxyl and Sulfate Radical-Mediated Oxidation of Pharmaceuticals in Wastewater Effluents. *Environmental Science & Technology* **2017,** *51*, (5), 2954-2962.

40. Fang, J.; Fu, Y.; Shang, C., The Roles of Reactive Species in Micropollutant Degradation in the UV/Free Chlorine System. *Environmental Science & Technology* **2014,** *48*, (3), 1859-1868.

41. Beitz, T.; Bechmann, W.; Mitzner, R., Investigations of Reactions of Selected Azaarenes with Radicals in Water. 2. Chlorine and Bromine Radicals. *The Journal of Physical Chemistry A* **1998,** *102*, (34), 6766-6771.

42. Beitz, T.; Bechmann, W.; Mitzner, R., Investigations of Reactions of Selected Azaarenes with Radicals in Water. 1. Hydroxyl and Sulfate Radicals. *The Journal of Physical Chemistry A* **1998,** *102*, (34), 6760-6765.

43. Kang, J.; Duan, X.; Wang, C.; Sun, H.; Tan, X.; Tade, M. O.; Wang, S., Nitrogen-doped bamboo-like carbon nanotubes with Ni encapsulation for persulfate activation to remove emerging contaminants with excellent catalytic stability. *Chemical Engineering Journal* **2018,** *332*, (Supplement C), 398-408.

44. Yin, R.; Guo, W.; Wang, H.; Du, J.; Zhou, X.; Wu, Q.; Zheng, H.; Chang, J.; Ren, N., Selective degradation of sulfonamide antibiotics by peroxymonosulfate alone: Direct oxidation and nonradical mechanisms. *Chemical Engineering Journal* **2018,** *334*, 2539-2546.

45. Haag, W. R.; Hoigne´, J. r.; Gassman, E.; Braun, A. M., Singlet oxygen in surface waters — Part I: Furfuryl alcohol as a trapping agent. *Chemosphere* **1984,** *13*, (5), 631-640.

46. Zhou, Y.; Jiang, J.; Gao, Y.; Ma, J.; Pang, S.-Y.; Li, J.; Lu, X.-T.; Yuan, L.-P., Activation of Peroxymonosulfate by Benzoquinone: A Novel Nonradical Oxidation Process. *Environmental Science & Technology* **2015,** *49*, (21), 12941-12950.

47. Duan, X.; Sun, H.; Wang, S., Metal-Free Carbocatalysis in Advanced Oxidation Reactions. *Accounts of Chemical Research* **2018,** *51*, (3), 678-687.

48. Boreen, A. L.; Arnold, W. A.; McNeill, K., Photochemical Fate of Sulfa Drugs in the Aquatic Environment: Sulfa Drugs Containing Five-Membered Heterocyclic Groups. *Environmental Science & Technology* **2004,** *38*, (14), 3933-3940.

Chapter 4: Nitrogen-doped bamboo-like carbon nanotubes with Ni encapsulation for removal of emerging contaminants with excellent catalytic stability

This chapter has been published on journal "Chemical Engineering Journal", DOI: 10.1016/j.cej.2017.09.102.

ABSTRACT

Nitrogen-doped bamboo-like carbon nanotubes encapsulated with nickel nanoparticles (Ni@NCNTs) were feasibly fabricated by a one-pot pyrolysis route. The characterization techniques revealed the surface morphology, structure and chemical composition of the as-prepared catalysts synthesized in different conditions. Ni@NCNTs were employed as both adsorbents and catalysts for activating persulfate to remove an emerging pollutant, antibiotic sulfachloropyridazine. The nitrogen modification enhanced both adsorption capacity and catalytic ability of Ni@NCNTs and proved to be a promising alternative to metal oxides and other carbon catalysts. Moreover, Ni@NCNTs showed an excellent stability because of nitrogen heteroatom doping and Ni nanoparticle encapsulation. Electron paramagnetic resonance (EPR) and classical radical quenching tests discovered a simultaneous radical/non-radical mechanism in Ni@NCNTs/persulfate system. The results indicated that the novel nano-architectured catalyst materials can show emerging functionalities for environmental remediation processes.

4.1 Introduction

Worldwide drinking water scarcity has become more intense because of the wide water contaminations, which appears as one of the most critical challenges in the world. Many water treatment techniques have been employed to cope with the rapid deterioration of water pollution in terms of the discharge quantity and ever-increasing complexity.[1] Recently, emerging contaminants, for instance pharmaceuticals and personal care products (PPCPs), have attracted tremendous attention. Their intrinsic properties, the continuous and fast development of new species, ubiquity in all surface waters, difficulty of complete remediation and tardy action in early days, as well as lack of understanding of their possible jeopardization to the environment, have brought out great issues to the development of remediation technologies.[2, 3]

As a representative and main contributor of PPCPs, sulfonamide antibiotics have been intensively used in animal husbandry and human medicine owing to their low cost and good therapeutic effect. [4-8] As a pharmaceutical product, sulfonamides are extremely recalcitrant to complete natural biodegradation because they are biological active.[9] Many studies have detected various sulfonamide compounds in aqueous environment. Even at a low level, a continuous and long-term exposure to such chemicals could lead to appreciable adverse effects on human health.[10] Therefore, the complexity, fine water solubility and trace amount have made them difficult to reach complete degradation via traditional wastewater treatment measures in wastewater treatment plants (WWTP). [11, 12] Recently, advanced oxidation processes (AOPs) have attracted massive attention as they are very effective for the degradation and mineralization of refractory organic pollutants in the aquatic environment.[13] Typically, AOPs are involving oxidants and superoxides such as ozone, oxygen, hydroperoxide, and various radicals that are capable of destroying target organics to harmless species. Hydroxyl radicals (•OH) have been most consequently observed in AOPs such as Fenton reaction, UV

oxidation and ozonation owing to their superior oxidation ability towards organic pollutants with almost no selectivity. [14, 15] Yet, the drawbacks of many •OH-related Fenton-like reactions, such as excess sludge production, narrow pH (~3) requirement and metal leaching, are the bottleneck limits. Comparably, strong oxidizing sulfate radical ($SO_4^{\bullet-}$) offers an excellent alternative to hydroxyl radical (•OH) because $SO_4^{\bullet-}$ has a higher oxidation potential (2.5–3.1 V) than the hydroxyl radicals (2.7 V) and a better flexibility of pH tolerance. [15-17] Analogous to Fenton-like oxidation reactions, sulfate radicals can be obtained by activating persulfate (PS) through various activation methods, such as UV-light irradiation, heating, carbon catalysis, metal ion and metallic oxide catalysis, for organic contaminant degradation. [18-21] Among the catalysts used in AOPs, carbon-based nanomaterials stand out owing to the exceptional adsorption capacity, catalysis ability and environmentally friendly nature. [22] Graphene oxide, reduced graphene oxide, carbon nanotubes, and nanodiamonds have been employed in water treatment as an excellent alternative to metal-based catalysts and shown great competitiveness in terms of avoiding metal toxics and associated contamination. [23] However, pristine carbocatalysts suffer from poor stability in heterogeneous reactions, and the heteroatom doping with N, S, P or B into carbon honeycomb network offers an effective strategy to tackle such an issue. [24-32]

Herein, we demonstrate a one-pot facile synthesis of high quality N-doped carbon nanotubes with nickel nanoparticle encapsulation (Ni@NCNT) via direct pyrolysis of melamine as carbon/nitrogen co-precursor and nickel chloride as a Ni source. The prepared product presented a high N-doping level (6.6%) and successful Ni encapsulation. In addition, due to the synergistic effect of N-doping and Ni decoration, the catalytic oxidation and reusability were dramatically enhanced comparing with CNT and N-NCNT in activation of PS to effectively remove sulfachloropyridazine (SCP) in water. Electron paramagnetic resonance

(EPR) and quenching tests were used to investigate the mechanism of PS activation and SCP oxidation.

4.2 Experimental

4.2.1 Chemicals and materials

Nickel chloride hexahydrate ($NiCl_2 \bullet 6H_2O$, 98%), phenol (99%), sulfachloropyridazine (99%), 5, 5-dimethyl-1-pyrroline (DMPO), potassium persulfate, and hydrochloride acid (32%) were obtained from Sigma-Aldrich. Multi-walled carbon nanotubes (MWCNTs) were purchased from Timesnano, China. Graphene oxide (GO) was prepared via a modified Hummers' approach and reduced graphene oxide (rGO) was fabricated by annealing the obtained GO in a tubular furnace under nitrogen atmosphere at 700 ^oC for 1 h. Nitrogen doped reduced graphene oxide (N-rGO) was prepared through a hydrothermal approach, as detailed in previous studies. [32-34] All the chemicals were of analytical grade or higher and used as received without further purification. Deionized (DI) water was used in all the experiments.

4.2.2 Synthesis of Ni@NCNT

Nitrogen-doped carbon nanotubes with nickel encapsulation were fabricated by a controlled pyrolysis process using melamine and nickel chloride hexahydrate as carbon/nitrogen and nickel precursors, respectively. In a typical synthesis, melamine ($C_3N_6H_6$, 10 g) was dissolved in 20 mL of DI water at 65 ^oC under continuous stirring for 1 h until the melamine was dissolved completely. $NiCl_2 \bullet 6H_2O$ as a nickel precursor with designed loading (1, 2, 3.3, or 7 g) was introduced to the melamine solution to form a homogenous greenish solution. Later, the mixed solution was heated and kept at 80 ^oC overnight to completely remove water. The resulting precipitates were placed inside a tube furnace and allowed nitrogen gas to flow through for three hours to purge out the air residue. And then the samples were annealed at 700, 800 or 900 ^oC for 6 h under N_2 atmosphere with a heating rate of 5 $^oC\ min^{-1}$. After the

pyrolysis, the sample was naturally cooled down to room temperature. Finally, the resultant black product was ground to fine powders, followed by thoroughly washing with excessive concentrated hydrochloride acid (32%), by stirring in the acid solution for 6 h. The obtained precipitates were then washed with ethanol and DI water for a few times until the clear solution pH achieved at the value of 7. The as-prepared catalysts were denoted as Ni@NCNT-T-M (where T represents the calcination temperature and M represents the initial weight ratio of melamine to nickel chloride), for instance Ni@NCNT-700-3 means Ni@NCNT with 3:1 melamine to $NiCl_2 \bullet 6H_2O$ and heated at 700 ^oC.

4.2.3 Catalyst characterization

The crystal structure of the samples determined by X-ray powder diffraction patterns were recorded on a Bruker D8 Advance X-ray diffractometer using Cu Kα radiation (λ = 1.5406 Å) at 40 mA and 40 kV with a scanning speed of 0.2° (2θ) min^{-1}. The Raman spectra were obtained using a laser with an excitation wavelength of 785 nm at room temperature on a Renishaw Raman microscope. The surface contents and types of carbon, nitrogen and metals were measured by X-ray photoelectron spectroscopy (XPS) on a VG Multi lab 2000 spectrometer (Kratos AXIS Ultra DLD) with Al Kα radiation as the X-ray source (300 W). The C 1s line at 284.6 eV was applies as a calibration to correct the binding energies. By deducting the Shirley-type background, the core level spectra were deconvoluted into their components with Gaussian-Lorentzian (20:80) shape lines using the CasaXPS software. The Brunauer−Emmett−Teller (BET) specific surface area and pore-size distribution of the samples were determined by N_2 adsorption−desorption at −196 °C using a Micromertics Tristar 3000. The samples were degassed in vacuum at 110 °C overnight before the tests. The morphologies of the carbon samples were characterized using scanning electron microscopy (SEM; FEI Verios XHR 460) and transmission electron microscopy (TEM; JEOL 2100). The thermal stability was collected by the thermogravimetric analysis (TGA) using a TGA/DSC1 STAR^e

system, Mettler-Toledo thermal analyzer under flowing air. The reactive radicals were detected by electron paramagnetic resonance (EPR) on a Bruker EMS-plus instrument with DMPO as a spin-trapping agent, and the Xeon software (Bruker) was used to analyze the quantitative information. The Ni concentration in reaction solutions was evaluated by an Inductively Coupled Plasma Optical Emission Spectrometer (ICP-OES).

4.2.4 Adsorption and catalytic oxidation of SCP solutions

SCP adsorption was performed in a 500 mL conical flask at 25 °C, unless other temperature specifically mentioned. Typical adsorption experiments were carried out by dispersing the Ni@NCNT samples (0.2 g L^{-1}) in SCP (20 mg L^{-1}, pH = 7) solutions. At determined intervals, 1 mL of solution was withdrawn and immediately filtered by a 0.22 μm Millipore syringe filter to remove the solid particles.

4.2.5 Catalytic oxidation of SCP solutions

The degradation experiments were conducted by introducing designed amount of PS into the reaction solutions when the adsorption/desorption equilibrium was reached. After the reaction was initiated, 1 mL of solution was extracted at planned time intervals, and then injected into an UHPLC vial mixed with 0.5 mL methanol as the quenching agent. Each experiment and analysis was repeated twice and the results were reproducible with relative errors less than ± 5%. The concentrations of SCP were analyzed with an UHPLC system (Thermo-Fisher Scientific 3000) using an UV detector at a detection wavelength of 270 nm. An Acclaim RSLC C-18 column (2.2 μm) was used as a separation column. The mobile phase was a mixture of diluted acetic acid and methanol (70:30, v/v) with a flow rate of 0.3 mL min^{-1} and 20 μL of injection volume. [32] Total organic carbon (TOC) was measured using a Shimadzu TOC-5000 CE analyzer for a few selected samples. For TOC measurement, 10 mL sample was withdrawn at a designed interval, filtered and quenched with 10 mL of 0.3 M sodium nitrite solution, and

then the mixed solution was analyzed. [35] Data shown in the figures are mean values of at least three experiments. The error represents the mean deviation of the single values from the mean value.

4.3 Results and discussion

4.3.1 Characterization of carbon nanotubes materials

X-ray diffraction (XRD) was employed to investigate the crystalline structure of the prepared CNTs. **Figure** 4.1A displays the XRD spectra of CNT, NCNT and Ni@NCNTs composites synthesized at various pyrolysis temperatures. All the carbon nanotubes showed a broad reflection peak at $2\theta = 26.5^{o}$, corresponding to the (002) plane of graphitic carbon with an interlayer spacing of 0.34 nm. The peak intensity increased when temperature elevated from 700 to 800 ^{o}C and then decreased at 900 ^{o}C. Additionally, the XRD spectra of Ni@NCNT at different nitrogen loading amounts are shown in **Figure** 4.1B. It is noticed that the broad background band centred at $2\theta = 26^{o}$ might be owing to the successfully incorporated nitrogen defects in the graphitic structure. [36] Aside from the graphitic carbon peak, three pronounced peaks can be observed at $2\theta = 44.5$, 51.9 and 76.4^{o}, corresponding to the (111), in comparison with CNT and N-CNT, (200) and (311) reflections of Ni nanoparticles, respectively and confirming the incorporation of Ni nanoparticles in the CNT catalysts. [37] A less conspicuous peak appearing at 41^{o} indicated the existence of nickel carbide (Ni_3C) in the CNTs. It is worth to notice that there is no obvious nickel oxide peak detected, typically at around $2\theta = 37^{o}$, which might be attributed to the reduction of nickel ions to nickel nanoparticles by carbon atoms. It was found that nickel ions could be reduced to nickel metal nanoparticles by using amorphous carbon as a reductant in argon atmosphere at 500 ^{o}C and that nickel oxide particles could be reduced by natural graphite at a high pyrolysis temperature. [38] [39] Moreover, the CNT compartment layers may also provide the embedded nickel particles a protection shell from being oxidized.

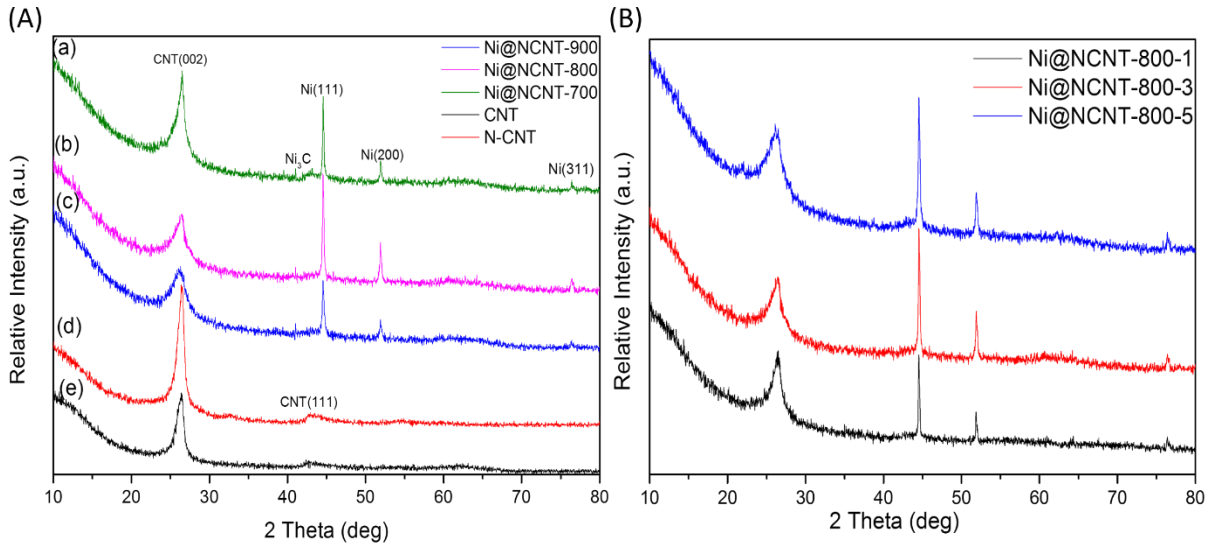

Figure 4.1 (A) XRD patterns of (a) Ni@NCNT-900-3, (b) Ni@NCNT-800-3, (c) Ni@NCNT-700-3, (d) N-CNT, (e) modified CNT samples. (B) XRD patterns of Ni@NCNT-800-1, Ni@NCNT-800-3, and Ni@NCNT-800-5.

Raman spectroscopy as one of the most sensitive and informative techniques is widely used to evaluate graphitic materials for graphitization degree, graphene layer number or carbon nanotube wall layers, nanotube diameter, disorder level in sp^2 network and doping grade. **Figure** 4.2 shows the Raman spectra of Ni@NCNT at various pyrolysis temperatures, e.g. 700, 800 and 900 ^oC, CNT and N-CNT. Three prominent peaks are observed at 1330, 1573 and 2648 cm^{-1}, which are attributed to the D, G and 2D bands, respectively.

The intensity ratio of D band to G band (I_D/I_G) is often used to evaluate the structural disorder of carbon materials. The I_D/I_G of N-CNT (1.38) showed a higher value than modified CNT (1.29), indicating that nitrogen doping on the sp^2 carbon network could largely boost the defect density. The I_D/I_G ratio of Ni@NCNT decreases from 1.33 to 1.22 with increasing pyrolysis temperature from 700 to 900 ^oC, suggesting that the carbon nanotubes possess less lattice defects and disorders derived from high pyrolysis temperature. The disorder property of the catalysts will be further confirmed by electron microscopy. The G band peak width is another

indicator of heteroatom doping. [40], [41] **Figure** 4.2 shows that G band width of CNT synthesized at various temperatures came along with an order of Ni@NCNT-700 > Ni@NCNT-800 > Ni@NCNT-900, confirming the successful N doping, and that the doping degree reduced with elevated pyrolysis temperature. **Figure** 4.2 also shows the variation of I_D/I_G ratio along with the nitrogen precursor weight percentage, indicating that a higher nitrogen precursor content would give rise to a higher N doping level. However, when the nitrogen and nickel precursors loading ratio was raised to 7, the I_D/I_G ratio dropped, suggesting that higher nitrogen precursor amount would not always give a higher disorder level.

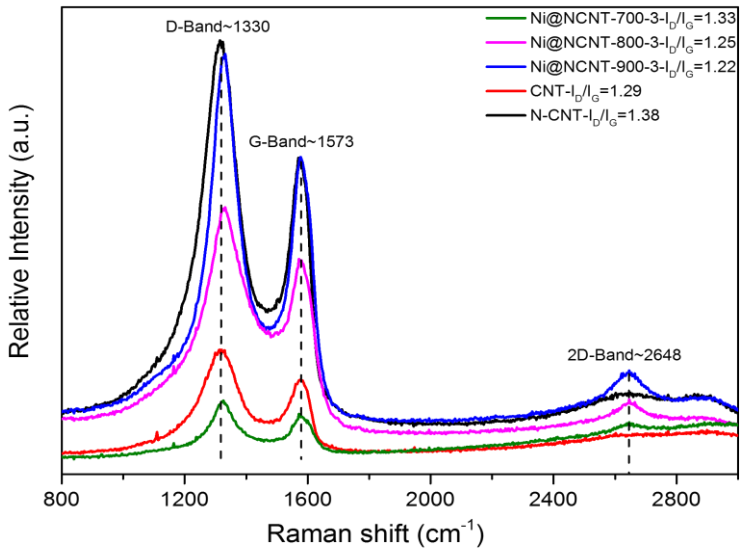

Figure 4.2 Raman spectra of Ni@NCNT at different annealing temperatures, CNT and N-CNT.

The surface morphology of the as-synthesized Ni@NCNTs nanostructures was characterized by SEM and TEM imaging. The SEM images in **Figure** 4.3 (a) reveal that the product fabricated at 800 ^oC contains well grown nanotubes with a herringbone structure and is free from impurities such as amorphous carbon and polyhedral carbon particles. The diameter of the tubes ranges from 70 to 400 nm, and length can be up to dozens of micrometres. TEM

images in **Figure** 4.3 (b) and (c) further confirm that they are hollow CNTs with a typical bamboo-like and compartmentalized structure. It was also shown that the pea-pod like nickel particles are encapsulated inside the carbon tubes. The inner tube diameter and the wall thickness of a typical carbon nanotube were measured to be 45 and 20 nm, respectively. In addition, it was observed that most of the nickel nanoparticles were kept inside the CNTs after being washed in concentrated hydrochloride acid solution for hours, indicating that the nickel nanoparticles are quite inaccessible from being affected by outside environment, acid solution and oxidation. To further confirm such a point, **Figure** 4.3 (d) shows the morphology of CNTs before acid treatment. The nickel particles (black dots) are randomly dispersed over the CNTs both inside and outside. On the other hand, the acid treated tubes in **Figure** 4.3 (b) show a nice and clean tube surface. Many metal-based catalysts have been extensively applied for AOPs, yet the metal leaching is surely a barrier for their further development. [29] In this study, the Ni content of Ni@NCNTs/PS reaction solutions was tested by ICP-OES and it was shown that the Ni concentration was as low as 0.47 mg L^{-1}, which is within the limit of nickel range 0.02 – 1 mg L^{-1} of the world drinking water quality.[42] In addition, the magnetic property of Ni@NCNTs before and after acid wash is shown in **Figure** 4.4. The raw Ni@NCNT showed strong magnetism, and the magnetism was largely reserved even after acid wash, which is due to the carbon layers on Ni particles. Such magnetic property can be very convenient for post catalyst recycling process.

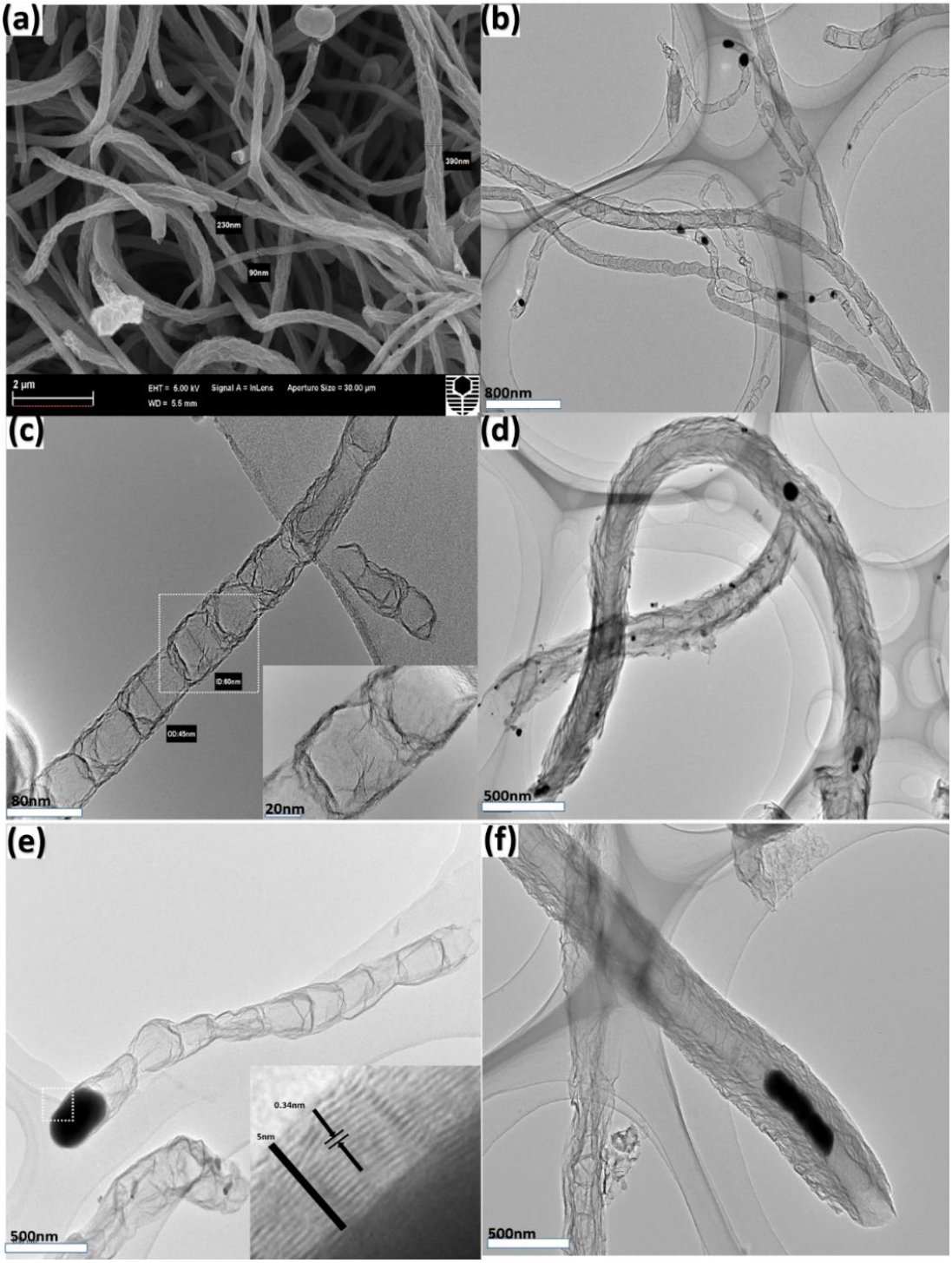

Figure 4.3 SEM and TEM characterization of the Ni encapsulated N-doped carbon nanotube. (a) SEM image of the Ni@NCNT-800-3. (b) TEM image of Ni@NCNT-800-3 with pea-pod like Ni particle encapsulation. (c) TEM images of bamboo like CNT structure with compartments; inset shows the magnified part of the compartments. (d) TEM image of Ni@NCNT-800-3 before acid treatment. (e) TEM image of Ni@NCNT-800-3 with tip Ni

encapsulation; inset displays the graphitic layers of the carbon shell. (f) TEM image of Ni@NCNT-800-3 with worm like Ni particle accumulation at the tube end.

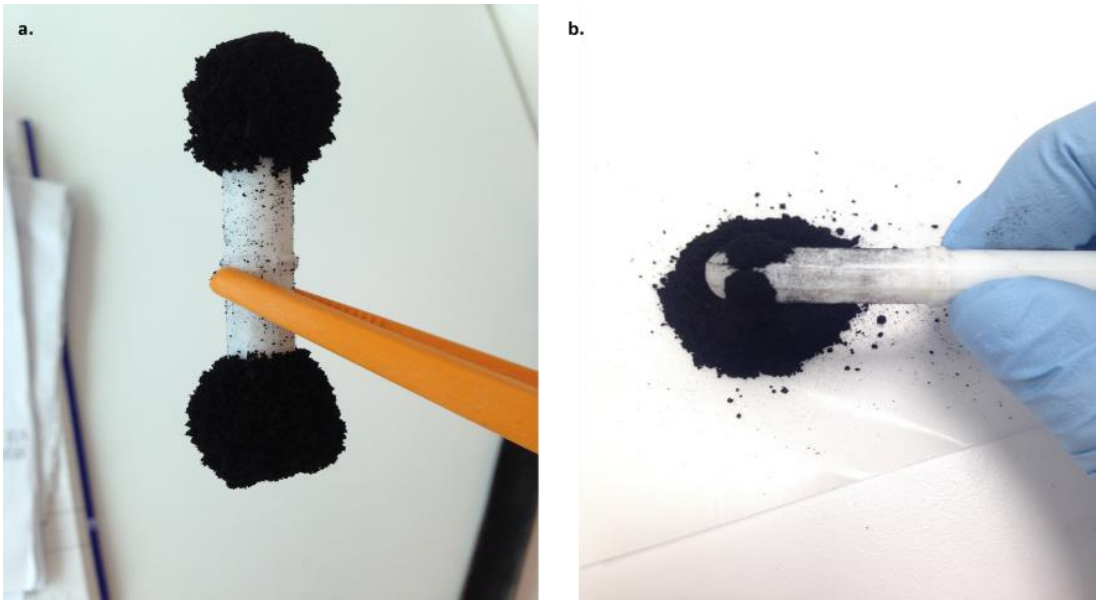

Figure 4.4 Magnetic property of (a) Ni@NCNTs before acid treatment, (b) Ni@NCNTs after acid treatment.

In **Figure** 4. 3(e), nickel particles are detected at the tip of the CNTs, which implies that a tip-growth mechanism might be responsible for the formation of carbon nanotube. Besides, the motion trail of nickel particles is illuminated in **Figure** 4.3 (f), suggesting that the nickel particles are able to diffuse along the tube axis and aggregate at the tube end to form a worm-like Ni catalyst lump. A magnified TEM image of encapsulated nickel particles is shown in **Figure** 4.3(e) (inset). The nickel nanoparticles are embedded in a graphitic shell composing of well-ordered carbon layers, and the inter plane spacing of the fringe lattices is in a range from 0.34 to 0.38 nm, which increased with growing tube diameter and agreed to the size effect's rule. [43] In order to systematically study the influences of the pyrolysis temperature and amount of nitrogen precursor on CNTs morphology and microstructure, the SEM images of CNTs synthesized at different conditions are displayed in **Figure** 4.5. At 700 ^{o}C, the obtained sample represents a chrysanthemum-like carbon nanotube cluster with irregular tube sizes and short length, and the graphene like carbon material can be observed (**Figure**s. 4.5 and 4.6). As

the SEM image was taken from the overlook-angle, one can clearly see that many of the growing tubes are observed to be open ended and interestingly showing a multi-walled carbon tube structure, which is consistent with the Raman results.

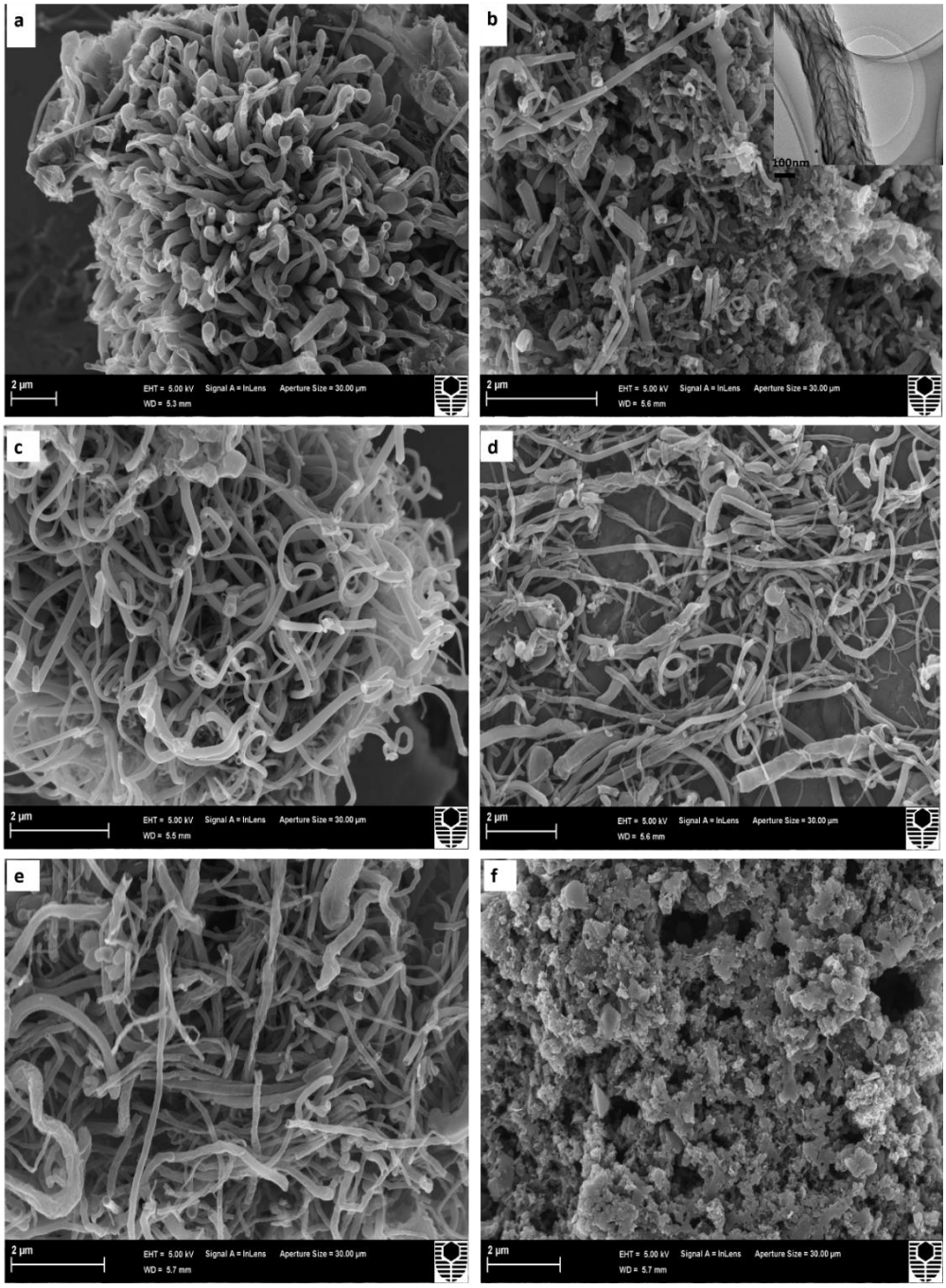

Figure 4.5 SEM images of (a) Ni@NCNT-700-3, (b) Ni@NCNT-900-3; inset shows the herringbone structure and highly roughness tube surface, (c) Ni@NCNT-800-1, (d) Ni@NCNT-800-5, (e) Ni@NCNT-800-3 after third stability experiment, (f) Ni@NCNT-800-10 (The tube-shape morphology completely disappeared when the melamine ratio was raised to a much higher value.)

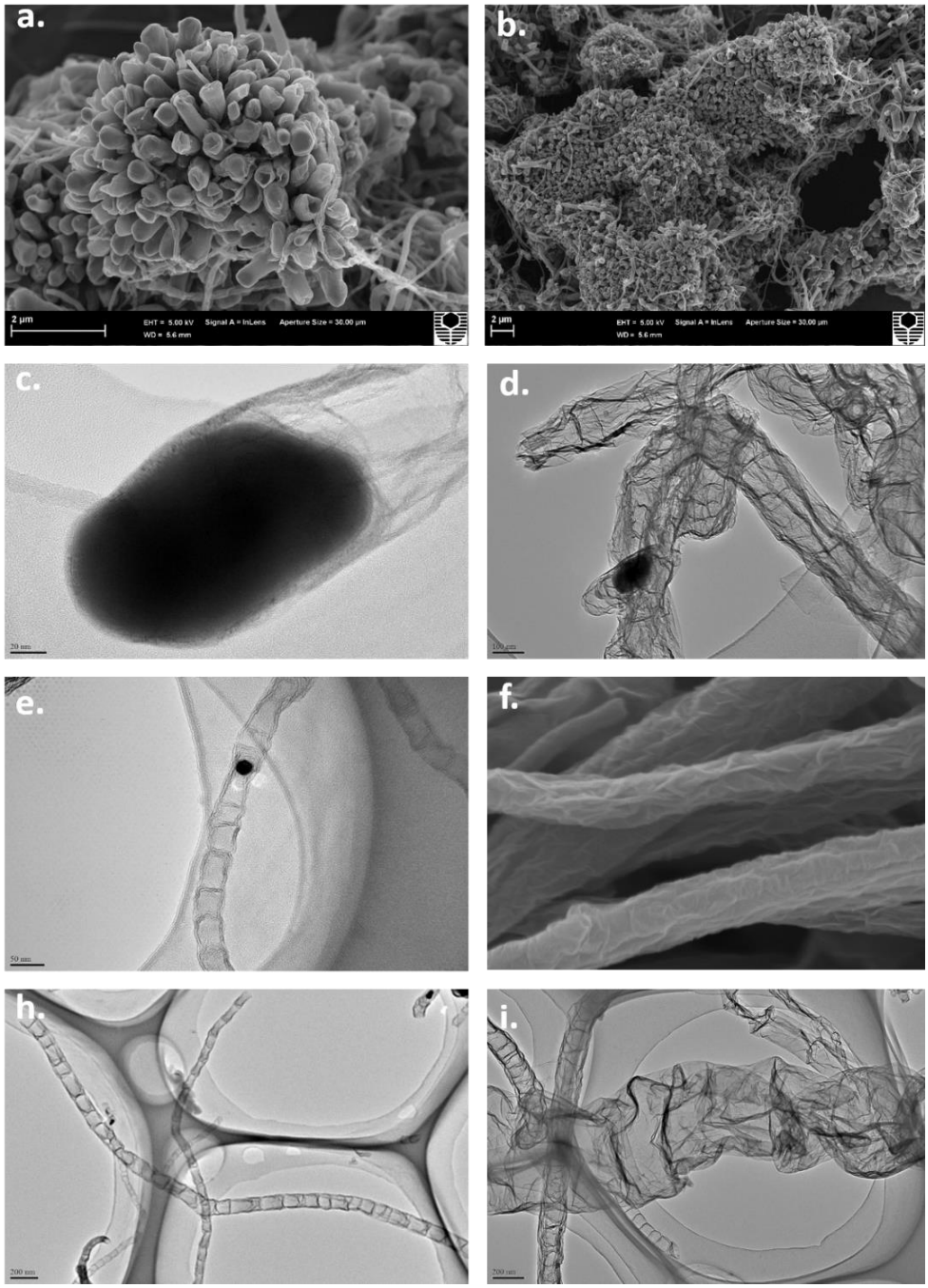

Figure 4.6 (a) Magnified SEM image of chrysanthemum-like Ni@NCNT-700. (b) Large scale SEM image of Ni@NCNT-700. (c) Magnified TEM image of Ni nanoparticle encapsulated at the carbon tube end, confirming tip-growing mechanism. (d) TEM image of Ni@NCNT-900, showing enhance surface roughness and increased tube wall thickness. (e) SEM image of a typical Ni nanoparticle encapsulated in the tube body. (f) SEM image of Ni@NCNT-800-3, showing a higher N doping level leads to greater surface roughness. (h) TEM image of a typical bamboo-like tube structure. (i) TEM image of Ni@NCNT-700 showing graphene like impurity appearance.

Table 6.1. Elemental analysis and detailed breakdown of N1s spectra of the as-synthesized catalysts.

	C (%)	N(%)	O(%)	Ni(%)	N1(%)	N2(%)	N3(%)	N4(%)
Ni@NCNT-800-1	91.44	5.77	2.12	0.68	52.28	32.74	9.86	5.12
Ni@NCNT-800-3	91.35	6.59	1.64	0.42	53.02	33.23	8.80	5.95
Ni@NCNT-800-5	87.78	7.66	3.70	0.86	56.52	30.61	8.08	4.79
Ni@NCNT-700-3	88.75	9.12	1.55	0.59	56.14	29.13	8.67	6.05
Ni@NCNT-900-3	92.02	5.16	2.29	0.53	48.72	36.35	10.38	4.55

The chemical composition and state of the nitrogen doped carbon nanotubes were analyzed by XPS. **Figure** 4.7 displays the XPS survey showing C 1s, N 1s, O 1s and Ni 2p spectra. The emergence of N 1s peak in all samples confirmed that nitrogen atoms were successfully doped into carbon catalysts. Moreover, the XPS element analysis shows the N doping levels are 9.12%, 6.59% and 5.15% in Ni@NCNT synthesized at 700, 800 and 900 ^{o}C, respectively, which are superior to many other reported approaches such as physical vapor deposition (PVD) of 3.5% and chemical vapor deposition (CVD) of 4%. [31, 44] The high nitrogen doping level also indicated that melamine as an excellent nitrogen precursor can efficiently incorporate nitrogen atoms into carbon nanotube network during the CNTs formation process. **Table** 6.1 shows the N doping levels in Ni@NCNTs at different synthesis conditions.

The chemical states of different types of N dopants were studied by high resolution of N1s spectrum in a specific range (392-408 eV). **Figure** 4.7(b) illustrates the N1s spectrum was deconvoluted into four types of N peaks at 398.9, 401.1, 402.7 and 405.2 eV, corresponding to pyridinic N (N at the edges of the graphene layers bonded to two carbon atoms), pyrrolic N (N in five-membered rings), graphitic N or quaternary N (N in six-membered rings within the graphene layers) and oxidized N, respectively. **Figure** 4.7(c) shows that the graphitic N content gradually increased from 8.67 to 10.38% with elevated temperature, 700 to 900 ^{o}C. This may

be due to the better thermal stability of graphitic N and the loss of unstable N at high temperature. [45-49] The oxygen and nickel contents in these samples are also listed in **Table** 6.1. All the samples represented a very low oxygen content due to pyrolysis in the inert gas atmosphere at a high temperature, which enables most of the oxygen containing groups to react with carbon to form CO_X. The thermal stability of the typical Ni@NCNT was investigated by TGA-DSC and a total of 32% of the initial weight was remaining which can be nickel compounds such as NiO and Ni_2O_3, at Ni content of roughly 22%.

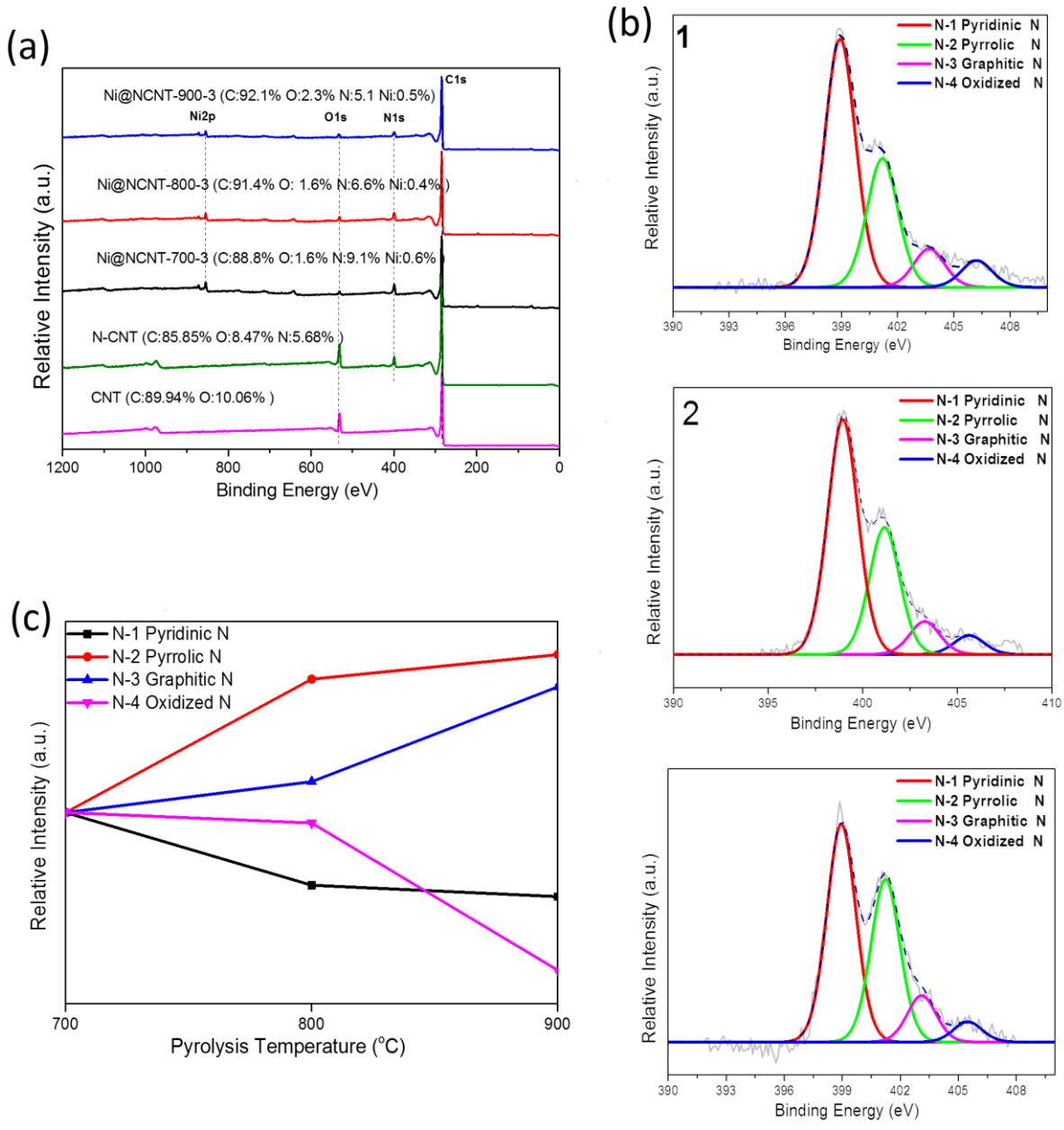

Figure 4.7 (a) XPS survey of Ni@NCNT-700, Ni@NCNT-800, Ni@NCNT-900, CNT and N-CNT. (b) N 1s scan of 1. Ni@NCNT-700, 2. Ni@NCNT-800 and 3. Ni@NCNT-900. (c) Density change of N components at different temperatures.

Figure 4.8 shows the BET specific surface areas and pore structure of the as-synthesized samples at various fabrication temperatures. All the samples demonstrated a type IV isotherm with a H3 hysteresis loop that gradually increases at low pressure followed by a sharp jump at half way, illuminating the mesoporous structure. [50] The hysteresis loop of each sample in **Figure** 4.8 (a) shows quite a similarity, Ni@NCNT-800-3 was slightly broader than the other two, suggesting a higher N doping content would create more defect sites and lead to a more porous structure with a greater surface area and pore volume. The catalysts fabricated at 700 ^{o}C had a smaller surface area (135 m^2/g) than 800 ^{o}C (155 m^2/g). But at 900 ^{o}C, the BET (145 m^2/g) declined due to the collapse and aggregation of carbon nanotube. The pore size distribution (PSD) of samples is displayed in **Figure** 4.8 (b), in which a sharp peak appears in all the three catalysts at 2.2 nm, indicating that the Ni@NCNTs are mostly composed of micropores (< 2 nm) and mesopores (2-50 nm).

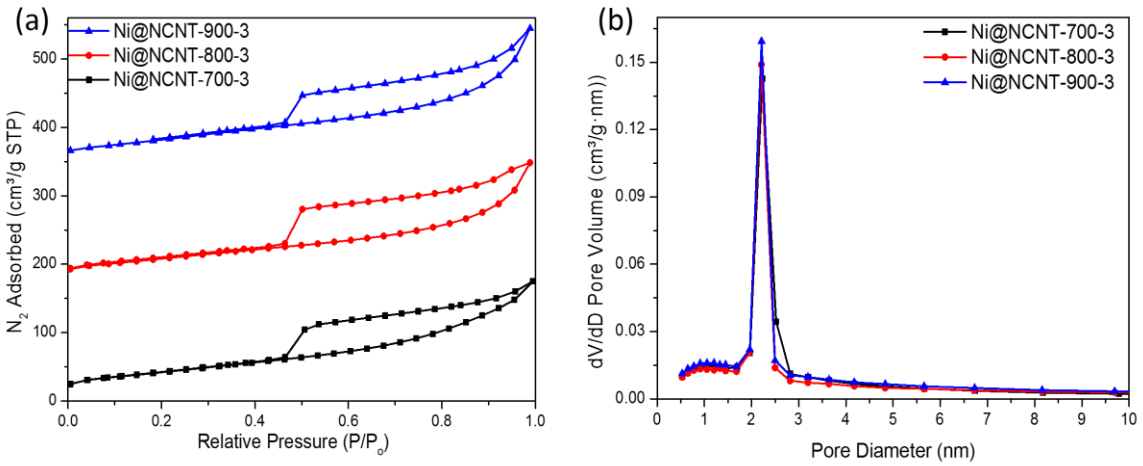

Figure 4.8 (a) Nitrogen sorption isotherms and (b) pore size distributions of Ni@NCNTs at various synthesising temperatures.

4.3.2 Catalytic SCP removal performance of carbon nanotubes

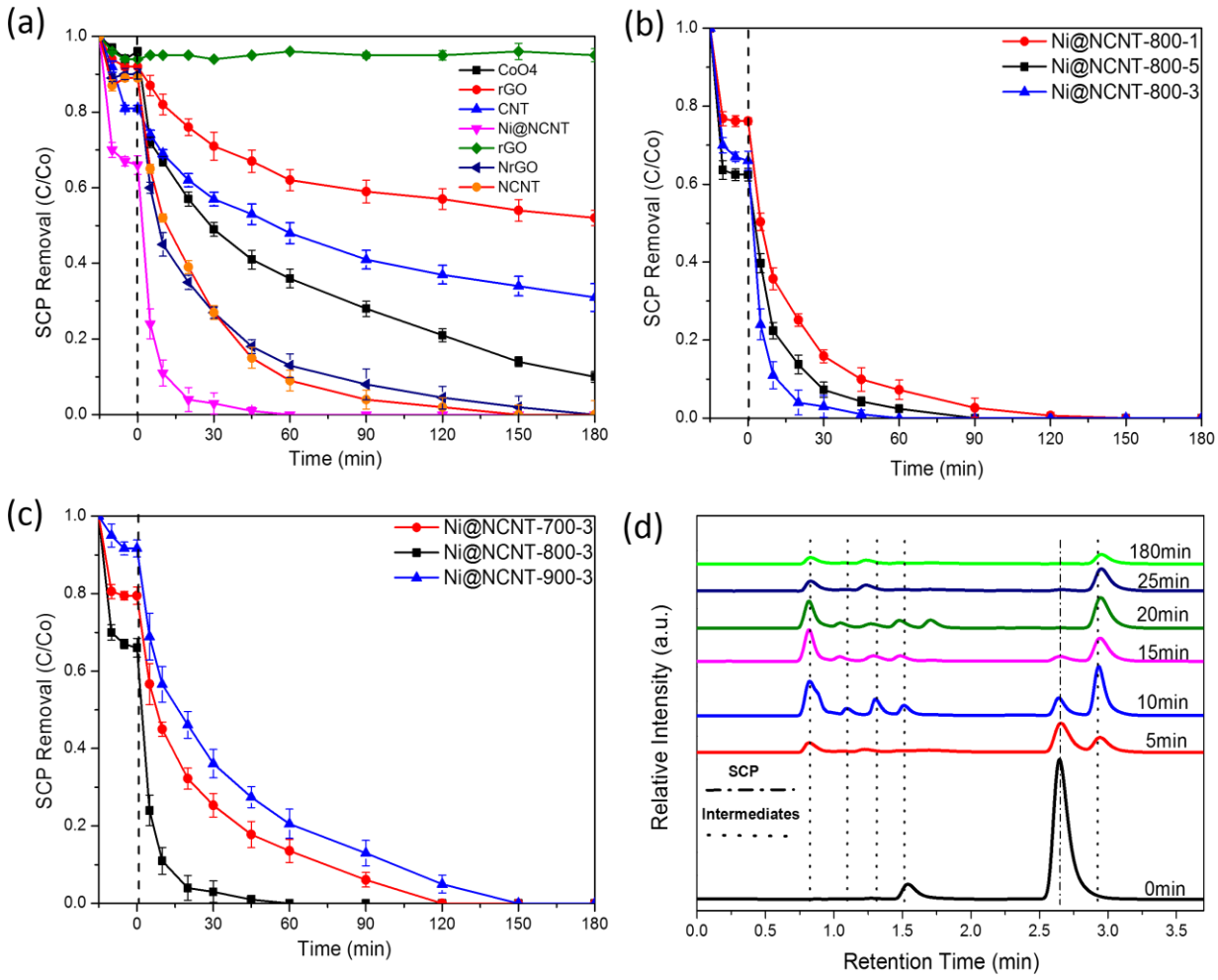

Figure 4.9 (a) PS activation over various catalysts. (b) Effect of nitrogen/nickel precursor loading of Ni@NCNT-800 on SCP removal. (c) Effect of catalyst fabrication temperature on SCP removal. (d) HPLC spectra of SCP degradation in a 180 min experiment. (Initial SCP concentration = 20 mg/L, catalyst loading = 0.2 g/L, PS concentration = 2 g/L, and temperature at 25 ^{o}C.)

Comparative studies of various carbocatalysts and metal oxides were firstly carried out in catalytic activation of PS for SCP oxidation in aqueous solutions. Before the PS was introduced into the solution, a 15-min pre-adsorption was performed in order to distinguish the SCP removal achieved by adsorption. When PS was added individually, a limited amount of SCP removal (< 5%) was reached, suggesting that PS could barely oxidize SCP compounds without catalytic activation. Both rGO and N-rGO showed low adsorption of SCP, however, the

catalysis of N-rGO was greater than rGO. As our previous studies demonstrated, N doping could remarkably improve the carbocatalytic activity by enhancing the π- π bond of the carbon matrix through the lonely pair of electrons of doped nitrogen atoms. [27, 30, 32] In this study, a similar case occurred. Comparing the catalysis on modified commercial CNT and as-prepared Ni@NCNT-800-3, the latter achieved 100% SCP oxidation efficiency within 1 h whereas the MWCNT only reached less than 35% of SCP removal, indicating the N doping induced catalytic enhancement. Moreover, Co_3O_4 as a typical metal based catalyst was employed to compare with the as-prepared Ni@NCNT on PS activation. **Figure** 4.9 (a) shows that Co_3O_4 presented a poor adsorption capacity and a moderate catalytic activity at 5% SCP adsorption and around 90% oxidation in 180 min, respectively, indicating that Ni@NCNT is more effective than the conventional metal oxide and other carbon catalysts for PS activation.

It is believed that a higher N doping level can lead to a more advanced catalysis.[51-53] **Figure** 4.9 **(b)** shows the effect of the nitrogen doping level on SCP removal. As shown in **Table** 6.1, the nitrogen contents for Ni@NCNT-800-1, Ni@NCNT-800-3 and Ni@NCNT-800-5 are 5.8, 6.6 and 7.7%, respectively. The 15-min pre-adsorption tests show that SCP adsorption capacities are 0.08, 0.11 and 0.13 mol g^{-1} for Ni@NCNT-800-1, Ni@NCNT-800-3 and Ni@NCNT-800-5, respectively. Interestingly, the catalytic ability, however, does not follow the adsorption capacity trend where the reaction rate increases in an order of Ni@NCNT-800-3> Ni@NCNT-800-5 > Ni@NCNT-800-1.

The catalysis of Ni@NCNTs was first improved when the nitrogen content increased from 5.8 to 6.6% and more nitrogen functional groups on the CNT surface would work as active sites. However, when the N doping reached its optimum level, a further increased N doping (7.7%) would cause destruction of graphitic network structure and deterioration of the catalyst activity instead.

The influence of pyrolysis temperature at 700, 800 and 900 ^{o}C on catalytic oxidation was investigated (**Figure** 4.9(c)). The adsorption capacity and catalytic oxidation of SCP of the three counterparts are in an order of Ni@NCNT-900-3 < Ni@NCNT-700-3 < Ni@NCNT-800-3, where Ni@NCNT-800-3 exhibited the best performance of complete decomposition of SCP in 60 min. This indicates that a higher pyrolysis temperature did not necessarily endow greater catalysis and adsorption. Moreover, SEM images showed that high annealing temperature can trigger the destruction and aggregation of carbon nanotubes, which might be a main reason for the deactivation of Ni@NCNT. The decay of the SCP during the oxidation process was monitored by UHPLC as illustrated in **Figure 4.9 (d)**. It can be seen that a well-defined SCP peak appeared at retention time (t_R) = 2.65 min and its peak intensity gradually decreased while a number of by-products were emerged during the oxidation process. To further investigate the mineralization of SCP oxidation, total organic carbon (TOC) was determined. The TOC trend chart is well aligning with UHPLC results that SCP was degreased rapidly in the first 30 min and then became relatively steady and achieved 78% of TOC removal in 180 min, indicating that most of the SCP and its intermediates were oxidized into harmless chemicals such as water and carbon dioxide.

4.3.3 Effects of several reaction parameters on SCP removal

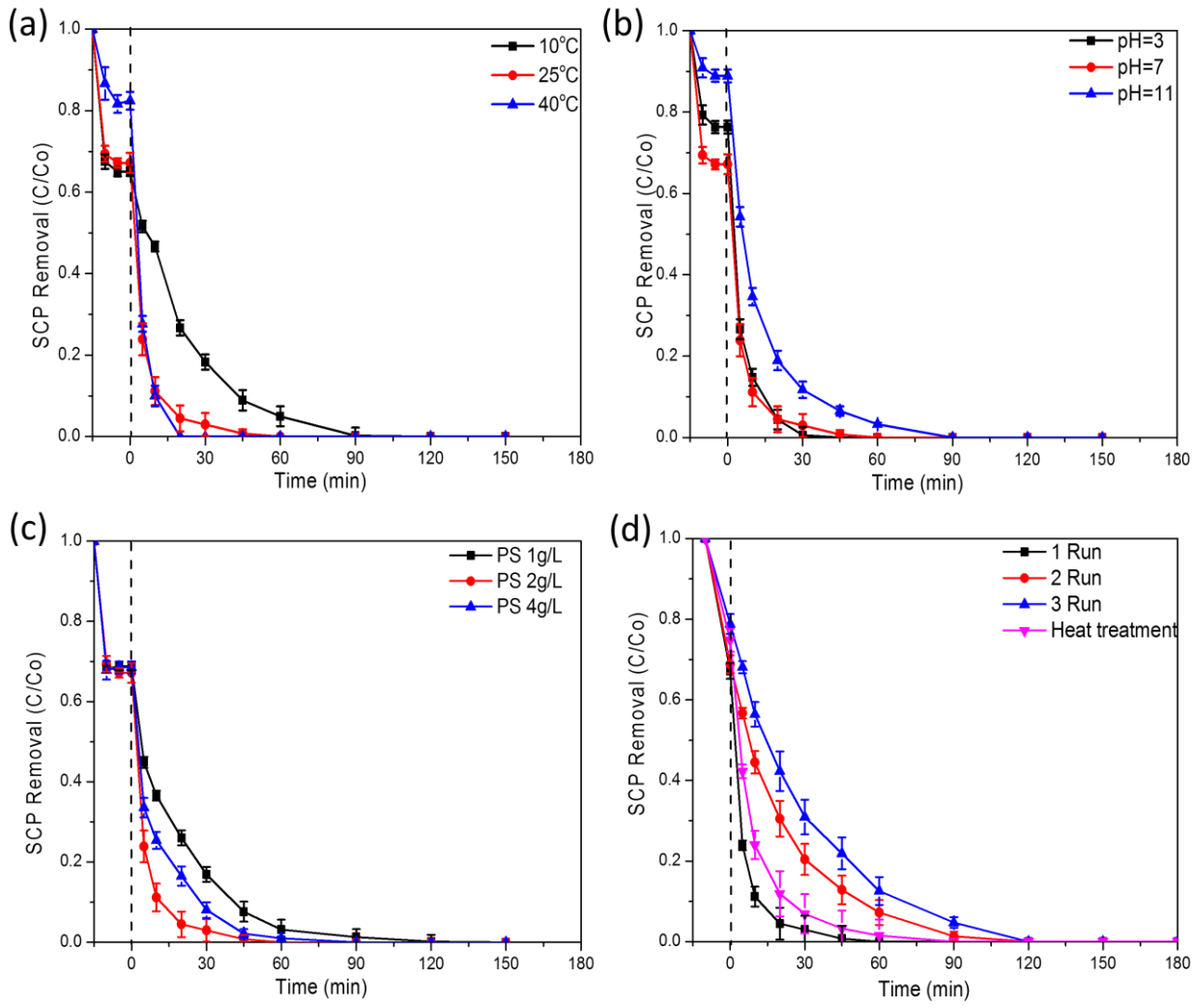

Figure 4.10 (a) Effect of reaction temperature on SCP removal. (b) Effect of reaction solution pH values on SCP removal. (c) Effect of PS loading on SCP removal. (d) Stability and reusability of Ni@NCNT-800-3. (Unless specific mentioned, initial SCP concentration = 20 mg/L, catalyst loading = 0.2 g/L, PS concentration = 2 g/L, and temperature at 25 ^{o}C.)

Figure 4.10 (a) displays the SCP removal by a synergetic effect of Ni@NCNT-800-3 adsorption and heterogeneous oxidation of PS in a temperature range of 10-40 ^{o}C. The change of the solution temperature had a noticeable effect on the adsorption of Ni@NCNT, in an order of 0.06 mol g^{-1} (40 ^{o}C) < 0.11 mol g^{-1} (25 ^{o}C) < 0.12 mol g^{-1} (10 ^{o}C), suggesting a better adsorption ability to SCP at a lower temperature. The complete SCP removal was obtained in

90, 60 and 20 min at 10, 25, and 40 °C, respectively. The reaction rate constants (**Table** 6.2) at different temperatures were well fitted by the first-order kinetics (Eq. 1) with great regression coefficient values (R^2 = 0.99) and the activation energy was calculated to be 37.9 kJ mol^{-1} according to the Arrhenius equation. The first order kinetic model is listed below:

$$\ln\left(\frac{C}{Co}\right) = kt \qquad (\textbf{Eq}.\ 6.1)$$

Where k is the reaction constant and C and C_o are the SCP concentrations at reaction time (t) =t and t=0, respectively.

Figure 4.10 (b) shows that Ni@NCNT-800-3 presented the best adsorption (0.11 mol g^{-1}) performance at pH = 7. When pH reached as high as 11, the adsorptive SCP removal dropped. Moreover, it is noted that a complete degradation of the antibiotic SCP was achieved in all three cases, depending on the various solution pH values. The reaction rate constants are k = 0.15, 0.09 and 0.07 min^{-1} for pH = 3, 7 and 11, respectively. The influence of PS loading on SCP degradation rate was studied in the range of 1-4 g L^{-1} (**Figure** 4.10 (c)). The change of the PS loading had an effect on the SCP oxidation reaction, the reaction rate constant k varied from 0.05 min^{-1} for 1 g L^{-1} to 0.09 and 0.07 min^{-1} for 2 and 4 g L^{-1}, respectively. Our previous studied have proven that the oxidation reaction rate is consistent with the increase of PS/PMS loading. However, a further adding of PS after the optimum concentration may cause self-quenching reaction, leading to reduced oxidation efficiency[54].

Table 4.2 Reaction rate constants and activation energy.

Temp °C	*Reaction rate constant: k(min^{-1})*	*Regression coefficients: R^2*	*E_a: Activation energy* kJ mol^{-1}
10	0.04	0.997	
25	0.09	0.997	37.9
40	0.21	0.999	

4.3.4 Stability tests

The stability and reusability of as-prepared Ni@NCNT and modified commercial CNT were tested by repeated SCP oxidation experiments and heat treatment at 350 ^{o}C in nitrogen atmosphere for 1 h. In **Figure** 4.10 (d), Ni@NCNT showed outstanding stability being able to achieve completely SCP decomposition in 120 min in all four tests, where the fresh catalyst completely degraded SCP in 60 min, and it will degrade SCP in 90 and 120 min for the second and third runs, respectively. What more stunning is, after ultrasonic cleaning and heat treatment, the sample catalysis was recovered showing almost equivalent catalytic ability to the fresh sample. Such good catalysis stability was comparable to or even better than some metal based catalysts. [55-57] The total organic carbon removal result shows the reusability of conventional MWCNT on PS activation for SCP degradation. It decomposed 70% SCP in 180 min in the first run, and the SCP decomposition efficiencies were 49% and 20% for the second and third runs, respectively. It can be inferred that the nickel encapsulation might be acting as supporting beans inside the nanotubes and prevent the catalyst from collapsing and destructing so that it could maintain good catalysis after numbers of usage. Moreover, the encapsulated Ni particles can accelerate the PS activation efficiency by transferring electrons from the inner Ni metals to the outer carbon tube walls. This effect can be largely conserved due to the carbon wall protection when the catalyst was reused successively.

4.3.5 EPR studies

In PS activation involved AOPs, it is well accepted that reactive radicals such as sulfate ($SO_4^{-\bullet}$) and hydroxyl radicals ($^{\bullet}OH$) are the predominant active species in attacking organic pollutants. [58-60] Herein, EPR was carried out to probe the detailed catalytic oxidation mechanism and identify the reactive species of Ni@NCNT activating PS for SCP degradation. A spin-trapping agent, 5, 5-dimethylpyrroline-oxide (DMPO), was employed to capture the free radicals in the activation reaction. **Figure** 4.11 (a) shows that no obvious radical peak was observed without

adding DMPO and strong characteristic signals of both $SO_4^{-\bullet}$ and $^{\bullet}OH$ were observed after DMPO introduction. It can be seen that Ni@NCNT was able to activate PS to generate a high intensity of hydroxyl radicals and relatively lower amount of sulfate radicals throughout the oxidation reaction. Duan *et al*. recently investigated PS activation on phenol oxidation and suggested persulfate molecules can mainly be activated and decomposed to produce $SO_4^{-\bullet}$, yet the generation of hydroxyl radicals were presumably attributed to oxidization of water molecules absorbed on carbocatlysts through a one electron transfer process. [60] The variation of free radical concentration versus time was depicted in **Figure** 4.11 (a). PS was able to produce a minor amount of radicals without introducing a catalyst, however, the intensities of radical peaks were largely enhanced after Ni@NCNT catalyst was added and reached the maximum in 10 min, which is well agreed with the change of SCP degradation rate. Moreover, both $SO_4^{-\bullet}$ and $^{\bullet}OH$ showed a minor receding after first 10 min, ascribed to the consumption of SCP oxidation, and then appeared no obvious change afterwards. This can be attributed to the outstanding catalytic ability and stability of Ni@NCNT that can continue to activate persulfate throughout the reaction. In lateral comparison among Ni@NCNT-800-1, Ni@NCNT-800-3 and Ni@NCNT-800-5, all the three catalysts displayed a similar change in radical concentration that increased first and started to reduce after reaching the maximum. In quenching tests, **Figure** 4.11 (b) shows that SCP removal efficiency was slightly decreased when ethanol was added at an ethanol/PS molar ratio of 500 and the degradation efficiency kept reducing with increasing addition of ethanol. Interestingly, the SCP solution was still able to reach complete removal in 180 min when the aqueous solution was completely replaced by ethanol, suggesting occurrence of non-radical reactions. In our previous studies, a series of catalysts were carried out on controlled quenching experiments, cobalt oxide (Co_3O_4) and carbon nanotubes (CNT) were showing harsh catalytic decreasing after ethanol was presented in the solution and the organic degradation was totally prevented when all water was substituted

to ethanol. [30] In contrast, nitrogen doped carbon nanotubes (N-CNT) displayed a minor influence from ethanol and maintained good oxidation efficiency even in ethanol solution. It was reported that the sp^2 carbon network can be activated for a better catalytic activity through conjugation with the lone-pair electrons of N atoms, thus, the activated electrons would work together with PS to react with the adsorbed SCP molecules. [34] [26] As a result, the co-existing radical and non-radical reactions in Ni@NCNT/PS system would accelerate the completion of SCP decomposition. From the experiments above and the previous studies, the possible mechanism of Ni@NCNT/PS activation system is illustrated in **Figure** 5.12.

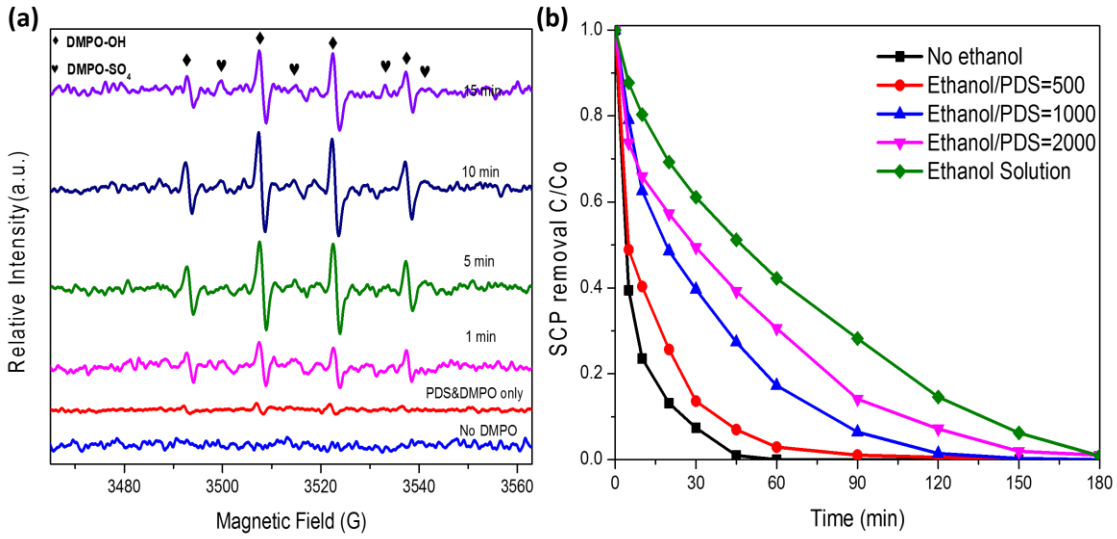

Figure 4.11 (a) EPR spectra of PS activation with Ni@NCNT-800-3 different time intervals. (b) Effect of radical quenching on SCP degradation.

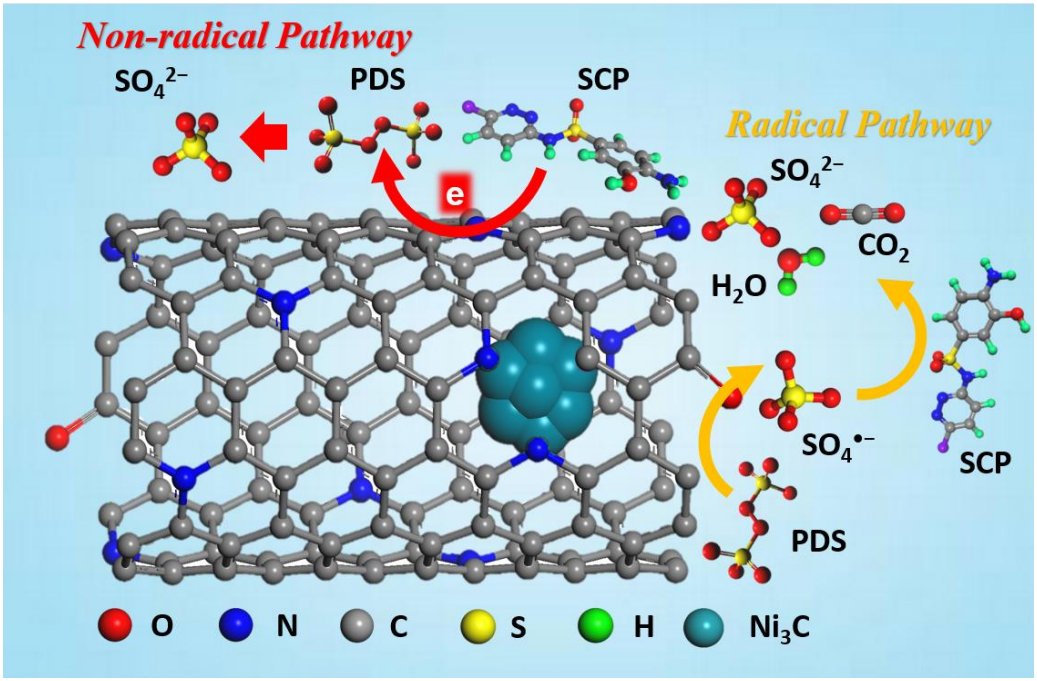

Figure 4.12 Possible reaction mechanism for organic SCP oxidation by the Ni@NCNT/PS system.

4.4 Conclusions

Ni@NCNT was synthesized by a simple pyrolysis method. The fabrication conditions such as pyrolysis temperature and N precursor loading were closely related to the morphologies and catalysis of Ni@NCNT. It was observed that the Ni@NCNT was optimally prepared at 800 ^{o}C showing the most well-defined regular bamboo-like configuration and outstanding catalysis. The heterogeneous system of Ni@NCNT and PS was applied for SCP removal, showing efficient adsorption capacity and oxidation efficiency. The effects of reaction temperature, solution pH, PS dosage on the reaction were in detail investigated, indicating the oxidation reaction was effective in a wide pH range and could be improved by increasing reaction temperature and PS amount at a controlled level. The mechanistic study demonstrated that the promoted adsorption and catalytic performances of Ni@NCNT could be attributed to the unique nanotube morphology and the doping of nitrogen atoms, which acted as active sites for both the SCP adsorption and PS activation. In addition, the synergistic effect of N doping and

Ni encapsulation enables Ni@NCNT to present an excellent stability for reuse. The mechanistic insight of catalytic reaction for PS activation was investigated by EPR and quenching experiments, showing that radical ($SO_4^{-\bullet}$ and $^{\bullet}OH$) and non-radical reactions were involved in the activation processes.

4.5 References

[1] S.D. Richardson, S.Y. Kimura, Water Analysis: Emerging Contaminants and Current Issues, Anal. Chem., 88 (2016) 546-582.

[2] B. Sun, M. Sato, J.S. Clements, Oxidative Processes Occurring When Pulsed High Voltage Discharges Degrade Phenol in Aqueous Solution, Environ. Sci. Technol., 34 (2000) 509-513.

[3] S.A. Snyder, P. Westerhoff, Y. Yoon, D.L. Sedlak, Pharmaceuticals, Personal Care Products, and Endocrine Disruptors in Water: Implications for the Water Industry, Environ. Eng. Sci., 20 (2003) 449-469.

[4] F.C. Cabello, Heavy use of prophylactic antibiotics in aquaculture: a growing problem for human and animal health and for the environment, Environ. Microbiol., 8 (2006) 1137-1144.

[5] H. Gold, Anthrax: A review of sixty cases, with a report on the therapeutic use of sulfonamide compounds, Arch. Inter. Med., 70 (1942) 785-821.

[6] R. F.Bevill, Sulfonamide residues in domestic animals, Journal of Veterinary Pharmacology and Therapeutics, 12 (1989) 241-252.

[7] K. Kümmerer, Significance of antibiotics in the environment, J. Anti. Chem., 52 (2003) 5-7.

[8] A. Göbel, C.S. McArdell, M.J.F. Suter, W. Giger, Trace Determination of Macrolide and Sulfonamide Antimicrobials, a Human Sulfonamide Metabolite, and Trimethoprim in Wastewater Using Liquid Chromatography Coupled to Electrospray Tandem Mass Spectrometry, Anal. Chem., 76 (2004) 4756-4764.

[9] F. Ingerslev, B. Halling-Sørensen, Biodegradability properties of sulfonamides in activated sludge, Environ. Tox. Chem., 19 (2000) 2467-2473.

[10] W. Baran, E. Adamek, J. Ziemiańska, A. Sobczak, Effects of the presence of sulfonamides in the environment and their influence on human health, J. Hazar. Mat., 196 (2011) 1-15.

[11] A. Göbel, C.S. McArdell, A. Joss, H. Siegrist, W. Giger, Fate of sulfonamides, macrolides, and trimethoprim in different wastewater treatment technologies, Science of The Total Environment, 372 (2007) 361-371.

[12] A. Joss, E. Keller, A.C. Alder, A. Göbel, C.S. McArdell, T. Ternes, H. Siegrist, Removal of pharmaceuticals and fragrances in biological wastewater treatment, Water Res., 39 (2005) 3139-3152.

[13] Y. Yang, J.J. Pignatello, J. Ma, W.A. Mitch, Comparison of Halide Impacts on the Efficiency of Contaminant Degradation by Sulfate and Hydroxyl Radical-Based Advanced Oxidation Processes (AOPs), Environ. S. Technol., 48 (2014) 2344-2351.

[14] E. Neyens, J. Baeyens, A review of classic Fenton's peroxidation as an advanced oxidation technique, J. Haz. Mat., 98 (2003) 33-50.

[15] S. Wang, A Comparative study of Fenton and Fenton-like reaction kinetics in decolourisation of wastewater, Dyes and Pigments, 76 (2008) 714-720.

[16] L. Hu, X. Yang, S. Dang, An easily recyclable Co/SBA-15 catalyst: Heterogeneous activation of peroxymonosulfate for the degradation of phenol in water, App. Catal., B, 102 (2011) 19-26.

[17] S.B. Hammouda, F. Zhao, Z. Safaei, V. Srivastava, D. Lakshmi Ramasamy, S. Iftekhar, S. kalliola, M. Sillanpää, Degradation and mineralization of phenol in aqueous medium by heterogeneous monopersulfate activation on nanostructured cobalt based-perovskite catalysts ACoO3 (A=La, Ba, Sr and Ce): Characterization, kinetics and mechanism study, App. Catal., B, 215 (2017) 60-73.

[18] G.P. Anipsitakis, D.D. Dionysiou, Degradation of Organic Contaminants in Water with Sulfate Radicals Generated by the Conjunction of Peroxymonosulfate with Cobalt, Environ. Sci. Technol., 37 (2003) 4790-4797.

[19] Y. Wang, H. Sun, H.M. Ang, M.O. Tadé, S. Wang, 3D-hierarchically structured MnO2 for catalytic oxidation of phenol solutions by activation of peroxymonosulfate: Structure dependence and mechanism, App. Catal., B, 164 (2015) 159-167.

[20] E. Saputra, S. Muhammad, H. Sun, H.M. Ang, M.O. Tadé, S. Wang, Different Crystallographic One-dimensional MnO2 Nanomaterials and Their Superior Performance in Catalytic Phenol Degradation, Environ. Sci. Technol., 47 (2013) 5882-5887.

[21] P. Hu, M. Long, Cobalt-catalyzed sulfate radical-based advanced oxidation: A review on heterogeneous catalysts and applications, Applied Catalysis B: Environmental, 181 (2016) 103-117.

[22] P. Hu, M. Long, X. Bai, C. Wang, C. Cai, J. Fu, B. Zhou, Y. Zhou, Monolithic cobalt-doped carbon aerogel for efficient catalytic activation of peroxymonosulfate in water, J Haz. Mat., 332 (2017) 195-204.

[23] S. Wang, H. Sun, H.M. Ang, M.O. Tadé, Adsorptive remediation of environmental pollutants using novel graphene-based nanomaterials, Chem. Eng. J., 226 (2013) 336-347.

[24] T. Liu, Y. Li, Q. Du, J. Sun, Y. Jiao, G. Yang, Z. Wang, Y. Xia, W. Zhang, K. Wang, H. Zhu, D. Wu, Adsorption of methylene blue from aqueous solution by graphene, Colloid. Surface. B, 90 (2012) 197-203.

[25] D. Lin, B. Xing, Adsorption of Phenolic Compounds by Carbon Nanotubes: Role of Aromaticity and Substitution of Hydroxyl Groups, Environ. Sci. Technol., 42 (2008) 7254-7259.

[26] W. Tian, H. Zhang, X. Duan, H. Sun, M.O. Tade, H.M. Ang, S. Wang, Nitrogen- and Sulfur-Codoped Hierarchically Porous Carbon for Adsorptive and Oxidative Removal of Pharmaceutical Contaminants, ACS App. Mater. Inter., 8 (2016) 7184-7193.

[27] X. Duan, Z. Ao, H. Sun, S. Indrawirawan, Y. Wang, J. Kang, F. Liang, Z.H. Zhu, S. Wang, Nitrogen-Doped Graphene for Generation and Evolution of Reactive Radicals by Metal-Free Catalysis, ACS App. Mater. Inter., 7 (2015) 4169-4178.

[28] Y. Wang, H. Sun, X. Duan, H.M. Ang, M.O. Tadé, S. Wang, A new magnetic nano zero-valent iron encapsulated in carbon spheres for oxidative degradation of phenol, App. Catal. B, 172-173 (2015) 73-81.

[29] H. Sun, Y. Wang, S. Liu, L. Ge, L. Wang, Z. Zhu, S. Wang, Facile synthesis of nitrogen doped reduced graphene oxide as a superior metal-free catalyst for oxidation, Chem. Com., 49 (2013) 9914-9916.

[30] X. Duan, H. Sun, Y. Wang, J. Kang, S. Wang, N-Doping-Induced Nonradical Reaction on Single-Walled Carbon Nanotubes for Catalytic Phenol Oxidation, ACS Catalysis, 5 (2015) 553-559.

[31] K. Gong, F. Du, Z. Xia, M. Durstock, L. Dai, Nitrogen-Doped Carbon Nanotube Arrays with High Electrocatalytic Activity for Oxygen Reduction, Science, 323 (2009) 760-764.

[32] J. Kang, X. Duan, L. Zhou, H. Sun, M.O. Tadé, S. Wang, Carbocatalytic activation of persulfate for removal of antibiotics in water solutions, Chem. Eng. J., 288 (2016) 399-405.

[33] X. Duan, H. Sun, J. Kang, Y. Wang, S. Indrawirawan, S. Wang, Insights into Heterogeneous Catalysis of Persulfate Activation on Dimensional-Structured Nanocarbons, ACS Cat., 5 (2015) 4629-4636.

[34] X. Duan, Z. Ao, L. Zhou, H. Sun, G. Wang, S. Wang, Occurrence of radical and nonradical pathways from carbocatalysts for aqueous and nonaqueous catalytic oxidation, App. Catal. B, 188 (2016) 98-105.

[35] Y. Wang, S. Indrawirawan, X. Duan, H. Sun, H.M. Ang, M.O. Tadé, S. Wang, New insights into heterogeneous generation and evolution processes of sulfate radicals for phenol degradation over one-dimensional α-MnO2 nanostructures, Chem. Eng. J., 266 (2015) 12-20.

[36] L. Qu, Y. Liu, J.-B. Baek, L. Dai, Nitrogen-Doped Graphene as Efficient Metal-Free Electrocatalyst for Oxygen Reduction in Fuel Cells, ACS Nano, 4 (2010) 1321-1326.

[37] A. Ul-Hamid, A. Quddus, H. Saricimen, H. Dafalla, Corrosion Behavior of Coarse- and Fine-Grain Ni Coatings Incorporating NaH2PO4.H2O Inhibitor Treated Substrates, Mater. Res., 18 (2015) 20-26.

[38] Y. Koltypin, A. Fernandez, T.C. Rojas, J. Campora, P. Palma, R. Prozorov, A. Gedanken, Encapsulation of Nickel Nanoparticles in Carbon Obtained by the Sonochemical Decomposition of Ni(C8H12)2, Chem. Mater., 11 (1999) 1331-1335.

[39] J. Yuan, Y. Zhu, L. Li, Highly efficient bimetal synergetic catalysis by a multi-wall carbon nanotube supported palladium and nickel catalyst for the hydrogen storage of magnesium hydride, Chem. Commun., 50 (2014) 6641-6644.

[40] M.A. Pimenta, G. Dresselhaus, M.S. Dresselhaus, L.G. Cancado, A. Jorio, R. Saito, Studying disorder in graphite-based systems by Raman spectroscopy, Phys. Chem. Chem. Phys., 9 (2007) 1276-1290.

[41] C. Cong, T. Yu, H. Wang, Raman Study on the G Mode of Graphene for Determination of Edge Orientation, ACS Nano, 4 (2010) 3175-3180.

[42] W.H. Organization, Guidelines for drinking-water quality - Volume 1: Recommendations, 2008.

[43] C.H. Kiang, M. Endo, P.M. Ajayan, G. Dresselhaus, M.S. Dresselhaus, Size Effects in Carbon Nanotubes, Physical Review Letters, 81 (1998) 1869-1872.

[44] R. Sen, B. C. Satishkumar, A. Govindaraj, K. R. Harikumar, M. K. Renganathan, C. N. R. Rao, Nitrogen-containing carbon nanotubes, Journal of Materials Chemistry, 7 (1997) 2335-2337.

[45] Z.-H. Sheng, L. Shao, J.-J. Chen, W.-J. Bao, F.-B. Wang, X.-H. Xia, Catalyst-Free Synthesis of Nitrogen-Doped Graphene via Thermal Annealing Graphite Oxide with Melamine and Its Excellent Electrocatalysis, ACS Nano, 5 (2011) 4350-4358.

[46] D. Deng, X. Pan, L. Yu, Y. Cui, Y. Jiang, J. Qi, W.-X. Li, Q. Fu, X. Ma, Q. Xue, G. Sun, X. Bao, Toward N-Doped Graphene via Solvothermal Synthesis, Chemistry of Materials, 23 (2011) 1188-1193.

[47] J. Long, X. Xie, J. Xu, Q. Gu, L. Chen, X. Wang, Nitrogen-Doped Graphene Nanosheets as Metal-Free Catalysts for Aerobic Selective Oxidation of Benzylic Alcohols, ACS Catalysis, 2 (2012) 622-631.

[48] X. Li, H. Wang, J.T. Robinson, H. Sanchez, G. Diankov, H. Dai, Simultaneous Nitrogen Doping and Reduction of Graphene Oxide, Journal of the American Chemical Society, 131 (2009) 15939-15944.

[49] K. Kinoshita, Carbon: electrochemical and physicochemical properties, John Wiley Sons,New York, NY; None1988.

[50] J. Lee, J. Kim, T. Hyeon, Recent Progress in the Synthesis of Porous Carbon Materials, Advanced Materials, 18 (2006) 2073-2094.

[51] J. Zhang, X. Liu, R. Blume, A. Zhang, R. Schlögl, D.S. Su, Surface-Modified Carbon Nanotubes Catalyze Oxidative Dehydrogenation, Science, 322 (2008) 73-77.

[52] G. Zhong, H. Wang, H. Yu, F. Peng, Nitrogen doped carbon nanotubes with encapsulated ferric carbide as excellent electrocatalyst for oxygen reduction reaction in acid and alkaline media, J. Power Sources, 286 (2015) 495-503.

[53] B. Frank, J. Zhang, R. Blume, R. Schlögl, D.S. Su, Heteroatoms Increase the Selectivity in Oxidative Dehydrogenation Reactions on Nanocarbons, Angew. Chem. Int. Edit., 48 (2009) 6913-6917.

[54] P.R. Shukla, S. Wang, H. Sun, H.M. Ang, M. Tadé, Activated carbon supported cobalt catalysts for advanced oxidation of organic contaminants in aqueous solution, App. Catal. B, 100 (2010) 529-534.

[55] P. Shukla, H. Sun, S. Wang, H.M. Ang, M.O. Tadé, Co-SBA-15 for heterogeneous oxidation of phenol with sulfate radical for wastewater treatment, Catal. Today, 175 (2011) 380-385.

[56] P. Shukla, H. Sun, S. Wang, H.M. Ang, M.O. Tadé, Nanosized Co3O4/SiO2 for heterogeneous oxidation of phenolic contaminants in waste water, Sep.Purif. Technol., 77 (2011) 230-236.

[57] Y. Wang, H. Sun, H.M. Ang, M.O. Tadé, S. Wang, Magnetic Fe3O4/carbon sphere/cobalt composites for catalytic oxidation of phenol solutions with sulfate radicals, Chem. Eng. Journal, 245 (2014) 1-9.

[58] Y. Ji, C. Ferronato, A. Salvador, X. Yang, J.-M. Chovelon, Degradation of ciprofloxacin and sulfamethoxazole by ferrous-activated persulfate: Implications for remediation of groundwater contaminated by antibiotics, Sci. Total Environ., 472 (2014) 800-808.

[59] Y. Ji, Y. Fan, K. Liu, D. Kong, J. Lu, Thermo activated persulfate oxidation of antibiotic sulfamethoxazole and structurally related compounds, Water Res., 87 (2015) 1-9.

[60] X. Duan, C. Su, L. Zhou, H. Sun, A. Suvorova, T. Odedairo, Z. Zhu, Z. Shao, S. Wang, Surface controlled generation of reactive radicals from persulfate by carbocatalysis on nanodiamonds, App. Catal. B, 194 (2016) 7-15.

Chapter 5: Nickel in hierarchically structured nitrogen-doped graphene for robust and promoted degradation of antibiotics

This chapter has been published on journal "Journal of Cleaner Production", DOI: 10.1016/j.jclepro.2019.01.323.

Abstract

Nickel nanoparticles encapsulated in nitrogen-doped porous graphene (Ni@NPG) were synthesized through a one-pot method as a novel material for catalytic activation of persulfate (PS). The Ni@NPG catalysts were evaluated for adsorptive and catalytic removals of antibiotic sulfachloropyridazine (SCP) as an emerging pollutant. Ni@NPG exhibits excellent adsorption and catalysis with 100% SCP removal from water in only 30 min. Meanwhile, great stability and reusability can be achieved with satisfactory organic degradation after 4 successive runs. In addition, the metal leaching was prohibited from metal@carbon catalysts due to the protection of carbon walls. The influences of humid acid and inorganic anions (HCO_3^-, Cl^-, Br^- and $H_2PO_4^-$) on SCP degradation at various concentrations were further investigated and the present study shows that all these species promoted the SCP degradation at a low concentration whereas an inhibition effect occurred at higher concentrations due to radical quenching. Electron paramagnetic resonance (EPR) and quenching experiments reveal the PS activation mechanism involving generation of $SO_4^{\bullet-}$, $^{\bullet}OH$ and $^{\bullet}O_2^-$ without singlet oxygen. The synergistic effect of radical and nonradical pathway played crucial roles during the SCP oxidation process.

5.1 Introduction

The great advances in human therapy and animal husbandry/aquaculture have significantly increased the use and production of sulfonamide antibiotics in pharmaceuticals and personal care products (PPCPs)[1]. However, in recent decades, the occurrence of different antibiotics in natural aquatic environment has raised increasing concerns on their potentially adverse ecological effects, for example, bacterial drug resistance and microflora disorder [2-4]. Currently, sulfonamides are detected at a trace level in water body or soils, nevertheless, these organics are non-biodegradable and reluctant to be completely removed in the ecosystem [5, 6]. A number of technologies have been established to remove sulfonamides, such as adsorption [7, 8], oxidation [9], and membrane filtration [10].

Recently, advanced oxidation processes (AOPs) have received considerable attention due to the great capability for complete decomposition of organic contaminants [11, 12]. Fenton reaction using hydroxyl radicals ($^{\bullet}OH$) from Fe^{2+}/H_2O_2 is able to oxidize a wide range of hazardous pollutants [13]. However, the inherent limitations such as strict pH requirement (~ 3), low stability of the chemicals, and inevitable introduction of metal ions have restricted the green and sustainable strategy for large-scale industrial applications. More recently, sulfate radicals ($SO_4^{\bullet-}$) based advanced oxidation processes (SR-AOPs) using peroxymonosulfate (PMS) or persulfate (PS) salts have emerged as a promising alternative owing to the higher redox potential of $SO_4^{\bullet-}$ (2.5-3.1 V vs 2.7 V of $^{\bullet}OH$) and wider pH range tolerance [12, 14, 15].

Previously, metal-based oxides were usually employed, but they suffered from metal leaching and secondary pollution. Recently, nanocarbons (graphene, carbon nanotubes, and nanodiamonds) as metal-free carbocatalysts have been utilized for environmental remediation by SR-AOPs. [16-18] In addition, peer studies found that heteroatom doping with N, B, S or P not only could modulate the graphitic carbon frameworks to create more active sites, but also triggered a nonradical pathway for PMS/PS activation [19-21]. Moreover, a porous framework of

carbon materials provides large accessible surface areas for both adsorption and catalytic reaction, further enhancing the catalytic activity [22, 23]. However, metal-free carbocatalysts presented less activity and stability than metal oxides. Therefore, a new material with integration of metal/metal-oxide and porous nanocarbon will provide advantages to overcome the issues in SR-AOPs.

This study reports a direct pyrolysis approach for one-pot preparation of nitrogen-doped graphene with a hierarchically porous structure and nickel encapsulation (Ni@NPG) and its performance in adsorptive and oxidative removal of sulfonamide antibiotic sulfachloropyridazine (SCP) in catalytic activation of persulfate. It was found that the synergistic effect of nitrogen doping and Ni nanoparticle encapsulation within a carbocatalyst endowed Ni@NPG with unique properties such as the accelerated electron transfer and magnetic property, which demonstrated superior catalytic performances on PS activation to the counterparts such as GO, rGO and NiO. In addition, taking the advantage of the magnetic property of Ni@NPG, it can be readily recycled magnetically for reuse and regeneration, which addresses the recycling issue in carbon-based AOPs. The mechanism of PS activation with Ni@NPG was explored at the co-existence of natural organic matters and/or versatile inorganic ions in the novel oxidative system. This study dedicates to providing a robust and green nanocarbon catalyst for environmental remediation as well as insights into persulfate activation.

5.2 Experimental

5.2.1 Materials

Urea (CH_4N_2O, > 99.0%), nickel chloride ($NiCl_2 \cdot 6H_2O$, >99.9%), potassium peroxymonosulfate ($2KHSO_5 \cdot 3KHSO_4 \cdot K_2SO_4$, Oxone®), peroxydisulfate (PS), sodium azide (NaN_3), p-benzoquinone (PBQ), and 5, 5-dimethylpyrroline-oxide (DMPO, >99.0%), and 2, 2, 6, 6-tetramethyl-4-piperidinol (TMP, 99.0%) were purchased from Sigma-Aldrich, Australia.

Sulfachloropyridazine (SCP, >99.0%), ethanol and nitric acid (73.0%) were obtained from Chem-Supply, Australia. High purity nitrogen gas (99.999%) was obtained from BOC. Ultrapure water was used in all the experiments. All the chemicals are of analytical grade and were used as received without any further purification.

5.2.2 Preparation of Carbocatalysts

In a typical synthesis procedure, 0.1 mol (6 g) of urea (CH_4N_2O), as the carbon and nitrogen precursor, was dissolved in 50 mL of ultrapure water and stirred to form a homogeneous solution. Then, 0.1 mol (24 g) $NiCl_2 \cdot 6H_2O$ as the nickel source was introduced to the solution to form a greenish homogeneous solution with continuously stirring for 24 h at 70 ^oC. A gel-like solution was then obtained and dried in an oven at 60 ^oC for a week to remove the moisture. Subsequently, the sample was ground into fine powders, and then the resulting greenish sample was annealed in a tube furnace at 1000 ^oC with a heating rate of 5 ^oC/min and held for 1 h under the flowing argon to obtain the porous nitrogen-doped graphene with encapsulated nickel particles ($Ni@NPG^{raw}$, 2.8 g), with a yield of 15.1%. The sample was cooled down to room temperature naturally in argon atmosphere. Finally, the resulting products were washed with 100 mL of concentrated nitric acid under vigorous stirring for 6 h to remove the superficial Ni particles, and then with excessive ethanol and ultrapure water for several times until the pH of filtrate reached 7. The final product was 1.1 g with a yield of 5.4%. The final sample obtained was labelled as Ni@NPG and the scheme for the whole process of Ni@NPG synthesis is illustrated in **Figure 5.1**.

The synthesis methods of GO and N-rGO and the modification of commercial CNT were reported in our previous papers. [19]

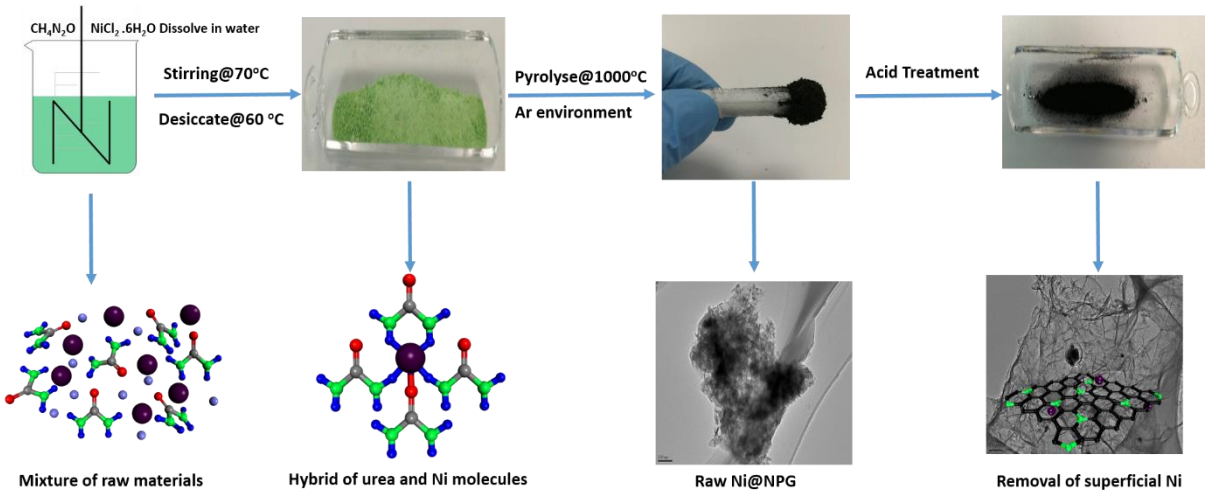

Figure 5.1 Schematic illustration of the Ni@NPG catalyst preparation.

5.2.3 Characterizations of Carbon Materials

The morphologies of the synthesized materials were investigated by transmission electron microscopy (TEM; JEOL 2100) and scanning electron microscopy (SEM, Zeiss Neon 40EsV FIBSEM). The crystal phases of the samples were evaluated by X-ray diffraction on a D8-Advanced diffractometer system from Bruker with Cu Kα radiation (λ = 1.5418 Å). Raman spectra were obtained on an ISA argon-laser Raman spectrometer. Thermogravimetric-differential thermal analysis (TG-DTA) was performed on a PerkinElmer Diamond thermal analyzer within a temperature range of 25 - 800 °C at a heating rate of 10 °C/min in air. X-ray photoelectron spectroscopy (XPS) was performed on a Thermo Escalab 250 system using an Al Kα X-ray source to detect the surface elemental compositions of carbon materials. A Perkin-Elmer Diamond TGA/DTA thermal analyzer was utilized to perform thermogravimetric-differential thermal analysis (TG-DTA) via heating the samples in an air flow of 100 mL min^{-1} at a heating rate of 10 °C min^{-1}. The specific surface area and pore-size distribution of the samples were evaluated by N_2 sorption isotherms at −196 °C with the Brunauer−Emmett−Teller (BET) and Barrett−Joiner−Halenda (BJH) methods, respectively, on a Micrometics TriStar 3000 instrument. The samples were degassed under vacuum conditions at 110 °C for 6 h and refilled with helium to expel the surface adsorbed gases and moisture

before the test. The Bruker EMS-plus electron paramagnetic resonance (EPR) was applied to in situ probe the generated free radicals produced by PS activation and captured by trapping agents of 5,5-dimethylpyrroline-oxide (DMPO) and 2,2,6,6-tetramethyl-4-piperidinol (TMP). The EPR tests were performed with a centre field of 3515 G, sweep width of 100 G, power setting of 18.75 mW, microwave frequency of 9.86 GHz and scan number of 5. The quantitative information was analyzed by the spin-fitting package of Bruker Xeon software.

5.2.4 Adsorption and Catalytic Oxidation Procedures

Kinetic adsorption of SCP was tested in a 500 mL conical flask with a SCP solution (20 ppm). The catalyst (0.05 g L^{-1}) was dispersed into the solution under continuous stirring (300 rpm) in a temperature controlled water bath. At set time intervals, 1 mL of the solution was withdrawn by a syringe and filtered through a 0.45 μm Millipore film into a vial. The SCP concentration was analyzed on an ultrahigh performance liquid chromatography (UHPLC). The organics were separated by a C-18 column and analyzed by a UV detector (270 nm). The mobile phase was made of 30% methanol and 70% 3 mM acetic acid at a flow rate of 0.3 mL min^{-1}. The catalytic oxidation of SCP was carried out in a similar experiment to the adsorption test except that PS (2 g L^{-1}) was added with the catalyst simultaneously to initiate the reaction. In the case of catalytic activity comparison with other catalysts, a 30 min of pre-adsorption was run to subtract the adsorption effect on the total SCP removal rate. The filtered reaction solution was mixed with 0.5 mL of methanol to terminate the oxidation after sampling. The leached nickel ions were determined by an Optima 8300 ICP-OES Spectrometer (PerkinElmer). Total organic carbon (TOC) was measured on a Shimadzu TOC-vcph analyzer. Kinetic experiments were also conducted to study the effects of reaction parameters, such as PS dosage, catalyst loading, reaction temperature, initial solution pH, reaction solution pH and inorganic anions, on the SCP degradation efficiency. To ensure the reliability of the experimental results, all the degradation experiments were performed in at least triplicate tests and presented with mean values.

5.2.5 Stability Tests

Used catalysts were collected by a magnetic process after a typical oxidation experiment and washed thoroughly with excessive ultrapure water and ethanol for several times and dried in an oven at 60 ^{o}C overnight for reuse. After the third cycle, the used catalyst was heated in argon at 350 ^{o}C for 1 h to remove the adsorbed contaminants and retain a better reductive degree. The tests were conducted under the similar conditions to the fresh catalyst.

5.3 Results and Discussion

The catalysts are characterized by a series of advanced techniques including electron microscopies, XRD, Raman spectroscopy, N_2 sorption and XPS and the results are discussed accordingly. In addition, the catalytic performances of Ni@NPGs were evaluated in SCP degradation. The oxidation mechanism was elucidated and implications of background matters were investigated in this section.

5.3.1 Characterization of materials

The structural morphologies of the as-synthesized catalysts were investigated by SEM and TEM images (**Figure**s 5.2 and 5.3). Ni@NPG presented a 3D porous structure with cellular micro- and meso-pores. The porous architecture and crumpled topography would significantly enlarge the SSA for the interaction between the catalyst and the reactant (PS and SCP), herein promoting the organic removal efficiency. The formation of cellular pores might be due to the release of ammonia and carbon dioxide from urea pyrolysis, which inflated the laminar graphene layers and modified the porous carbon matrix [24]. As seen in **Figure** 5.2d, TEM and high resolution TEM images revealed that the nickel nanoparticles with an average diameter of 35 nm were encapsulated inside a graphene shell with a lattice spacing of 0.34 nm. In **Figure** 5.3b, the SEM and TEM images of Ni@NPG^{raw} illustrated that abundant nickel particles were located above/beneath the sample surfaces. The TEM images further confirmed the existence

of nickel particles, referred to the dark spots. The transformation of the morphology of Ni@NPG before and after acid pickling suggests that most of the nickel particles were successfully removed, which would be verified by the structural analyses of XRD and surface elemental quantification by XPS in later discussions.

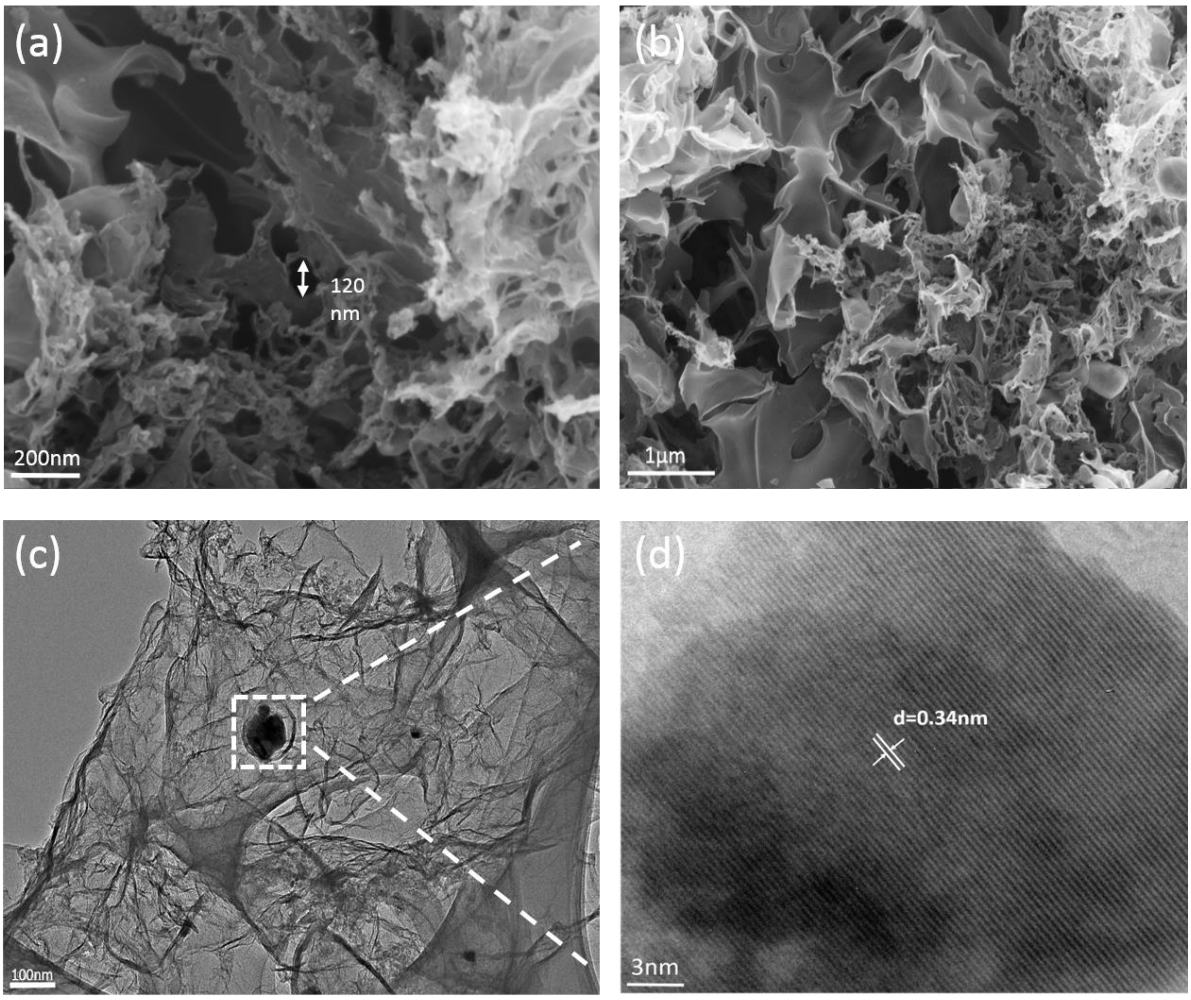

Figure 5.2 (a) and (b) SEM images of Ni@NPG, (c) TEM image of Ni@NPG, and (d) magnified TEM image of the encapsulated Ni particles.

The crystalline structures of the prepared Ni@NPG before and after acid washing were evaluated by XRD (**Figure** 5.4a). Ni@NPG^{raw} represented three main reflection peaks at 44.5^{o}, 51.8^{o} and 76.4^{o}, corresponding to the crystal planes of Ni (111), (220) and (311), respectively. A minor peak at 26.5^{o} could be indexed to the (002) plane of the graphitic carbon. By contrast,

Ni@NPG showed the same nickel diffraction peaks but at a much lower intensity and the graphitic carbon peak was significantly magnified. After acid treatment, the nickel particles adhered on the catalyst surface were removed. In addition, the diffraction peak of graphitic carbon was then sharpened, suggesting that the degree of graphitization of Ni@NPG was notably improved by wiping off the Ni particles. The result was in good agreement with the TEM images that only those Ni encapsulated between graphene layers were preserved.

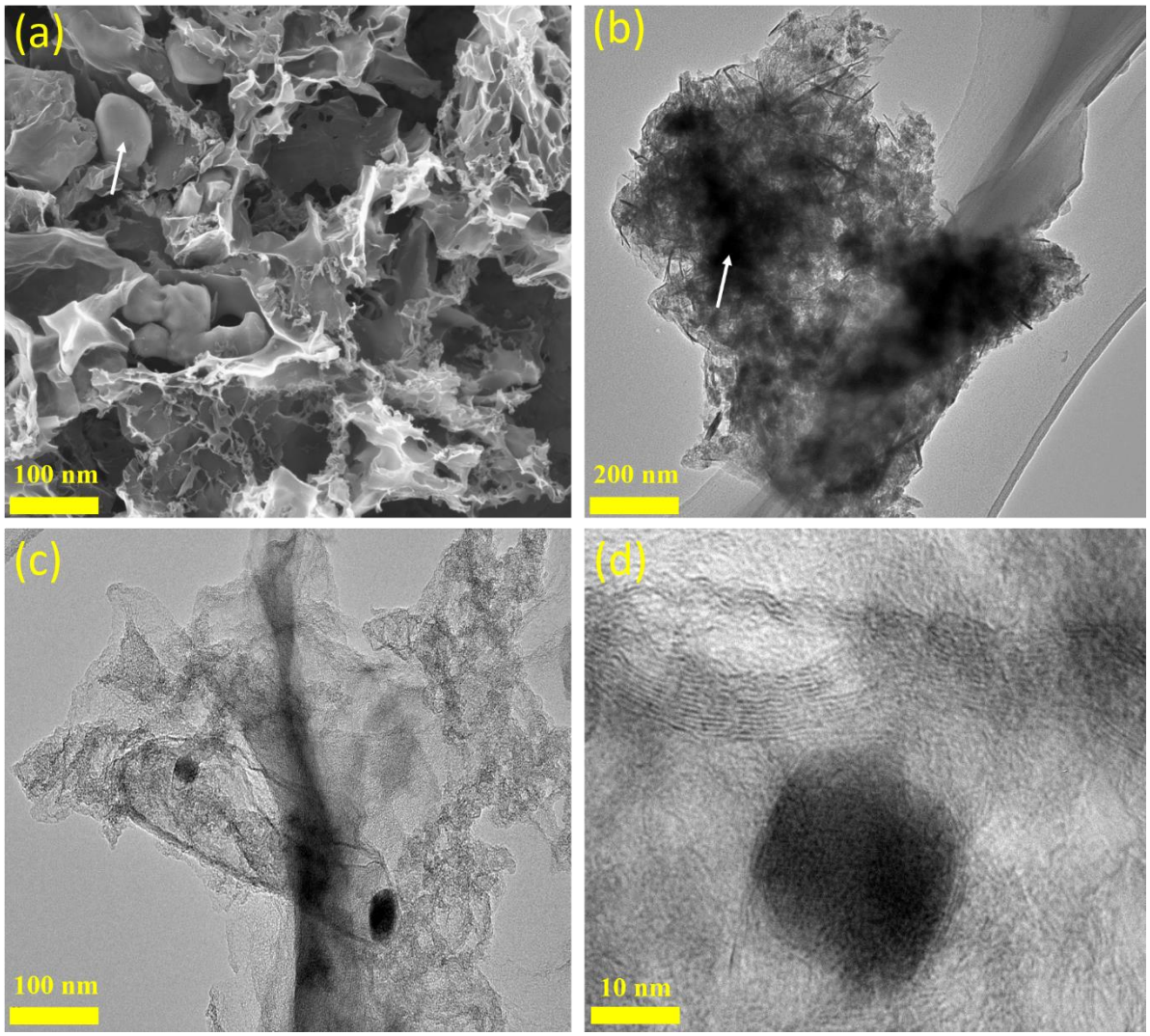

Figure 5.3 (a) and (b) SEM and TEM images Ni@NPG^{raw}, in which nickel particles were indicated by arrows. (c) TEM image Ni@NPG, and (d) HRTEM image of encapsulated nickel particles.

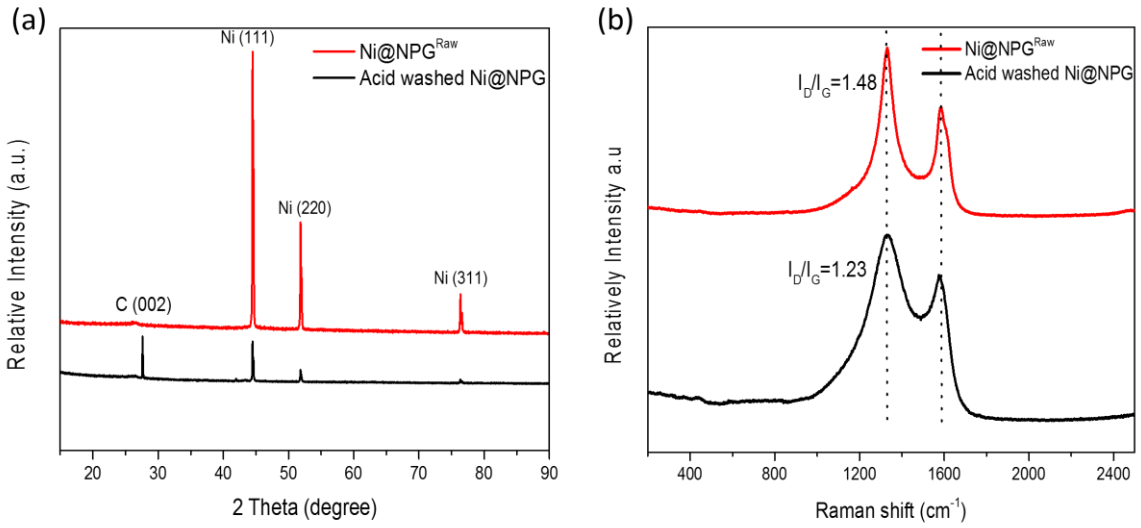

Figure 5.4 (a) XRD patterns and (b) Raman spectra of Ni@NPG and Ni@NPG^{raw}.

Raman spectroscopy is employed to investigate the defective degree, layer numbers, and structural distortion of carbon materials. The Raman spectra of the as-synthesized Ni@NPG (**Figure** 5.4b) present two dominant peaks at ~1330 (D band) and ~1590 cm^{-1} (G band), indicating the vibrational mode induced by the disordered structure and the E_{2g} vibration of sp^2-hybridized carbon network, respectively. The intensity ratio of I_D/I_G was typically utilized to reflect the degree of defects. As we can see, the I_D/I_G ratio was reduced from 1.48 to 1.23 for Ni@NPG after acid washing, suggesting that a greater crystalline graphene with less defects was achieved by removing the Ni particles on the catalyst surface.

Figures 5.5a and 5.5b display N_2 sorption isotherms and pore size distributions, as well as specific surface areas (SSAs) of Ni@NPG and Ni@NPG^{raw}. In **Figure** 5.5a, the two samples showed a typical type IV isotherms with H3-type hysteresis loops and the SSAs of the carbon materials were enlarged from 500 to 1000 m^2 g^{-1} after acid washing. In addition, **Figure** 5.5b reveals that a narrow pore size distribution of microspores occurred in the range of 1.0 ~ 2.0 nm. The large proportion of microspores was beneficial to creating more surface areas for

adsorption of organic pollutants as well as interacting with the reactants (PS) in the catalytic processes.

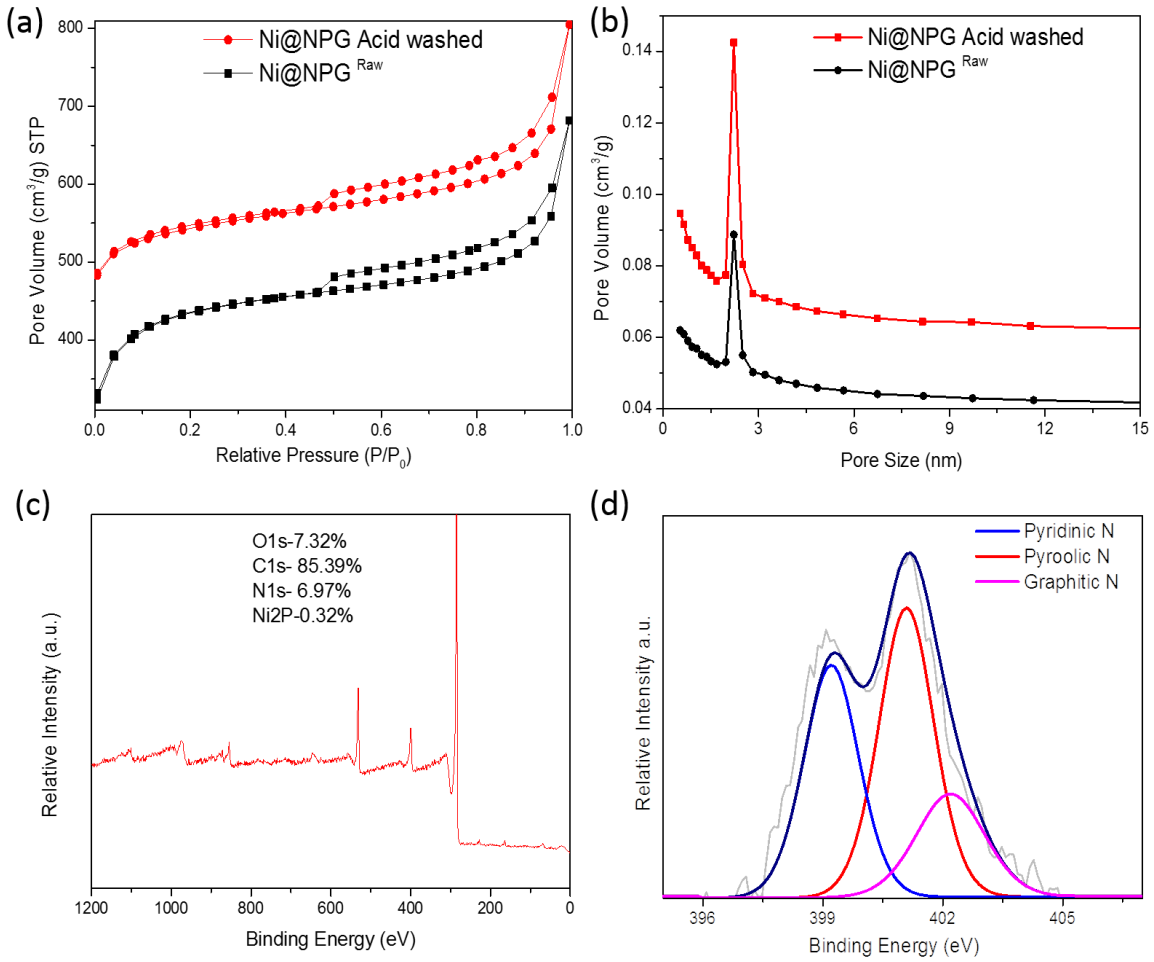

Figure 5.5 (a) Nitrogen sorption isotherms of the carbocatalysts, and (b) pore size distributions calculated from N_2 desorption isotherms for Ni@NPG^{raw} and Ni@NPG, (c) XPS spectra of Ni@NPG, and (d) high resolution N 1s of Ni@NPG.

The surface chemical compositions and states of Ni@NPG were probed by XPS and are presented in **Figure**s 5.5c-d. In the full XPS survey, C 1s, N 1s, O 1s, and Ni 2p are presented with contents of 85.39, 6.97, 7.32 and 0.32%, respectively [21, 25]. The XPS survey of Ni@NPG^{raw} shows that the Ni content is 3.16%. Moreover, the high-resolution XPS N 1s spectrum of Ni@NPG was fitted into three individual peaks at around 399.2, 401.1 and 402.2

eV, corresponding to the pyridinic, pyrrolic and graphitic N, respectively [21]. The carbon and nickel high-resolution spectra illustrate that C-C/C=C and Ni^0 $2p_{1/2}$ are the main chemical states for carbon and nickel on Ni@NPG, accordingly.

5.3.2 Catalytic performance of Ni@NPG in SCP degradation.

The catalytic performances of Ni@NPG and some typical carbon catalysts were investigated in aqueous SCP oxidation by the catalytic activation of PS (**Figure** 5.6a). It is revealed that PS could be hardly activated in the ambient temperature for oxidizing the target pollutant without a catalyst. A good organic adsorption was attained for Ni@NPG at 16% SCP removal owing to the large surface area of the catalyst. Several carbocatalysts were applied to compete the catalyst activity with Ni@NPG on SCP degradation. According to **Figure** 5.6a, Ni@NPG exhibited the best catalytic activity, reaching complete SCP degradation in less than 10 min, and the reaction rate constant was obtained at $0.46 \pm 2.3\times10^{-3}$ min^{-1}. This is much higher than other carbon materials including graphene oxide (GO), nitrogen doped reduced graphene oxide (N-rGO) and multi-walled carbon nanotubes (MWCNTs) at rate constants of $0.006 \pm 1.0\times10^{-5}$, $0.02 \pm 2.1\times10^{-4}$ and $0.009 \pm 8.4\times10^{-4}$ min^{-1}, respectively. It is necessary to spotlight the promotion effect of Ni nanoparticle encapsulation, by which Ni@NPG presented a seventy-fold enhancement over the reaction rate of pristine graphene oxide in the absent of Ni encapsulation and N-doping. In a similar study, iron nanoparticles encapsulated carbon nanotubes reached 100% phenol decomposition at half of the time for the N-doped CNTs [26]. In another study, Fe/Ni alloy encapsulated CNTs have proved to possess superior catalytic activity than Pt electrode in terms of electrochemical impedance spectroscopy, cyclic voltammetry and Tafel polarization [27]. In comparison with graphene oxide, the existence of metal nanoparticles within the porous graphene can modify the electronic structure and reduce the local surface work function of carbon walls, promoting the electron transfer from the metal to carbon [27].

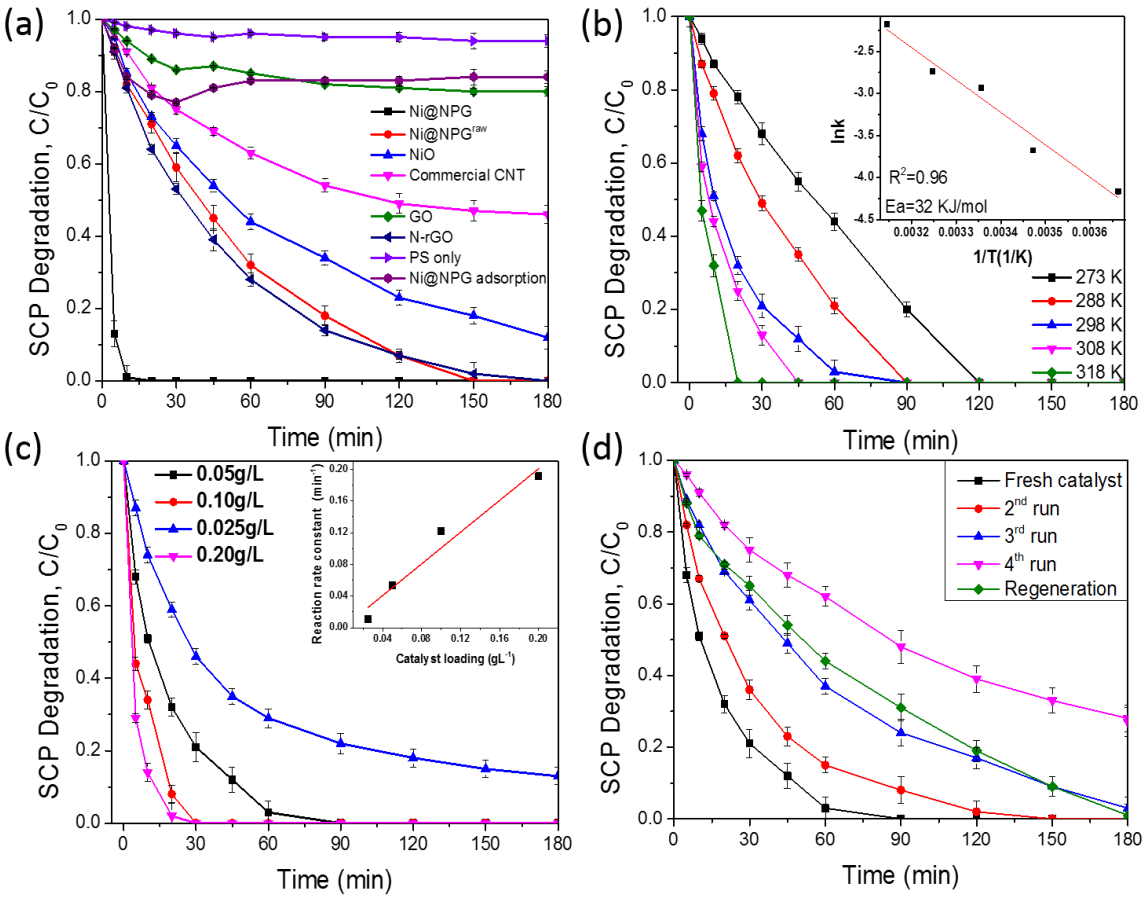

Figure 5.6 (a) SCP removal on various materials (catalyst loading: 0.2 g L^{-1}, PS: 2 g L^{-1}), (b) effects of reaction temperature on catalytic activity and estimation of activation energy (inset), (c) effects of catalyst loading on SCP degradation and linear relation between catalyst loading and rate constant (inset), (d) stability test of PS/Ni@NPG. Reaction conditions: SCP 20 ppm, catalyst concentration 0.05 g L^{-1}, PS 1 g L^{-1}, reaction temperature 25 °C, unless specifically mentioned.

Moreover, it is worth noting that the rate constant of SCP oxidation on Ni@NPG (0.46 ± 2.3×10^{-3} min^{-1}) was even higher than that of NiO (0.016 ± 1.1×10^{-4} min^{-1}), a benchmark metal oxide catalyst, implying the prospective of replacing traditional metal oxides with greener and efficient carbon materials for PS activation. In addition, it was discovered that the acid-washed Ni@NPG presented 20-fold enhancement of SCP degradation over $Ni@NPG^{raw}$ (0.46 ±

2.3×10^{-3} *vs* $0.020 \pm 3.2\times10^{-4}$ min^{-1}). The remarkable enhancement of catalytic performance of Ni@NPG might be due to the surface morphology modification. As SEM and TEM images showed earlier, nickel particles were distributed throughout the $Ni@NPG^{raw}$ surface. As a result, abundant carbon active sites and pores would be exposed by removing the metal particles through acid wash, consequently increasing the catalytic activity. The thermal stability analysis (TGA) of catalysts also suggests that the $Ni@NPG^{raw}$ presented a much higher remaining weight ratio than Ni@NPG, indicating the high Ni content. Additionally, in an environmental perspective, removing the surface Ni could prevent metal leaching in waters. Furthermore, the ICP result reveals that a smidgeon amount of Ni ion (0.1 mg L^{-1}) was detected in the reacted solution, indicating the successful removal of surface Ni on Ni@NPG.

Figure 5.6b presents the catalytic performances of Ni@NPG at different reaction temperatures. It was found that the catalytic efficiency increased at elevated temperatures, and the best reaction rate ($0.11 \pm 1.9\times10^{-4}$ min^{-1}) occurred at 45 °C. Specifically, the reaction rate constants were increased by 22% and 68% at 35 and 45 °C, respectively, compared with the rate at 25 °C. This might be due to the self-activation reaction of PS under higher temperatures. [28] Another possible reason was that the oxidative attack on SCP by reactive radicals was enhanced at higher temperatures so that the SCP removal rate was accelerated. On the other hand, the reaction rate was slightly retarded when the reaction temperature was cooled down to 15 °C. Surprisingly, the oxidation process was only marginally affected when the reaction temperature was controlled at 0 °C, and a complete SCP removal was achieved in 2 h. The robust catalysis of Ni@NPG at low temperature can be attributed to nitrogen doping, which could minimize the thermal effect on AOPs. [29] The experiment suggests that the PS/Ni@NPG system could be adapted in a wide range of temperature conditions. In addition, the catalytic performances of Ni@NPG derived at different annealing temperatures were tested. Ni@NPG-1000 exhibited

the best catalytic activity among all the Ni@NPG catalysts prepared at different temperatures, thus Ni@NPG-1000 was selected for further investigation in this study.

The effect of catalyst loading was then studied on the SCP degradation (**Figure** 5.6c). It was found that a linear relationship was established between the catalyst loading and degradation rate constants (inset of **Figure** 5.6c). It proves that a higher catalyst loading (0.2 g L^{-1}) would lead to a better degradation efficiency ($0.19 \pm 1.1\times10^{-3}$ min^{-1}), which was attributed to that more active sites were available in the PS activation processes. The effect of PS concentration was also investigated. It was indicated that the SCP degradation rate was promoted at a higher PS concentration (2 g L^{-1}), however continuously increasing the PS concentration after 4 g L^{-1} would not further bring enhancement to the oxidation process due to the limited amount of catalyst. Moreover, SCP initial concentration as an important factor was studied and the results reveal that the reaction rate was dramatically undermined when the SCP concentration was increased (20 to 60 ppm), implying the SCP degradation efficiency is heavily depended on SCP concentration. The recyclability and stability of Ni@NPG catalyst as an important factor was evaluated by consecutive tests of SCP oxidation (**Figure** 5.6d). The fresh catalyst reached 100% SCP removal in 90 min and such strong catalysis was maintained in the second and third runs, depicted that the complete SCP removal was achieved in 150 and 180 min accordingly. At the fourth run, the catalytic ability of Ni@NPG slightly decreased and is 73% SCP removal in 3 h. The high reusability of Ni@NPG can be concluded in several aspects. Firstly, the honeycomb structure of Ni@NPG endows it with large SSAs as well as stable structure to resist the oxidation collapse when repeatedly used. Secondly, N-doping has been proved to be an effective strategy to enhance the catalytic stability of carbon materials by modifying the surface chemistry and maintaining the structure. [30] Moreover, the encapsulated Ni particles can break the chemical inertness of carbon by electron transfer. In addition, the unique enclosed structure

enables Ni particles to be protected by carbon walls, as a result, the activity of surface carbon layers was reserved with a good stability.

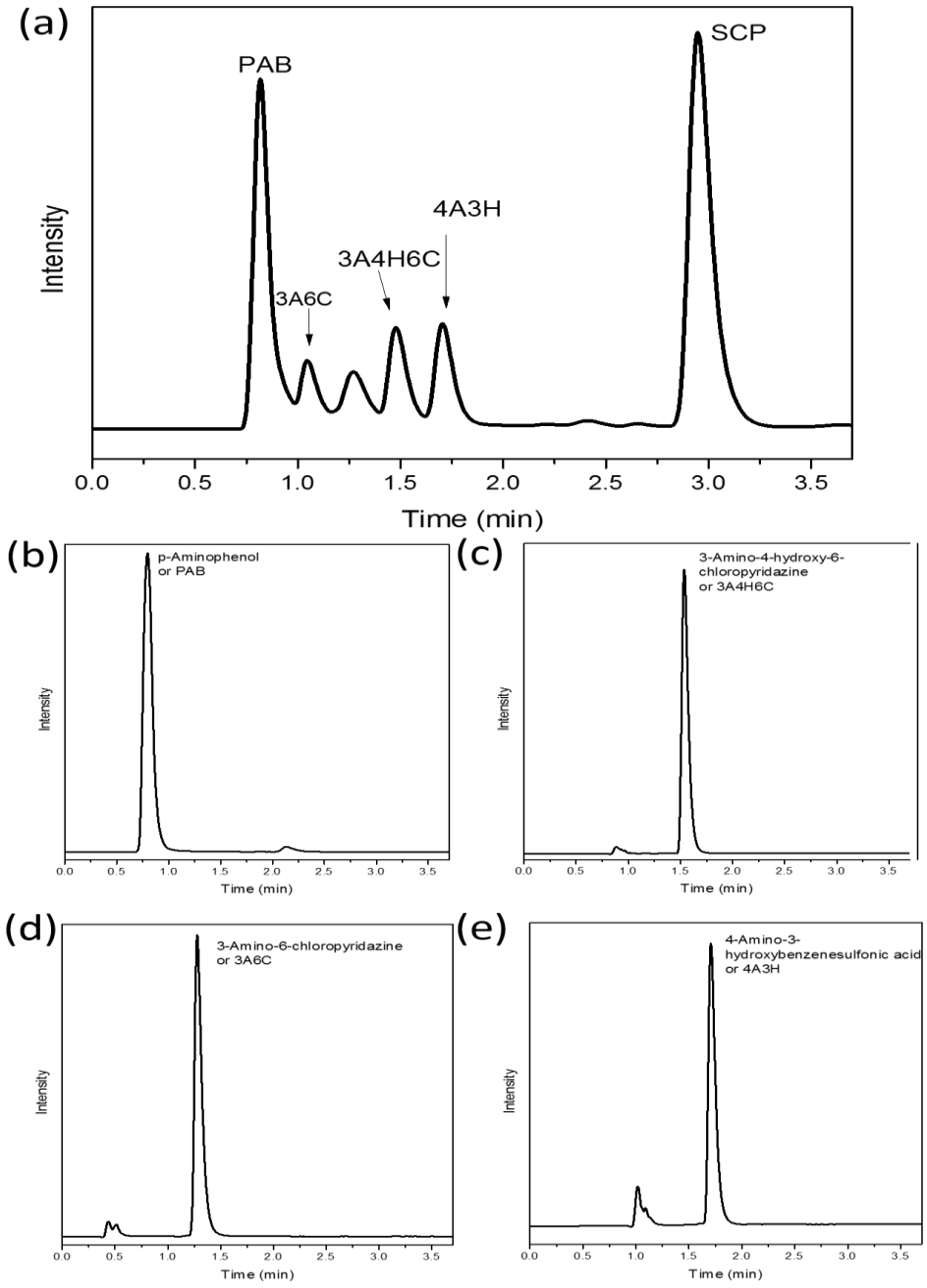

Figure 5.7 Intermediates of PS/Ni@NPG of SCP degradation. (a) HPLC spectrum of SCP degradation test at 5 min. (b-e) possible SCP degradation intermediates. (UV 270 nm, mobile phase: diluted acetic acid and methanol (70:30, v/v), flow rate 0.3 mL/min).

However, the decline of Ni@NPG catalytic activity after repeated use suggested the coverage of the active sites by SCP and degradation intermediates. The textural investigation confirmed that the surface area and pore size were diminished after three cycles of reuse. A mild pyrolysis process was applied on Ni@NPG after the 4th stability test at 350 ^{o}C in an inert gas to burn off the adsorbed degradation intermediates (**Figure** 5.7). The results show an obvious restoration of catalysis on Ni@NPG and the SCP oxidation was comparable to the third stability test. However, the catalytic stability still requires improvement in future studies.

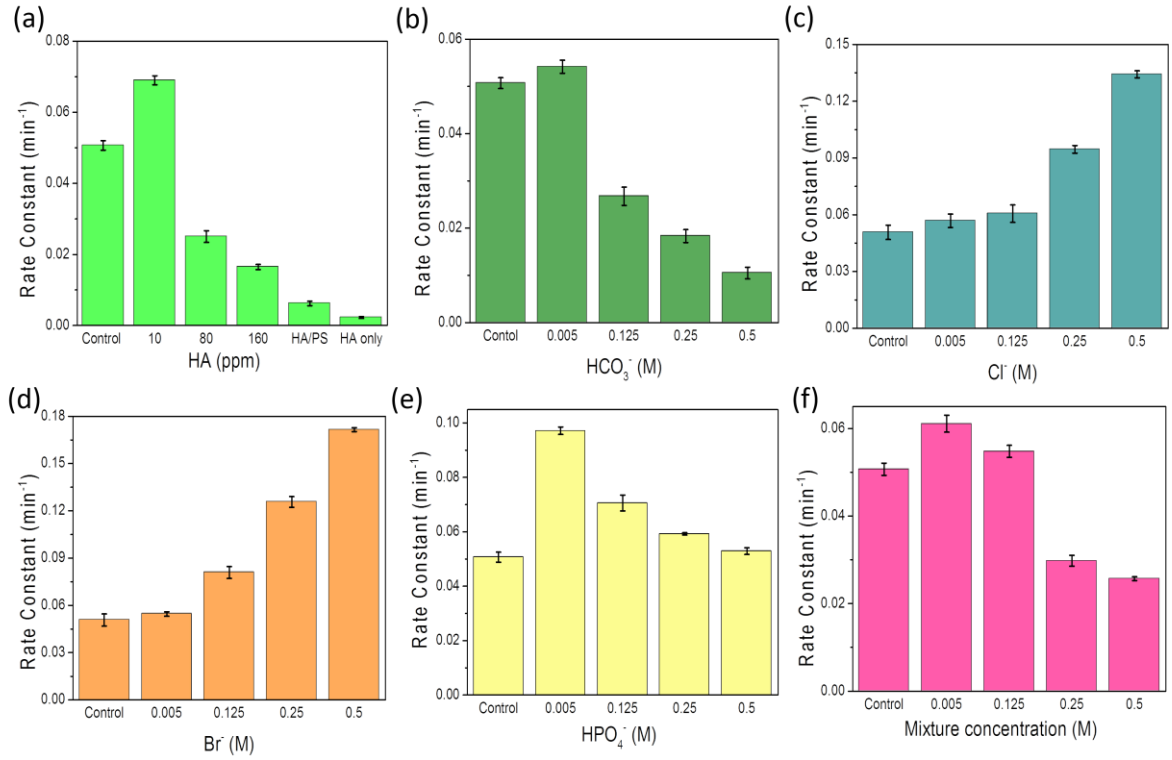

Figure 5.8 Rate constants of SCP degradation on Ni@NPG with addition of various amounts of (a) HA, (b) $NaHCO_3$, (c) NaBr, (d) NaCl, (e) NaH_2PO_4, (f) HA and inorganic ion mixture. Control test is absent of HA and inorganic ions. Reaction conditions: SCP 20 ppm, catalyst concentration 50 mg L^{-1}, PS 1 g L^{-1}, reaction temperature 25 ^{o}C.

5.3.3 Effect of NOMs

Humic acid (HA), as a model of natural organic matters (NOMs), was applied to investigate its effect on carbon-based AOPs [31, 32]. **Figure** 5.8a shows that HA (10 ppm) itself had a negligible

effect on SCP degradation. However, an obvious enhancement in oxidation reaction can be observed when PS was also added, and this may be contributed to the quinone groups in HA (Eqs. (1) and (2)) for moderate activation of PS [31]. Moreover, an increase of 19% in SCP degradation ($0.069 \pm 1.8\times10^{-4}$ min^{-1}) with the addition of Ni@NPG was found, compared with the control test ($0.051 \pm 4.2\times10^{-4}$ min^{-1}). However, a further increase in HA concentration would exert an adverse effect on SCP degradation rate, about $0.025 \pm 1.5\times10^{-4}$ and $0.017 \pm 8.1\times10^{-4}$ min^{-1} of SCP degradation rate constants were attained in 30 min with 80 and 160 ppm HA, respectively. The results indicate that HA at low concentrations could stimulate PS activation to produce reactive species such as $SO_4^{\bullet-}$ and $^{\bullet}OH$ while an inhibition effect may occur at a high HA concentration (over 80 ppm). The inhibition may be due to the excessive HA with a big molecule and plentiful electrons that would act as radical quenching agents to scavenge the free radicals. Thus, the stimulation effect was overwhelmed by its quenching effect at a high HA concentration. Additionally, in a HA superabundant environment, a considerable amount of HA was adsorbed by Ni@NPG, which might block the catalytic sites for PS activation and SCP adsorption, herein hindering the oxidation reaction.

$$\text{Quinones} + H_2Q \rightarrow 2\text{Semiquinone}^{\bullet-} + 2H^+ \qquad \textbf{(Eq. 5.1)}$$

$$2\text{Semiquinone}^{\bullet-} + S_2O_8^{2-} \rightarrow 2SO_4^{\bullet} + \text{Quinones} \qquad \textbf{(Eq. 5.2)}$$

Table 5.1 Standard deviation of rate constants.

Reaction		Standard deviation	Reaction		Standard deviation
Various catalysts			$NaHCO_3$:0.005 M	d	1.1×10^{-4}
Ni@NPG	a	2.3×10^{-3}	$NaHCO_3$:0.125 M	d	1.3×10^{-4}
GO	a	1.0×10^{-5}	$NaHCO_3$:0.25 M	d	1.2×10^{-4}
N-rGO	a	2.1×10^{-4}	$NaHCO_3$: 0. 5 M	d	4.4×10^{-4}
MWCNTs	a	8.4×10^{-4}	**Chloride ion effect**		
NiO	a	1.1×10^{-4}	NaCl: 0.005 M	d	9.1×10^{-4}
$Ni@NPG^{raw}$	a	3.2×10^{-4}			
Temperature effect			NaCl: 0.125 M	d	1.1×10^{-4}
Ni@NPG: 0 °C	b	1.3×10^{-4}	NaCl: 0.25 M	d	2.4×10^{-4}
Ni@NPG: 15 °C	b	1.1×10^{-4}	NaCl: 0.5 M	d	2.8×10^{-4}
Ni@NPG: 25 °C	b	9.2×10^{-5}	**Phosphate ion effect**		
Ni@NPG: 35 °C	b	2.1×10^{-4}	NaH_2PO_4: 0.005 M	d	1.4×10^{-4}
Ni@NPG: 45 °C	b	1.9×10^{-4}	NaH_2PO_4: 0.125 M	d	2.4×10^{-4}
Catalyst dosage effect ±			NaH_2PO_4: 0.25 M	d	1.8×10^{-4}
Ni@NPG: 0.025 g L^{-1}	c	1.1×10^{-4}	NaH_2PO_4: 0.5 M	d	1.1×10^{-4}
Ni@NPG: 0.05 g L^{-1}	c	4.2×10^{-4}	**Bromide ion effect**		
Ni@NPG: 0.1 g L^{-1}	c	8.3×10^{-4}	NaBr: 0.005M	d	1.0×10^{-4}
Ni@NPG: 0.2 g L^{-1}	c	1.1×10^{-3}	NaBr: 0.125M	d	1.1×10^{-4}
Humic Acid effect			NaBr: 0.25M	d	1.5×10^{-4}
HA: 10 ppm	d	1.8×10^{-4}	NaBr: 0. 5M	d	2.1×10^{-4}
HA: 80 ppm	d	1.5×10^{-4}	**Mixture of NOMs and common ions effect**		
HA: 160 ppm	d	8.1×10^{-4}	Mixture: 0.005M	d	2.3×10^{-4}
HA/PS	d	4.1×10^{-4}	Mixture: 0.125M	d	5.6×10^{-5}
HA only	d	1.1×10^{-4}	Mixture: 0.25M	d	8.4×10^{-4}
Carbonate ion effect			Mixture: 0.5M	d	5.6×10^{-4}

Reaction conditions.
a: catalyst concentration 0.2 g L^{-1}, PS: 2 g L^{-1}, reaction temperature 25 °C.
b: catalyst concentration 0.05 g L^{-1}, PS: 1 g L^{-1}.
c: PS 1 g L^{-1}, reaction temperature 25 °C.
d: catalyst concentration 50 mg L^{-1}, PS 1 g L^{-1}, reaction temperature 25 °C.

5.3.4 Effect of inorganic ions

Since inorganic anions such as halide, carbonate and phosphate ubiquitously exist in natural resources and wastewaters, it is significant to investigate their influences on the AOPs. These inorganic anions are often believed to be radical scavengers in AOPs as they can promptly react with reactive species such as $SO_4^{\bullet-}$ and $^{\bullet}OH$ to form secondary reactive radicals such as $Cl^{\bullet}$, $HCO_3^{-\bullet}$ and $H_2PO_4^{-\bullet}$ (Eqs. 5.3 ~ 5.9) [33-40]. As shown in **Figure** 5.8 b, at a lower concentration of HCO_3^- (0.005M), the SCP removal rate ($0.055 \pm 1.1\times10^{-4}$ min^{-1}) was slightly accelerated compared with the control test ($0.051 \pm 4.2\times10^{-4}$ min^{-1}). The promotion in SCP oxidation at low concentrations of HCO_3^- may be caused by the following reasons: (1) carbonate radicals ($HCO_3^{-\bullet}$ and $CO_3^{-\bullet}$) formed in Eqs. 5.6 and 5.7 were reactive toward organic compounds despite that they are less effective than $^{\bullet}OH$ and $SO_4^{\bullet-}$ [31, 39, 41]; (2) pH effect experiment indicates that the pH value changed from 7.5 to 8.7 during the oxidation process which is favorable for base activation of persulfate [13]. The rate constants at the concentrations of 0.125, 0.25 and 0.5 M carbonate anion for SCP degradation dropped to $0.027 \pm 1.3\times10^{-4}$, $0.019 \pm 1.2\times10^{-4}$ and $0.011 \pm 4.4\times10^{-4}$ min^{-1}, respectively. Conversely, a quenching effect occurred when higher dosage of carbonate anions were introduced into the solution.

$SO_4^{\bullet-}$ has a higher redox potential (2.5 ~ 3.1 V) towards target organic pollutant than $^{\bullet}OH$, whereas it has been reported that $SO_4^{\bullet-}$ is more sensitive in terms of quenching effect in the existence of halogen. The reaction between Cl^- and $^{\bullet}OH$ (**Eq.** 5.4) was reversible and the reaction rate of its backward reaction was higher than the forward reaction, thus, the chloride ion was believed to have a minor scavenging effect on $^{\bullet}OH$ mediated AOPs. [35, 42, 43] In **Figure**s 5.8c-d, it was found that halogen ions (Br^- and Cl^-) exhibited a similar trend; nevertheless, Br^- exerted a stronger influence on SCP removal, which might be due to its high chemical reactive. Interestingly, the SCP oxidation rate was accelerated at higher halogen dosages and the SCP removal rate constants were achieved at $0.061\pm 1.1\times10^{-4}$, $0.094 \pm 2.4\times10^{-4}$ and $0.134 \pm 2.8\times10^{-}$

^{4} min^{-1} for 0.125, 0.25 and 0.5 M Cl^{-}, respectively, and 0.051± 4.2×10^{-4} min^{-1} in the control test. It might be due to the acidification of the reaction solution by adding Cl^{-}, where the pH value was changed from 8 to 5.2, where $SO_4^{\bullet-}$ and chlorine radicals ($Cl^{\bullet}$ and $Cl_2^{\bullet-}$) are more active in acidic environment [44]. Moreover, the relatively high redox potential of halogen radicals, $Cl_2^{\bullet-}$ (2.0V), $Cl^{\bullet}$ (2.4V), $Br_2^{\bullet-}$ (1.6V) and $Br^{\bullet}$ (1.9V) would partially contribute to the oxidative removal of SCP. [45-47]

$Cl^- + SO_4^{\bullet-} \rightarrow SO_4^{2-} + Cl^{\bullet}$ (**Eq.** 5.3)

$Cl^- + {}^{\bullet}OH \rightarrow ClOH^{\bullet}$ (**Eq.** 5.4)

$Cl^{\bullet} + Cl^- \rightarrow Cl_2^{\bullet-}$ (**Eq.** 5.5)

$HCO_3^- + SO_4^{\bullet-} \rightarrow SO_4^{2-} + HCO_3^{-\bullet}$ (**Eq.** 5.6)

$HCO_3^- + {}^{\bullet}OH \rightarrow CO_3^{-\bullet} + H_2O$ (**Eq.** 5.7)

$H_2PO_4^- + SO_4^{\bullet-} \rightarrow SO_4^{2} + H_2PO_4^{-\bullet}$ (**Eq.** 5.8)

$H_2PO_4^- + {}^{\bullet}OH \rightarrow OH^- + H_2PO_4^{-\bullet}$ (**Eq.** 5.9)

$HO^{\bullet} + CO_3^{2-} \rightarrow CO_3^{\bullet-} + HO^-$ (**Eq.** 5.10)

$SO_4^{\bullet-} + CO_3^{2-} \rightarrow CO_3^{\bullet-} + SO_4^{2-}$ (**Eq.** 5.11)

$Cl^{\bullet} + CO_3^{2-} \rightarrow CO_3^{\bullet-} + Cl^-$ (**Eq.** 5.12)

$Cl^{\bullet} + HCO^{3-} \rightarrow CO_3^{\bullet-} + Cl^- + H^+$ (**Eq.** 5.13)

$Cl_2^{\bullet-} + CO_3^{2-} \rightarrow CO_3^{\bullet-} + 2Cl^-$ (**Eq.** 5.14)

$Cl_2^{\bullet-} + HCO_3^- \rightarrow CO_3^{\bullet-} + 2Cl^- + H^+$ (**Eq.** 5.15)

$HO^{\bullet} + Br^- \rightarrow BrOH^{\bullet-}$ (**Eq.** 5.16)

$SO_4^{\bullet-} + Br^- \rightarrow Br^{\bullet} + SO_4^{2-}$ (**Eq.** 5.17)

$Br^{\bullet} + Br^{\bullet} \rightarrow Br_2$ (**Eq.** 5.18)

$Br^{\bullet} + CO_3^{2-} \rightarrow CO_3^{\bullet-} + Br^-$ (**Eq.** 5.19)

$Br^{\bullet} + HCO_3^- \rightarrow CO_3^{\bullet-} + Br^- + H^+$ (**Eq.** 5.20)

$Cl^{\bullet} + Br^- \rightarrow BrCl^{\bullet-}$ (**Eq.** 5.21)

$Br^{\bullet} + Cl^- \rightarrow BrCl^{\bullet-}$ (**Eq.** 5.22)

$BrCl^{\bullet-} + CO_3^{2-} \rightarrow CO_3^{\bullet-} + Br^- + Cl^-$ (**Eq.** 5.23)

$BrCl^{\bullet-} + HCO_3^- \rightarrow CO_3^{\bullet-} + Br^- + HCl$ (**Eq.** 5.24)

$H_2PO_4^- + SO_4^{\bullet-} \rightarrow HSO_4^- + HPO_4^{-\bullet}$ (**Eq.** 5.25)

$HPO_4^{-\bullet} + SO_4^{\bullet-} \rightarrow H_2SO_4 + PO_4^{2-\bullet}$ (**Eq.** 5.26)

Furthermore, a series of halogenated compounds have been generated during the oxidation process, which can be witnessed by UHPLC in **Figure** 5.9. In Cl^- introduced solution, a series of intermediate peaks emerged during SCP oxidation reaction, whereas not showing in the control test. Moreover, the halogenated intermediates peaks did not show reduction along with the experiment continued, suggesting that the refractory halogenated compounds were generated. Total organic carbon analysis was applied to further prove the emerging of halogen intermediates. The TOC results showed that the TOC value diminished at a higher Cl^- dosage (0.5 M) and only 39% TOC was reached, much less than that 69% in the control test, suggesting the newly formed halogenates were resistant to be further oxidized.

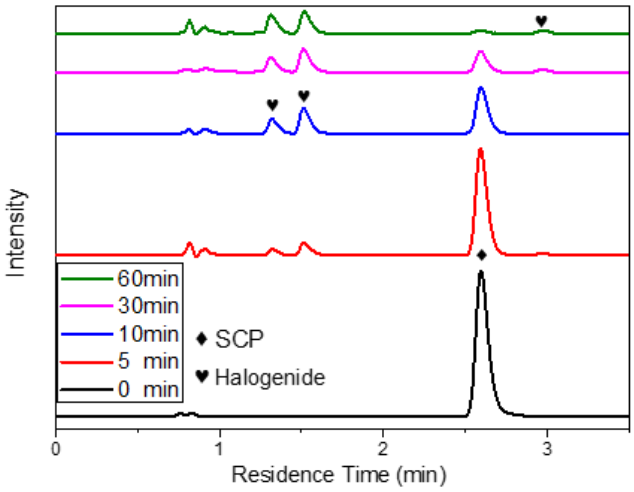

Figure 5.9. HPLC spectra for intermediates of Cl^- introduced SCP degradation.

The impact of phosphate on PS activation was also studied. Unlike other anions, phosphate ions presented a promotion effect on the SCP oxidation reaction regardless of its concentration. **Figure** 5.8e illustrates that the SCP degradation rate constants for 0.005, 0.0125 and 0.5 M $H_2PO_4^-$ were 0.097 ± 1.4×10^{-4}, 0.071 ± 2.4×10^{-4}, and 0.053 ± 1.1×10^{-4} min^{-1}, faster than the control (0.051 ± 4.2×10^{-4} min^{-1}). This could be ascribed to the formation of $H_2PO_4^{-\bullet}$ through the reaction between reactive radicals ($^{\bullet}OH$ and $SO_4^{\bullet-}$) and $H_2PO_4^-$ (Eqs. 5.25 and 5.26). It was reported that, the reactivity is similar to $SO_4^{\bullet-}$ that can readily oxidize many organic compounds.[39] However, the reaction rate was retarded when the $H_2PO_4^-$ dosage was increased.

This can be attributed to the scavenging effect of $^{\bullet}OH$ and $SO_4^{\bullet-}$ which were substituted by less reactive phosphate radicals such as $HPO_4^{\bullet-}$ and $PO_4^{\bullet 2-}$.[39] Moreover, it is realistic that NOM and versatile anions coexist in natural systems and wastewater. Whereas, to the best of our knowledge, very limited work on the synergistic effects of NOM and various anions on SR-AOPs has been done. In a further study, HA, Cl^-, Br^-, HCO_3^-, and $H_2PO_4^-$ were introduced simultaneously into the solution at various concentrations of 0.005, 0.125, 0.25, and 0.5 M. **Figure** 5.8f illustrated that the mixture at 0.005 and 0.125 M presented faster SCP removal and the rate constants were $0.061 \pm 2.3\times10^{-4}$ and $0.057 \pm 5.6\times10^{-5}$ min^{-1}, respectively. However, at 0.25 and 0.5 M mixture concentrations, the inhibiting effect happened and the rate constants were estimated to be $0.030 \pm 8.4\times10^{-4}$ and $0.026 \pm 5.6\times10^{-4}$ min^{-1}, respectively. It is believed that complicated reactions took place because different ions and organic compounds might react with each other as shown in Eqs 5.8 ~ 5.24 (??) [48-54]. Secondary reactive radicals such as $H_2PO_4^{-\bullet}$ and $BrCl^{\bullet-}$ were produced when the mixture reacted with $^{\bullet}OH$ and $SO_4^{\bullet-}$ or inter-reaction at a low concentration, and these radicals could also contribute to oxidize target organic pollutants. Conversely, at higher concentrations, the quenching effect would gradually take effects.

5.3.5 The mechanisms of PS activation and SCP oxidation on Ni@NPG

In the previous studies, reactive radicals ($^{\bullet}OH$ and $SO_4^{\bullet-}$) generated from PS activation played a dominant role in attacking and oxidizing organics. [17, 55, 56] Herein, in situ EPR was applied to investigate the radical generation and evolution. **Figure** 5.10a demonstrated that Ni@NPG was able to effectively activate PS to produce both $^{\bullet}OH$ and $SO_4^{\bullet-}$ and the optimum production rate reached at 5 min. The intensity of these radicals decreased in 20 min, which can be attributed to the consumption of PS by SCP degradation. Moreover, competitive radical tests were also performed to investigate the mechanisms of SCP degradation on carbon based catalysts. Ethanol is often used as a sensitive probe for $^{\bullet}OH$ and $SO_4^{\bullet-}$ detection because of its rapid

reaction with $^{\bullet}OH$ and $SO_4^{\bullet-}$. **Figure** 5.10b illustrated that, a rapid SCP degradation rate was remained when excess ethanol was introduced at a molar ratio of 500:1 (ethanol: PS), with complete SCP removal in 2 h. In addition, there was no obvious decrease of SCP degradation rate when the ethanol was further increased to 1000:1 and 2000:1, reaching 100% SCP removal in 120 and 150 min, respectively. Interestingly, when the water was replaced by ethanol, 80% SCP degradation reaction was still achieved. However, it is worthy to point out that, the inhibition effect of ethanol on PS activation can also due to the reduced adsorption of Ni@NPG. The adsorption capacity of SCP on Ni@NPG was reduced by 63% in ethanol. Therefore, it is believed that $^{\bullet}OH$ and $SO_4^{\bullet-}$ are partially responsible for the SCP degradation, meanwhile nonradical processes and other active radicals such as singlet oxygen ($^1O_2$) and $^{\bullet}O_2^-$ could also be involved.

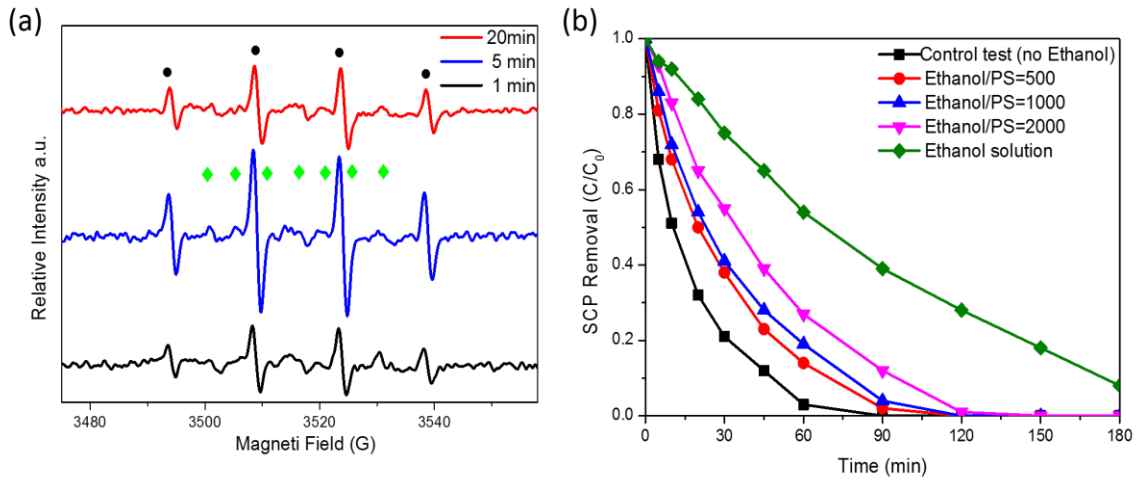

Figure 5.10 (a) EPR spectra of PS activation with Ni@NPG (● DMPO-OH; ♦ DMPO-SO_4) (b) Effects of ethanol as the quenching agent at different molar ratios on SCP degradation. Reaction conditions: SCP 20 ppm, catalyst concentration 50 mg L^{-1}, PS 1 g L^{-1}, reaction temperature 25 ^{o}C.

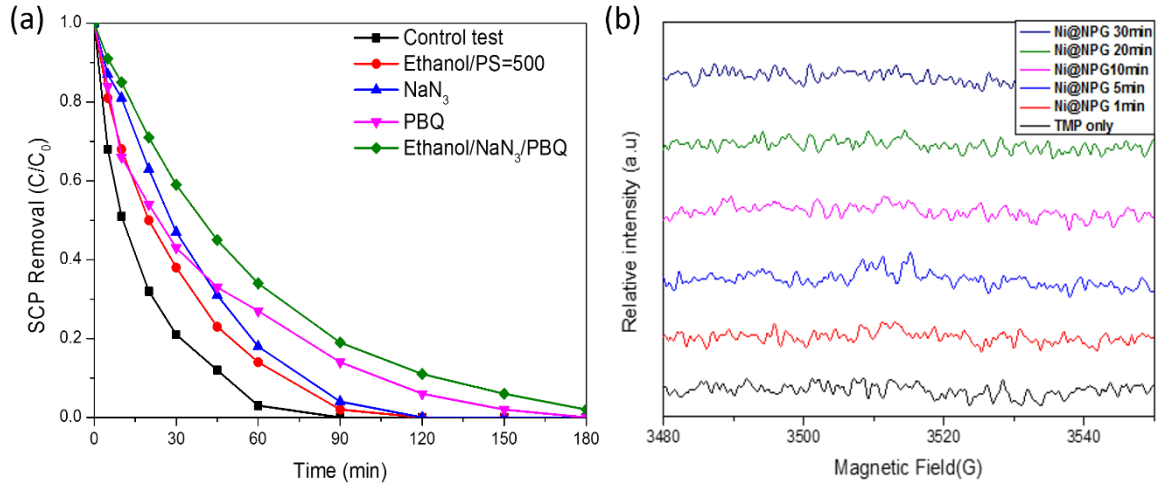

Figure 5.11 (a) Effects of various quenching agents on SCP degradation (NaN_3: 50 mM, PBQ: 50 mM), (b) EPR spectra of TEPN on Ni@NPG at various time internals from 1 min to 30 min. Reaction conditions: Reaction conditions: SCP 20 ppm, catalyst concentration 50 mgL^{-1}, PS loading 1 g L^{-1}, reaction temperature 25 ^oC.

In addition, sodium azide (NaN_3) and p-benzoquinone (PBQ), as effective quenching agents for $^1O_2$ and $^{\bullet}O_2^-$ accordingly, were applied to investigate their contributions to the organic oxidation (**Figure** 5.11a). After 50 mM of NaN_3 and PBQ were introduced in the reaction separately, the SCP degradation rate was slightly reduced and achieved complete degradation in 2 and 3 h, respectively. In **Figure** 5.11b, the negligible signal of $^1O_2$ and $^{\bullet}O_2^-$ were detected, suggesting that neither $^1O_2$ nor $^{\bullet}O_2^-$ was involved in the PS/Ni@NPG system, and the decreased degradation efficiency caused by NaN_3 and PBQ was presumably due to the elimination of $^{\bullet}OH$ and $SO_4^{\bullet-}$ in the solution [57]. Meanwhile, to study the contribution of nonradical oxidation pathway, various quenching agents were applied simultaneously, ethanol (500 times of PS), NaN_3 (50 mM), and PBQ (50 mM). It is noteworthy that, during the reaction, where all the potential free radicals were quenched out, the SCP degradation was mildly influenced and reached 100% removal in 3 h. Moreover, the mechanisms of PS activation and SCP oxidation on Ni@NPG were further investigated by radical intensity and quenching tests compared to the benchmark catalysts (**Figure** 5.12). The mechanisms of PS activation and SCP oxidation

on Ni@NPG were further investigated by radical intensity and quenching tests compared to the benchmark NiO and N-rGO. The EPR spectra ($^{\bullet}OH$ and $SO_4^{\bullet-}$) in **Figure** 5.12a shows that Ni@NPG presented a higher radical intensity than both NiO and N-rGO throughout the experiment, indicating that N doping and Ni nanoparticle encapsulation would synergistically enhance the PS activation for the generation of radical species.

Ethanol was applied as a radical scavenger to quickly quench both hydroxyl and sulfate radicals generated in the activation process. As shown in **Figure** 5.12b, c and d, the effects of ethanol on SCP catalytic oxidation over Ni@NPG, N-rGO and Ni_3O_4 are noticeably different. Both Ni@NPG and N-rGO are insensitive to ethanol, which can be attributed to the nonradical processes. A previous study has illustrated that the catalytic behaviours of pristine CNT and N-CNT are intrinsically different[19]. Specifically, pristine CNT can activate PMS to generate free radicals whereas N-CNT/PMS is a nonradical process that the PMS will be directly activated on activated carbon atoms adjacent to N dopants to form a metastable surface complex which will directly oxidize the organic via electron transfer. Therefore, the outstanding catalytic activity of Ni@NPG on SCP degradation can be summarized into two aspects:

1. Nitrogen doping creates new active sites to form positively carbon atoms which account for the nonradical process.
2. Nickel nanoparticle encapsulation would greatly accelerate the electron transfer to the graphene surface, which efficiently optimizes the electronic structure of the graphene surface, thereby promoting the PS activation.

According to the results, the synergistic effect of radical and nonradical process was responsible for the rapid SCP removal in the PS/Ni@NPG system whereas the nonradical process was proved to play a more important role.

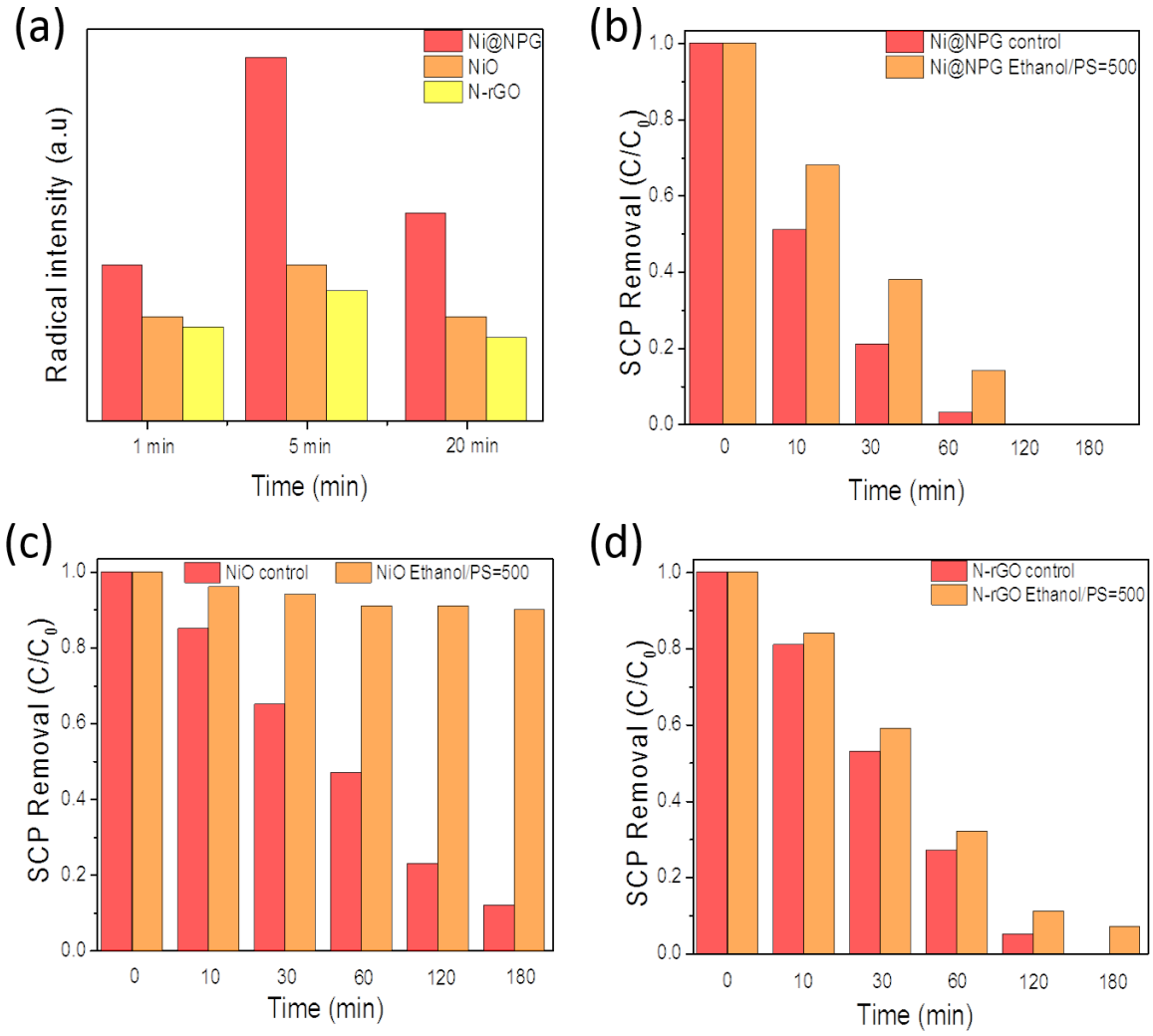

Figure 5.12. (a) Radical relatively intensity under various catalyst. Effect of radical quenching on SCP degradation: (b) Ni@NPG, (c) NiO and (d) N-rGO. Reaction conditions: SCP 20 ppm, Ni@NPG catalyst concentration 0.05 g L^{-1}, PS 1 g L^{-1}, reaction temperature 25 ºC.

5.4 Conclusion

A facile one-pot pyrolysis technique was proposed to synthesize magnetic catalysts with outstanding catalytic activities for PS activation and antibiotic (SCP) degradation. The considerably enhanced catalytic performances of the hybrids were benefited from 3-dimentional porous architecture, and the synergistic effect of nickel encapsulation and N doping. This hybrid structure integrates the metal-free property and fast electronic transfer from

metal core to carbon layer for heterogeneous catalysis. Moreover, Ni@NPG manifested excellent reusability and stability due to the robust carbon structure and protective carbon shells, which prevented the imbedded nickel nanoparticles from leaching to the aquatic environment. The activity of the passivated catalyst could be mostly recovered through facile thermal treatment. In addition, the presence of natural organic matters and inorganic anions (HA, HCO_3^-, Cl^-, Br^- and $H_2PO_4^-$) at low concentrations would promote the radical production and oxidation pathways. More importantly, a non-radical pathway was revealed and identified to play the dominant role in catalytic SCP removal. With the mild oxidative potential of the nonradical reaction, the Ni@NPG/PS system could be applied as an effective approach to remediate antibiotics in complicated water matrix, which will provide a robust application in environmental remediation. Furthermore, this high-performance Ni@NPG/PS system can be expected to remediate a wide spectrum of other emerging pollutants in wastewater without secondary contamination.

5.5 References

1. Henry, R. J., THE MODE OF ACTION OF SULFONAMIDES. *Bacteriological Reviews* **1943,** *7*, (4), 175-262.

2. Daughton, C. G.; Ternes, T. A., Pharmaceuticals and personal care products in the environment: agents of subtle change? *Environmental Health Perspectives* **1999,** *107*, (Suppl 6), 907-938.

3. Kümmerer, K., *PHARMACEUTICALS IN THE ENVIRONMENT*. 2008.

4. Kolpin, D. W.; Furlong, E. T.; Meyer, M. T.; Thurman, E. M.; Zaugg, S. D.; Barber, L. B.; Buxton, H. T., Pharmaceuticals, Hormones, and Other Organic Wastewater Contaminants in U.S. Streams, 1999−2000: A National Reconnaissance. *Environmental Science & Technology* **2002,** *36*, (6), 1202-1211.

5. Zessel, K.; Mohring, S.; Hamscher, G.; Kietzmann, M.; Stahl, J., Biocompatibility and antibacterial activity of photolytic products of sulfonamides. *Chemosphere* **2014,** *100*, 167-174.

6. Ingerslev, F.; Halling-Sørensen, B., Biodegradability properties of sulfonamides in activated sludge. *Environmental Toxicology and Chemistry* **2000,** *19*, (10), 2467-2473.

7. Braschi, I.; Blasioli, S.; Gigli, L.; Gessa, C. E.; Alberti, A.; Martucci, A., Removal of sulfonamide antibiotics from water: Evidence of adsorption into an organophilic zeolite Y by its structural modifications. *Journal of Hazardous Materials* **2010,** *178*, (1–3), 218-225.

8. Braschi, I.; Gatti, G.; Paul, G.; Gessa, C. E.; Cossi, M.; Marchese, L., Sulfonamide Antibiotics Embedded in High Silica Zeolite Y: A Combined Experimental and Theoretical Study of Host−Guest and Guest−Guest Interactions. *Langmuir* **2010,** *26*, (12), 9524-9532.

9. Gao, Y.-q.; Gao, N.-y.; Deng, Y.; Yin, D.-q.; Zhang, Y.-s.; Rong, W.-l.; Zhou, S.-d., Heat-activated persulfate oxidation of sulfamethoxazole in water. *Desalination and Water Treatment* **2015,** *56*, (8), 2225-2233.

10. Adams, C.; Wang, Y.; Loftin, K.; Meyer, M., Removal of Antibiotics from Surface and Distilled Water in Conventional Water Treatment Processes. *Journal of Environmental Engineering* **2002,** *128*, (3), 253-260.

11. Asghar, A.; Abdul Raman, A. A.; Wan Daud, W. M. A., Advanced oxidation processes for in-situ production of hydrogen peroxide/hydroxyl radical for textile wastewater treatment: a review. *Journal of Cleaner Production* **2015,** *87*, 826-838.

12. da Silva, S. W.; Klauck, C. R.; Siqueira, M. A.; Bernardes, A. M., Degradation of the commercial surfactant nonylphenol ethoxylate by advanced oxidation processes. *Journal of Hazardous Materials* **2015,** *282*, 241-248.

13. Neyens, E.; Baeyens, J., A review of classic Fenton's peroxidation as an advanced oxidation technique. *Journal of Hazardous Materials* **2003,** *98*, (1–3), 33-50.

14. Wang, Y. X.; Sun, H. Q.; Ang, H. M.; Tade, M. O.; Wang, S. B., Magnetic Fe3O4/carbon sphere/cobalt composites for catalytic oxidation of phenol solutions with sulfate radicals. *Chemical Engineering Journal* **2014,** *245*, 1-9.

15. Saputra, E.; Muhammad, S.; Sun, H. Q.; Ang, H. M.; Tade, M. O.; Wang, S. B., Shape-controlled activation of peroxymonosulfate by single crystal alpha-Mn2O3 for catalytic phenol degradation in aqueous solution. *Applied Catalysis B-Environmental* **2014,** *154*, 246-251.

16. Indrawirawan, S.; Sun, H. Q.; Duan, X. G.; Wang, S. B., Nanocarbons in different structural dimensions (0-3D) for phenol adsorption and metal-free catalytic oxidation. *Applied Catalysis B-Environmental* **2015,** *179*, 352-362.

17. Duan, X. G.; Sun, H. Q.; Kang, J.; Wang, Y. X.; Indrawirawan, S.; Wang, S. B., Insights into Heterogeneous Catalysis of Persulfate Activation on Dimensional-Structured Nanocarbons. *Acs Catalysis* **2015,** *5*, (8), 4629-4636.

18. Duan, X. G.; Sun, H. Q.; Ao, Z. M.; Zhou, L.; Wang, G. X.; Wang, S. B., Unveiling the active sites of graphene-catalyzed peroxymonosulfate activation. *Carbon* **2016,** *107*, 371-378.

19. Duan, X.; Sun, H.; Wang, Y.; Kang, J.; Wang, S., N-Doping-Induced Nonradical Reaction on Single-Walled Carbon Nanotubes for Catalytic Phenol Oxidation. *ACS Catalysis* **2015,** *5*, (2), 553-559.

20. Kang, J.; Duan, X. G.; Zhou, L.; Sun, H. Q.; Tade, M. O.; Wang, S. B., Carbocatalytic activation of persulfate for removal of antibiotics in water solutions. *Chemical Engineering Journal* **2016,** *288*, 399-405.

21. Duan, X.; Ao, Z.; Sun, H.; Indrawirawan, S.; Wang, Y.; Kang, J.; Liang, F.; Zhu, Z. H.; Wang, S., Nitrogen-Doped Graphene for Generation and Evolution of Reactive Radicals by Metal-Free Catalysis. *ACS Applied Materials & Interfaces* **2015,** *7*, (7), 4169-4178.

22. Huang, J.; Wang, J.; Wang, C.; Zhang, H.; Lu, C.; Wang, J., Hierarchical Porous Graphene Carbon-Based Supercapacitors. *Chemistry of Materials* **2015,** *27*, (6), 2107-2113.

23. Tian, W. J.; Zhang, H. Y.; Duan, X. G.; Sun, H. Q.; Tade, M. O.; Ang, H. M.; Wang, S. B., Nitrogen- and Sulfur-Codoped Hierarchically Porous Carbon for Adsorptive and Oxidative Removal of Pharmaceutical Contaminants. *Acs Applied Materials & Interfaces* **2016,** *8*, (11), 7184-7193.

24. Yim, S. D.; Kim, S. J.; Baik, J. H.; Nam, I. S.; Mok, Y. S.; Lee, J.-H.; Cho, B. K.; Oh, S. H., Decomposition of Urea into NH3 for the SCR Process. *Industrial & Engineering Chemistry Research* **2004,** *43*, (16), 4856-4863.

25. Deng, Y.; Xie, Y.; Zou, K.; Ji, X., Review on recent advances in nitrogen-doped carbons: preparations and applications in supercapacitors. *Journal of Materials Chemistry A* **2016,** *4*, (4), 1144-1173.

26. Wang, C.; Kang, J.; Liang, P.; Zhang, H. Y.; Sun, H. Q.; Tade, M. O.; Wang, S. B., Ferric carbide nanocrystals encapsulated in nitrogen-doped carbon nanotubes as an outstanding environmental catalyst. *Environmental Science-Nano* **2017,** *4*, (1), 170-179.

27. Zheng, X. J.; Deng, J.; Wang, N.; Deng, D. H.; Zhang, W. H.; Bao, X. H.; Li, C., Podlike N-Doped Carbon Nanotubes Encapsulating FeNi Alloy Nanoparticles: High-Performance Counter Electrode Materials for Dye-Sensitized Solar Cells. *Angewandte Chemie-International Edition* **2014,** *53*, (27), 7023-7027.

28. Fan, Y.; Ji, Y.; Kong, D.; Lu, J.; Zhou, Q., Kinetic and mechanistic investigations of the degradation of sulfamethazine in heat-activated persulfate oxidation process. *Journal of Hazardous Materials* **2015,** *300*, 39-47.

29. Sun, H.; Wang, Y.; Liu, S.; Ge, L.; Wang, L.; Zhu, Z.; Wang, S., Facile synthesis of nitrogen doped reduced graphene oxide as a superior metal-free catalyst for oxidation. *Chemical Communications* **2013,** *49*, (85), 9914-9916.

30. Chun, K.-Y.; Lee, H. S.; Lee, C. J., Nitrogen doping effects on the structure behavior and the field emission performance of double-walled carbon nanotubes. *Carbon* **2009,** *47*, (1), 169-177.

31. Fang, G.; Gao, J.; Dionysiou, D. D.; Liu, C.; Zhou, D., Activation of Persulfate by Quinones: Free Radical Reactions and Implication for the Degradation of PCBs. *Environmental Science & Technology* **2013,** *47*, (9), 4605-4611.

32. Guan, Y.-H.; Ma, J.; Ren, Y.-M.; Liu, Y.-L.; Xiao, J.-Y.; Lin, L.-q.; Zhang, C., Efficient degradation of atrazine by magnetic porous copper ferrite catalyzed peroxymonosulfate oxidation via the formation of hydroxyl and sulfate radicals. *Water Research* **2013,** *47*, (14), 5431-5438.

33. Rincón, A.-G.; Pulgarin, C., Effect of pH, inorganic ions, organic matter and H2O2 on E. coli K12 photocatalytic inactivation by TiO2: Implications in solar water disinfection. *Applied Catalysis B: Environmental* **2004,** *51*, (4), 283-302.

34. Lipczynska-Kochany, E.; Sprah, G.; Harms, S., Influence of some groundwater and surface waters constituents on the degradation of 4-chlorophenol by the Fenton reaction. *Chemosphere* **1995,** *30*, (1), 9-20.

35. Lian, L.; Yao, B.; Hou, S.; Fang, J.; Yan, S.; Song, W., Kinetic Study of Hydroxyl and Sulfate Radical-Mediated Oxidation of Pharmaceuticals in Wastewater Effluents. *Environmental Science & Technology* **2017,** *51*, (5), 2954-2962.

36. Kläning, U. K.; Wolff, T., Laser Flash Photolysis of HClO, ClO−, HBrO, and BrO− in Aqueous Solution. Reactions of Cl- and Br-Atoms. *Berichte der Bunsengesellschaft für physikalische Chemie* **1985,** *89*, (3), 243-245.

37. Yu, X. Y.; Barker, J. R., Hydrogen peroxide photolysis in acidic aqueous solutions containing chloride ions. I. Chemical mechanism. *Journal of Physical Chemistry A* **2003,** *107*, (9), 1313-1324.

38. Das, T. N., Reactivity and Role of SO5•- Radical in Aqueous Medium Chain Oxidation of Sulfite to Sulfate and Atmospheric Sulfuric Acid Generation. *The Journal of Physical Chemistry A* **2001,** *105*, (40), 9142-9155.

39. Neta, P.; Huie, R. E.; Ross, A. B., Rate Constants for Reactions of Inorganic Radicals in Aqueous Solution. *Journal of Physical and Chemical Reference Data* **1988,** *17*, (3), 1027-1284.

40. von Sonntag, C., *Free-radical-induced DNA damage and its repair*. Springer: 2006.

41. Vione, D.; Maurino, V.; Minero, C.; Pelizzetti, E., An Empirical, Quantitative Approach to Predict the Reactivity of Some Substituted Aromatic Compounds Towards Reactive Radical Species (Cl2-·, Br2-·, ·NO2, SO3-·, SO4-·) in Aqueous Solution (3 pp). *Environmental Science and Pollution Research* **2006,** *13*, (4), 212-214.

42. Anipsitakis, G. P.; Dionysiou, D. D.; Gonzalez, M. A., Cobalt-Mediated Activation of Peroxymonosulfate and Sulfate Radical Attack on Phenolic Compounds. Implications of Chloride Ions. *Environmental Science & Technology* **2006,** *40*, (3), 1000-1007.

43. De Laat, J.; Truong Le, G.; Legube, B., A comparative study of the effects of chloride, sulfate and nitrate ions on the rates of decomposition of H2O2 and organic compounds by Fe(II)/H2O2 and Fe(III)/H2O2. *Chemosphere* **2004,** *55*, (5), 715-723.

44. Liu, X.-W.; Sun, X.-F.; Li, D.-B.; Li, W.-W.; Huang, Y.-X.; Sheng, G.-P.; Yu, H.-Q., Anodic Fenton process assisted by a microbial fuel cell for enhanced degradation of organic pollutants. *Water Research* **2012,** *46*, (14), 4371-4378.

45. Beitz, T.; Bechmann, W.; Mitzner, R., Investigations of reactions of selected azaarenes with radicals in water. 2. Chlorine and bromine radicals. *Journal of Physical Chemistry A* **1998,** *102*, (34), 6766-6771.

46. Fang, J.; Fu, Y.; Shang, C., The Roles of Reactive Species in Micropollutant Degradation in the UV/Free Chlorine System. *Environmental Science & Technology* **2014,** *48*, (3), 1859-1868.

47. Merenyi, G.; Lind, J., REACTION-MECHANISM OF HYDROGEN ABSTRACTION BY THE BROMINE ATOM IN WATER. *Journal of the American Chemical Society* **1994,** *116*, (17), 7872-7876.

48. Buxton, G. V.; Greenstock, C. L.; Helman, W. P.; Ross, A. B., Critical Review of rate constants for reactions of hydrated electrons, hydrogen atoms and hydroxyl radicals (·OH/·O− in Aqueous Solution. *Journal of Physical and Chemical Reference Data* **1988,** *17*, (2), 513-886.

49. Zuo, Z.; Cai, Z.; Katsumura, Y.; Chitose, N.; Muroya, Y., Reinvestigation of the acid–base equilibrium of the (bi)carbonate radical and pH dependence of its reactivity with inorganic reactants. *Radiation Physics and Chemistry* **1999,** *55*, (1), 15-23.

50. Kim, S. D.; Cho, J.; Kim, I. S.; Vanderford, B. J.; Snyder, S. A., Occurrence and removal of pharmaceuticals and endocrine disruptors in South Korean surface, drinking, and waste waters. *Water Research* **2007,** *41*, (5), 1013-1021.

51. Peyton, G. R., The free-radical chemistry of persulfate-based total organic carbon analyzers. *Marine Chemistry* **1993,** *41*, (1), 91-103.

52. Matthew, B. M.; Anastasio, C., A chemical probe technique for the determination of reactive halogen species in aqueous solution: Part 1 – bromide solutions. *Atmos. Chem. Phys.* **2006,** *6*, (9), 2423-2437.

53. Herrmann, H.; Ervens, B.; Jacobi, H.-W.; Wolke, R.; Nowacki, P.; Zellner, R., CAPRAM2.3: A Chemical Aqueous Phase Radical Mechanism for Tropospheric Chemistry. *Journal of Atmospheric Chemistry* **2000,** *36*, (3), 231-284.

54. Maruthamuthu, P.; Neta, P., Phosphate radicals. Spectra, acid-base equilibriums, and reactions with inorganic compounds. *The Journal of Physical Chemistry* **1978,** *82*, (6), 710-713.

55. Sun, H.; Kwan, C.; Suvorova, A.; Ang, H. M.; Tadé, M. O.; Wang, S., Catalytic oxidation of organic pollutants on pristine and surface nitrogen-modified carbon nanotubes with sulfate radicals. *Applied Catalysis B: Environmental* **2014,** *154–155*, 134-141.

56. Zeng, L.; Cui, X.; Chen, L.; Ye, T.; Huang, W.; Ma, R.; Zhang, X.; Shi, J., Non-noble bimetallic alloy encased in nitrogen-doped nanotubes as a highly active and durable electrocatalyst for oxygen reduction reaction. *Carbon* **2017,** *114*, 347-355.

57. Liang, P.; Zhang, C.; Duan, X.; Sun, H.; Liu, S.; Tade, M. O.; Wang, S., An insight into metal organic framework derived N-doped graphene for the oxidative degradation of persistent contaminants: formation mechanism and generation of singlet oxygen from peroxymonosulfate. *Environmental Science: Nano* **2017,** *4*, (2), 315-324.

Chapter 6: Magnetic Ni-Co alloy encapsulated N-doped carbon nanotubes for catalytic membrane degradation of emerging contaminants

This chapter has been published on journal "Chemical Engineering Journal", DOI: 10.1016/j.cej.2019.01.035.

Abstract

Nitrogen-doped carbon nanotubes encapsulated with Ni-Co alloy nanoparticles (NiCo@NCNTs) were readily synthesized by annealing Ni/Co salts with dicyandiamide. The magnetic nanocarbons were assembled as a flat membrane for heterogeneous degradation of organic toxins. The synergistic effect of nitrogen doping and metal alloy encapsulation significantly enhanced the catalytic activity and stability of NCNTs in catalytic activation of peroxymonosulfate (PMS) for purification of an emerging pollutant, ibuprofen. The hybrid catalyst yielded a fast reaction rate of 0.31 min^{-1}, which was 23.4 and 5.8 times higher than that of pristine CNTs and monometallic (Ni or Co) encased CNTs, respectively. The robust membrane catalysis was further confirmed by degrading other organic aqueous pollutants, such as naproxen, sulfachloropyridazine, phenol, methylene blue, and methyl orange. Mechanistic investigations were performed using electron paramagnetic resonance and competitive radical screening tests, which indicated that radical ($^{\bullet}OH$ and $SO_4^{\bullet-}$) oxidation and nonradical pathway co-existed and played critical roles in the catalytic degradation. The study provides a novel advanced oxidation system with catalytic membrane for wastewater remediation.

6.1 Introduction

Pharmaceuticals have emerged as contaminants in water effluents, which have attracted intensive attention due to their ubiquity and serious adverse effects on the environment. Ibuprofen (IBP) is a typical non-steroidal anti-inflammatory drug (NSAID) and has been extensively utilized in the past decades for quick pain release [1]. However, its anti-inflammation and high water solubility have made it recalcitrant to biodegradation in traditional wastewater treatment units, leading to the accumulation and contamination in municipal and natural water systems [2]. Recently, advanced oxidation processes (AOPs) have offered an effective solution to address the ever-increasing challenge utilizing the chemically reactive oxygen species (ROS) to efficiently and non-selectively degrade those recalcitrant organic pollutants [3].

Fenton reaction, as one of the most popular hydroxyl radicals ($^{\bullet}OH$) based AOPs, has been widely studied and applied in wastewater treatment. More recently, sulfate radicals ($SO_4^{\bullet-}$) with a higher redox potential (3.1 V versus 2.7 V of $^{\bullet}OH$) and a greater pH tolerance in comparison with $^{\bullet}OH$ have been applied for oxidation of organic contaminants [3-6]. Numerous approaches have been employed to activate peroxymonosulfate (PMS) to generate $SO_4^{\bullet-}$ by heat, ultraviolet (UV) radiation and catalysis, among which catalytic PMS activation is more favorable owing to high $SO_4^{\bullet-}$ productivity, mild condition and low energy consumption [7]. Among the catalytic sulfate radical based AOPs (SR-AOPs), transition metal ions (Fe^{2+}, Co^{2+}, and Mn^{2+}) and their oxides are benchmarks that have been extensively used because of their excellent catalytic ability, good stability and potential magnetic separation [8-10]. Nevertheless, the inevitable metal leaching, strict reaction environment requirement (pH < 3) and sludge production implicated by metal catalysts have hindered their large-scale application in the water treatment [11].

Nanocarbon materials such as graphene oxide (GO) and carbon nanotubes (CNTs) have exhibited the merits of abundant carbon sources, environmental-friendly nature, large theoretical surface area, unique physicochemical and electronic properties. Recently, nanocarbons have been successfully applied as promising alternatives to metal catalysts in oxygen reduction reaction (ORR), oxygen evolution reaction (OER) and AOPs [12, 13]. In our previous studies, CNTs and reduced graphene oxide (rGO) have shown excellent efficiency in PMS/persulfate (PS) activation for organics degradation, even surpassing most transition metal oxides [14, 15].

However, carbon catalysts in AOPs suffer from the drawbacks of poor stability and inconvenient recycling, severely stalling their further application. It was suggested that structural and compositional modifications were effective strategies to enhance the performances of carbocatalysts. Sun et al. reported that N doping in graphene demonstrated a phenomenal promotion in the PMS activation [16]. Anchoring metal nanocrystals on nanocarbons would also be beneficial because the metals are enriched with electrons which endow carbons with high electron conductivity and electron-transfer capacity. It has been reported that encapsulation of metal nanoparticles (NPs) in carbon can produce excellent catalytic activity and stability for PS activation, realizing 100% sulfachloropyridazine (SCP) degradation even after four times of reuse [17].

With such an inspiration, we fabricated pod-like nitrogen-doped carbon nanotubes with encapsulation of Ni-Co alloy NPs. The nanohybrids were applied in PMS activation. In addition, we employed the materials in a flat membrane operation in contrast with the previous heterogeneous systems. This work demonstrates a novel approach in tailored nanomaterials for SR-AOPs with excellent catalytic activity and superior stability.

6.2 Experimental

6.2.1 Materials and chemicals.

Dicyandiamide (> 99.0%), nickel nitrate hexahydrate ($Ni(NO_3)_2 \cdot 6H_2O$, > 99.9%), cobalt nitrate hexahydrate ($Co(NO_3)_2 \cdot 6H_2O$, >99.9%), sodium bicarbonate ($NaHCO_3$, >99.9%), potassium peroxymonosulfate ($2KHSO_5 \cdot 3KHSO_4 \cdot K_2SO_4$, Oxone), p-benzoquinone (PBQ), *tert*-butyl alcohol (TBA), ibuprofen (> 99.9%, IBP), phenol (> 99.9%), methylene blue (MB) (> 99.9%), methyl orange (MO) (> 99.9%), naproxen (> 99.9%), sulfachloropyridazine (SCP) and 5, 5-dimethylpyrroline-oxide (DMPO, > 99.0%) were purchased from Sigma-Aldrich. Phenol (> 99.0%), acetone, ethanol and hydrochloric acid (32-37 wt%) were obtained from Chem-Supply. As reference materials, commercial nickel oxide (NiO, 99.9%) and cobalt oxide (CoO, 99.8%) were obtained from Fluka. High purity nitrogen gas (99.999%) was obtained from BOC. Deionized water (DI) was used in all of the experiments. All the chemicals used herein were of analytic grade and used as received without any further purification.

6.2.2 Synthesis of NiCo@NCNT and membrane fabrication.

NiCo@NCNT was synthesized using nickel nitrate hexahydrate ($Ni(NO_3)_2 \cdot 6H_2O$), cobalt nitrate hexahydrate ($Co(NO_3)_2 \cdot 6H_2O$) and dicyandiamide ($C_2H_4N_4$) as the precursors via a direct pyrolysis method. In a typical synthesis, $Ni(NO_3)_2 \cdot 6H_2O$ (3 g) and $Co(NO_3)_2 \cdot 6H_2O$ (3 g) were put into a beaker with 100 mL of DI water under a stirring rate of 300 rpm. After stirring for 3 h, $C_2H_4N_4$ (6 g) and $NaHCO_3$ (0.08 g) were added into the dark purplish water solution. Then, the resultant solution was kept stirring at 300 rpm for overnight at 60 ^oC until the water level dropped to 50 mL. After the mixture was dried in an oven at 80 ^oC for three days, the solid mixture was subsequently ground into fine powders and then put into a furnace for calcination at designed temperature (700, 800 or 900 ^oC) for 6 h in argon atmosphere, denoted as NiCo@NCNT-700, NiCo@NCNT-800 and NiCo@NCNT-900, respectively. Finally, the resultant raw NiCo@NCNT was washed by 32% HCl overnight to remove the

Ni/Co NPs adhered on the CNT surface. The acid treated material was then washed by ethanol and excess DI water for several times until the pH reached neutral (pH 7 ± 0.5). The weight ratio of 1:1:2 for $Ni(NO_3)_2 \cdot 6H_2O$, $Co(NO_3)_2 \cdot 6H_2O$ and $C_2H_4N_4$ accordingly was used for a control catalyst (NiCo@NCNT-1:1). Meanwhile, different weight ratios of metal and carbon precursors were used for investigating the effect of different Ni/Co ratios on catalytic activity of NiCo@NCNT. Specifically, weight ratios of 1:2:3 and 2:1:3 ($Ni(NO_3)_2 \cdot 6H_2O$: $Co(NO_3)_2 \cdot 6H_2O$: $C_2H_4N_4$) were used for NiCo@NCNT-1:2 and NiCo@NCNT-2:1, respectively.

The catalyst (0.01 g) was first treated by ultrasonics in DI water for 5 min and then the well-dispersed catalyst solution was slowly vacuum deposited on a 50 mm (diameter) and 0.45 μm (pore size) Teflon filter paper. Subsequently, a thin NiCo@NCNT flat membrane with a thickness of about 100 μm was formed on the top of the filter paper. Finally, another Teflon filter paper was rested on the top of the catalyst layer.

6.2.3 Characterizations.

The morphologies of samples were investigated with field emission scanning electron microscopy on FE-SEM, Zeiss Neon 40 EsB, transmission electron microscopy (TEM) on JEOL 2100 and energy-dispersive X-ray spectroscopy (EDX) elemental mapping on FEI Titan G2 80-200 TEM/STEM. X-ray diffraction (XRD) patterns were performed on a Bruker D8-Advanced X-ray instrument using a Cu-Kα radiation with λ at 1.5418 Å. Raman spectroscopy analysis was recorded on an ISA dispersive Raman spectrometer with the argon ion laser (514 nm). Nitrogen sorption isotherms were acquired on a Tristar II 3020 in liquid nitrogen (-196 ^oC) and the samples were degassed for three hours at 100 ^oC prior to the analysis. The specific surface area and pore size distribution were evaluated by the Brunauer-Emmett-Teller (BET) equation and the Barrett-Joyner-Halenda (BJH) method, respectively. The magnetization

behavior of the samples was measured using an Oxford vibrating sample magnetometer (VSM) 3001 at room temperature. X-ray photoelectron spectroscopy (XPS) was carried out on a Thermo ESCALAB 250 XPS microscope with monochromatic Al-Kα X-rays at a photon energy of 1486.7 eV, and with a base pressure less than 1×10^{-9} mBar under ultra-high vacuum (UHV) conditions. (Pass energy = 160 eV, dwell time = 120 s, number of scan = 1) And the high-resolution spectra were collected using an analysis area of ≈ 300 μm × 700 μm. The *in situ* characterization method of electron paramagnetic resonance (EPR) was applied to probe the active radicals using DMPO as the spin-trapping agent. The EPR spectra were analyzed and exported by the spin-fitting package of Bruker Xeon software for DMPO-SO_4 (α_H = 0.78, α_H = 1.48, α_H = 9.6, and α_H = 13.2) and DMPO-OH (α_H = 14.8, α_H = 14.8) under the reaction conditions (IBP = 20 mg/L, catalyst = 0.05 g/L, PMS = 0.65 mM, DMPO = 0.08 M, temperature = 25 ^oC).

6.2.4 Adsorption and catalytic oxidation of IBP solutions.

Typical adsorption experiments were conducted in a flat membrane operation by allowing 200 mL IBP (20 mg/L) solution to permeate a NiCo@NCNT cake at 10 mL min^{-1}, 25 ^oC under gravity. At each cycle in about 20 min, a small volume of the solution was sampled and analyzed on ultra-high performance liquid chromatography (UHPLC, Thermo-Fisher Scientific 3000) with a UV detector at the wavelength of 210 nm. An Acclaim RSLC C-18 column was used and a mixed solution of 40% acetonitrile and 60% acetic acid was applied as the mobile phase at a constant flow rate of 0.2 mL/min. To exclude the adsorption effect of Teflon filter paper on IBP, the adsorption capacity of the filter paper to IBP was initially evaluated.

Ibuprofen degradation was then performed in a similar process to the adsorption experiment except for the introduction of PMS to the IBP solution before permeating through the catalyst

bed. When each degradation cycle was completed, a small volume of the solution was sampled and quenched immediately by adding absolute ethanol. The catalyst was used directly after each cycle without any treatment. The concentration of IBP was then determined by the UHPLC. At least three tests of the key adsorption and degradation experiments were carried out for presenting mean values and standard deviations.

6.2.5 Catalyst recycling and stability.

The used catalyst after four successive cycle tests was recycled from the membrane bed. In an effort to address the IBP oxidation performance in natural waters, the reaction solution was buffered at pH 7.2 by phosphate solution ($H_2PO_4^-$) with a lowered IBP concentration at 0.5 mg L^{-1}. All the catalysts were washed thoroughly with excessive ultrapure water for several times and dried in an oven at 60 ^oC overnight. Then another 200 mL IBP solution (20 mg/L) was used for a new set of degradation tests. In addition, after the third set of catalytic reaction, the used catalyst was recovered and heated in argon at 350 ^oC for 3 h for regeneration.

6.2.6 Mechanistic studies of the catalytic processes.

The mechanism of PMS activation on NiCo@NCNT was investigated by EPR from Bruker. A spin-trapping agent, 5, 5-dimethylpyrroline-oxide (DMPO), was selected for $SO_4^{\bullet-}$ and $^{\bullet}OH$ during the PMS activation. The operation conditions were set as follows: centre field of 3515 G; sweep width of 100 G; microwave frequency of 9.87 GHz; power setting of 18.75 mW; and scan number of 3. The radical quantitative information was acquired from the Spin Fitting from a Bruker Xenon Software Package. Quenching tests were also conducted using ethanol and *tert*-butyl alcohol (TBA) to verify the contributions from $SO_4^{\bullet-}$ and $^{\bullet}OH$.

6.3 Results and discussion

6.3.1 Characterizations of NiCo@NCNT.

The morphologies and structures of as-prepared NiCo@NCNT were studied by SEM and TEM. The SEM image (**Figure** 6.1a) of NiCo@NCNT shows that the regular straight CNTs are at 20 - 200 nm in outer diameters and 10 µm in length. The TEM images of NiCo@NCNT-800 in **Figure**s 6.1b and 6.1c show that the NiCo NPs are completely isolated within the CNT compartments. A single NiCo NP (10-100 nm in diameter) is contained in each compartment, exhibiting a well-defined pea-pod-like structure. Moreover, NiCo NPs were coated with several graphitic layers with an interlayer spacing of 0.34 nm in **Figure**s 6.1d-f, which provides dual protection of metal NPs from oxidation and leaching. The effect of pyrolysis temperature on the CNTs morphology is shown in **Figure** 6.2. The SEM image of NiCo@NCNT-700 (**Figure** 6.2a) reveals that some graphite has not yet grown into a full tube while the CNTs prepared at 900 ^{o}C (**Figure** 6.2b) presented the least tube shape due to the breakdown of CNTs at a high temperature. The TEM images (**Figure** 6.2c and d) show that some NiCo NPs are encapsulated in the individual graphene sphere instead of CNTs. Therefore, it can be concluded that, the encapsulation of NiCo NPs into a graphene sphere is in the initial stage of the CNT growth at 700 ^{o}C.

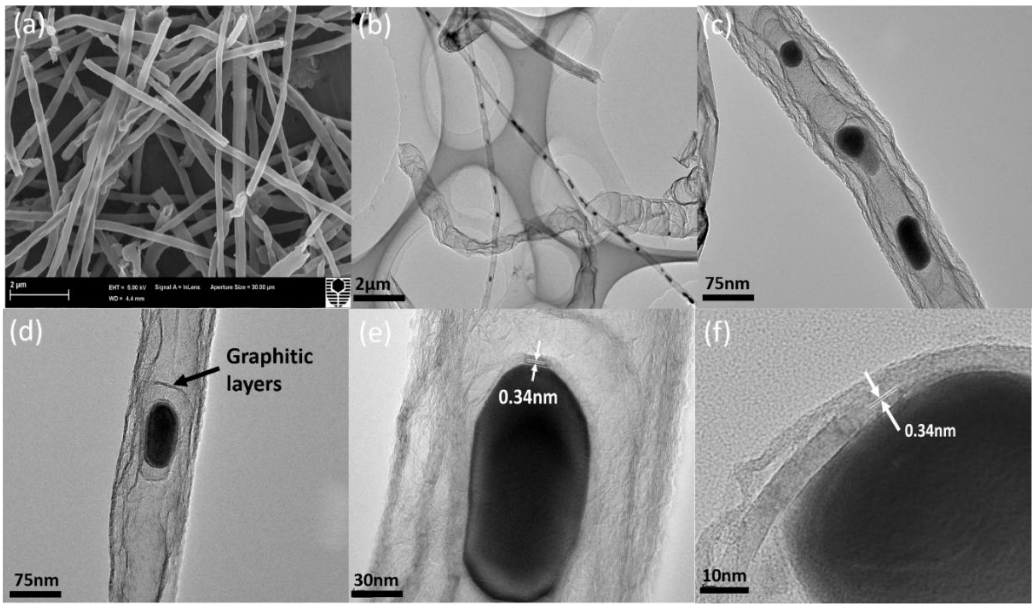

Figure 6.1 (a) SEM image, (b), (c) and (d) TEM images, (e) and (f) HRTEM images of NiCo@NCNT-800.

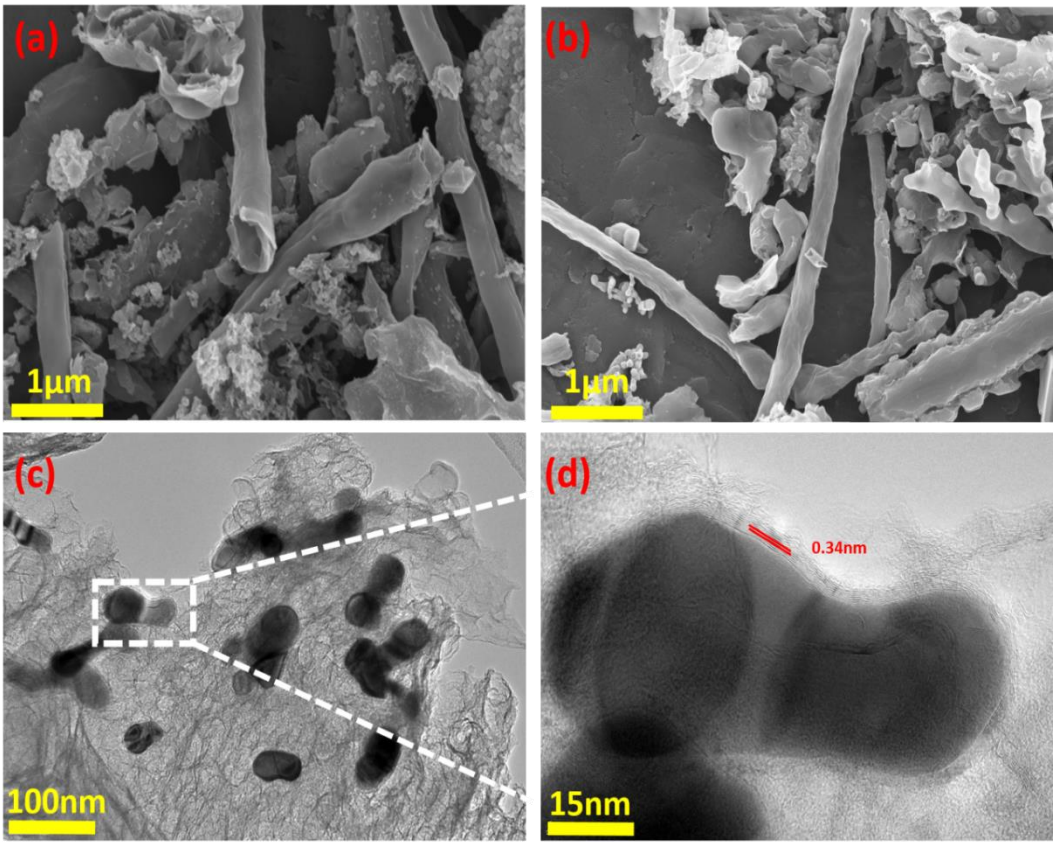

Figure 6.2 SEM images of (a) NiCo@NCNT-700, (b) NiCo@NCNT-900, (c) TEM image of NiCo@NCNT-700, and (d) HRTEM of NiCo@NCNT-700.

XRD patterns of NiCo@NCNT are shown in **Figure** 6.3a, where the broad diffraction peak centered at 2θ ≈ 26.2° is assigned to the (002) facet of graphite carbon. As the synthesis temperature elevates from 700 to 900 ºC, the intensity of the graphite peak increases accordingly, indicating the disappearance of some functional groups at higher temperatures [18]. In comparison with CNT, the XRD patterns of NiCo@NCNT show the (002) peak shifts to a higher 2θ degree, implying a better reducibility due to nitrogen modification [19]. The diffraction peaks at 44.5°, 51.7° and 76.3° are corresponding to the (111), (200) and (220) planes of the NiCo alloy, respectively. The XRD results also show that all the samples with different Ni/Co ratios have the same diffraction peaks. However, when the Ni: Co ratio increases from 0.5 to

2, the peak intensity is largely amplified. This can be attributed to the easier reduction of Ni^{2+} than Co^{2+} during the pyrolysis process [20]. Moreover, the NiCo alloy peaks diminished considerably after acid washing, which indicates the successful removal of unstable metal NPs on the surfaces.

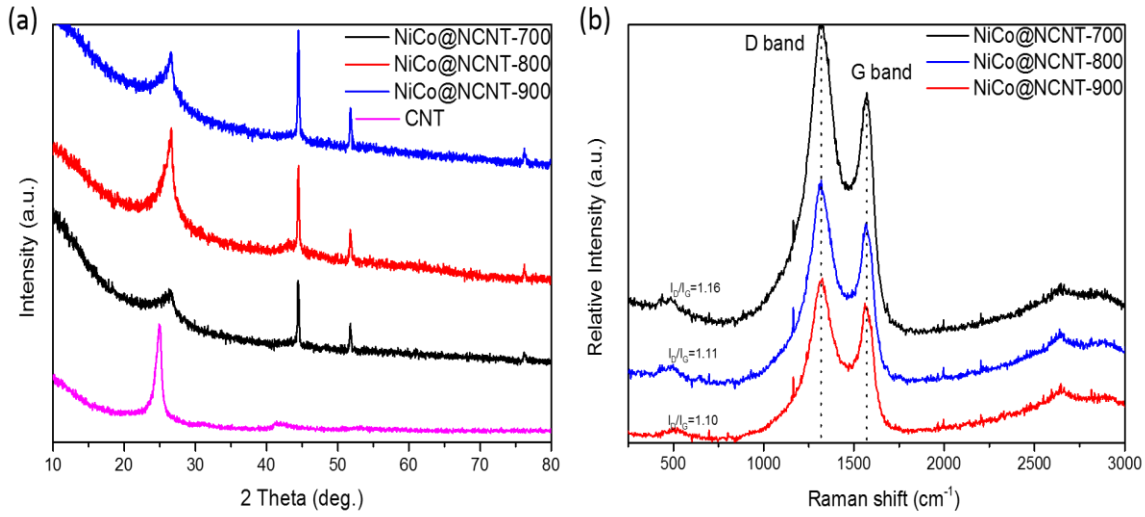

Figure 6.3 (a) XRD patterns of NiCo@NCNT-700, -800, -900 and CNT, (b) Raman spectra of NiCo@NCNT-700, -800, and -900.

Two typical carbonaceous peaks, representative of D (1326 cm^{-1}) and G (1567 cm^{-1}) bands are exhibited in Raman spectra (**Figure** 6.3b). It is shown that the I_D/I_G ratio gradually reduces from 1.16 to 1.10 with increasing fabrication temperature from 700 to 900 ^oC, suggesting the increase of CNTs crystallinity at a higher fabrication temperature [21]. In addition, NiCo@NCNT-800 shows a greater I_D/I_G value (1.11) than CNT (0.99), which can be attributed to both the incorporation of N dopants and metal encapsulation.

N_2 adsorption/desorption isotherms and the pore size distributions of NiCo@NCNT catalysts at different synthesis temperatures are shown in **Figure** 6.4. It can be seen that the N_2 adsorption increases with the synthesis temperature. The specific surface areas of

NiCo@NCNT-700, NiCo@NCNT-800 and NiCo@NCNT-900 are calculated to be 445.6, 537.5 and 801.4 m^2/g, respectively.

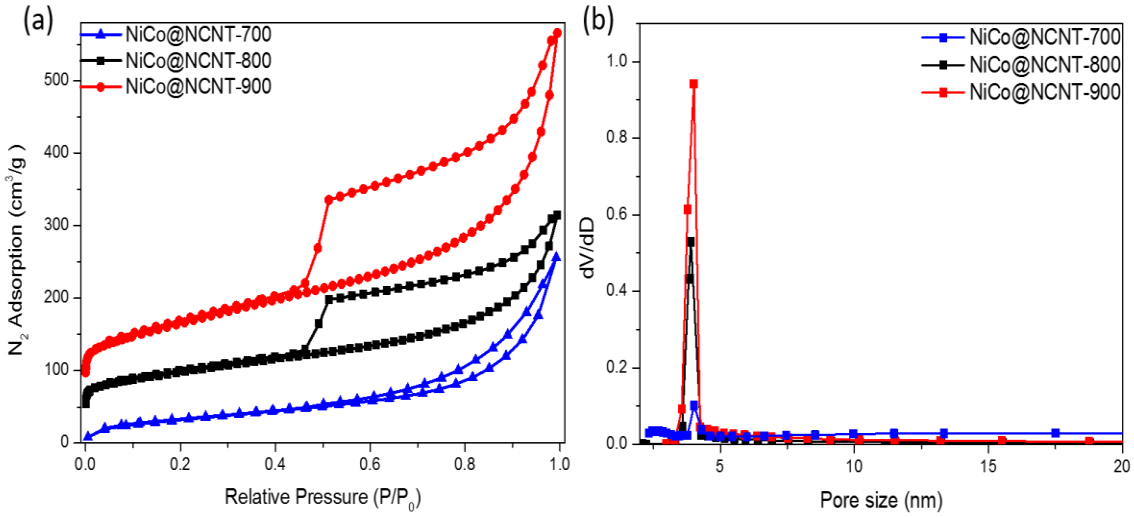

Figure 6.4 (a) N_2 sorption isotherms, and (b) pore size distributions of NiCo@NCNT-700, -800 and -900.

The enhancement is due to the formation of porous structure and the breakdown of carbon nanotubes at higher temperatures, hereby creating more edging sites and structural defects. In addition, all the three samples exhibit a typical IV isotherm with a H3 type hysteresis loop at a relative pressure P/P_0 of 0.4 - 0.9, indicating the mesoporous structures of NiCo@NCNT composites [22]. **Figure** 6.4b reveals a single mode of pore size distributions centered at around 4 nm for all the catalysts, which suggests the minor influence of pyrolysis temperature on the CNT pore size.

In **Figure** 6.5a, the XPS survey spectra of NiCo@NCNT in different fabrication conditions show the peaks at around 285, 400, 532, 780, and 855 eV, corresponding to C 1s, N 1s, O 1s, Co 2p and Ni 2p, respectively. The N doping level (N/C ratio) decreased from 0.08 to 0.07 for the sample prepared at temperatures from 700 to 900 ^oC, revealing that the doping degree of N

species in the carbon structure is largely dependent on the fabrication temperature [17, 23]. It was reported that both the doping levels and chemical states of N with graphitic carbon scaffold and other species could influence the catalytic performance of N-doped carbon materials [24]. As shown in **Figure** 6.5b, the high-resolution XPS N 1s spectrum of NiCo@NCNT can be fitted into four peaks with binding energies at 398.8, 401.1, 403.2 and 405.9 eV, corresponding to pyridinic N, pyrrolic N, graphitic N and oxidized N, respectively. Their atomic structures of different N species in CNT are shown in **Figure** 6.6. The effect of preparation conditions on N species are further analyzed (**Figure** 6.5f). With the increase of temperature, the contents of oxynitride, pyridinic-N and pyrrolic-N reduce accordingly while graphitic N was more thermally stable. In addition, the oxygen contents of the samples are at very low levels and continually decline with the increased pyrolysis temperatures. The peaks in C 1s spectrum deconvoluted at C-C, C-Ni/Co (284.9 eV), C-N (286.1 eV), C-O (287.5 eV), C=O (289.2 eV) and O-C=O (291.1 eV) bonds, respectively (**Figure** 6.5c) [25-28]. Because that XPS is an insensitive tool to quantify the sp^2 and sp^3 hybridized carbons, which typically manifests a difference with 0.6 eV. In this work, the two types of carbon have been combined to assign at 284.9 eV. By using a Shirley background fitting method, the Co 2p peak was best fitted with two spin-orbit doublets, Co^{2+} and Co^{3+}, and two Co^0 satellites (**Figure** 6.5d). In addition, the Ni 2p spectrum was split into three peaks, Ni^{2+} and Ni^{3+}, and two Ni^0 (**Figure** 6.5e) [28-30]. $Co^{2+/3+}$ and $Ni^{2+/3+}$ are located at the outer surface of NiCo alloy nanoparticles owing to the exposure to air. The metallic states of Co and Ni are both found in the XPS spectra, which can further indicate that the nanoparticles on the N doped carbon nanofibers are NiCo alloy.

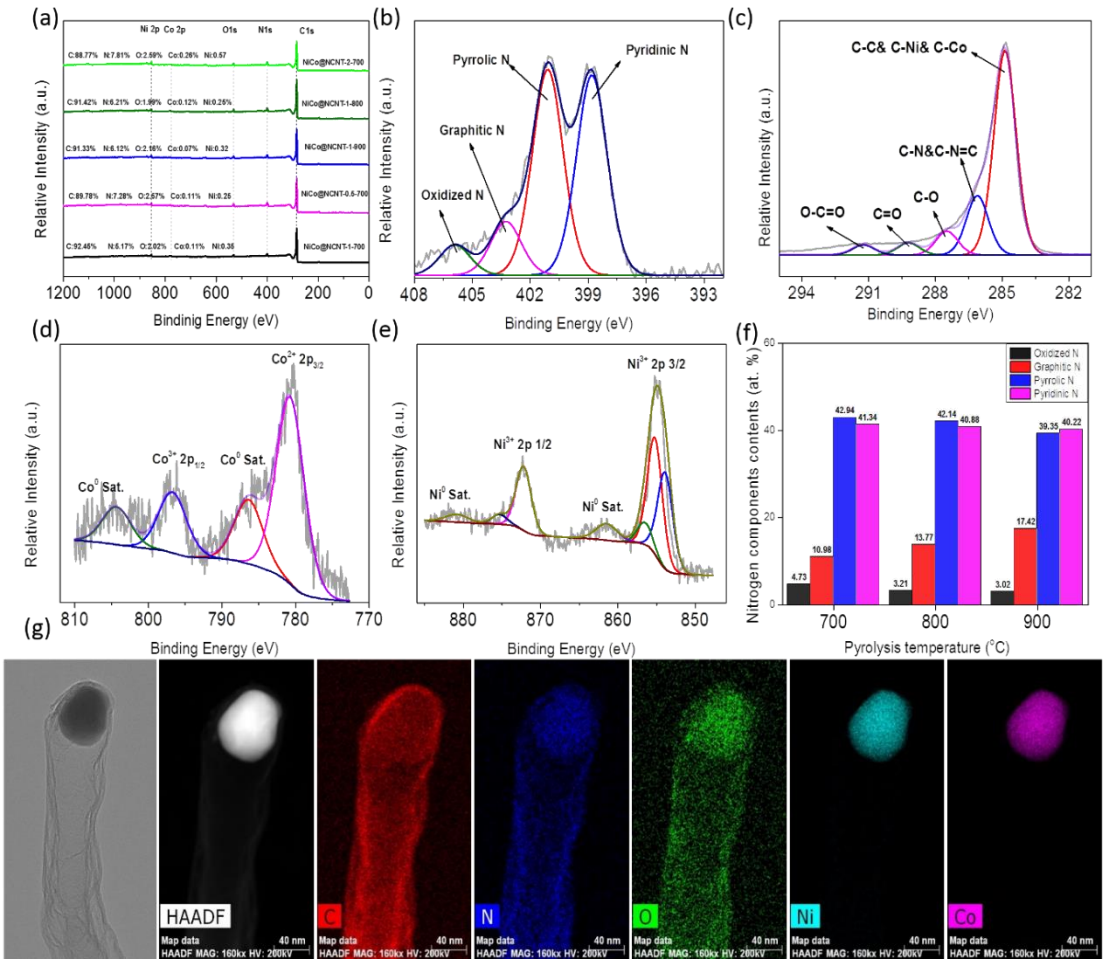

Figure 6.5 (a) XPS survey of NiCo@NCNT-700, -800 and -900; (b) C 1s spectra, (c) N 1s spectra, (d) Ni 2p spectra, (e) Co 2p spectra of NiCo@NCNT-800, (f) contents of four N species at different temperature, and (g) high angle annular dark field scanning TEM image (HAADF-STEM) of NiCo@NCNT-800 and its energy-dispersive X-ray spectroscopy (EDX) elemental mapping images.

It is also indicated that Ni and Co levels are kept at a relatively low level for all the samples due to the synergistic effect of acid treatment and geometric carbon confinement, which is revealed by the TEM images (**Figure** 6.1). The elemental mapping (**Figure** 6.5g) together with EDS analysis illustrate the inner structure and elemental distributions of the composites. It can be seen that C, N, and O elements are uniformly dispersed along the carbon nanotubes while

Ni and Co are primarily distributed in the encapsulated metal particles in the form of Ni/Co alloy, which is consistent with the above XPS results.

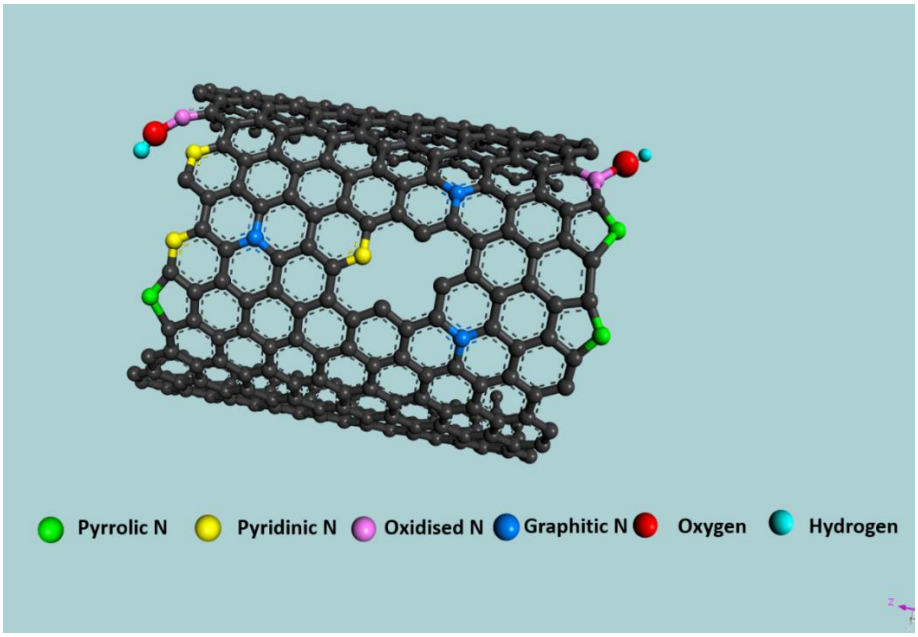

Figure 6.6 Different types of N-doping in carbon network.

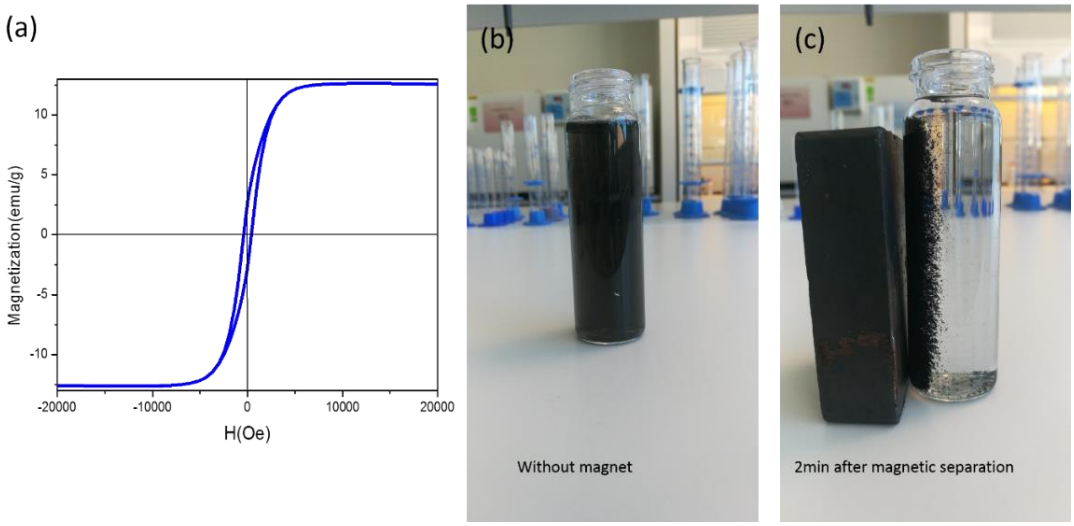

Figure 6.7 (a) Magnetisation curve of magnetic NiCo@NCNT-800. (b) Photo of the well-dispersed NiCo@NCNT-800 in water. (c) Photo of magnetic separation of NiCo@NCNT-800.

The encapsulation of metal alloy nanocrystals (MAN) in CNT during the fabrication not only brings in unique structural morphology, but also endows CNT of magnetic property. The

magnetic property of synthesized NiCo@NCNT was investigated by VSM and shown in **Figure** 6.7a. The magnetic hysteresis loop of NiCo@NCNT-800 was obtained between ± 20 kOe at room temperature, exhibits that the saturated magnetization (Ms) and coercivity (Hc) are 12.6 emu/g and 592 Oe, respectively, thus exhibiting the superparamagnetic characteristic. The difficulty in recycling of a carbon catalyst can significantly hinder its extensive application in wastewater treatment. Thus, by taking advantage of the magnetic property of NiCo@NCNT, the catalyst can be easily recycled for multiple usages. **Figure** 6.7b displays that the NiCo@NCNT-800 can be readily dispersed in water to form a stable solution. In addition, the catalyst responded rapidly to the external magnet owing to its excellent magnetic properties (**Figure** 6.7c). After 2 min of magnetic separation, most of the NiCo@NCNT catalyst particles were drawn to the bottle sidewall. As a result, this dispersion and separation process can be repeatedly applied on NiCo@NCNT by an external magnetic field, which is convenient to its reusability in water treatment and minimizes the secondary pollution. The mass loss of catalysts in each time of the reuse was negligible (< 5%).

6.3.2 Catalytic performance of NiCo@NCNT in IBP degradation.

As shown in **Figure** 6.8a, almost no IBP was removed by PMS alone, meaning PMS itself could hardly oxidize IBP at ambient temperature. Meanwhile, without the addition of PMS, the adsorption capacity of NiCo@NCNT-800 on IBP was also investigated, where a moderate of 6% of IBP removal was achieved via four consecutive cycles of adsorption tests. In our previous studies, a nitrogen doped carbonaceous catalyst showed an improvement in catalysis to activate PMS for phenol degradation, compared to other pristine nanocarbons such as graphene and single-wall carbon nanotubes [14, 31, 32]. In this study, unmodified CNT presents a relatively low catalytic activity in PMS activation and 36% of IBP is degraded, whilst N-doped CNT shows nearly doubled efficiency at 71% IBP removal after the 4th degradation cycle. The density functional theory calculations have unveiled that the incorporation of N species can

manipulate the charge density of the adjacent carbon atoms to be positivity charged which is beneficial for the interaction with the negatively charged peroxide O-O bond in PMS. Moreover, the N atoms would act as Lewis basic sites to conduct an electron-transfer reaction for evolution of free radicals [27].

Moreover, it can be found that NiCo@NCNT exhibited the highest IBP removal efficiency among all samples, where the complete removal was reached during the 3rd cycle, presenting 2.8 and 1.3-fold higher over CNT and NCNT in IBP removal rates. This reveals the dramatic catalytic enhancement might be realized by NiCo NPs encapsulation. The PMS activation and IBP oxidation rely on electron transfer from IBP (electron donor) to PMS (electron accepter), which NiCo@NCNT catalyst acts as a facile electron transfer mediator [33]. The NiCo alloy NPs can efficiently excite electrons to enrich the charge density of CNTs surface, which is believed to be responsible for the catalytic enhancement in PMS activation. Such an electron transfer would be facilitated as NiCo@NCNT surface serves to bring together electron donor and acceptor pairs to a close proximity [33]. A recent study reported that the transition metal (TM) species could be extracted by nitrogen atoms to form TM-N bonds in the carbon support, which were believed to be catalytic active sites [34]. Thus, the geometric confinement of NiCo NPs within the N doped carbon structures could generate highly active TM-N sites. In addition, the loading of TM into carbon substrate could improve the affinity of metal to carbon and further promote the electron transfer from the metal to the interacted carbon region. Specifically, the hybrid structure changes the electronic structure and reduces the surface work function of the carbon walls, consequently enhancing the electron migration process [30, 35]. Based on the analysis mentioned above, it is deduced that the superior catalysis of NiCo@NCNT towards IBP oxidation can be attributing to the increased active sites induced by N-doping and effective electron transfer ability [36]. To clarify the important role of the synergetic effect of Ni-Co alloy

in CNT, control experiments using monometallic encased CNTs (Ni@NCNT and Co@NCNT) as catalysts on IBP degradation were conducted. In comparison to NCNT, the enhanced catalysis performance of Ni@NCNT and Co@NCNT than NCNT confirms that TM encapsulation in CNT might be a more powerful strategy to upgrade carbonaceous catalytic activity than nitrogen doping alone. Furthermore, both Ni@NCNT and Co@NCNT are showing inferior catalysis in IBP oxidation than NiCo alloy modified NCNT, indicating the synergistic effect of Ni-Co alloy for the promoted performances. Thus, the excellent catalytic activity of NiCo@NCNT would be attributed to the contribution from N-doping and NiCo MAN [34].

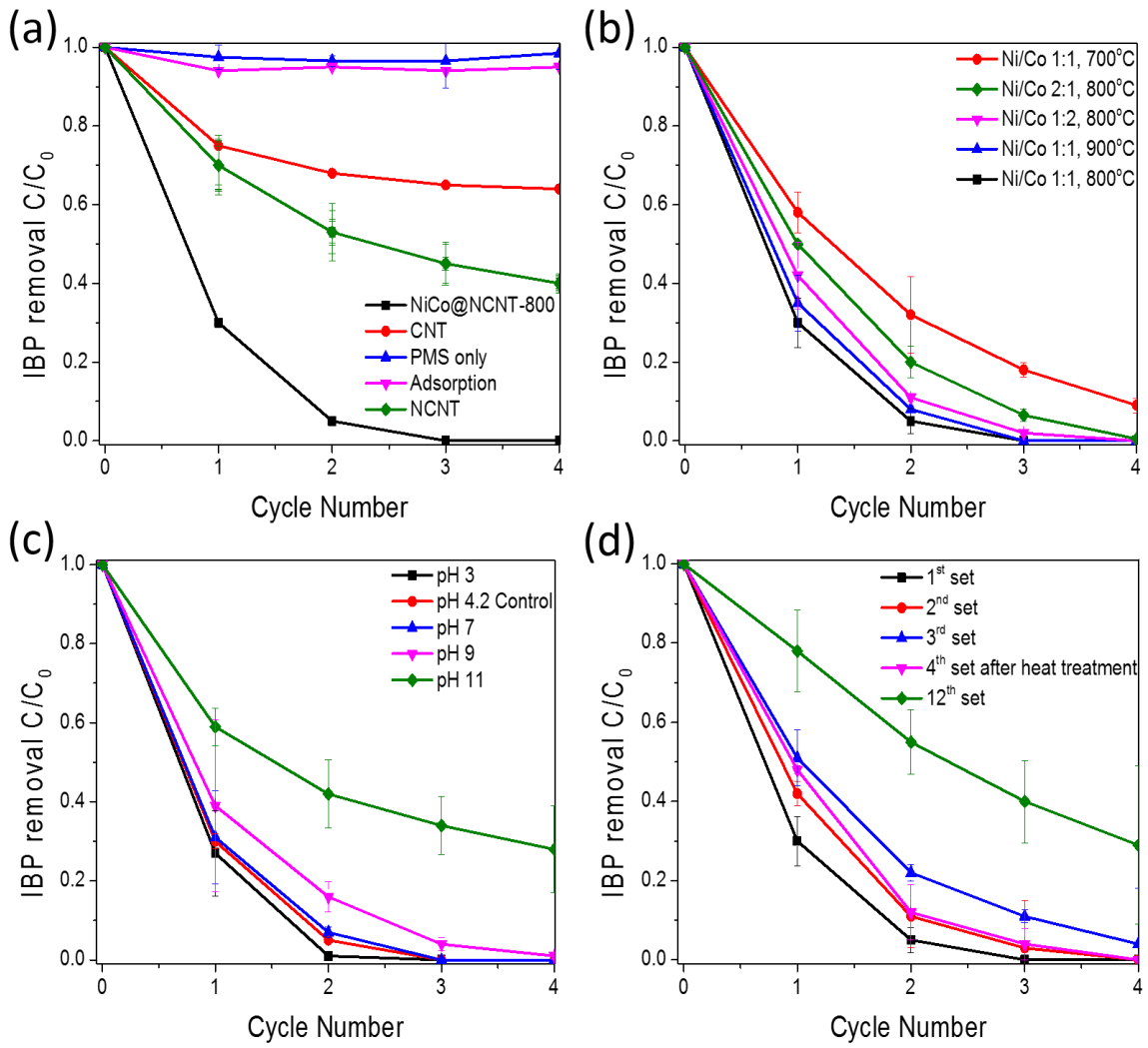

Figure 6.8 (a) IBP degradation under various reaction conditions; (b) effects of pyrolysis temperature and Ni/Co precursor ratio w/w on IBP removal; (c) effect of initial solution pH on IBP removal; (d) stability and recyclability studies of NiCo@NCNT-800. (Catalyst, 0.05 g/L; PMS, 0.65 mM; IBP, 20 mg/L; Temperature, 25 ^{o}C).

Figure 6.8b further shows the influence of NiCo@NCNT fabricated with different Ni/Co ratios, 1:1(Control), 2:1 and 1:2. Among the three NiCo@NCNT samples fabricated at different Ni/Co ratios, NiCo@NCNT-1:1 demonstrated the most outstanding activity for IBP oxidation than 1:2 and 2:1, verifying the importance of the Co-Ni alloy at the molar ratio. The basic rationale for the bimetallic encapsulated carbon catalyst approach by the introduction of a second metal to form MAN stems from the consideration of additional synergistic properties in terms of the difference in redox potentials and structural or chemical ordering [37]. By taking advantage of synergy of NiCo alloy, the catalytic activity of NiCo@NCNT can be optimized by tuning Ni/Co ratio. Additionally, **Figure** 6.8b exhibits the catalytic performance of NiCo@NCNT derived from different pyrolysis temperature. It is found that NiCo@NCNT-800 gives a better catalytic performance on IBP oxidation than NiCo@NCNT prepared at 700 ^{o}C. Interestingly, by continually increasing the pyrolysis temperature to 900 ^{o}C, the NiCo@NCNT showed a reduced activity in catalysis instead. This can be explained that more quaternary nitrogen with a greater thermal stability and better catalytic ability would be produced at a higher annealing temperature [38]. However, at high temperature (900 ^{o}C), the CNT structure can be destroyed to lead to the N-C bond breakup and metal leaching, which would deteriorate the catalytic activity. If not specifically mentioned, the catalyst used for the following kinetic experiments was NiCo@NCNT-800-1:1 due to its best catalytic performance.

Figure 6.8c shows the effect of initial solution pHs (pH = 3, 4, 7, 9 and 11) on the IBP degradation in the system of NiCo@NCNT and PMS. IBP solution itself has an initial pH value of 4.2. The degradation rate increases with decreasing pH value from 4.2 to 3, achieving 96% of the IBP removal during the 2nd cycle. According to our previous studies, $^{\bullet}OH$ and $SO_4^{\bullet-}$ were found to be the primary reactive species generated in CNT/PMS system, and the oxidation potential of $^{\bullet}OH$ could be optimized at an acidic environment, ranging within 2.5 - 3 V at pH 3, and weakened at a higher pH value, dropping to 1.9 V at pH 7 [14]. There is negligible efficiency change when the pH is elevated from 4.2 to 7 and this can be due to the acidification of the reaction solution caused by the oxidation intermediates. The pH effect study showed that the pH values of reactions with initial pH 4 and 7 are both reduced to around 3 after the 1st run and kept unchanged later on. In the case of pH 9, the degradation efficiency of IBP is retarded and eventually completed at 100% in the 4th run.

The removal efficiency continually decreases by further increasing the pH to 11, however, an 80% IBP removal was still achieved after the 4th reaction cycle. The outstanding pH tolerance of NiCo@NCNT is attributed to the synergistic effect of the insensitivity of sulfate radical activation to pH and the involvement of nonradical oxidation pathway [14, 39].

6.3.3 Stability.

The stability and reusability of NiCo@NCNTs were evaluated by successive sets of IBP degradation experiments under the same reaction conditions and each set contains four degradation cycles (**Figure** 6.8d). Taking advantages of the NiCo@NCNT's unique magnetic property, it was facilely collected by an external magnet and washed thoroughly with DI water and ethanol for the next set of tests. IBP reached 100% degradation in the 3rd cycle on fresh NiCo@NCNT. In comparison, in the 2nd and 3rd sets 100% and 95% IBP removals were obtained at the end of the 4th cycle, respectively. A thermal treatment was applied to burn off the adsorbed intermediates on the active sites and edges of the catalyst at 350 ^{o}C in Ar. The

activity of NiCo@NCNT is then greatly recovered and reaches 100% IBP degradation after the 4th cycle, which is comparable to the 2nd set test. Astonishingly, a 78% IBP removal was reached after the 12th set of tests, demonstrating the outstanding catalytic stability of NiCo@NCNT. The minor deactivation of carbon catalyst might be due to the following reasons. (i) Intricate influences come from the surface chemistry and structure changes in terms of the coverage of surface active sites by IBP oxidation intermediates, changes of pore properties, and dopants re-allocation in the carbon network. The degradation intermediates study was shown in **Figure** 6.9. (ii) The loss of the catalysts during the wash and recovery process [31]. (iii) The partial oxidation of carbon surface would reduce the electron transfer ability for PMS activation.

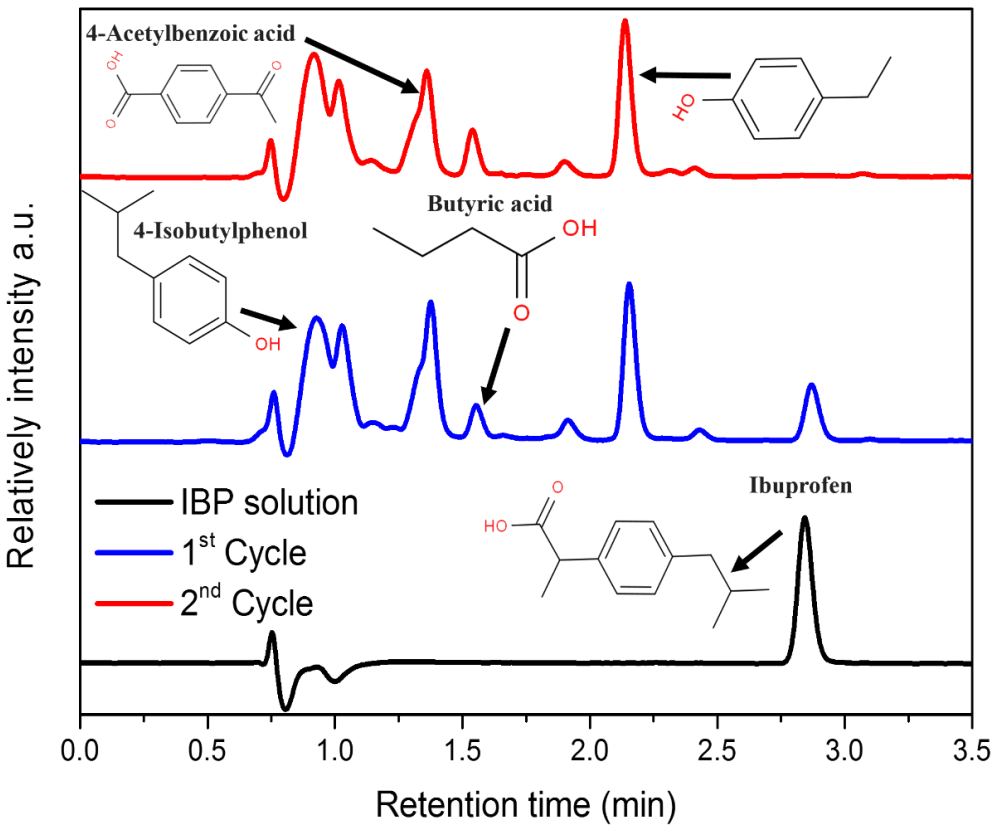

Figure 6.9 Intermediates test of NiCo@NCNT/PMS during the first 2 cycles. (Catalyst, 0.05 g/L; PMS, 0.65 mM; IBP, 20 mg/L; Temperature, 25 °C).

In previous studies, we discovered that 3D CNTs possessed a more robust stability than 2D nanocarbon materials, graphene oxide (GO), owing to the geometrical advantage of rolled graphene shells of multiwall CNT and the inner support from encapsulated metal particles, which would largely avoid structural collapse and aggregation [14, 17]. The high stability of NiCo@NCNT will be further discussed below in a description of our mechanistic studies. Furthermore, the metal leaching concentrations were monitored and analyzed by ICP during the stability experiments (**Figure** 6.10). For fresh NiCo@NCNT, the accumulated metal concentration reached 130 and 180 µg/L for Ni and Co, respectively, which are much lower than the limit of the Australian Drinking Water Guideline, 500 µg/L [40]. The metal concentration decreases as the stability test continues, both Ni and Co concentrations reduced to 50 µg/L after the 12th set in the reusability tests. This can be attributed to several factors: (i) The pre-acid washing treatment removed most of unstable metal species adhered on the surface of CNTs; (ii) the NiCo NPs are protected by graphene shells from leaching to solution. In contrast, the metal leaching concentration of NiO as a catalyst under the same reaction condition was 10-fold higher than NiCo@NCNT and reached as high as 1700 µg/L.

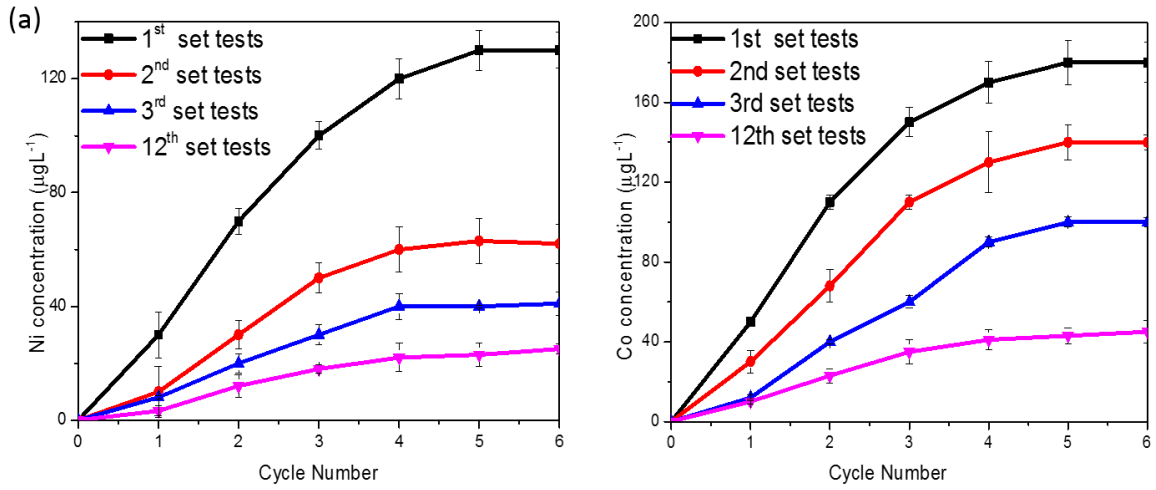

Figure 6.10 ICP analysis of (a) Ni and (b) Co leaching concentrations of the reaction solution. (NiCo@NCNT, 0.05 g/L; PMS, 0.65 mM; IBP, 20 mg/L; Temperature, 25 ºC).

6.3.4 Kinetics.

The influence of reaction temperature for PMS activation was studied in a range of 0 - 45 ^{o}C (**Figure** 6.11a). In detail, 100% IBP removal was achieved in the 4th cycle for control test at 25 ^{o}C, and the oxidation reaction was accelerated and achieved complete IBP removal in the third and second cycles at 35 and 45 ^{o}C, respectively. The enhanced IBP degradation efficiency indicates that PMS activation process is an endothermic reaction and a higher ROS production rate occurred at higher temperatures. Interestingly, a 98% of IBP removal was yet achieved when the oxidation reaction proceeds at 0 ^{o}C, showing an excellent catalytic stability at a wide temperature range. In order to rule out the heat-induced PMS activation, the effect of PMS self-activation by heat is also provided in the low-temperature region in **Figure** 6.11b. It can be seen that the influence of temperature is insignificant on PMS activation in this system and only 10% improvement is witnessed at 0-45 ^{o}C, confirming the enhanced oxidation efficiency at high temperatures was attributed to the superior catalysis of NiCo@NCNT and the heat-induced PMS self-activation. The activation energy for NiCo@NCNT was evaluated to be 14.4 kJ mol^{-1}, which is much lower than 43.8 kJ mol^{-1} on the CNT, indicating the improvement of CNT catalysis by the synergistic effect of nitrogen modification and metal encapsulation [14].

Figure 6.11c shows the effect of different initial IBP concentrations of 20, 40 and 80 mg/L. The removal efficiency reduces with an increased IBP concentration, where reaching 100% IBP removal during the third and fourth cycles for 20 and 40 mg/L, respectively, and 80% removal for 80 mg/L IBP initial concentration, indicating a higher IBP dosage would lead to a larger PMS consumption. At the same time, the IBP removal efficiencies were also measured at different PMS concentrations of 0.33, 0.65, 1.3 and 3.2 mM (**Figure** 6.11d). It is noticed that the enhancement in degradation efficiency is directly proportional to the PMS dosage increase from 0.33 to 1.3 mM. However, a further increase of PMS dosage to 3.2 mM brings a reduction on degradation efficiency instead. This might be ascribed to the self-quenching effect between

PMS and the excessive radicals (Eq. 1) [41]. It was reported that the IBP concentration in real water matrices can reach 30 µg/L [42, 43]. The IBP concentration range applied in this manuscript was 20 to 80 mg/L, which is much higher than that in the real water body. To verify the feasibility of NiCo@NCNT/PMS system on real IBP environmental concentration, its degradation performance was carried out at an ultra-low concentration (50 µg/L). **Figure** 6.11a indicated that the NiCo@NCNT/PMS system could remove 80% of IBP in an 80 mg/L solution after the 4th cycle. Therefore, this oxidative system would easily realize the complete removal of IBP at a lower concentration. In addition, degradation test on ultra-low IBP concentration solution was performed to verify the above assumption. Total organic carbon analysis (TOC) was applied to measure the IBP degradation efficiency at the low concentration. **Figure** 6.12 exhibits the TOC change during the oxidation of low-concentration IBP solution (50 µg/L) by NiCo@NCNT/PMS system. It shows that approximately 80% IBP and its degradation intermediates were efficiently converted to carbon dioxide and water in the first cycle. The oxidation process slowed down afterwards due to production of reluctant degradation intermediates and finally reached 96% of TOC removal after 4 cycles.

$$HSO_5^- + SO_4^{\bullet -} \rightarrow SO_5^{\bullet -} + SO_4^{2-} + H^+ \qquad (1)$$

In addition, the effect of catalyst loading is shown in **Figure** 6.11e and the IBP removal rate is accelerated by increasing the catalyst loading, which is due to more available active sites to enhance the PMS activation efficiency. Furthermore, various types of organic compounds, *i.e.*, methylene blue (MB), methylene orange (MO), naproxen, SCP and phenol, were carried out in the NiCo@NCNT/PMS system and demonstrated great degradation efficiencies of 99%, 100%, 89%, 85%, 78%, respectively, at the end of the 2nd run (**Figure** 6.11f). The variation in removal efficiencies might be due to the difference in intramolecular structures. This result confirms that NiCo@NCNT can be employed as an excellent catalyst to effectively activate PMS and brings about complete degradation of various organic contaminants. Additionally,

common anions, such as Cl^-, HCO_3^-, $H_2PO_4^-$ and natural organic matters (NOMs), humic acid (HA), were also introduced into the reaction, and the results showed that phosphate ions ($H_2PO_4^-$) and humic acid (HA) had negligible effect on IBP removal rate, on the other hand, chloride (Cl^-) and carbonate ions (HCO_3^-) presented enhancing and inhibiting influences, respectively. Moreover, the feasibility of NiCo@NCNT/PMS system in different water matrices such as river water, seawater and tap water was studied and the results showed a marginal deterioration in IBP degradation efficiency was observed due to the existence of impurities like NOMs and various anions.

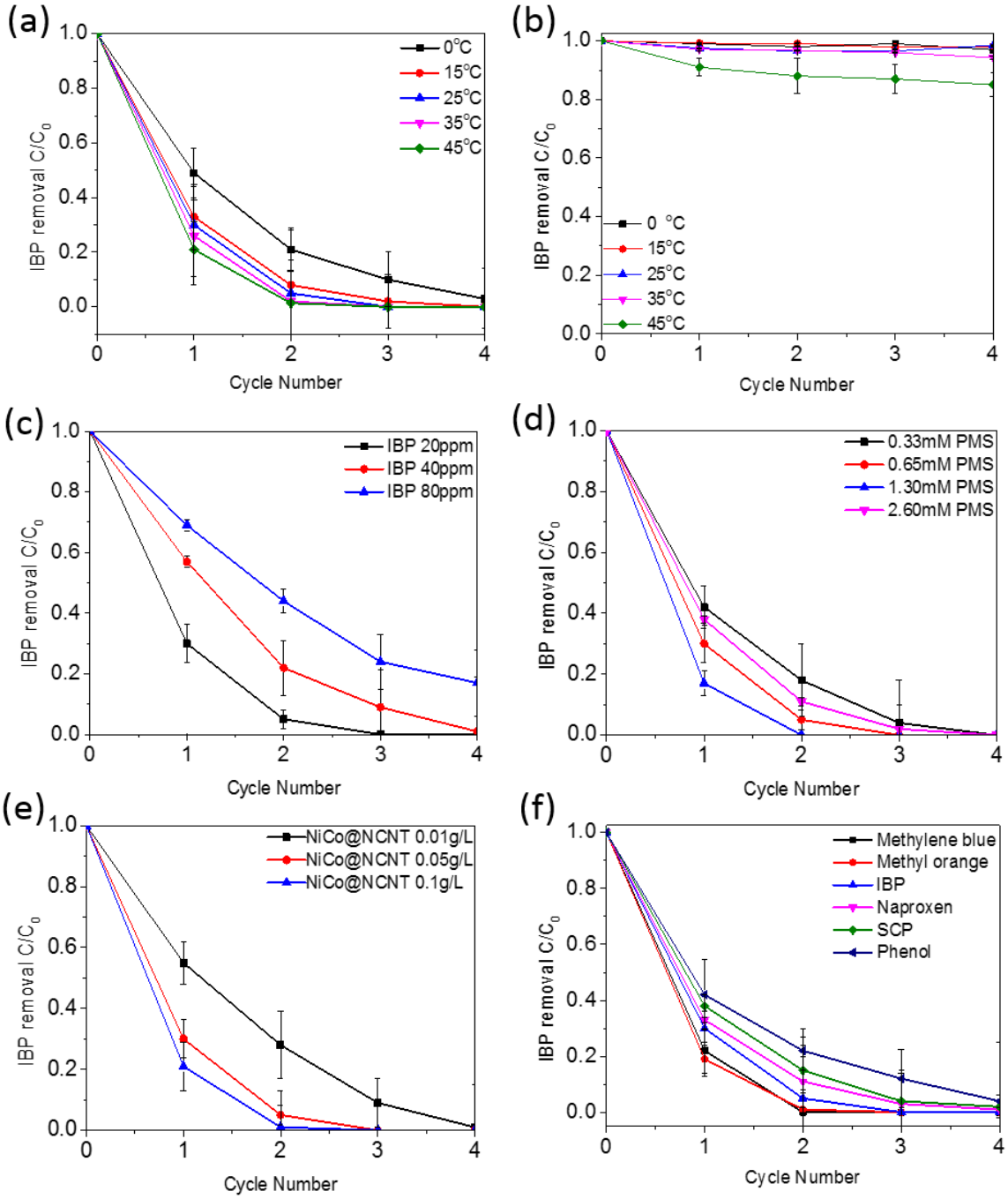

Figure 6.11 (a) Effect of reaction temperature; (b) Effect of reaction temperature without a catalyst; (c) Effect of initial IBP concentration; (d) Effect of PMS dosage; (e) Effect of catalyst loadings on IBP removal, and (f) the catalytic degradation of different organics by NiCo@NCNT-800. (Unless otherwise stated, the reaction conditions are based on Catalyst, 0.05 g/L; PMS, 0.65 mM; IBP, 20 mg/L; T, 25 °C).

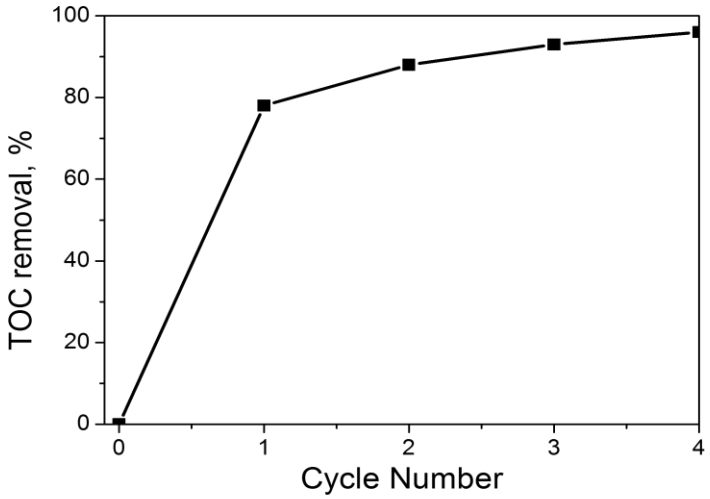

Figure 6.12. Effect of low IBP concentration on total organic carbon removal, reaction condition: Catalyst, 0.05 g/L; PMS, 0.65 mM; IBP, 50 µg/L; Temperature, 25 ^{o}C).

6.3.5 Mechanism of radical generation.

To understand the mechanism of the NiCo@NCNT based AOPs and determine the responsible reactive oxygen species (ROS) in IBP degradation reaction, several scavengers were applied for this purpose. In general, ethanol is used as an effective radical scavenger for both $SO_4^{\bullet-}$ and $^{\bullet}OH$ with rate constants of 1.6-7.7 $\times 10^7$ and 1.2-2.8 $\times 10^9$ M^{-1} s^{-1}, respectively. TBA was particularly employed to identify the role of $SO_4^{\bullet-}$ because its reaction rate with $^{\bullet}OH$ (3.8-7.6 $\times 10^9$ M^{-1} s^{-1}) is approximately 4 order of magnitudes greater than that with $SO_4^{\bullet-}$ (4.0-9.1$\times 10^5$ M^{-1} s^{-1}) [44]. As shown in **Figure** 6.13a, in comparison with the control test of 100% IBP removal in the 3rd run, the IBP degradation efficiency diminished to 85% and 70% after the 3rd cycle when TBA and ethanol were introduced into the reaction, respectively. Such results suggest that both $SO_4^{\bullet-}$ and $^{\bullet}OH$ are contributing to the IBP oxidation and $SO_4^{\bullet-}$ might be playing a more dominant role. However when excess amount of ethanol was added in the reaction, the IBP oxidation was not terminated immediately though most of the free $SO_4^{\bullet-}$ and $^{\bullet}OH$ were quenched out. On the contrary, 68% IBP was removed after the 5th cycle, indicating the $SO_4^{\bullet-}$ and $^{\bullet}OH$ are partially accounted for the IBP degradation.

In a recent study, superoxide radicals ($^{\bullet}O_2^-$) and singlet oxygen ($^1O_2$) were proved to be the major ROS in catalytic PMS phenol degradation [45]. Herein, the contributions of $^{\bullet}O_2^-$ and $^1O_2$ in IBP degradation were determined using *p*-benzoquinone (p-BQ) and furfuryl alcohol (FFA) due to their high reaction rate with $^{\bullet}O_2^-$ (1×10^9 M^{-1} s^{-1}) and $^1O_2$ (1.2×10^8 M^{-1} s^{-1}), respectively. As shown in **Figure** 6.13a, the addition of p-BQ had a negligible effect on IBP degradation in the NiCo@NCNT/PMS system, suggesting the insignificant role of $^{\bullet}O_2^-$ in attacking IBP molecules. On the other hand, when FFA was presented in the solution, an apparent reduction in IBP degradation was viewed (75%), which indicates the possible contribution of singlet oxygen. However, it is worth noting that FFA is highly reactive towards $^{\bullet}OH$ (1.5×10^{10} M^{-1} s^{-1}) and, presumably, $SO_4^{\bullet-}$ [46]. To rule out the quenching effect of FFA on $^{\bullet}OH$ and $SO_4^{\bullet-}$, $^{\bullet}OH$ and $SO_4^{\bullet-}$ were quenched out by adding excess amount of ethanol in the reaction together with FFA. The result shows that 71% of IBP was degraded after the 5th cycle, which is very similar to the case of ethanol alone (78%), suggesting the minor contribution of $^1O_2$ in the NiCo@NCNT/PMS system. Surprisingly, when all the possible free ROS were scavenged out in the IBP solution by adding ethanol and FFA, the NiCo@NCNT/PMS still managed to remove 74% IBP, showing the IBP oxidation process is not solely relying on free ROS attack.

In our previous studies, Duan *et al.* reported that a nonradical process occurred when the nitrogen modified CNTs was applied to activate PMS for phenol degradation, where the PMS was firstly bonded with the sp^2-hybridized carbon framework system and then reacted with the adsorbed organic pollutants [14]. In this investigation, a similar nonradical process of IBP degradation was found which was originated from N doping in CNTs. Furthermore, in comparison with NCNT, when the same amount of ethanol and FFA was added to the reaction solution, the NiCo@NCNT presented a less influence on IBP oxidation, where 61% and 74% IBP was degraded on NCNT and NiCo@NCNT accordingly. This implies that NiCo encased

NCNT has an enhanced catalysis than NCNT in nonradical oxidation process, which can be ascribed to the improved electron transfer efficiency between catalyst adhered PMS and IBP molecules. The mechanism of co-existence of radical and nonradical pathways is illustrated in **Figure** 6.14. Subsequently, the generated radicals reacted with the adsorbed organic pollutants, which would offer an improved tolerance to temperature and radical quenching substances [17].

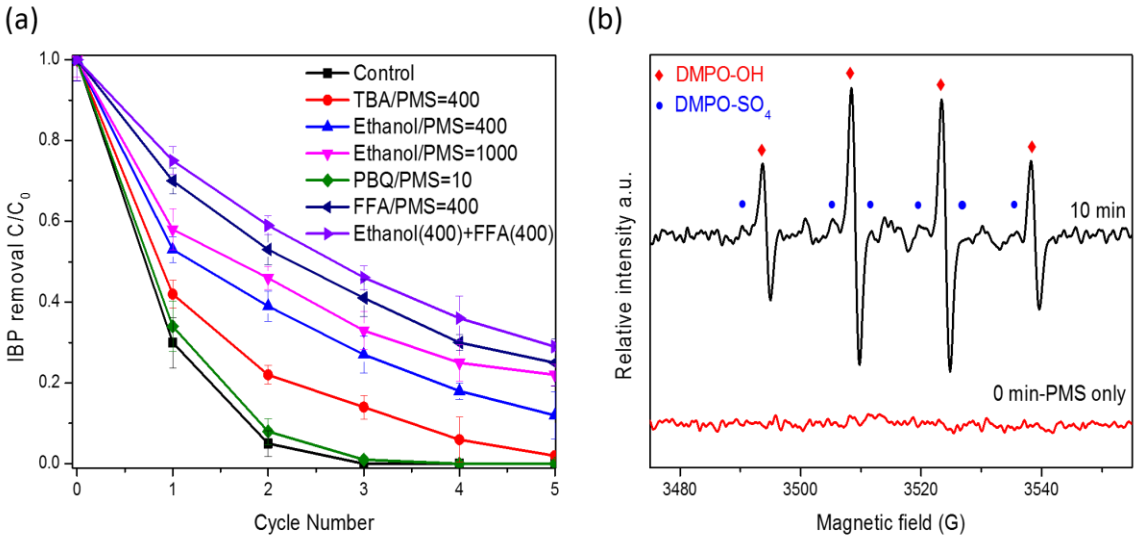

Figure 6.13(a) Effect of radical quenching on IBP degradation; (b) EPR spectra of DMPO adducts under different conditions.

EPR was also employed to *in situ* detect the free radicals in aqueous IBP degradation system. **Figure** 6.13b shows the different peak properties when PMS is solely presented and the radicals produced by PMS self-activation was negligible, which is consistent with the aforementioned oxidation results. After 10 min reaction, the DMPO-OH peaks are more intense than the DMPO-SO_4 peaks. This can be attributed to the mutual transformation between $SO_4^{\bullet-}$ and $^{\bullet}OH$ in Eqs. 2 and 3, which is greatly influenced by the solution pH. As mentioned above, the initial IBP solution has a pH value of 4.2 and the reaction solution is continually acidified due to the formation of mineralized by-products during the NiCo@NCNT induced SR-AOP. Moreover,

the correlation between PMS decomposition rate and IBP degradation efficiency was investigated and the results showed a direct proportional relationship.

$$SO_4^{\bullet -} + OH^- \rightarrow SO_4^{2-} + OH^{\bullet} \quad (2)$$

$$OH^{\bullet} + SO_4^{2-} \rightarrow SO_4^{\bullet -} + OH^- \quad (3)$$

In comparing to metal based catalysts, the inferior catalytic stability of carbon-based material inhibits its extensive application. It has been revealed that the activated sp^2 carbon network induced by the substantial N doping could improve the CNT activity and stability in reuses [14]. Inspired by this, the stability of NiCo@NCNT in IBP degradation was compared with metal-free NCNT. The results showed that 31% of IBP was removed during the 3rd set for NCNT, while a complete IBP removal for NiCo@NCNT. The apparent improvement in catalytic stability by introduction of MAN could be attributed to the unique confined architecture of NiCo NPs within the nitrogen-doped carbon structure. As the encased NiCo NPs contribute the robust catalysis via accelerated electron transfer to PMS, it was more difficult to make damage to the inner structure and the surface chemistry of the NiCo with the carbon multi-wall protection during the oxidation process.

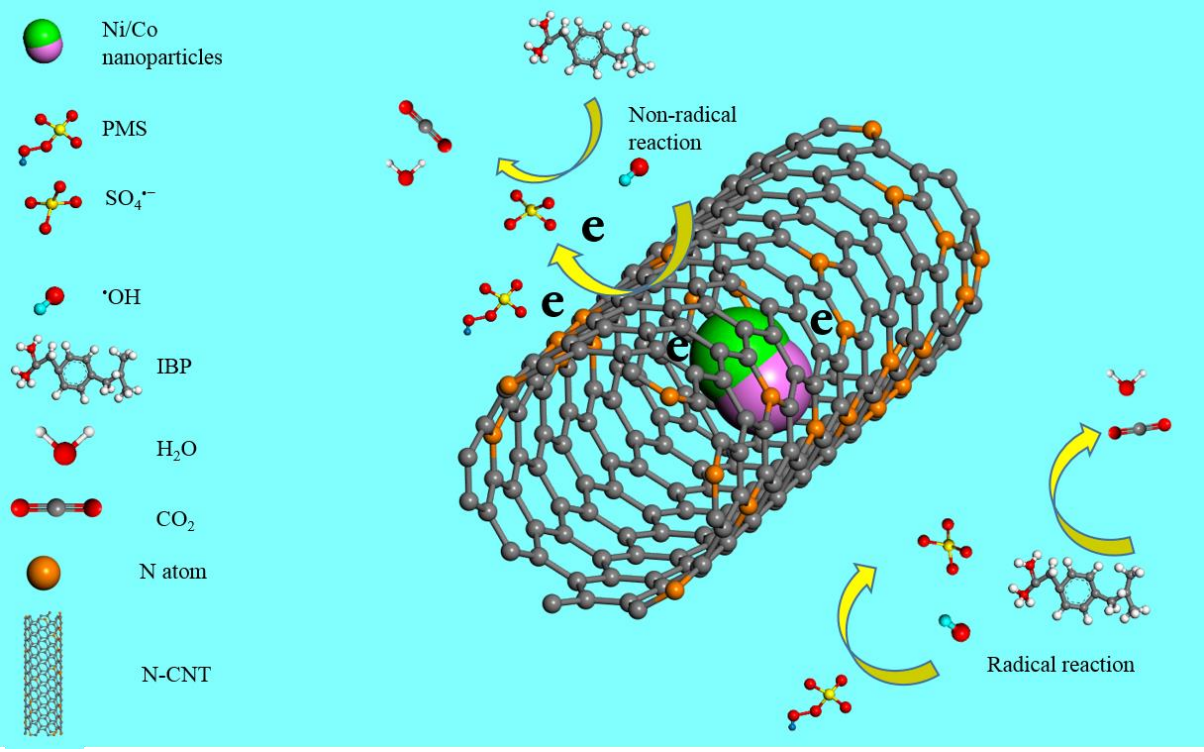

Figure 6.14 Mechanism for IBP degradation by NiCo@NCNT/PMS systems.

6.4 Conclusions

In summary, a green facile synthesis method was developed to prepare NiCo encapsulated in nitrogen-doped carbon nanotubes with both structural and compositional modifications. Characterization studies showed that the prepared NiCo@NCNT reached its optimum morphology and N doping level (6.2%) at 800 ºC with a Ni/Co ratio of 1:1. NiCo@NCNT demonstrated a superior performance in catalytic activation of PMS for IBP, which could be attributed to the synergistic effect of encapsulated NiCo NPs and nitrogen doped carbon network. The incorporated alien atoms break the chemical inertness of pristine nanocarbons and the metal nanoparticles further lower the local surface work function of carbon wall, collaboratively, efficient electron transfer and robust catalytic activity have been realized. Meanwhile, due to the dual carbon protection of the unique NiCo encapsulation, the catalyst largely avoided the metal leaching into water body. Kinetic studies revealed that IBP

concentration and PMS/catalyst loading would influence the degradation efficiency, whereas the reaction temperature and pH only showed marginal effects after nitrogen modification. Stability experiments indicated that the as-prepared catalyst presented an outstanding stability for reuse, in which a complete degradation was reached after a number of repeated tests and the catalysis was better recovered by mild thermal treatment. Quenching experiments and EPR techniques were used to observe the reactive radical generation status, discovering that both radical mainly $^{\bullet}OH$ and $SO_4^{\bullet-}$ and nonradical oxidation pathways are responsible for the IBP degradation. We believe that this novel synthetic approach, unique structure and proposed mechanism may pave the way for the further study of environmentally friendly, stable, economical and highly efficient carbon catalysts for AOPs.

6.5 Reference

1. Brausch, J. M.; Connors, K. A.; Brooks, B. W.; Rand, G. M., Human Pharmaceuticals in the Aquatic Environment: A Review of Recent Toxicological Studies and Considerations for Toxicity Testing. In *Reviews of Environmental Contamination and Toxicology Volume 218*, Whitacre, D. M., Ed. Springer US: Boston, MA, 2012; pp 1-99.

2. Brozinski, J.-M.; Lahti, M.; Meierjohann, A.; Oikari, A.; Kronberg, L., The Anti-Inflammatory Drugs Diclofenac, Naproxen and Ibuprofen are found in the Bile of Wild Fish Caught Downstream of a Wastewater Treatment Plant. *Environmental Science & Technology* **2013,** *47*, (1), 342-348.

3. Lian, L.; Yao, B.; Hou, S.; Fang, J.; Yan, S.; Song, W., Kinetic Study of Hydroxyl and Sulfate Radical-Mediated Oxidation of Pharmaceuticals in Wastewater Effluents. *Environmental Science & Technology* **2017,** *51*, (5), 2954-2962.

4. Anipsitakis, G. P.; Dionysiou, D. D., Degradation of Organic Contaminants in Water with Sulfate Radicals Generated by the Conjunction of Peroxymonosulfate with Cobalt. *Environmental Science & Technology* **2003,** *37*, (20), 4790-4797.

5. Zhou, Y.; Wang, X.; Zhu, C.; Dionysiou, D. D.; Zhao, G.; Fang, G.; Zhou, D., New insight into the mechanism of peroxymonosulfate activation by sulfur-containing minerals: Role of sulfur conversion in sulfate radical generation. *Water Research* **2018,** *142*, 208-216.

6. Al-Anazi, A.; Abdelraheem, W. H.; Han, C.; Nadagouda, M. N.; Sygellou, L.; Arfanis, M. K.; Falaras, P.; Sharma, V. K.; Dionysiou, D. D., Cobalt ferrite nanoparticles with controlled composition-peroxymonosulfate mediated degradation of 2-phenylbenzimidazole-5-sulfonic acid. *Applied Catalysis B: Environmental* **2018,** *221*, 266-279.

7. Yang, S.; Wang, P.; Yang, X.; Shan, L.; Zhang, W.; Shao, X.; Niu, R., Degradation efficiencies of azo dye Acid Orange 7 by the interaction of heat, UV and anions with common oxidants: Persulfate, peroxymonosulfate and hydrogen peroxide. *Journal of Hazardous Materials* **2010,** *179*, (1), 552-558.

8. Wang, Y. X.; Sun, H. Q.; Ang, H. M.; Tade, M. O.; Wang, S. B., Magnetic Fe3O4/carbon sphere/cobalt composites for catalytic oxidation of phenol solutions with sulfate radicals. *Chemical Engineering Journal* **2014,** *245*, 1-9.

9. Hou, Z. S.; Yang, C. Q.; Zhang, W. B.; Lu, C. B.; Zhang, F.; Zhuang, X. D., Cobalt/nitrogen co-doped porous carbon nanosheets as highly efficient catalysts for the oxygen reduction reaction in both basic and acidic media. *Rsc Advances* **2016,** *6*, (85), 82341-82347.

10. Zhang, T.; Zhu, H.; Croué, J.-P., Production of Sulfate Radical from Peroxymonosulfate Induced by a Magnetically Separable CuFe2O4 Spinel in Water: Efficiency, Stability, and Mechanism. *Environmental Science & Technology* **2013,** *47*, (6), 2784-2791.

11. Hu, L.; Yang, X.; Dang, S., An easily recyclable Co/SBA-15 catalyst: Heterogeneous activation of peroxymonosulfate for the degradation of phenol in water. *Applied Catalysis B: Environmental* **2011,** *102*, (1-2), 19-26.

12. Cheng, Y. H.; Tian, Y. Y.; Fan, X. Z.; Liu, J. G.; Yan, C. W., Boron Doped Multi-walled Carbon Nanotubes as Catalysts for Oxygen Reduction Reaction and Oxygen Evolution Reactionin in Alkaline Media. *Electrochimica Acta* **2014,** *143*, 291-296.

13. Yang, L.; Jiang, S.; Zhao, Y.; Zhu, L.; Chen, S.; Wang, X.; Wu, Q.; Ma, J.; Ma, Y.; Hu, Z., Boron-Doped Carbon Nanotubes as Metal-Free Electrocatalysts for the Oxygen Reduction Reaction. *Angewandte Chemie* **2011,** *123*, (31), 7270-7273.

14. Duan, X.; Sun, H.; Wang, Y.; Kang, J.; Wang, S., N-Doping-Induced Nonradical Reaction on Single-Walled Carbon Nanotubes for Catalytic Phenol Oxidation. *ACS Catalysis* **2015,** *5*, (2), 553-559.

15. Kang, J.; Duan, X. G.; Zhou, L.; Sun, H. Q.; Tade, M. O.; Wang, S. B., Carbocatalytic activation of persulfate for removal of antibiotics in water solutions. *Chemical Engineering Journal* **2016,** *288*, 399-405.

16. Sun, H.; Wang, Y.; Liu, S.; Ge, L.; Wang, L.; Zhu, Z.; Wang, S., Facile synthesis of nitrogen doped reduced graphene oxide as a superior metal-free catalyst for oxidation. *Chemical Communications* **2013,** *49*, (85), 9914-9916.

17. Kang, J.; Duan, X.; Wang, C.; Sun, H.; Tan, X.; Tade, M. O.; Wang, S., Nitrogen-doped bamboo-like carbon nanotubes with Ni encapsulation for persulfate activation to remove emerging contaminants with excellent catalytic stability. *Chemical Engineering Journal* **2018,** *332*, (Supplement C), 398-408.

18. Sun, H.; Kwan, C.; Suvorova, A.; Ang, H. M.; Tade, M. O.; Wang, S., Catalytic oxidation of organic pollutants on pristine and surface nitrogen-modified carbon nanotubes with sulfate radicals. *Applied Catalysis B-Environmental* **2014,** *154*, 134-141.

19. Qu, L.; Liu, Y.; Baek, J.-B.; Dai, L., Nitrogen-Doped Graphene as Efficient Metal-Free Electrocatalyst for Oxygen Reduction in Fuel Cells. *ACS Nano* **2010,** *4*, (3), 1321-1326.

20. Li, Y. D.; Li, L. Q.; Liao, H. W.; Wang, H. R., Preparation of pure nickel, cobalt, nickel-cobalt and nickel-copper alloys by hydrothermal reduction. *Journal of Materials Chemistry* **1999,** *9*, (10), 2675-2677.

21. Chen, C.-C.; Bao, W.; Theiss, J.; Dames, C.; Lau, C. N.; Cronin, S. B., Raman Spectroscopy of Ripple Formation in Suspended Graphene. *Nano Letters* **2009,** *9*, (12), 4172-4176.

22. Wang, Y.; Liu, Y.; Liu, W.; Chen, H.; Zhang, G.; Wang, J., Morphological control of N-doped carbon nanotubes and their electrochemical properties. *Materials Letters* **2015,** *154*, (Supplement C), 64-67.

23. Wang, C.; Kang, J.; Liang, P.; Zhang, H. Y.; Sun, H. Q.; Tade, M. O.; Wang, S. B., Ferric carbide nanocrystals encapsulated in nitrogen-doped carbon nanotubes as an outstanding environmental catalyst. *Environ Sci-Nano* **2017,** *4*, (1), 170-179.

24. Wang, J.; Huang, R.; Zhang, Y.; Diao, J.; Zhang, J.; Liu, H.; Su, D., Nitrogen-doped carbon nanotubes as bifunctional catalysts with enhanced catalytic performance for selective oxidation of ethanol. *Carbon* **2017,** *111*, (Supplement C), 519-528.

25. Yin, J.; Fan, Q.; Li, Y.; Cheng, F.; Zhou, P.; Xi, P.; Sun, S., Ni–C–N Nanosheets as Catalyst for Hydrogen Evolution Reaction. *Journal of the American Chemical Society* **2016,** *138*, (44), 14546-14549.

26. Li, Y.; Zhao, Y.; Cheng, H.; Hu, Y.; Shi, G.; Dai, L.; Qu, L., Nitrogen-Doped Graphene Quantum Dots with Oxygen-Rich Functional Groups. *Journal of the American Chemical Society* **2012,** *134*, (1), 15-18.

27. Liang, Q.; Ma, W.; Shi, Y.; Li, Z.; Yang, X., Easy synthesis of highly fluorescent carbon quantum dots from gelatin and their luminescent properties and applications. *Carbon* **2013,** *60*, 421-428.

28. Alexander V. Naumkin, A. K.-V., Stephen W. Gaarenstroom, and Cedric J. Powell NIST X-ray Photoelectron Spectroscopy Database (September 15, 2012),

29. Laifa, S.; Jie, W.; Guiyin, X.; Hongsen, L.; Hui, D.; Xiaogang, Z., NiCo2S4 Nanosheets Grown on Nitrogen-Doped Carbon Foams as an Advanced Electrode for Supercapacitors. *Advanced Energy Materials* **2015,** *5*, (3), 1400977.

30. Zhou, C.; Szpunar, J. A.; Cui, X., Synthesis of Ni/Graphene Nanocomposite for Hydrogen Storage. *ACS Applied Materials & Interfaces* **2016,** *8*, (24), 15232-15241.

31. Duan, X.; Ao, Z.; Sun, H.; Indrawirawan, S.; Wang, Y.; Kang, J.; Liang, F.; Zhu, Z. H.; Wang, S., Nitrogen-Doped Graphene for Generation and Evolution of Reactive Radicals by Metal-Free Catalysis. *ACS Applied Materials & Interfaces* **2015,** *7*, (7), 4169-4178.

32. Duan, X.; O'Donnell, K.; Sun, H.; Wang, Y.; Wang, S., Sulfur and Nitrogen Co-Doped Graphene for Metal-Free Catalytic Oxidation Reactions. *Small* **2015,** *11*, (25), 3036-3044.

33. Lee, H.; Kim, H.-i.; Weon, S.; Choi, W.; Hwang, Y. S.; Seo, J.; Lee, C.; Kim, J.-H., Activation of Persulfates by Graphitized Nanodiamonds for Removal of Organic Compounds. *Environmental Science & Technology* **2016,** *50*, (18), 10134-10142.

34. Zeng, L.; Cui, X.; Chen, L.; Ye, T.; Huang, W.; Ma, R.; Zhang, X.; Shi, J., Non-noble bimetallic alloy encased in nitrogen-doped nanotubes as a highly active and durable electrocatalyst for oxygen reduction reaction. *Carbon* **2017,** *114*, 347-355.

35. Xiaojia, Z.; Jiao, D.; Nan, W.; Dehui, D.; Wen-Hua, Z.; Xinhe, B.; Can, L., Podlike N-Doped Carbon Nanotubes Encapsulating FeNi Alloy Nanoparticles: High-Performance Counter Electrode Materials for Dye-Sensitized Solar Cells. *Angewandte Chemie International Edition* **2014,** *53*, (27), 7023-7027.

36. Yao, Y.; Lian, C.; Wu, G.; Hu, Y.; Wei, F.; Yu, M.; Wang, S., Synthesis of "sea urchin"-like carbon nanotubes/porous carbon superstructures derived from waste biomass for treatment of various contaminants. *Applied Catalysis B: Environmental* **2017,** *219*, 563-571.

37. Wanjala, B. N.; Fang, B.; Loukrakpam, R.; Chen, Y.; Engelhard, M.; Luo, J.; Yin, J.; Yang, L.; Shan, S.; Zhong, C.-J., Role of Metal Coordination Structures in Enhancement of Electrocatalytic Activity of Ternary Nanoalloys for Oxygen Reduction Reaction. *ACS Catalysis* **2012,** *2*, (5), 795-806.

38. Li, X.; Wang, H.; Robinson, J. T.; Sanchez, H.; Diankov, G.; Dai, H., Simultaneous Nitrogen Doping and Reduction of Graphene Oxide. *Journal of the American Chemical Society* **2009,** *131*, (43), 15939-15944.

39. Neyens, E.; Baeyens, J., A review of classic Fenton's peroxidation as an advanced oxidation technique. *Journal of Hazardous Materials* **2003,** *98*, (1–3), 33-50.

40. Council, A. G. N. H. a. M. R., Australian Drinking Water Guidelines (2011) - Updated October 2017. In 3.4 ed.; Council, N. H. a. M. R., Ed. Australian Government: Australia, 2011; Vol. 1167, p 1167.

41. Brandt, C.; Vaneldik, R., TRANSITION-METAL-CATALYZED OXIDATION OF SULFUR(IV) OXIDES - ATMOSPHERIC-RELEVANT PROCESSES AND MECHANISMS. *Chemical Reviews* **1995,** *95*, (1), 119-190.

42. Roberts, P. H.; Thomas, K. V., The occurrence of selected pharmaceuticals in wastewater effluent and surface waters of the lower Tyne catchment. *Science of The Total Environment* **2006,** *356*, (1), 143-153.

43. Ashton, D.; Hilton, M.; Thomas, K. V., Investigating the environmental transport of human pharmaceuticals to streams in the United Kingdom. *Science of The Total Environment* **2004,** *333*, (1), 167-184.

44. Chen, L.; Peng, X.; Liu, J.; Li, J.; Wu, F., Decolorization of Orange II in Aqueous Solution by an Fe(II)/sulfite System: Replacement of Persulfate. *Industrial & Engineering Chemistry Research* **2012,** *51*, (42), 13632-13638.

45. Wang, C.; Kang, J.; Liang, P.; Zhang, H.; Sun, H.; Tade, M. O.; Wang, S., Ferric carbide nanocrystals encapsulated in nitrogen-doped carbon nanotubes as an outstanding environmental catalyst. *Environmental Science: Nano* **2017,** *4*, (1), 170-179.

46. Yang, Y.; Banerjee, G.; Brudvig, G. W.; Kim, J.-H.; Pignatello, J. J., Oxidation of Organic Compounds in Water by Unactivated Peroxymonosulfate. *Environmental Science & Technology* **2018,** *52*, (10), 5911-5919.

Chapter 7: Catalytic degradation of cosmetic microplastics by hydrothermal carbocatalysis: A new approach with magnetic carbon nanosprings and sulfate radicals

This chapter has been published on journal "Matter", DOI: 10.1016/j.matt.2019.06.004. *Every reasonable effort has been made to acknowledge the owners of copyright material. I would be pleased to hear from any copyright owner who has been omitted or incorrectly acknowledged.*

Abstract

Microplastics (MPs) pollution in household wastewater and global aquatic systems has become an emerging issue and potential threat to the marine life and human health. Identification and environmental consequences of MPs have been recently researched, nevertheless, advanced technologies for efficient MPs control and purification remain largely underdeveloped. In this work, we contributed to a pioneering exploration by integrating carbocatalytic oxidation and hydrothermal (HT) hydrolysis for synergistic degradation of microplastics over nanostructured carbocatalysts. To this end, spring-like carbon nanotubes were fabricated bearing high-level nitrogen dopants and encapsulated metal nanoparticles. The robust and magnetic carbon hybrids exhibited outstanding catalytic performance in activation of peroxymonosulfate (PMS) to generate sulfate radicals for MPs degradation. The spiral architecture and highly graphitic degree guaranteed superb stability of the carbocatalysts in HT environment. By taking MPs from commercial facial cleansers as the target contaminants, 40 wt.% decomposition of MPs can be reached by the carbon/thermal/PMS system. The toxicity test indicated that the organic intermediates from MPs degradation were environmental-benign to the aquatic microorganisms and can serve as a carbon source for algae cultivation. The outcomes of this study dedicate to providing a novel

and green strategy by state-of-the-art carbocatalysis and nanotechnology for remediation of MP contamination in water.

7.1 Introduction

Microplastics (MPs), a subgroup of plastics, with an effective diameter less than 5 mm has become an emerging microcontaminants, owing to their widespread in aquatic systems and difficulty in recycling or elimination by conventional wastewater purification techniques [1]. MPs have been frequently detected in marine organisms such as shellfish, fish and seabirds and the resistance to ingestion would lead to starvations and death of organisms as well as the senior predators via the food chain in marine and terrestrial systems[2-5]. Natural decomposition of MPs can take up to decades and will release a diversity of hazardous organic substances from the polymers and additives (e.g. plasticizer and anti-oxidizer in manufacturing). Moreover, these microscale plastics are favorable to work as a medium or vector to accumulate and transport the toxic hydrophobic organic pollutants and heavy metals on their surface, giving rise to the bioaccumulation of contaminants and poisoning in marine lives[6-9]. MPs can be classified into primary and secondary MPs, which are mostly originated from household cosmetic products and breakdown of larger plastic pieces, respectively[10-12]. Recently, it was reported that the well-received rinse-off cosmetics contain abundant primary MPs exfoliators as "microbeads" or "micro-exfoliates", which are recklessly discharged into the sewage and are reluctant to be removed by water treatment plants[13]. It is therefore of vital significance to develop an advanced technology to remove MPs from water systems. However, the research in developing advanced techniques for MPs treatment is still in infancy[6, 14-16].

Recently, advanced oxidation processes (AOPs), referred to a chemical remediation technology involving diverse reactive oxygen species (ROS), have exhibited great capabilities in complete mineralization of persistent organic pollutants in water. Among AOPs, sulfate radical ($SO_4^{\bullet-}$,

E^0=3.1 V vs NHE) based AOPs (SR-AOPs) demonstrate as a powerful system to decompose a broad spectrum of refractory organic contaminants in complicated water matrix[17-19]. Peroxymonosulfate (PMS) as a typical persulfate salt with an asymmetric structure ($HO\text{-}SO_4^-$) has been widely applied to produce ROS such as $SO_4^{\bullet-}$ and hydroxyl radical ($^{\bullet}OH$, E^0=2.7 V vs NHE) for advanced oxidation. Transition metals such as Fe, Co, Mn and their oxides are excellent PMS activators to produce $SO_4^{\bullet-}$ for SR-AOPs[20]. However, the associated secondary pollution from metal leaching and massive sludge generation hinder the practical application.[21] Alternatively, metal-free nanocarbon materials such as graphene and carbon nanotubes (CNTs) emerge as promising alternatives to metal catalysts in AOPs, owing to their engineered dimensional structure, tunable physicochemical properties and environmental-benign nature[21]. One challenge with nanocarbon materials, however, is the trade-off between the superb catalytic performance and mediocre stability in oxidative environment. As a result, it is desirable to fabricate robust nanocarbon catalysts via green and facile approaches without the compromise in reactivity and stability.

In pioneering studies, we discovered that heteroatom doping (e.g. B, N, S and P) into the honeycomb of sp^2 carbons could create more active sites with enhanced catalytic activity for PMS activation[22-24]. Moreover, manganese oxides are high-performance catalysts in Fenton-like reactions and exhibit the merits of abundance on the earth and low toxicity to the environment[25, 26]. Inspired by the features of both metal and carbon catalysts, nanocomposites were developed by encapsulation of manganese carbide nanoparticles (Mn@NCNTs) in a helically N-doped carbon nanotubes via one-pot pyrolysis. The hybrids were applied for PMS activation and MPs degradation under hydrothermal (HT) conditions. It was found that both the HT ambience and carbon-driven SR-AOPs played indispensable roles in MPs mineralization. Comprehensive investigations into the intermediates and degradation pathway were performed. Furthermore, the toxicity of the intermediates from MPs degradation was

evaluated by analyzing the population of green algae (Chlorella vulgaris) in the reaction filtrate. To the best of our knowledge, this study is among the very first few works to explore feasibility in catalytic degradation of microplastics by SR-AOPs as well as the impacts on the environment. The outcomes of this research can facilitate mechanistic insights into MPs/SR-AOPs and provide a green and promising nanotechnology for effective MPs control in modern wastewater remediation.

7.2 Experimental

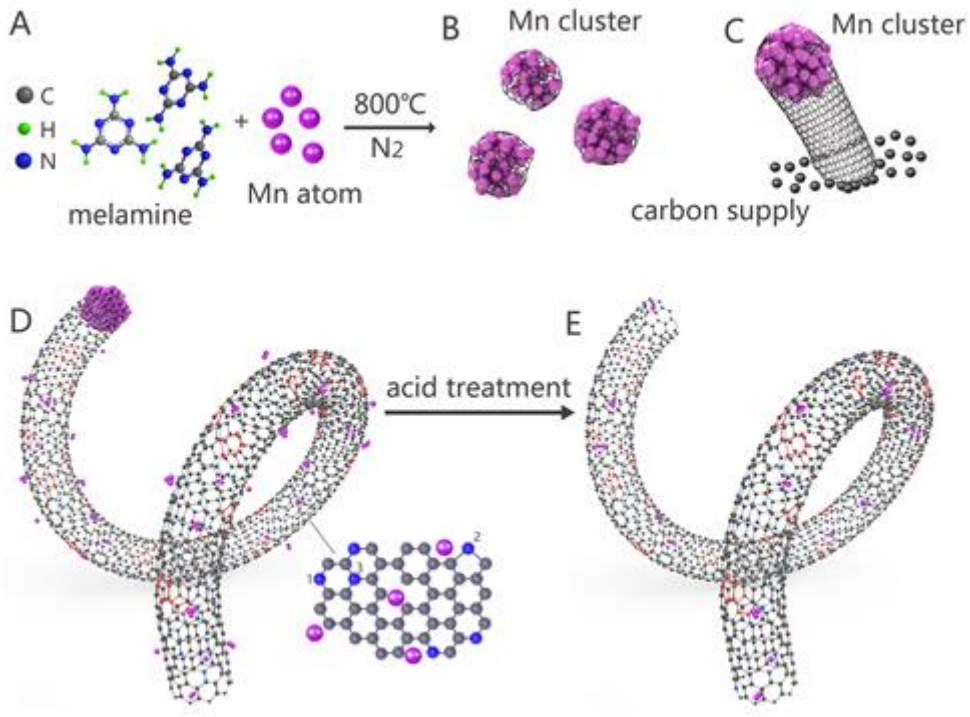

Scheme 7.1. Schematic illustration of the procedure for preparation of Mn@NCNTs.

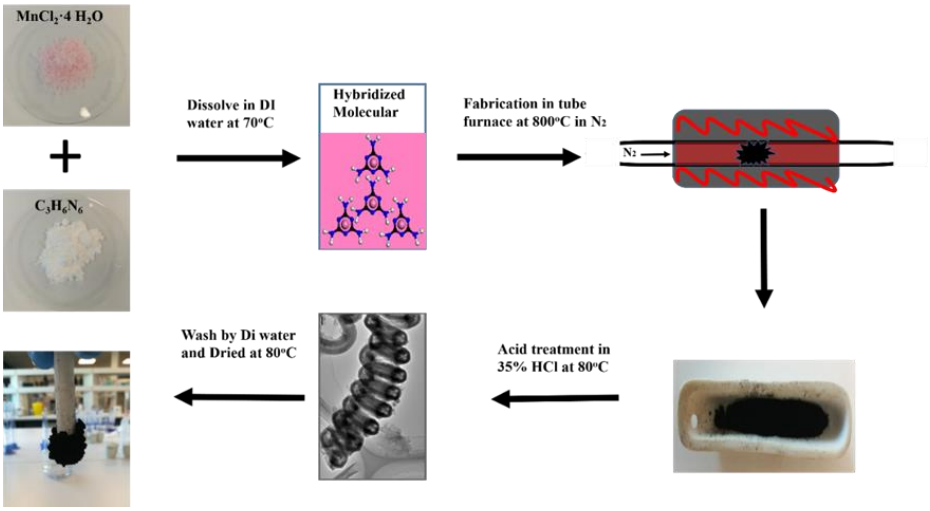

Scheme 7.2 . Schematic illustration of the procedure for preparation of Mn@NCNTs.

7.2.1 Materials and chemicals

Melamine (>99.0%), manganese (II) chloride tetrahydrate ($MnCl_2 \cdot 4H_2O$,>99.9%), potassium peroxymonosulfate ($2KHSO_5 \cdot 3KHSO_4 \cdot K_2SO_4$, Oxone), p-benzoquinone (PBQ), *tert*-butyl alcohol (TBA), ibuprofen (>99.9%), 5,5-dimethylpyrroline-oxide (DMPO, >99.0%) and pure standards of degradation intermediates listed in Table 7.1 were purchased from Sigma-Aldrich. Phenol (>99.0%), acetone, ethanol and hydrochloric acid (32-37%) were obtained from Chem-Supply. High purity nitrogen gas (99.999%) was obtained from BOC. Ultrapure water was used in all of the experiments. Four brands of facial cleansers were purchased from local Cole's supermarkets in Australia, Brand A: "Bioré-Blemish clearing scrub". Brand B: "ĹORÉAL-Hydra Energetic". Brand C: "Neutrogena-Foaming scrub". Brand D: "Clean&Clear-Morning Burst". The MPs from facial cleanser paste by diluted in deionized (DI) water under magnetic stirring at 50 rpm for 24 h and followed by filtration and washing with DI water on a 0.45 μm filter membrane several times. The remaining MPs were then air-dried at 25 °C for 3 d for further use.

7.2.2 Synthesis of Mn@NCNTs.

Mn@NCNTs catalysts were fabricated via direct thermal pyrolysis of melamine with $MnCl_2$. In a typical synthesis, 50 mM melamine and 50 mM $MnCl_2$•$4H_2O$ were mixed in 20 mL DI water. The resulting mixture was dried at 70 °C in an oven overnight. The dried precursors were well ground and calcined at 500 °C for 2 h, and then at 800 °C for 6 h in N_2 atmosphere. After naturally cooling to room temperature, the as-prepared materials were ground in a mortar to fine powders and washed with concentrated hydrochloride acid (35 wt.%) at 80 °C for 24 h to remove the surface unstable species such as supported metals and oxides. The resultant was denoted as Mn@NCNTs-800 and magnetic separation was applied to extract CNTs with higher Mn content. Then, the sample was washed with excessive DI water to neutral condition and dried at 80°C overnight. To investigate the effect of pyrolysis temperature on the morphology and catalysis of the carbocatalysts, we further prepared Mn@NCNTs at different temperatures (600, 700 and 900 °C) denoted as Mn@NCNTs-600, -700 and -900, respectively. The schematic illustration for the catalyst synthesis is illustrated in Scheme 7.1 and 7.2.

7.2.3 Catalyst characterizations

The morphologies of samples were investigated with field emission scanning electron microscopy (FE-SEM, Zeiss Neon 40 EsB). Transmission electron microscopy (TEM) images were measured on JEOL 2100 and energy-dispersive X-ray spectroscopy (EDX) elemental mappings were characterized by FEI Titan G2 80-200 TEM/STEM. The copper lacey grid with a diameter of 3.05 mm and square meshes to support the samples for TEM and EDX analysis. X-ray photoelectron spectroscopy (XPS) was carried out on a Thermo ESCALAB 250 XPS microscope with monochromatic Al-Kα X-rays at a photon energy of 1486.7 eV. The measurement was carried out in a Kratos AXIS Ultra DLD system under UHV conditions with a base pressure less than 1×10^{-9} mBar. X-ray diffraction (XRD) patterns were performed on a Bruker D8-Advanced X-ray instrument using a Cu-Kα radiation with λ at 1.5418 Å. Nitrogen

sorption isotherms were acquired on a Tristar II 3020 in liquid nitrogen (−196 °C) and samples were pre-degassed for three hours at 80 °C. The specific surface area and pore size distribution were evaluated by the Brunauer-Emmett-Teller (BET) equation and the Barrett-Joyner-Halenda (BJH) method, respectively. Raman spectra analysis was recorded on an ISA dispersive Raman spectrometer with argon ion laser (514 nm). A Perkin-Elmer Diamond TGA/DTA thermal analyzer was utilized to evaluate thermogravimetric-differential thermal analysis (TG-DTA) via samples heating in an air flow of 100 mL/min at a heating rate of 10 °C/min. The magnetization behavior of the samples was measured using an Oxford vibrating sample magnetometer (VSM) 3001 at room temperature. The in-situ electron paramagnetic resonance (EPR) was applied to probe the free radicals using 5,5-dimethyl-1-pyrroline N-oxide (DMPO, 99%, Sigma-Aldrich) as the spin trapping agent. The EPR spectra were analyzed and exported by the spin-fitting package of Bruker Xeon software for DMPO-SO_4 (α_H = 0.78, α_H = 1.48, α_H = 9.6, and α_H = 13.2) and DMPO-OH (α_H = 14.8, α_H = 14.8) under reaction conditions (MPs= 5 g/L, catalyst = 0.2 g/L, PMS = 6.5 mM, DMPO= 0.08 M, temperature = 25 °C). The operation conditions were set as the following conditions: centre field, 3515 G; sweep width, 100 G; microwave frequency, 9.87 GHz; power setting, 18.75 mW; scan number, 3. The radical quantitative information was acquired from the Spin Fitting from a Bruker Xenon Software Package.

7.2.4 Catalytic oxidation of MPs and determination of the weight loss.

All the experiments were performed in a 120 mL autoclave and heated in an oven at the set temperatures unless specifically mentioned. Brand A facial cleanser (MPs) was used for kinetic and mechanistic studies. A given amount of Mn@NCNTs catalysts were first dispersed into 80 mL DI water in an autoclave and the MPs were transferred into the mixture. The degradation reaction was triggered by adding a specific amount of PMS. Then, the autoclave was carefully sealed and placed in an oven at the set temperature. After the reaction, the autoclave was

naturally cooled down to the room temperature. The catalysts were collected by magnetic separation. The MPs residues were collected by filtration through a pre-weighed 0.45 μm membrane, washed with ethanol and DI water several times, then dried and weighed as the solid product. The mineralization efficiency was evaluated by the weight abatement of MPs and total organic carbon (TOC) content in the reaction solution. A simple method was adopted to measure the MPs degradation by measuring the weight loss of MPs after the reaction, which was calculated as below:

$$\text{WL}\,(\%) = \frac{m_i - m_f}{m_i} \times 100$$

where WL is the weight loss (%) of MPs, m_i is the initial sample weight (g), and m_f is the weight of MPs residue (g).

The reaction filtrates were analysed on an ultrahigh-performance liquid chromatography (UHPLC) system (Thermo-Fisher Scientific 3000) with a UV detector at the wavelength of 210 nm. An Acclaim RSLC C-18 column was used and a mixed solution of 40% acetonitrile and 60% acetic acid was applied as the mobile phase at a constant flow rate of 0.2 mL/min. The mechanism of PMS activation on Mn@NCNTs was investigated by electron paramagnetic resonance (EPR) from Bruker. DMPO was selected as the spin-trapping agent for $SO_4^{\bullet-}$ and $^{\bullet}OH$ during PMS activation. For TOC evaluation, the reaction solution was filtered by a 0.22 μm membrane, quenched by $Na_2S_2O_3$ and assayed on a Shimadzu TOC-vcph analyser. All the experiments were conducted in duplicates or triplicates and the mean values are presented. The organic degradation intermediates were identified by gaseous chromatography-mass spectroscopy (GC-MS, Agilent).

7.2.5 Toxicity study

The toxicity of the MPs oxidation solution was assessed by using the green algae Chlorella vulgaris (C. vulfaris). The green algae C. vulgaris (strain: CCAP 211/11B, CS-42) was supplied

by the Australian National Algae Culture Collection/CSIRO Microalgae Research and cultivated in Curtin University, Department of Chemical Engineering. The C. vulgaris was inoculated in a 250 mL Erlenmeyer flask that contained 50 mL of the standard medium at 10% concentration. The microalgae cells were cultivated in a shaker incubator at 100 rpm and 25°C under continuous illumination of white fluorescent light at 50 μE. Experiments were conducted in 200 mL cylindrical glass column with 100 mL working volume and the light was applied and removed every 12 h to mimic real-life conditions. For the toxicity tests, the reaction solution was centrifuged and filtered to remove the MPs particles and CNT catalyst. Then, the algae were exposed to different reaction solutions for 14 d at 25 ºC, and the results were compared with the control test, which DI water was used as the medium. After every 24-h exposure to the reaction solution, the inhibition rate (optical density) was analyzed by a UV-Vis spectrophotometer (Anglen) at 680 nm. All the sample tests and control experiments for C. vulgaris *na* were performed in triplicate and the mean value was used.

7.3 Results and discussion

7.3.1 Characterizations of Mn@NCNTs.

The XRD patterns in Figure 7.1 a reveal that Mn@NCNTs presented a higher peak intensity at 26.5 º than pristine CNTs, which implied a higher graphitic degree and a better reducibility attributed to the removal of surface oxygen functionalities and incorporation of nitrogen dopants.[27] In addition, typical diffraction peaks for manganese carbides were observed in a range of 30 - 50 º, which confirmed the successful decoration of Mn species into the carbon framework.[28] Two characteristic peaks, D and G bands of carbon, can be spotted in Raman spectroscopy (Figure 7.1 b), and the increased intensity ratio of the D band versus G band (I_D/I_G) unveiled the higher defective degree induced by nitrogen doping and manganese carbide incorporation. The effect of pyrolysis temperature was further investigated by Raman, suggesting that a higher graphitic degree could be achieved at elevated temperatures. However,

the carbon skeleton of Mn@NCNTs started to collapse and to form irregular nanostructures at 900 ^{o}C. In addition, BET analysis depicts that the specific surface area (SSA) and pore distribution of Mn@NCNTs dramatically increased with increased pyrolysis temperatures from 75.4 m^2g^{-1} (700 ^{o}C) to 217.1 m^2g^{-1} (900 ^{o}C).

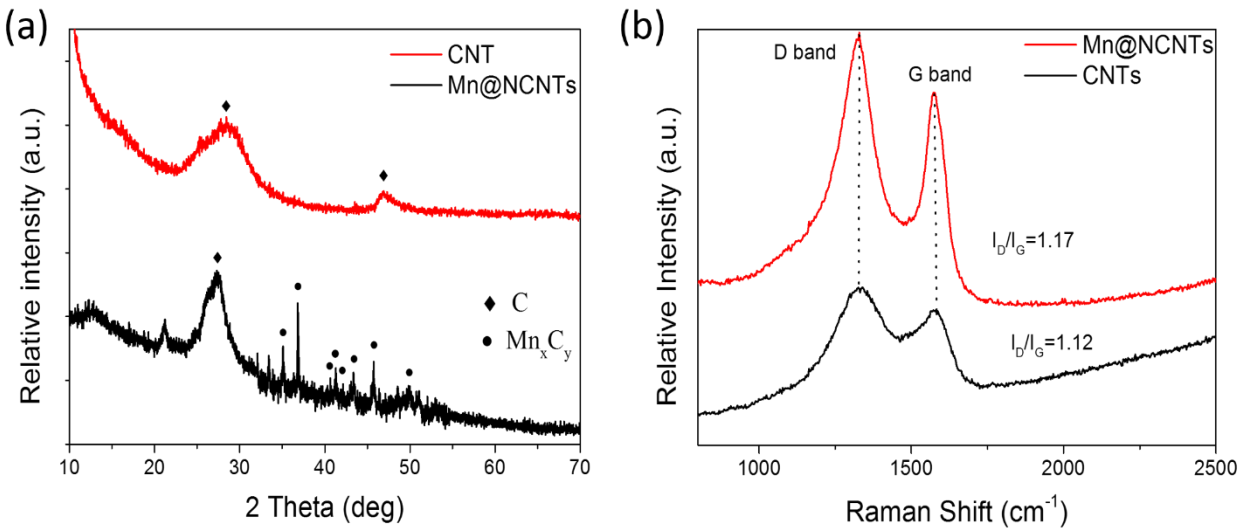

Figure 7.1. (a) XRD patterns of Mn@NCNTs-800 and CNT. (b) Raman spectra of Mn@NCNTs-800 and CNTs.

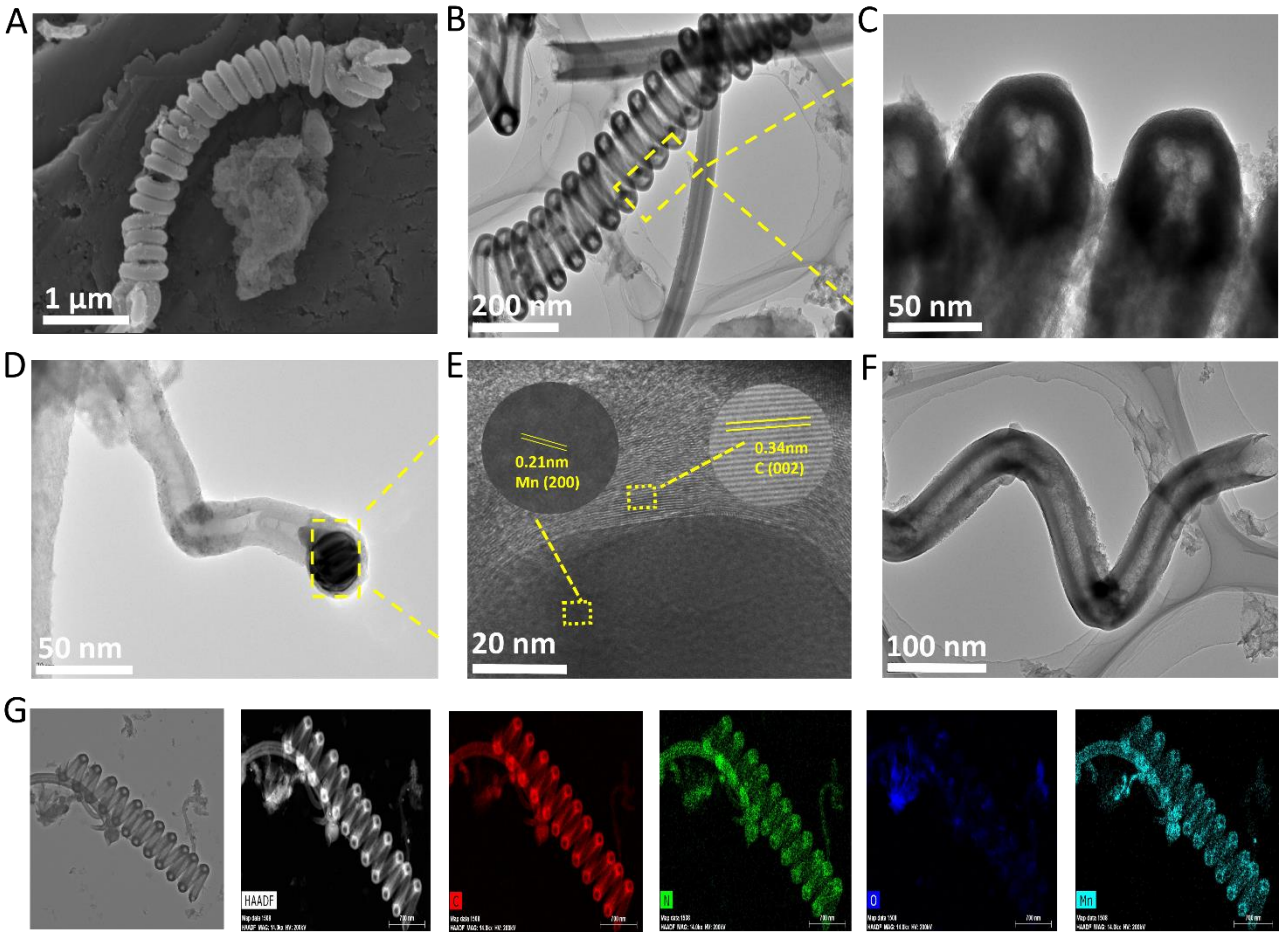

Figure 7.2. (A) SEM image, (B and C) TEM images of Mn@NCNTs-800, (D) TEM image of Mn@NCNTs-700 tip growing mechanism, (E) HRTEM image of Mn nanoparticle tip encapsulation, (F) TEM image of Mn@NCNTs-800 after acid treatment, (G) HAADF-STEM images of Mn@NCNTs-800 and the corresponding energy-dispersive X-ray spectroscopy (EDX) elemental mappings of C, N, O and Mn (from the third left to right).

The morphology and structure of Mn@NCNTs were investigated by SEM and TEM, and their images are shown in Figure 7.2 and 7.3. Figure 7.2 A and B reveal the spring-like morphology of Mn@CNTs-800 with a smooth surface and dimensions of 3-5 µm in length and 20-40 nm in ring diameter. Interestingly, the TEM image in Figure 7.2 C showed that the CNTs presented a hollow tubing structure with an inner tunnel diameter of around 20 nm. The effect of temperature on the catalyst morphology is displayed in Figure 7.3. As shown in the SEM image of Mn@CNTs-600 (Figure 7.3 A), most of the melamine has been converted to graphite and

Mn^{2+} was reduced to zero-valent Mn and manganese carbide particles under the N_2 flow. However, no sight of tubing shape was found. When the temperature increased to 700 ^oC, some curved CNTs were formed (Figure 7.3B), indicating the early-stage formation of helical tubes. By increasing the temperature to 800 ^oC, Mn@CNTs reached the optimal temperature, under which most of the tubes presented a helical shape (Figure 7.3C). Meanwhile, by continually raising the temperature to 900 ^oC, the CNTs were broken down into CNTs rings (Figure 7.3D).

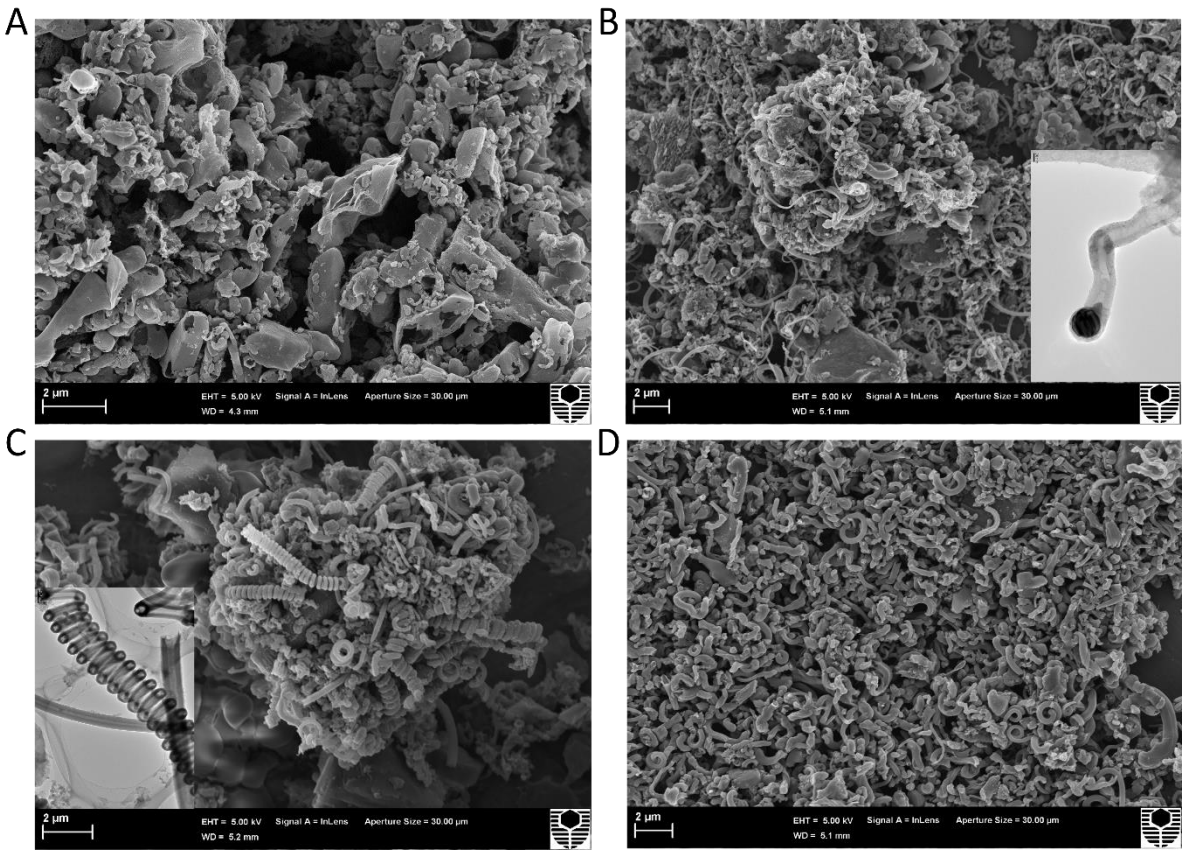

Figure 7.3. SEM images of Mn@NCNTs synthesised at (A) 600 °C, (B) 700 °C, (C) 800 °C and (D) 900 °C. (Insets in (B) and (C) are corresponding TEM images)

From the above SEM/TEM illustrations, the growing mechanism can be inferred. Firstly, Mn^0 nanoparticles were formed at 600 ^oC and started to serve as catalysts for the formation of graphitic cages. As the increased temperature to 700 - 800 ^oC, the graphite cages would serve

as a building block for CNTs formation and growth. Due to the fact that the high temperature may influence the metal species and carbon growth rate, the curved CNTs were bent and formed helical appearance in the resulting samples. Further increasing the temperature to 900 ^{o}C or above, helical tubes were broken into ring-like CNTs due to the thermal cutting of CNTs and decomposition of Mn_7C_3 under over-high temperatures. As illustrated in Scheme S1, Mn nanoparticles start to act as the catalysts at 800 ^{o}C to convert the carbon precursors into graphitic carbons. Then, CNTs start to grow and stretch from the tip of Mn NPs, while the Mn/C clusters are gradually consumed and bonded in the stable form of CNT and Mn_7C_3 (Scheme 7.2). After the harsh acid treatment, most of the superficial metal and oxide were removed, herein leaving the open-end and hollow helical tubes. The unique helical shape of CNTs were formed due to the relatively high surface tension of Mn carbides comparing with other transition metal carbides, such as iron (Fe) and lanthanum (La), which led to the distorted graphitic carbon networks from irregular carbon deposition rate around the Mn core[29, 30]. Due to the high surface energy and closed structure, topological defects such as fivefold and sevenfold carbon rings can be formed allowing the carbon tubes to grow in a tilted direction[31]. The enlarged TEM image of the region marked with rectangles in Figure 7.2E clearly illustrates the lattice fringes of 0.21 and 0.34 nm, corresponding to the d-spacings of the (200) manganese carbide and the (002) graphite basal planes, respectively[29, 32]. After acid treatment, the superficial Mn species and tip Mn particles were removed, and then a smooth and open-ended carbon nanotube was obtained as shown in Figure 7.2F. HAADF-STEM images (Figure 7.2G) display that N dopants were uniformly distributed on the surface and the imbedded Mn species could be spotted beneath the carbon layers. Furthermore, when the temperature was increased to 900 ^{o}C, the CNTs started to break up into shorter tubes (Figure 7.3D), which is consistent to the aforementioned BET and Raman analyses. The crystal structures of the as-prepared Mn@NCNTs were examined by powder XRD as shown in Figure 7.1. The strong diffraction

peaks at 26.5 ^{o} and 45.8 ^{o} were observed on CNTs, corresponding to the (002) and (101) planes of graphitic carbons.[1] For Mn@NCNTs, the diffraction peak at 26.5 ^{o} presented a higher intensity compared with the pristine CNTs and shifted to a higher 2θ degree. This implies a better graphitic degree and reducibility owing to the removal of surface oxygen functionalities and incorporation of nitrogen dopants.[2] In addition, other diffraction peaks located in the range of 30 - 50 ^{o} were discerned, which are the typical diffraction peaks for manganese carbides such as Mn_5C_2 and Mn_7C_3, confirming that Mn species were decorated into the carbon framework.[3] The graphitic degree of Mn@NCNTs was further studied by Raman spectroscopy. The G band (at 1350 cm^{-1}) represents for the perfect sp^2-hybridized carbon honeycomb units, and the D band (at 1570 cm^{-1}) stems from the structural defects such as disordered carbons, impurities, edges and imperfect units in graphene. [4] Therefore, the intensity ratio of the D band versus G band (I_D/I_G) can present the defective degree induced by nitrogen doping and manganese carbide incorporation. The result manifests a stronger D band on Mn@NCNTs than CNTs, indicating that the N doping and manganese carbide formation might significantly enhance the defect degree of the Mn@NCNTs. The effect of pyrolysis temperature was also investigated. The I_D/I_G ratios for Mn@NCNTs-700, -800 and -900 were 1.18, 1.17 and 1.19, respectively, suggesting that pyrolysis temperature impacted the defect population by regulating the graphitization degree and surface chemistry during the re-fabrication of carbon framework. Generally, a higher graphitic degree can be achieved at an elevated temperature. However, the carbon skeleton of Mn@NCNTs started to collapse and form irregular nanostructures with more edge defects at 900 ^{o}C, presenting a slightly higher I_D/I_G.

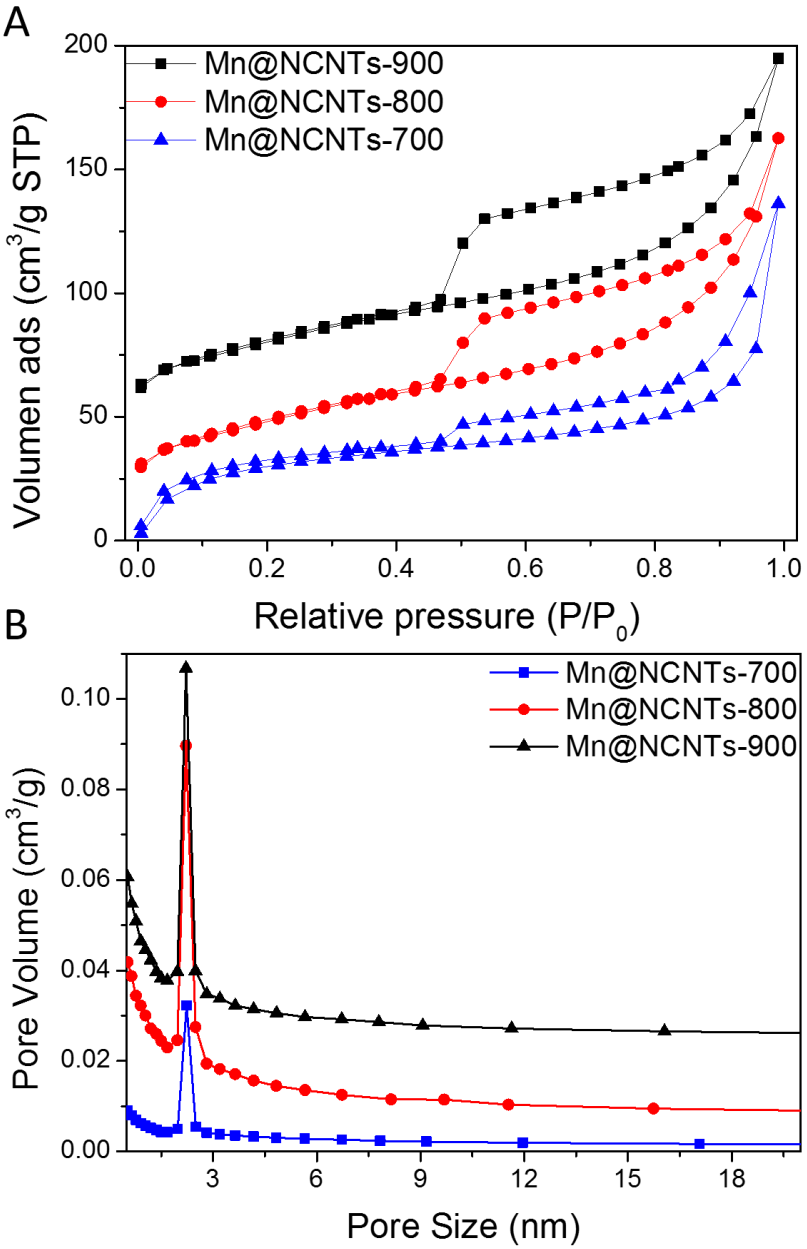

Figure 7.4. (A) N_2 sorption isotherms, and (B) pore size distributions of Mn@NCNTs-700, -800 and -900.

Figure 7.4A depicts N_2 adsorption isotherms and pore distribution of Mn@NCNTs prepared at different temperatures. Mn@NCNTs-900 possesses a higher Specific surface area (SSA 217.1 m^2g^{-1}) than Mn@NCNTs-800 (187.3 m^2g^{-1}) and Mn@NCNTs-700 (75.4 m^2g^{-1}). The dramatically increased SSA from 700 to 800 ^oC was due to the formation of porous structure at 800 ^oC. The SSA was further increased at 900 ^oC possibly due to the breakup of CNT at the high pyrolysis temperature. Figure 7.4 B shows that the pore structures of Mn@NCNTs

primarily consist of micro- and meso- pores (0-3 nm). In addition, X-ray photoelectron spectroscopy (XPS) analysis was carried out to investigate the compositions and surface chemical states of Mn@NCNTs. Figures 7.5 and 7.6 reveal the XPS survey of Mn@NCNTs. The composites were mainly composed of C, N, O, and Mn, whose contents are 85.12, 7.36, 8.14 and 0.79 at.%, respectively, for Mn@NCNTs-800. Trace amounts of impurities such as Si and Cu were also discovered, which was most likely due to the contaminations from the glassware during the synthesis and the copper stub during the XPS testing. In contrast to the EDS and TGA results (Figure 7.7), the surface Mn content detected by XPS is much lower, indicating that the surface Mn species was removed by the acid treatment and the detected Mn was imbedded into the carbon layers in the form of manganese carbide. Thus, the Mn atoms may be able to protected by the outer carbon shells to resist harsh environments like strong acidic and/or oxidative conditions. The Mn contents increased at higher temperatures, which are 0.72, 0.79 and 1.23 at.% at 700, 800 and 900 ^{o}C, respectively. This can be attributed to the decomposition of CNT at higher temperatures, where more manganese species are exposed. Meanwhile, XPS results show that the N 1s peak at the binding energy of around 400 eV was observed for all the samples, with high N doping levels of 6.42, 7.36 and 3.38 at.% for Mn@NCNTs-700, -800 and -900, accordingly. It is noticed that the N content was first increased from 700 to 800 ^{o}C, and then underwent a sharp decrease at 900 ^{o}C. Therefore, a moderate temperature (800 ^{o}C) was beneficial for incorporating more heteroatom dopants into the carbon skeleton, whereas the overheated ambience will lead to the breakup of C-N bonds and decomposition of N dopants during the thermal reconstruction. [5, 6] The values of saturation magnetization of the composite materials were determined. Mn@NCNTs exhibited a saturation magnetization of approximately 8 emu g^{-1} with little coercivity (124 Oe) and remanence (0.08 emu g^{-1}). The results suggest the derived Mn@NCNTs are magnetic and can be simply separated in the presence of an external magnet for recyclability. The high-resolution N 1s XPS

spectra of Mn@NCTNs at different temperatures are displayed in Figures 7.5 B, C and D. The N signals were fitted into four components: 398, 401, 403 and 406 eV, corresponding to pyrrolic N (nitrogen in a five-atom heterocyclic ring), pyridinic N (nitrogen in a six-atom heterocyclic ring), graphitic N (or quaternary N, sp^2-hybridized N neighboured with three sp^2-C) and oxidized N, respectively. The high content of pyrrolic N (five-atom ring) confirms that the existence of five-atom carbon ring due to the distortion of carbon network in formation of the coiled tubes. More graphitic N was implanted into CNTs at higher annealing temperatures, from 6.9 (700 ^oC) to 10.1 at.% (900 ^oC), indicating the better thermal stability of graphitic N among the nitrogen species. In addition, the high-resolution XPS spectra of Mn and C in Figure 7.6 illustrate two Mn components. Mn $2p_{3/2}$ (643.1 eV) and Mn $2p_{1/2}$ (655.2 eV) are the main chemical states for manganese carbides and manganese oxides in Mn@NCNTs. The C signal ranging from 282 to 292 eV was fitted into several sub-peaks including C-C or C-Mn at 284.8 eV, C=N-C at 285.9 eV, C-O at 287.1 eV, C=O at 288.9 eV and O-C=O at 290.9 eV.

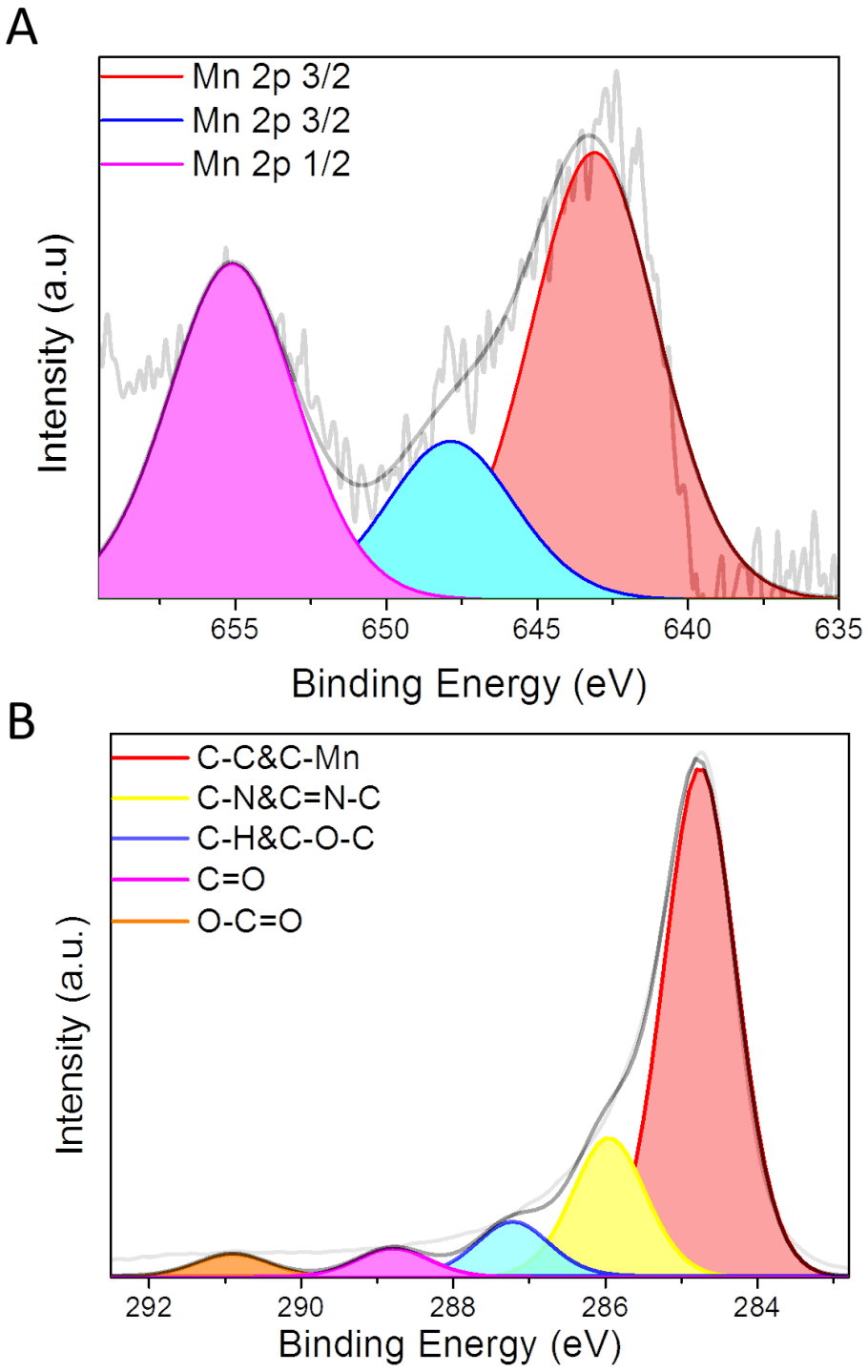

Figure 7.5. XPS spectra of (A) Mn 2p and (B) C 1s of Mn@NCNTs-800.

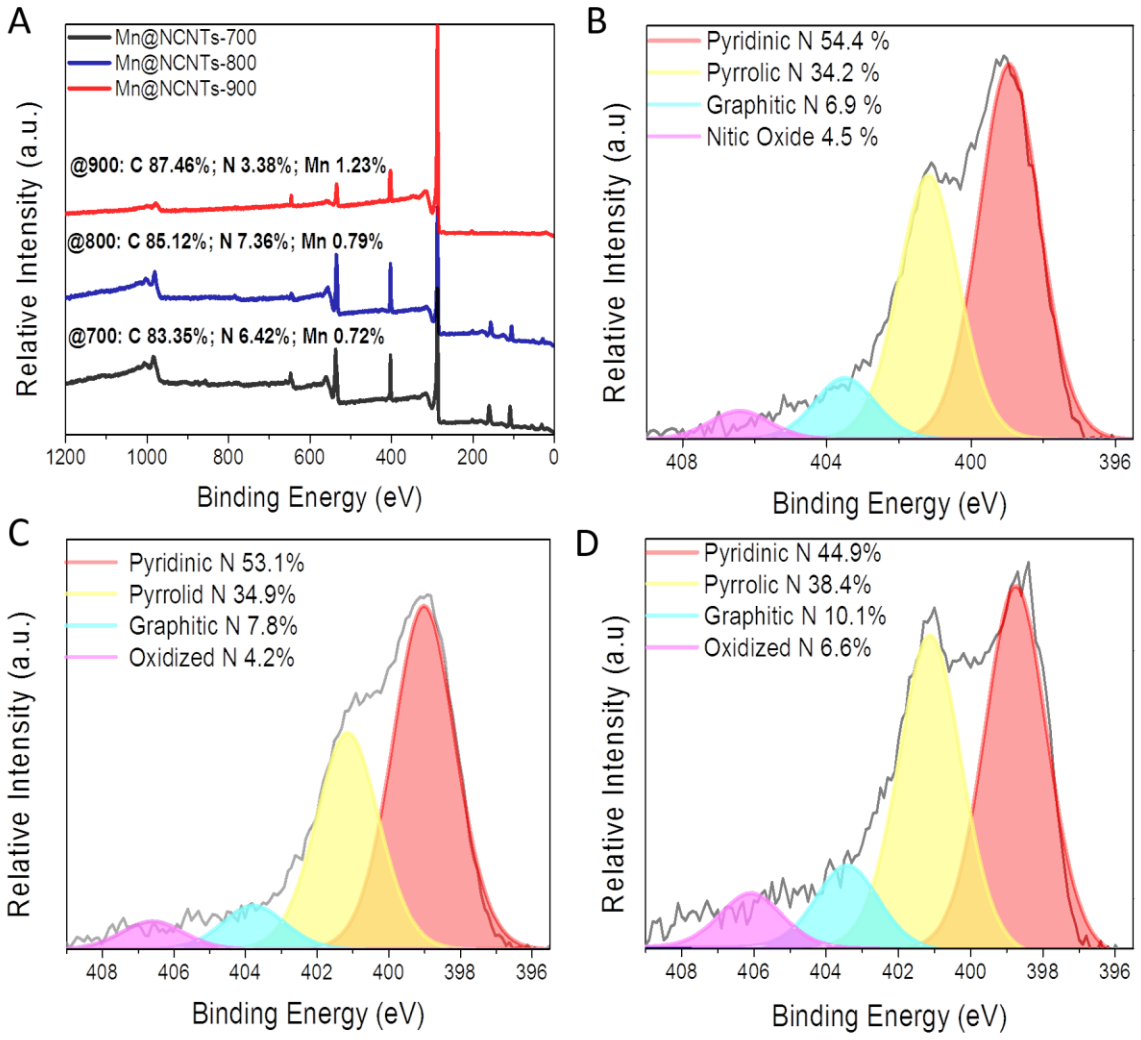

Figure 7.6. (A) XPS survey of Mn@NCNTs and high-resolution scans of N 1s for Mn@NCNTs-700 (B), -800 (C) and (D) -900.

The XPS survey of Mn@NCNTs (Figure 7.6), showing C 1s, N 1s , O 1s and Mn 2p peaks with contents of 85.12, 7.36, 8.14 and 0.79 at.%, respectively. In contrast to the EDS and TGA results, the surface Mn content estimated by the XPS is much lower, indicating that the surface Mn species was removed by the acid treatment and the residual Mn was imbedded into the carbon layers as manganese carbide. Furthermore, as shown in Figure 7.6, the N signals were fitted into four components: 398, 401, 403 and 406 eV, corresponding to pyrrolic N (nitrogen in a five-atom heterocyclic ring), pyridinic N (nitrogen in a six-atom heterocyclic ring),

graphitic N (or quaternary N, sp^2-hybridized N neighbored with three sp^2-C) and oxidized N, respectively. The high content of pyrrolic N (five-atom ring) confirms that the existence of five-atom carbon ring due to the distortion of carbon network in formation of the coiled tubes. Figure 7.6 shows that more graphitic N was implanted into CNTs at higher annealing temperatures, from 6.9 (700 °C) to 10.1 at.% (900 °C), indicating the better thermal stability of graphitic N among the nitrogen species. In order to further probe the chemical composition and their distribution, the corresponding element mapping and energy dispersive X-ray (EDS) were investigated (Figure 7.7). The EDS images confirm that Mn, C and N were uniformly dispersed through the carbon nanotubes. In addition, as shown in Figure 7.7 b, based on the thermogravimetric analysis (TGA) results of Mn@NCNTs before and after acid treatment, it is indicated that about 25 wt.% of Mn species on the catalyst surface could be efficiently removed through the acid washing. To the best of our knowledge, the manganese carbide based helical shape CNTs catalyst is for the first time reported here and the structure control will be further optimized in our future study.

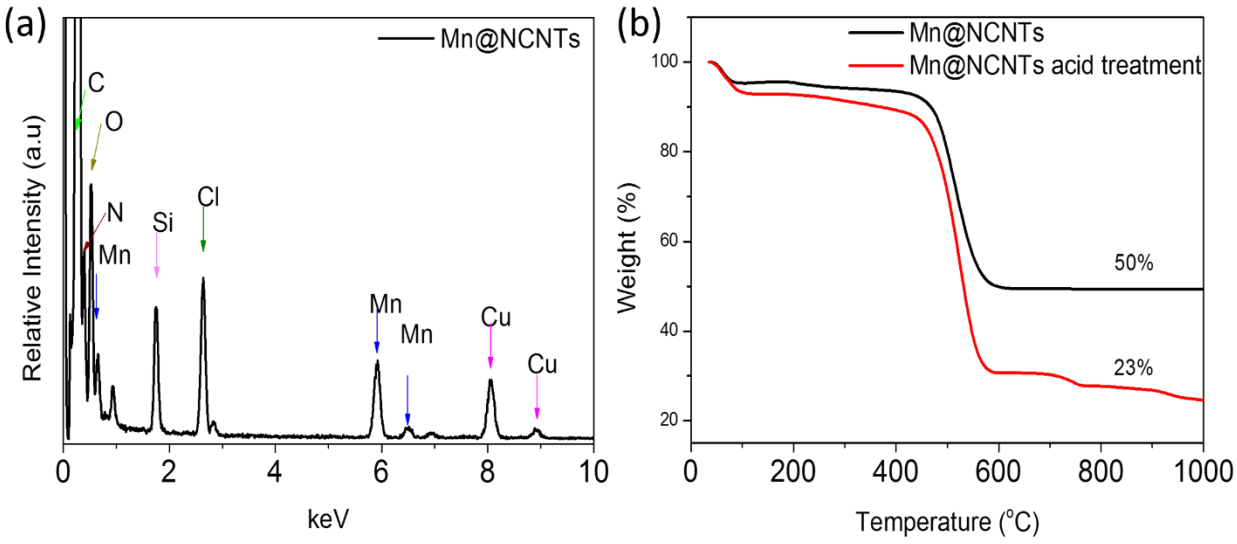

Figure 7.7. (a) EDS analysis of Mn@NCNTs-800; (b) TGA profiles of Mn@NCNTs-800 before and after acid wash treatment.

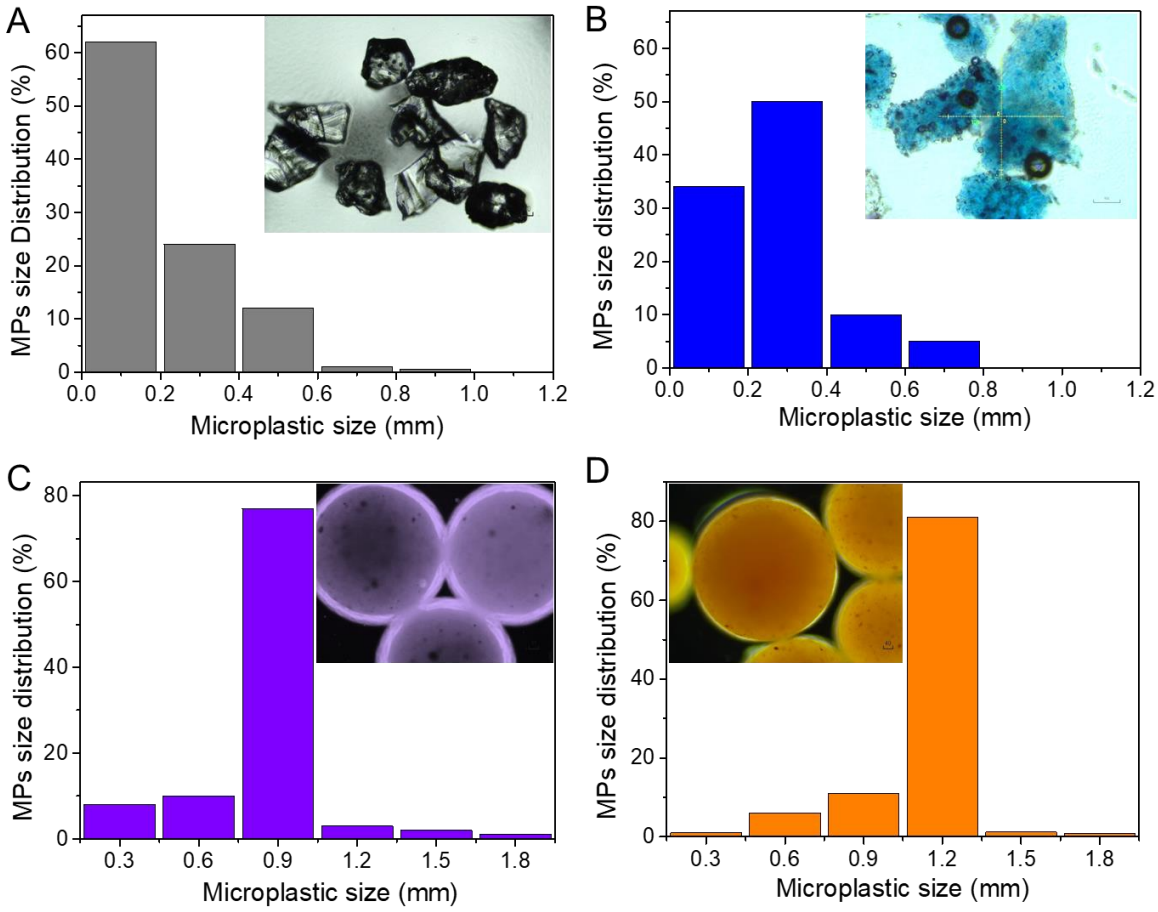

Figure 7.8. Photomicrographs of MPs in the commercial facial cleansers of Brand A (A), B (B), C (C) and D (D).

The optical microscopy images of four types of MPs from different facial cleanser brands are shown in Figure 7.8It reveals that the MPs in brand A and B present rough surfaces and irregular shapes, while brand C and D present a spherical structure. The MPs size distribution was investigated by measuring 80 random MPs particles from each brand on the microscope at different magnifications. A wide size range of MPs was spotted in these samples from 0.01 to 1.5 mm. However, the size distribution varies for different brands. For instance, 60% of MPs in brand A are less than 0.1 mm and 80% of MPs in brand B are less than 0.3 mm. Larger MPs were found for brand C and D. About 90% of MPs in brand C are less than 0.9 mm and 98% of MPs in brand D are less than 1.2 mm.

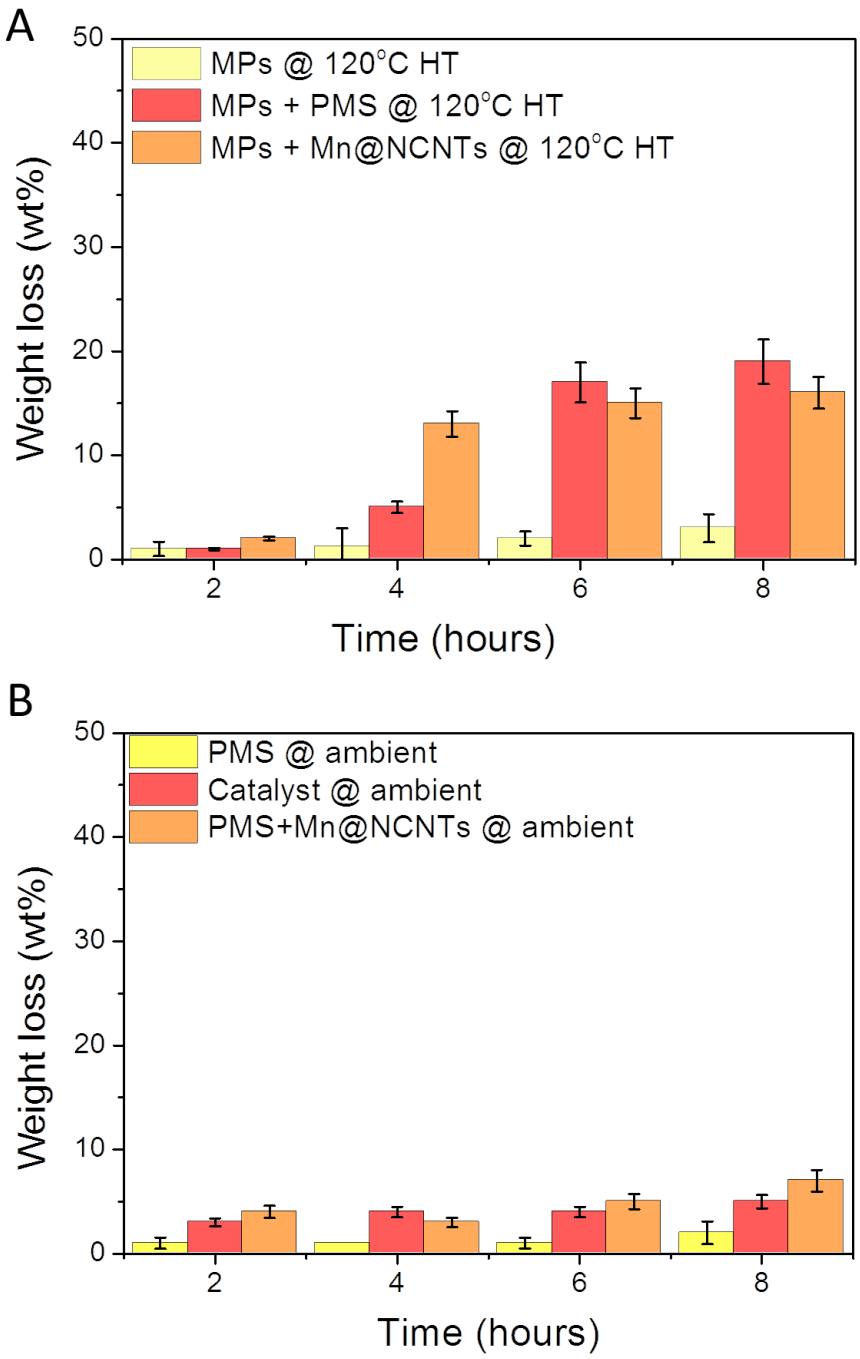

Figure 7.9. Catalytic and noncatalytic MPs degradation under (A) hydrothermal and (B) ambient conditions.

7.3.2 Hydrothermal assisted catalytic PMS activation for MPs degradation.

The catalytic performances of Mn@NCNTs were evaluated for PMS activation and MPs oxidative degradation. The MPs removal efficiencies under different conditions are shown in

Figure 7.9. In the blank experiment (Figure 7.9A), MPs can hardly be degraded with less than 5% weight loss at 120 ^{o}C without PMS and carbocatalyst. With PMS alone at 120 ^{o}C (HT), 17 wt.% of MPs was removed by the reactive free radicals generated from heat-induced PMS activation.[33] Interestingly, most weight loss was experienced during 2-8 h, which might be attributed to the initial breakup of MPs macromolecules triggered at the beginning of the reaction (0-2 h). It is believed that the long-chain polyethylene was firstly sheared into sub-polymers with shorter carbon chains, which leads to a limited weight loss at the early stage. Subsequently, these sub-polymers were attacked by ROS and broken into short chains with a lower molecular weight. In comparison, when Mn@NCNTs was added without PMS, only 16 wt.% MPs were removed after 8 h. To exclude the adsorption effect, an adsorption experiment was performed under room temperature with catalyst alone (Figure 7.9B), and negligible MPs (0.8 wt.%) removal was noticed. The poor adsorption capacity of Mn@NCNTs might be due to weak interactions between the microporous structure (≈ 2 nm) of Mn@NCNTs and micron-sized (≈ 1 mm) plastic particles. Therefore, it is suggested that the presence of a catalyst can lead to reduced apparent activation energy and speed up the self-aging and degradation of the polymer [34]. Furthermore, MPs could not be degraded under the ambient condition even in the presence of both PMS and catalyst. This indicates the significance of synergy of HT condition and carbocatalysis to evolve highly reactive ROS for mineralization of MPs and organic intermediates. Comparative MPs degradation experiments (Figure 7.10A) show that Mn@NCNTs exhibits a superior performance, surpassing graphene oxide (GO), N-doped CNT (NCNTs) and MnO_2. This indicates that manganese-carbides@carbon hybrids remarkably enhanced PMS activation and accelerated the catalytic decomposition of MPs. It was reported that metal could catalyze the dissociation of hydroperoxides and boost the oxidative chain scission of polyolefin.[35] Moreover, to prevent the possible metal leaching as secondary contamination, in this study, the manganese carbides in Mn@NCNTs were protected by multi-

layer carbon spheres, which greatly prevented the metal nanoparticles from corrosion and leaching into the waterbody. To verify this hypothesis, the Mn leaching in the reaction solution of MPs degradation was monitored by ICP-MS (Table S1). To our delight, Mn concentration from the Mn@NCNTs/PMS system (0.17 mg/L) is two-order of magnitude lower than that from MnO_2/PMS system (71.47 mg/L).

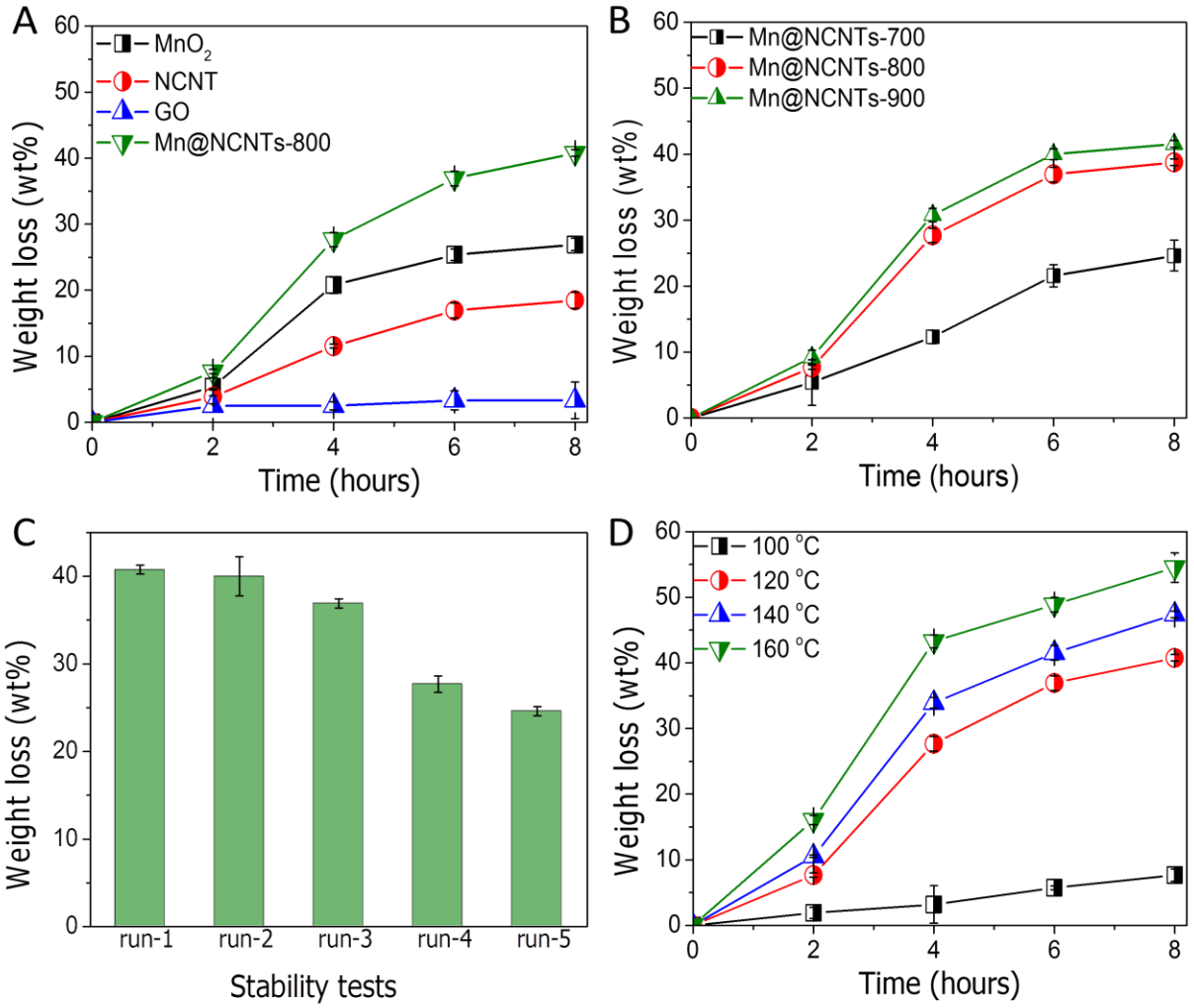

Figure 7.10. (A) MPs removals in PMS activation over different catalysts. (B) Effects of pyrolysis temperature of catalysts on MPs removal. (C) Recyclability tests of Mn@NCNTs-800. (D) Effect of HT temperature on MPs removal. (Catalyst, 0.2 g/L; PMS, 6.5 mM; MPs, 5 g/L; HT, 120 ^{o}C)

Moreover, Figure 7.10B shows the effect of pyrolysis temperature of Mn@NCNTs on the catalytic performances. Under the same reaction conditions, 25%, 41% and 44% of MPs decompositions were achieved on Mn@NCNTs-700, -800 and -900 accordingly in 8 h. The mediocre catalytic performance of Mn@NCNTs-700 is presumably due to the low SSA with fewer exposed catalytic sites, premature formation of manganese carbides and relatively low N-doping level. An obvious improvement in MPs degradation rate occurred on Mn@NCNTs-800. A slight improvement in catalysis was witnessed for Mn@NCNTs-900, which could be resulted from the enlarged SSA and abundant edging defects from the broken helical tubes. Moreover, the Mn leaching from Mn@NCNTs synthesized at different temperatures was monitored. Due to the fact that more metal particles were exposed in the shorter tubes, Mn@NCNTs-900 yields the highest Mn concentration (0.65 mg/L), which is approximately 3- and 4-fold higher than those of Mn@NCNTs-700 (0.21 mg/L) and Mn@NCNTs-800 (0.17 mg/L), respectively. From an environmental perspective, it is more reasonable to choose Mn@NCNTs-800 as the model catalyst for the subsequent kinetic and stability studies despite the trivially enhanced catalysis of Mn@NCNTs-900.

Heterogeneous AOPs typically require robust catalysts for the practical applications. Hence, the stability of Mn@NCNTs-800 was evaluated in consecutive cycles for MPs degradation. Figure 7.10 C shows that only marginal declines in MPs removal efficiency were experienced in the first three cycles, indicating the outstanding stability of Mn@NCNTs in catalytic oxidation. This can be attributed to the high graphitic degree, unique helical structure and formation of nanocomposites. Firstly, the encapsulated manganese carbide can lower the local work function of the interacted carbon shells and promote the electron migration from carbon to PMS to evolve ROS. In reverse, the graphitic carbon layers can reserve the Mn nanoparticles and prevent it from corrosion and leaching into the reaction solution.[36] Meanwhile, the helical Mn@NCNTs demonstrate high structural robustness against collapse and aggregation under

the HT conditions. Nevertheless, MPs removal was declined by 45% in the 5th run, due to the massive consumption of active sites (N-dopants), alteration of surface chemistry by ROS and structural changes such as coverage/blockage of the pores by the intermediates as well as the catalyst loss. The BET results showed that the SSA of Mn@NCNTs was declined by 50% after the 5th run. Furthermore, the XPS analysis of the used catalysts confirmed that, after the fifth cycle, O content was increased from 8.14 at.% (fresh catalyst) to 10.23 at.% (5th run), while N content was slightly decreased from 7.36 at.% (fresh catalyst) to 6.07 at.% (5th run). The alteration of surface chemistry can be ascribed to the oxidation of vulnerable edging defects/vacancies and N-dopants on Mn@NCNTs-800. The partially oxidized carbons would lead to an inferior reducibility and conductivity of the carbon lattice, which limit the electron transfer to PMS to generate reactive radicals. In contrast, Mn content remained unchanged, which confirmed the Mn species were well reserved.

Figure 7.10 D displays the effect of HT temperature on MPs degradation. It was found that the mineralization efficiency was impressively promoted at the elevated HT temperatures. Specifically, less than 10 wt.% of MPs was removed in 8 h at 100 ^{o}C, whereas 41, 47 and 54 wt.% of MPs removals were attained when the HT temperatures were raised to 120, 140 and 160 ^{o}C, accordingly. The apparent activation energy of Mn@NCNTs-800 (87.5 kJ/mol) was lower in comparison with CNT (106.2 kJ/ mol) and NCNT (98.1 kJ/mol), which was mainly attributing to the synergistic effect of nitrogen modification and metal encapsulation. Furthermore, the effects of some important reaction operational parameters, such as pH, MPs shape and size differences, MPs loading and catalyst concentration were investigated (Figure 7.11). The results indicated that the acidic condition and a higher catalyst concentration could speed up the oxidation process. Meanwhile, a larger MPs size and a greater MPs loading would diminish the decomposition efficiency.

The effects of initial solution pH of Mn@NCNTs/PMS system were investigated. As shown

in Figure 7.11 A, the catalytic system is effective for MPs degradation in a wide pH range from 3 – 10. The MPs removal rate was improved when the pH was adjusted to 3 compared to the neutral (pH = 7) and basic (pH = 10) conditions. Therefore, catalytic MPs decomposition in Mn@NCNTs/PMS favoured an acidic environment. Furthermore, the novel AOPs system was applied to degrade MPs from different sources (Figure 7.11 B) and oxidation rates turned out to be distinct. Since the microbeads in the selected brands in this study are all made of polyethylene, the differences in degradation resistance might be due to the variations in surface areas and additives in the MPs, which should be investigated in future studies.

Figure 7.11 C shows the effect of initial MPs loading and MPs removal efficiency decreased with increased initial MPs contents. Specifically, 41% MPs was removed in the control test (5 g/L), whereas only 24% and 9% MPs were degraded at 8 and 12 g/L, respectively. The fast consumption of reactive species and blockage of active sites on catalyst might be the major causes for the deteriorated removal efficiency of excessive MPs. Moreover, insufficient catalytic sites and PMS could also be the key factors limiting the degradation of high-concentration MPs. Moreover, Figure 7.11 D reveals the effect of catalyst concentration on MPs removal. The MPs degradation was dramatically abated from 34 wt.% to 15 wt.% when half dosage of the control catalyst was used. However, MPs removal efficiency was increased to 47 wt.% when the catalyst amount was doubled. The sufficient catalyst loading will bring more active sites for PMS activation, herein improving MPs decomposition efficiency.

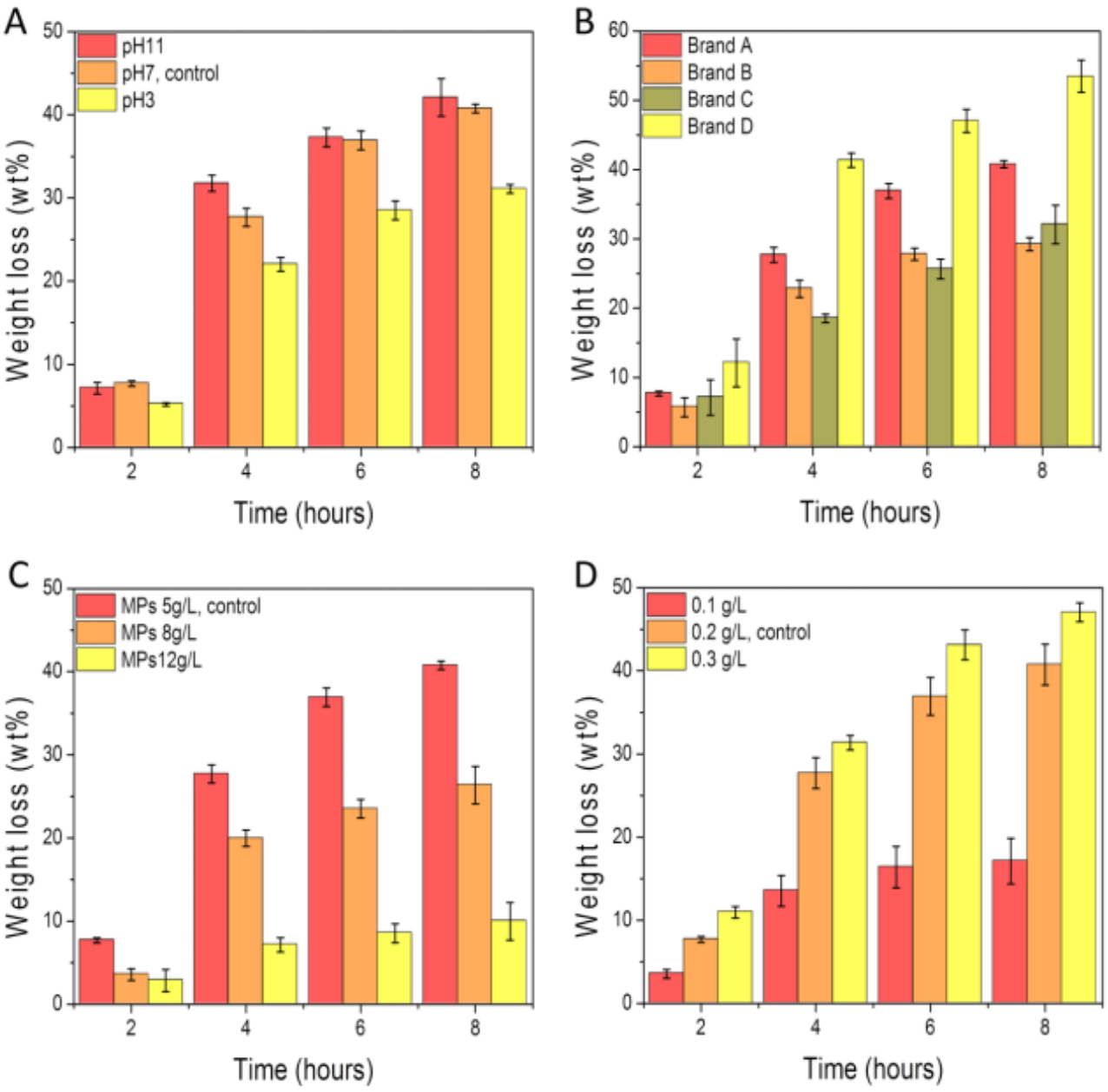

Figure 7.11. (A) MPs degradation under different pH values. (B) MPs from different brands (C) Effect of MPs loading on MPs removal. (D) Effect of catalyst dosage on MPs removal. (Catalyst, 0.2 g/L; PMS, 6.5 mM; MPs, 5 g/L; hydrothermal temperature, 120 ^{o}C, unless specifically mentioned)

7.3.3 Mechanism of generation and evolution of active radicals.

EPR and radical quenching experiments were carried out to identify the responsible ROS in

the Mn@NCNTs/PMS system for MPs degradation. In MPs oxidation process, polyvinyl alcohol (PA) has been identified as one of the dominant degradation intermediates, thus it was adopted as the target organic pollutant in the ROS investigation. EPR spectra were obtained using DMPO as the spin trapping agent for $^{\bullet}OH$ and $SO_4^{\bullet-}$. Figure 7.12A shows that no radical signals of $^{\bullet}OH$ or $SO_4^{\bullet-}$ in PMS solution in the absence of Mn@NCNTs at room temperature. This is consistent with the aforementioned MPs oxidation results. In comparison, high peak intensities of free radicals were noticed in the Mn@NCNTs/PMS system. It can be seen that DMPO-OH peaks are more intense than DMPO-SO_4 peaks, which might be due to the interconversion between $^{\bullet}OH$ and $SO_4^{\bullet-}$.[7] Furthermore, to reveal the hydrothermal effect on radical production, a parallel experiment was conducted where the reaction solution was heated in boiling water at 99 ^{o}C to afford *in situ* detection. Similarly, strong characteristic signals of both $^{\bullet}OH$ and $SO_4^{\bullet-}$ were observed when the heat was applied, suggesting that PMS can be effectively activated to produce ROS under the hydrothermal conditions. Additionally, classic radical quenching tests were also performed to investigate the principal ROS contributing to MPs degradation. Methanol and *tert*-butyl alcohol (TBA) were selected as the radical scavengers due to their distinct reaction rates with $SO_4^{\bullet-}$ and $^{\bullet}OH$ (Figure 7.12B). In the control test with free of radical scavengers, PA (45 ppm) was efficiently removed in 1 h. While the addition of 200 mM TBA (hydroxyl radical scavenger) only manifested a moderate inhibition on PA degradation rate with 90% PA oxidation. Methanol is an efficient scavenger for both $SO_4^{\bullet-}$ and $^{\bullet}OH$ and the addition of excessive amount of methanol (500 mM) gave further retardation on PA degradation, suggesting both $SO_4^{\bullet-}$ and $^{\bullet}OH$ contributed to PA decomposition. [8] It is worthy to point out that, the PA oxidation reaction was not completely ceased in the presence of methanol, despite that most of $SO_4^{\bullet-}$ and $^{\bullet}OH$ had been scavenged. Recently, a nonradical process was discovered upon N doping in carbon nanotubes in PMS-based AOPs[9]. In the nonradical pathway, the activated PMS molecule tends to bond with the

positively charged sp^2 carbon neighbouring to N dopants and then directly reacts with the adsorbed organics via electron transfer. The highly covalent π electrons are beneficial for activating the peroxide O-O bond in PMS, and the nitrogen dopants can activate the adjacent carbons for the promoted catalysis.[9] In addition, high concentrated methanol solution was applied to study its quenching effects on MPs degradation. As shown in Figure 7.12C, in the presence of methanol, 20 wt.% less of MPs removal was obtained due to the elimination of free radicals, indicating the significance of oxidation by $^{\bullet}OH$ and $SO_4^{\bullet-}$ radicals to polymer decomposition. Moreover, in comparison with the reaction when Mn@NCNTs was presented along, the quenched Mn@NCNTs/PMS system only showed marginal improvement. Herein, the nonradical oxidation also played a minor role in MPs oxidation under hydrothermal condition than in PA degradation at room temperature. In the previous studies, it was discovered that water oxidation was experienced via the reaction with $SO_4^{\bullet-}$ at the elevated reaction temperatures (>45 °C)[10]. The incorporation of N-dopants and transition metals into the carbon network can simultaneously enhance the binding strength with peroxide/water molecules, leading to efficient production of ROS[7, 11]. In this study, due to the hydrothermal condition (high temperature and pressure), the synergistic effect of thermal activation and catalytic activation can improve the free radical production efficiency, thereby dramatically enhancing the degradation of macromolecules. On the other hand, since the nonradical pathway relies on the direct contact between catalyst and pollutant, we suppose that the limited contact between insoluble MPs and Mn@NCNTs has largely restrained the nonradical oxidation.

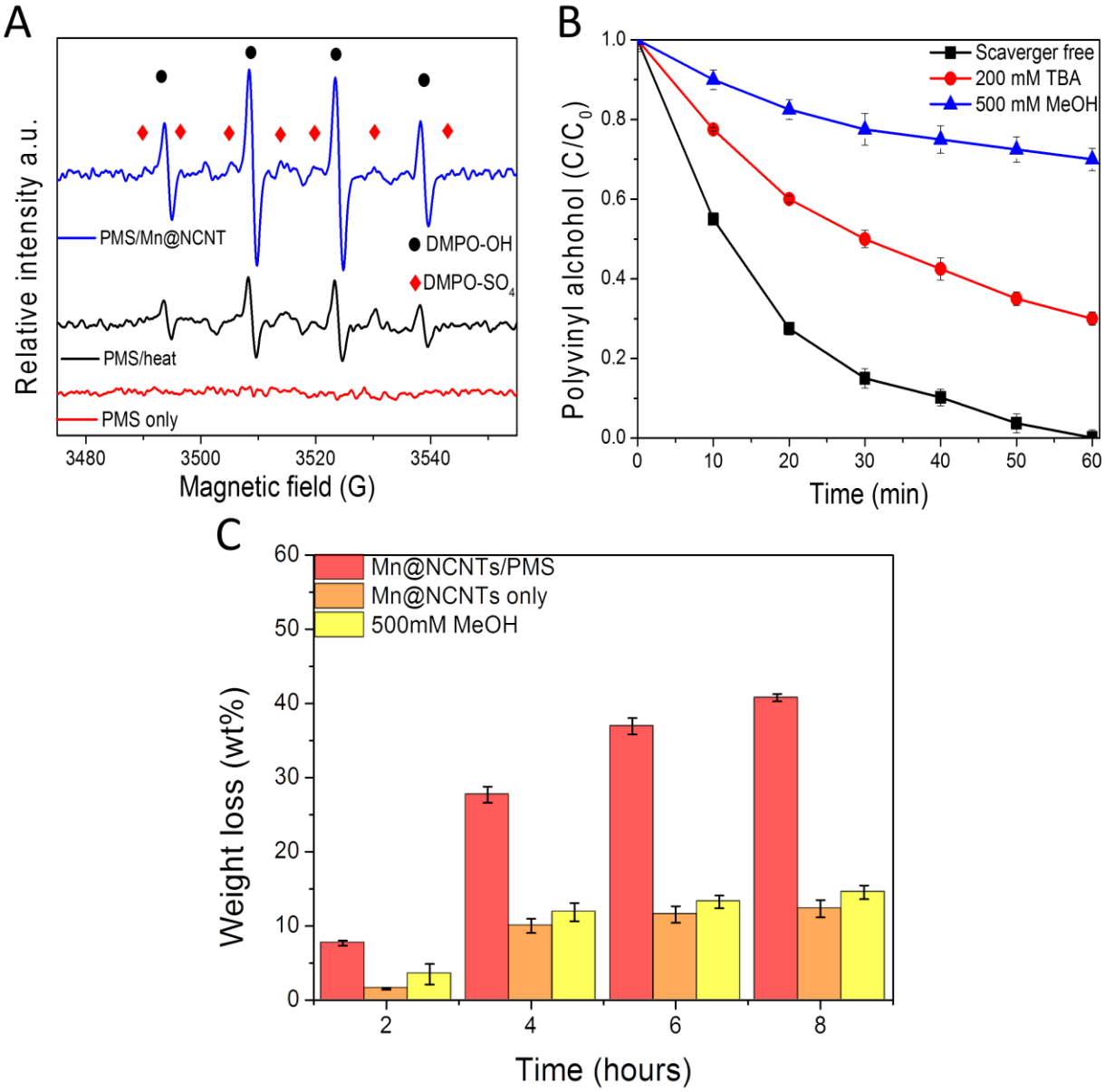

Figure 7.12. (A) EPR spectra of PMS activation with Mn@NCNTs (99 ^{o}C). (B) Effect of radical quenching by methanol on polyvinyl alcohol degradation. (C) Effects of radical quenching by methanol on MPs degradation. (Mn@NCNTs-800, 0.2 g/L; PMS, 6.5 mM; MPs, 5 g/ L; hydrothermal temperature, 120 ^{o}C unless specifically mentioned)

7.3.4 Morphology and FTIR analysis of oxidized MPs samples

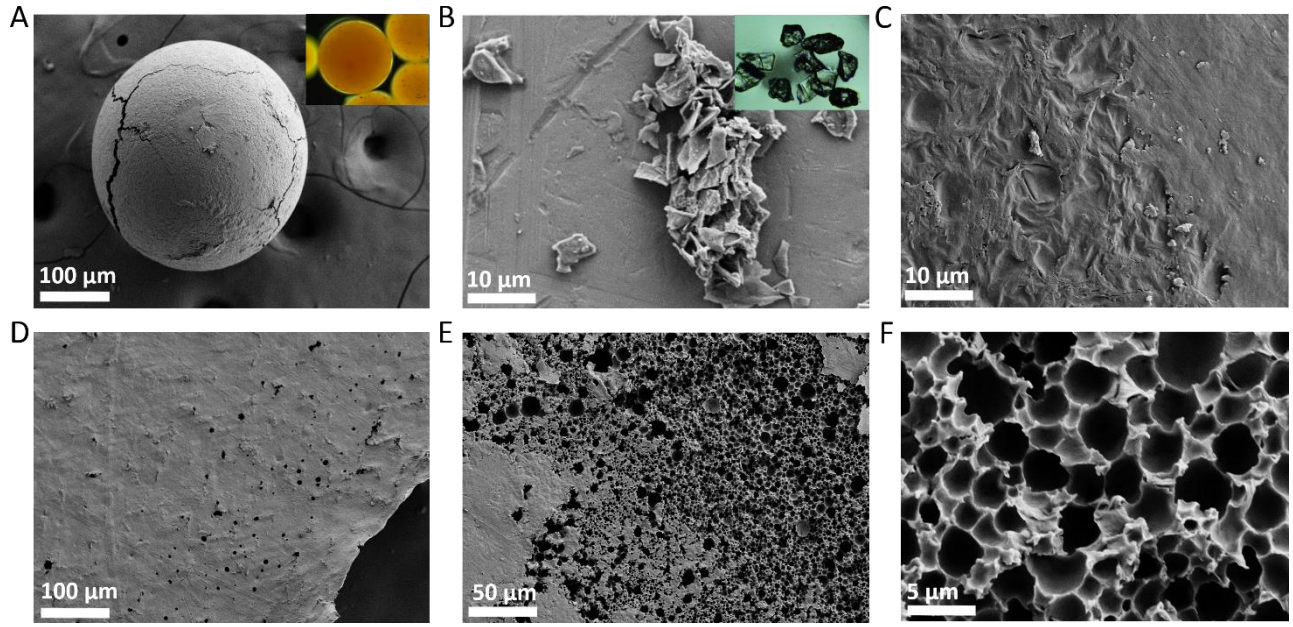

Figure 7.13. SEM images of MPs debris from (a) Brand A and (b) Brand B facial cleaner after 2 h degradation. MPs (Brand A) after (c) 4 h, (d) 6 h, (e) and (f) 8 h degradation. (Catalyst, 0.2 g/ L; PMS, 6.5 mM; MPs, 5 g/ L; HT, 120 ^{o}C)

Figure 7.13A and B display the surface morphology of plastic debris and microbeads after oxidation for 2 h in Mn@NCNTs/PMS. The MPs debris tended to aggregate and noticeable cracks appeared on the MPs bead surface. The original colors (shown in the insets) were faded to milky white and the mechanical property was dramatically deteriorated, turning MPs into brittle particles. Interestingly, after 4 h treatment, most of the MPs were fused together to form a thin polymer film (Figure 7.13C). When the oxidation was proceeded for 6 h, a rough surface with numerous pores (around 3 µm in diameter) formed on the polymer (Figure 7.13D), indicating that the composite film was partially decomposed with a rapid weight loss. Figure 7.13E and F exhibit that large amounts of cavities were generated after 8 h reaction, attributed to the MPs decomposition by the free radicals from Mn@NCNTs/HT/PMS system.

The MPs mineralization process was also analyzed by FTIR spectra to reveal the changes in chemical properties during the polymer degradation. The absorbance range of 1500–1400 cm^{-1}

in Figure 7.14A corresponded to –CH_2 stretching and presence of aromatic rings in the polymer chain.[37] The peaks emerge at 1715 cm^{-1} represent the stretching vibration of carbonyl group (C = O) or ketone moieties in the MPs polymer. The peak of C-O group was displayed in the range of 1015 to 1258 cm^{-1}. In comparison with the untreated MPs, the treated MPs showed several discernable changes such as peak shifting (peaks 8 and 10) to a lower wavenumber and intensity alternations (peaks 3, 4, 6 and10). Specifically, a broad peak at 3435 cm^{-1} was discovered for the treated MPs in Figure 7.14B, corresponding to the hydroxyl groups (O-H) with hydrogen bond or C≡C-H groups in the MPs, while the peak was inconspicuous in the spectra of the untreated MPs [37]. The peak intensity of OH at 3435 cm^{-1} was remarkably enhanced in the treated MPs [1] and the peak intensity of C=O at 1715 cm^{-1} was greatly increased after the reaction, suggesting the effective oxidation of MPs. Moreover, the main peaks at 2911 and 2848 cm^{-1} represent CH groups and asymmetric stretching of CH_2 in MPs, and the intensity was much weakened after the oxidative degradation [37 38].

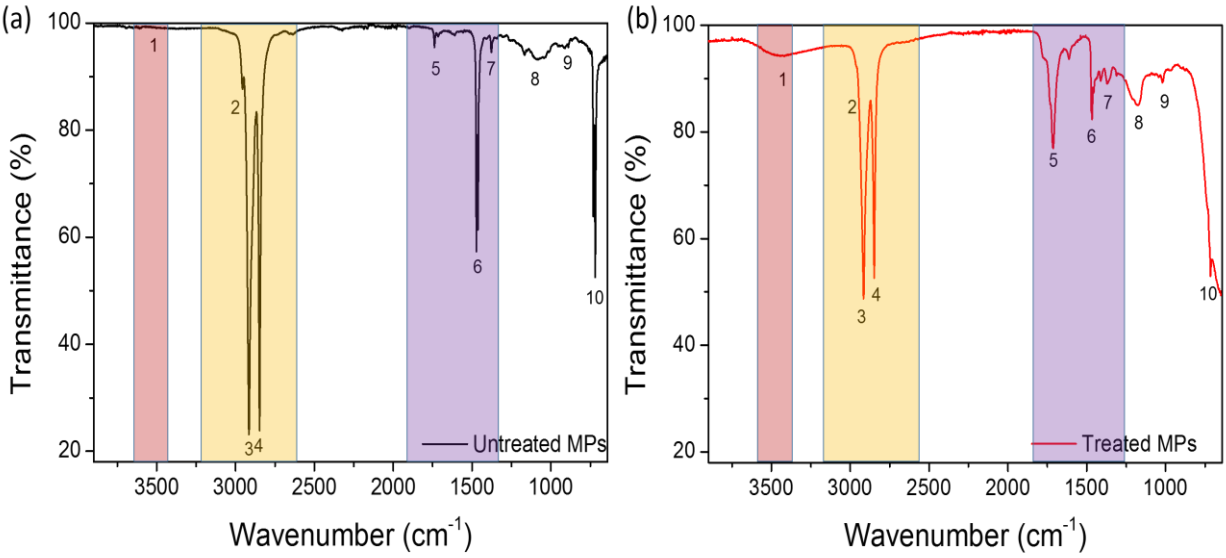

Figure 7.14. FTIR spectra of (a) untreated MPs and (b) oxidized MPs by Mn@NCNTs/PMS. (Catalyst, 0.2 g/ L; PMS, 6.5 mM; brand 1 MPs, 5 g/ L; hydrothermal T, 120 ^{o}C)

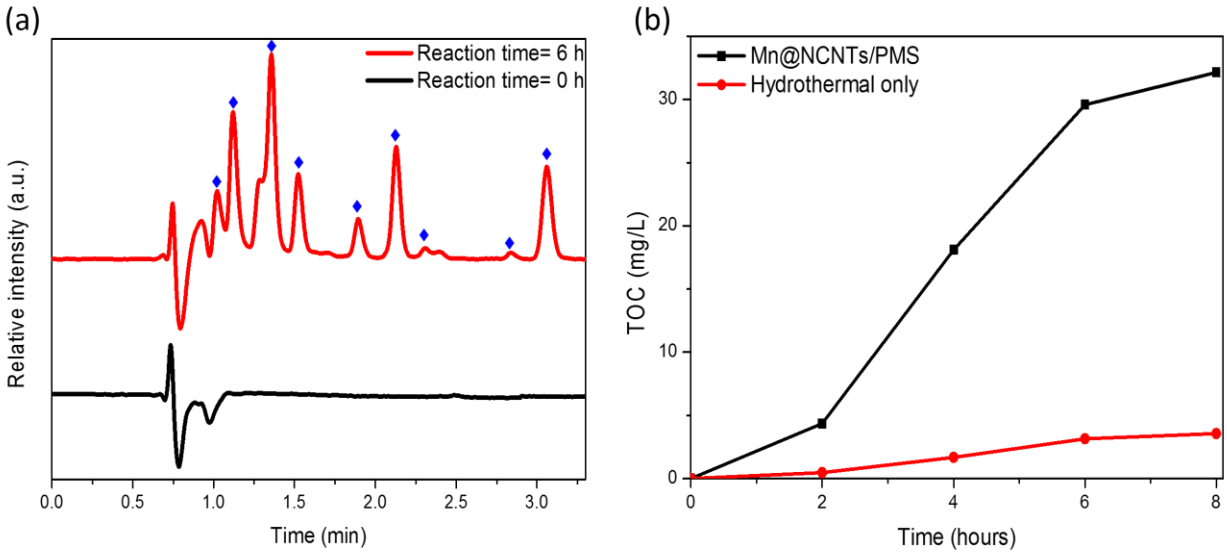

Figure 7.15. (a) HPLC spectra of MPs degradation solution. (b) Total organic carbon variations of MPs degradation. (Catalyst, 0.2 g/L; PMS, 6.5 mM; MPs, 5 g/ L; hydrothermal temperature, 120 ^{o}C)

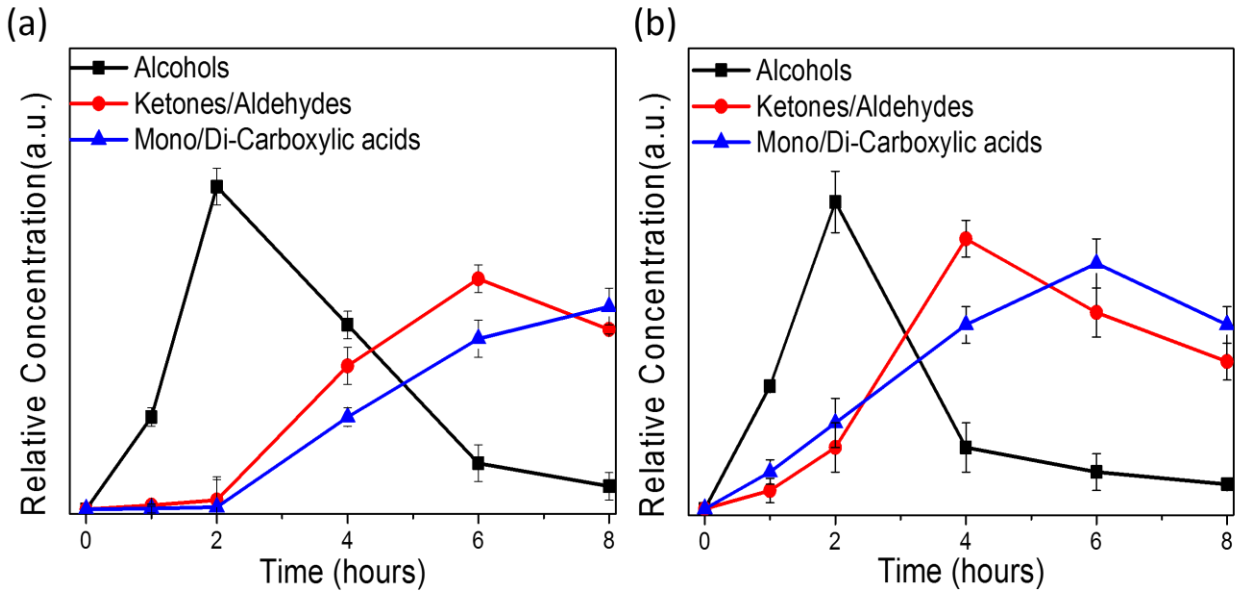

Figure 7.16. Evolution of organic intermediates in MPs oxidation at different hydrothermal temperatures, (a) 120 ^{o}C. (b) 160 ^{o}C.

7.3.5 Intermediates and degradation pathway.

Identification of MPs degradation products is an important step in understanding the mineralization mechanism and their environmental impacts. HPLC, GC-MS and TOC were applied to evaluate the intermediates during MPs oxidation. As shown in Figure 7.15A, new peaks emerged when MPs were treated by Mn@NCNTs/PMS system compared with the control experiment without catalyst or PMS. These peaks originated from low-weight molecules of oligomers or organics from the breakdown of long-chain polyethylene. Meanwhile, the TOC remained unchanged when MPs were treated in Mn@NCNTs/PMS under ambient condition (Figure 7.15B). Moreover, a negligible amount (4 mg/L) of TOC was detected in the presence of sole HT, which can be due to the incomplete hydrolysis of the polymer. Distinctly, when Mn@NCNTs/PMS was integrated with HT, a high TOC (30 mg/L) was detected in the solution. The impressively increased TOC contents confirm the vital roles of both carbocatalysis and HT condition during MPs degradation. The degradation intermediates were identified through GC-MS analysis on a Thermo scientific TRACE 1300 GC Ultra system with the electron ionization mode. A TG-5MS capillary column (15 m × 0.25 mm × 0.1 μm) was used for analysis. Prior to GC-MS analysis, the samples were extracted with toluene three times. The initial temperature of the column oven was held at 40 °C for 5 min, and then heated up to 285 °C at a ramping rate of 5 °C/min. Helium was used as the carrier gas. Mass spectrometric detection was operated with 70 eV electron impact (EI) mode at an ionization current of 50 μA and an ion source temperature of 250 °C. The mass spectra were recorded in a full scan mode (m/z 50-1000) for qualitative analysis.

Furthermore, the degradation intermediates were further investigated by GC-MS, where up to 21 short-chain organics were detected. The structure and formula of these products are summarized in Table 7.1. The identified substances include alkanes, alkenes, ketones, alcohols, aldehydes, mono/dicarboxylic acids, lactones, keto-acids and esters. According to their

abundance, three major functional groups, alcohol, aldehyde/ketone and carboxyl acid, were monitored during the oxidation. As shown in Figure 7.16 a, all the three organic groups were barely observed at the early stage of MPs degradation (120 ^{o}C), suggesting the initial oxidation mainly occurred at the macromolecule level for cleavage of long-chain carbons in the polymer. The concentration of alcohol products increased significantly in the second hour, implying that the alcohols might be the early-stage intermediates. Moreover, polyethylene could be subjected to HT effect to induce the breakup of C-C bond to produce two hydrocarbon radicals. Then, the hydrocarbon radicals would be decomposed to lower-weight molecules, followed by β-scission and hydrogen abstraction by other hydrocarbons to produce new hydrocarbon radicals[39]. In the Mn@NCNTs/PMS system, a large amount of hydroxyl and sulfate radicals were generated, which would rapidly react with hydrocarbon radicals and lead to chain breakage and boost the degradation rate. The aldehyde/ketone continually accumulated and reached the peaking level at 6 h, and then gradually declined to a low content due to the deeper mineralization. Therefore, the aldehyde/ketone was likely to be the transient intermediates, which would undergo further oxidation[35]. Meanwhile, the concentration of carboxylic acids steadily increased throughout the degradation process and became the dominant products after 8-hour reaction. Figure 7.16B shows the evolution of intermediates at a higher HT temperature (160 ^{o}C). It can be seen that the aldehyde/ketone concentration remarkably increased and reached the maximum in 4 h. Meanwhile, carboxylic acids were rapidly generated, indicating that a deeper oxidation at the elevated HT environment.

The HT condition is crucial to the MPs degradation because it simultaneously affords high pressure and physical tearing to the polyethylene chain via the boiling bubbles and vapor, which facilitates the MPs degradation. Moreover, the thermal condition is advantageous to both catalytic- and heat- driven PMS activation to generate more ROS for oxidation of MPs and intermediates, especially the hydrophilic species are more susceptible to ROS [40]. Specifically,

the MPs degradation is initialized by polyethylene backbone cleavage under the HT condition to trigger the production of hydrocarbon radicals. Then the metastable hydrocarbon species become the victims of ROS and result in a further chain cleavage into smaller segments with a low molecular weight such as alcohol, aldehydes/ketones and carboxylic acids. These organic intermediates are ultimately mineralized to CO_2 and H_2O by the powerful ROS to realize a high TOC removal efficiency.

Table 7.1. Intermediates formed upon Mn@NCNTs/PMS treatment of MPs, identified by GC-MS and HPLC analysis. Several pure standards were used to confirm the structure.

Compound	Structure	Molecular formula	Molecular mass g·mol^{-1}
Tetracosane	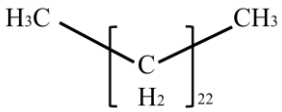	$C_{24}H_{50}$	338.65
Heneicosane	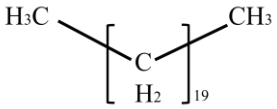	$C_{21}H_{44}$	296.58
Nonadecanol	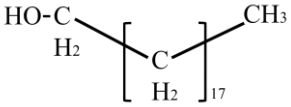	$C_{19}H_{40}O$	284.52
Pentadecanedioic acid	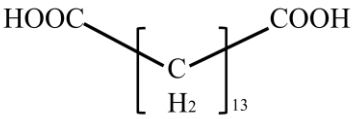	$C_{15}H_{28}O_4$	272.38
Nonadecane	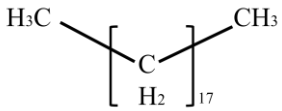	$C_{19}H_{40}$	268.52
Benzyl butyl phthalate	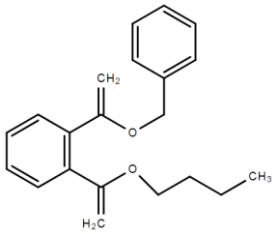	$C_{19}H_{20}O_4$	312.36
14-Methoxy-14-oxotetradecanoic acid	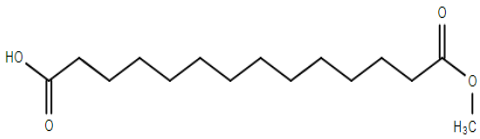	$C_{15}H_{28}O_4$	272.38
Dimethyl suberate	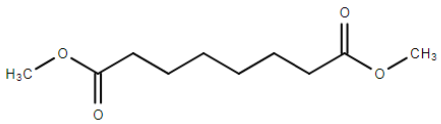	$C_{10}H_{18}O_4$	202.24

Methyl 10-undecynoate	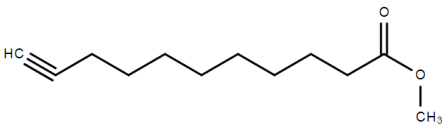	$C_{12}H_{20}O_2$	196.28
Decanoic acid	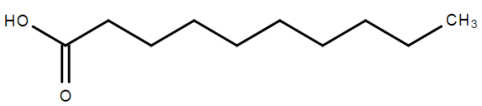	$C_{10}H_{20}O_2$	172.26
Methyl 8-oxooctanoate	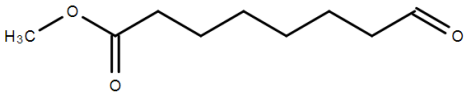	$C_9H_{16}O_3$	172.22
Pimelic acid	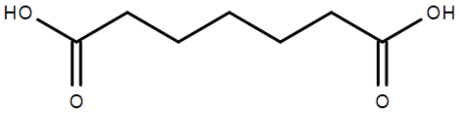	$C_7H_{12}O_4$	160.16
6-Decenal	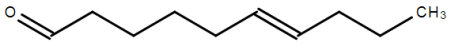	$C_{10}H_{18}O$	154.24
2-Ethylcaproic acid	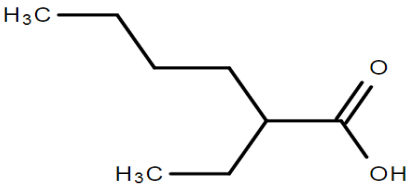	$C_8H_{16}O_2$	144.21
Succinic acid	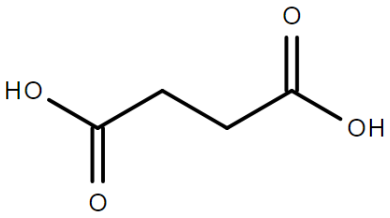	$C_4H_6O_4$	118.08
1-Hexanoic acid	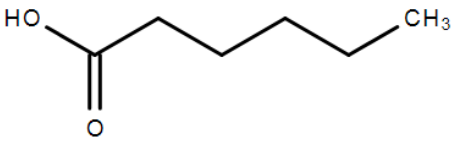	$C_6H_{12}O_2$	116.15
Levulinic acid	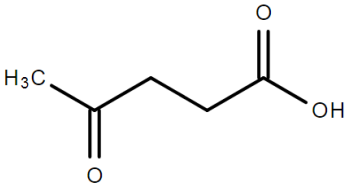	$C_5H_8O_3$	116.11
3-Butenoic acid	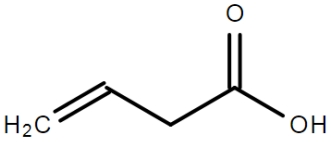	$C_4H_6O_2$	86.08

Propionic acid	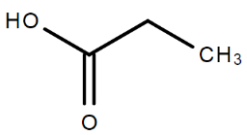	$C_3H_6O_2$	74.07
Acetic acid	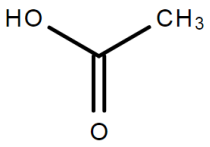	$C_2H_4O_2$	60. 05
Formic acid	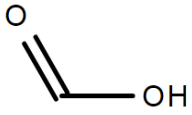	CH_2O_2	46.02

7.3.6 Toxicity study.

The C. vulgaris was employed to assess the toxicity of the degraded intermediates during MPs oxidation. Figure 7.17 and 7.18 illustrate the microalgae optical density in different media. There is a trivial change in microalgae growth when deionized water was replaced with the reaction filtrate (after MPs oxidation in 2 h), suggesting that the intermediates formed in the early stage are low in toxicity. Surprisingly, when MPs solutions after 6- and 8-h reaction were used, the optical densities of the microalgae increased by 8 and 12% accordingly compared with that in pure water. Therefore, the light-molecule by-products from MPs degradation can be harnessed as carbon sources for algae growth. Since microalgae is ubiquitously distributed in soil and aquatic system, the MPs treated wastewater with abundant less-toxic and small molecules can be harnessed by the natural organisms and ultimately to be converted into hydrocarbons and cycled in the ecosystem.[35] Thus, the organic intermediates from MPs may be digested by the microorganisms and converted to other value-added products (e.g. sugar, protein, biofuels), returning the carbons to nature or re-utilized by human being in a green and sustainable manner.

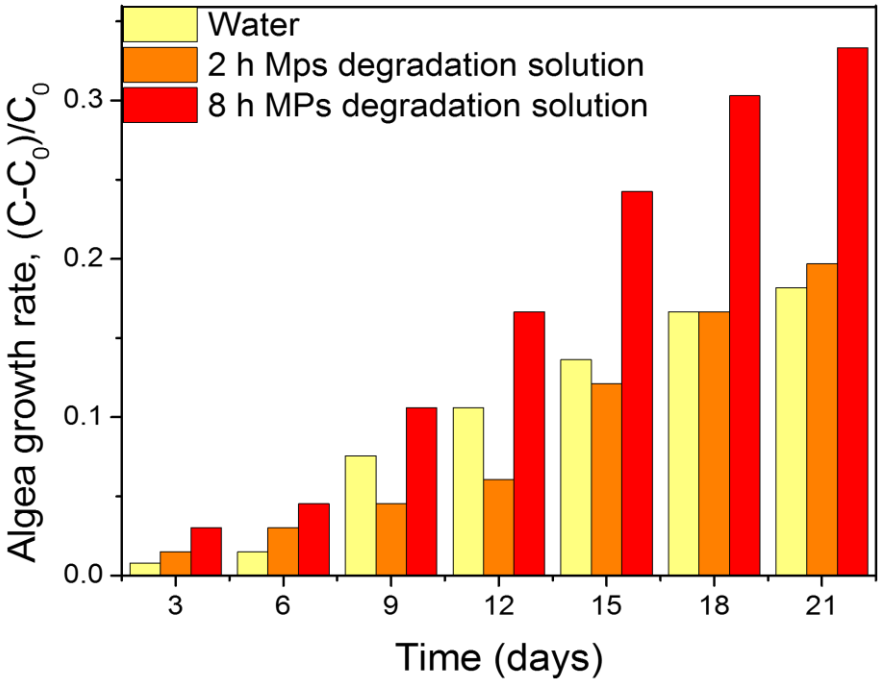

Figure 7.17. Microalgae optical density in different mediums in the 21 days growth.

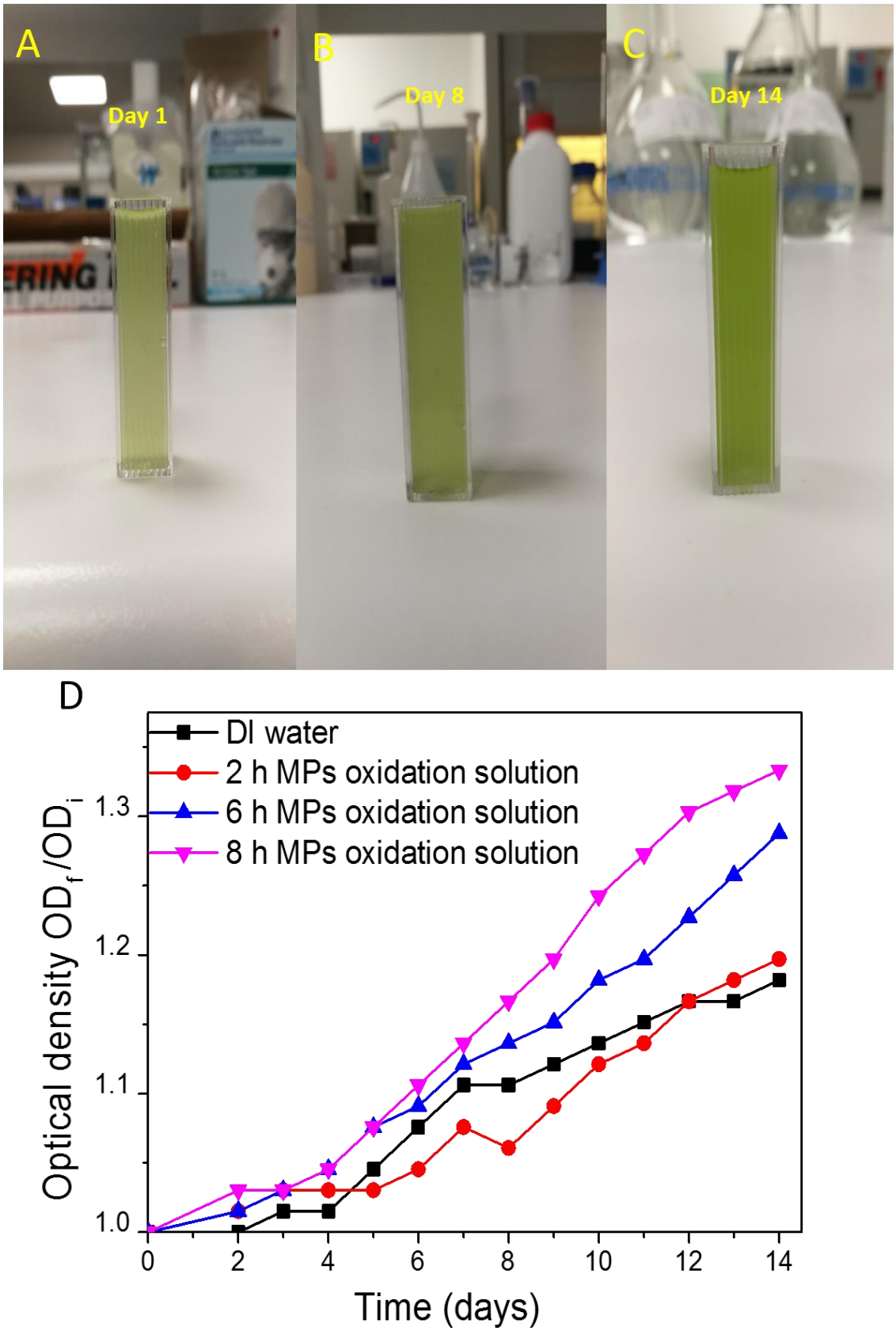

Figure 7.18. (A-C) The C. vulgaris algae growth in "8 h MPs oxidation solution" for 14 days. (D) The optical density change of algae cultivated in different reaction solutions.

7.4 Conclusion

This work extends the application of AOPs and provides a feasible strategy for microplastics remediation from the water. Thanks to the synergistic effect of nitrogen doping, transition metal (Mn) encapsulation and robust helical structure, the catalytic performance and stability of Mn@NCNTs is considerably increased in MPs degradation with a noticeably reduced activation energy. The results demonstrate that the Mn@NCNTs/PMS system can realize 50 wt.% of MPs removal by carbon catalyzed AOPs system assisted with hydrolysis. Our preliminary kinetic studies demonstrated that MPs removal is closely correlated with the initial MPs concentration, catalyst/PMS dosage and hydrolysis temperature, whereas a higher MPs concentration requires a greater catalyst/PMS dosage and a higher hydrolysis temperature. Thus, an optimized relationship between MPs amount and AOPs/hydrolysis intensity should be further investigated to achieve both energy and purification efficiency. The toxicity evaluation showed that the intermediates from MPs degradation did not pose any hazard to the microorganisms, and could serve as the nutrient for waterborne algae. Nevertheless, polyethylene based MPs was successfully decomposed by the integrated carbon/HT/persulfate system, and the technique is promising to break down other plastics such as high-density polyethylene (HDPE), polyvinyl chloride (PVC) and polypropylene (PP). Furthermore, due to the wide distribution of MPs in oceans and rivers, the feasibility of AOPs technique for *in situ* MPs control deserves further investigation in real water matrixes.

7.5 References

1. Moore, C. J., Synthetic polymers in the marine environment: A rapidly increasing, long-term threat. *Environ. Res*. **2008**, 108, (2), 131-139.

2. Mohamed Nor, N. H.; Koelmans, A. A., Transfer of PCBs from microplastics under simulated gut fluid conditions is biphasic and reversible. *Environ. Sci. Technol*. **2019,** 54, 1874-1883.

3. Barnes, D. K. A.; Galgani, F.; Thompson, R. C.; Barlaz, M., Accumulation and fragmentation of plastic debris in global environments. *Philos. T. R. Soc. B*. **2009**, 364, (1526), 1985-1998.

4. Cole, M.; Lindeque, P.; Fileman, E.; Halsband, C.; Goodhead, R.; Moger, J.; Galloway, T. S., Microplastic ingestion by zooplankton. *Environ. Sci. Technol*. **2013**, 47, (12), 6646-6655.

5. Dawson, A. L.; Kawaguchi, S.; King, C. K.; Townsend, K. A.; King, R.; Huston, W. M.; Bengtson Nash, S. M., Turning microplastics into nanoplastics through digestive fragmentation by Antarctic krill. *Nat. Commun.* **2018**, 9, (1), 1001.

6. Koelmans, A. A.; Bakir, A.; Burton, G. A.; Janssen, C. R., Microplastic as a vector for chemicals in the aquatic environment: Critical review and model-supported reinterpretation of empirical studies. *Environ. Sci. Technol*. **2016**, 50, (7), 3315-3326.

7. Mato, Y.; Isobe, T.; Takada, H.; Kanehiro, H.; Ohtake, C.; Kaminuma, T., Plastic resin pellets as a transport medium for toxic chemicals in the marine environment. *Environ. Sci. Technol*. **2001**, 35, (2), 318-324.

8. Turner, A.; Holmes, L. A., Adsorption of trace metals by microplastic pellets in fresh water. *Environ. Chem*. **2015**, 12, (5), 600-610.

9. Hermsen, E.; Mintenig, S. M.; Besseling, E.; Koelmans, A. A., Quality criteria for the analysis of microplastic in biota samples: A critical review. *Environ. Sci. Technol.* **2018**, 52, (18), 10230-10240.

10. Rummel, C. D.; Jahnke, A.; Gorokhova, E.; Kühnel, D.; Schmitt-Jansen, M., Impacts of biofilm formation on the fate and potential effects of microplastic in the aquatic environment. *Environ. Sci. Technol*. **2017**, 4, (7), 258-267.

11. Lehner, R.; Weder, C.; Petri-Fink, A.; Rothen-Rutishauser, B., Emergence of nanoplastic in the environment and possible impact on human health. *Environ. Sci. Technol.* **2019, 53**, (4), 1748-1765.

12. Diepens, N. J.; Koelmans, A. A., Accumulation of plastic debris and associated contaminants in aquatic food webs. *Environ. Sci. Technol.* **2018**, 52, (15), 8510-8520.

13. Fendall, L. S.; Sewell, M. A., Contributing to marine pollution by washing your face: Microplastics in facial cleansers. *Mar. Pollut. Bull.* **2009**, 58, (8), 1225-1228.

14. Yu, Y.; Zhou, D.; Li, Z.; Zhu, C., Advancement and challenges of microplastic pollution in the aquatic environment: a review. *Water Air Soil Pollut*. **2018**, 229, (5), 140.

15. Lares, M.; Ncibi, M. C.; Sillanpää, M.; Sillanpää, M., Occurrence, identification and removal of microplastic particles and fibers in conventional activated sludge process and advanced MBR technology. *Water Res.* **2018,** *133*, 236-246.

16. Sun, J.; Dai, X.; Wang, Q.; van Loosdrecht, M. C. M.; Ni, B.-J., Microplastics in wastewater treatment plants: Detection, occurrence and removal. *Water Res.* **2019,** *152*, 21-37.

17. Buxton, G. V.; Greenstock, C. L.; Helman, W. P.; Ross, A. B., Critical review of rate constants for reactions of hydrated electrons, hydrogen atoms and hydroxyl radicals ($^{\cdot}OH/^{\cdot}O^{-}$) in aqueous solution. *J. Phys. Chem. Ref. Data* **1988**, 17, (2), 513-886.

18. Neta, P.; Huie, R. E.; Ross, A. B., Rate Constants for reactions of inorganic radicals in aqueous solution. *J. Phys. Chem. Ref. Data* **1988**, 17, (3), 1027-1284.

19. Wang, C.; Kang, J.; Liang, P.; Zhang, H.; Sun, H.; Tade, M. O.; Wang, S., Ferric carbide nanocrystals encapsulated in nitrogen-doped carbon nanotubes as an outstanding environmental catalyst. *Environ. Sci. Nano* **2017**, 4, (1), 170-179.

20. Zhou, D.; Chen, L.; Li, J.; Wu, F., Transition metal catalyzed sulfite auto-oxidation systems for oxidative decontamination in waters: A state-of-the-art minireview. *Chem. Eng. J.* **2018**, 346, 726-738.

21. Duan, X.; Sun, H.; Wang, S., Metal-free carbocatalysis in advanced oxidation reactions. *Accounts Chem. Res.* **2018**, 51, (3), 678-687.

22. Tian, W.; Zhang, H.; Duan, X.; Sun, H.; Tade, M. O.; Ang, H. M.; Wang, S., Nitrogen- and sulfur-codoped hierarchically porous carbon for adsorptive and oxidative removal of pharmaceutical contaminants. *ACS Appl. Mater. Inter.* **2016**, 8, (11), 7184-7193.

23. Duan, X.; Sun, H.; Wang, Y.; Kang, J.; Wang, S., N-doping-induced nonradical reaction on single-walled carbon nanotubes for catalytic phenol oxidation. *ACS Catal.* **2015**, 5, (2), 553-559.

24. Duan, X.; O'Donnell, K.; Sun, H.; Wang, Y.; Wang, S., Sulfur and nitrogen co-doped graphene for metal-free catalytic oxidation reactions. *Small* **2015,** *11*, (25), 3036-3044.

25. Wang, Y.; Sun, H.; Ang, H. M.; Tadé, M. O.; Wang, S., 3D-hierarchically structured MnO_2 for catalytic oxidation of phenol solutions by activation of peroxymonosulfate: Structure dependence and mechanism. *Appl. Catal. B* **2015**, 164, 159-167.

26. Ma, Z.; Wei, X.; Xing, S.; Li, J., Hydrothermal synthesis and characterization of surface-modified δ-MnO_2 with high Fenton-like catalytic activity. *Catal. Commun.* **2015**, 67, 68-71.

27. Qu, L.; Liu, Y.; Baek, J.-B.; Dai, L., Nitrogen-doped graphene as efficient metal-free electrocatalyst for oxygen reduction in fuel cells. *ACS Nano* **2010**, 4, (3), 1321-1326.

28. Eom, C. H.; Min, D. J., Kinetics of the formation reaction of manganese carbide under various gases. *Met. Mater. Int.* **2016**, 22, (1), 129-135.

29. Liu, M.; Cowley, J. M., Encapsulation of manganese carbides within carbon nanotubes and nanoparticles. *Carbon* **1995**, 33, (6), 749-756.

30. Amelinckx, S.; Zhang, X. B.; Bernaerts, D.; Zhang, X. F.; Ivanov, V.; Nagy, J. B., A formation mechanism for catalytically grown helix-shaped graphite nanotubes. *Science* **1994**, 265, (5172), 635-639.

31. Ihara, S.; Itoh, S.; Kitakami, J.-I., Helically coiled cage forms of graphitic carbon. *Phys. Revi. B* **1993**, 48, (8), 5643-5647.

32. Yao, Y.; Chen, H.; Qin, J.; Wu, G.; Lian, C.; Zhang, J.; Wang, S., Iron encapsulated in boron and nitrogen codoped carbon nanotubes as synergistic catalysts for Fenton-like reaction. *Water Res*. **2016**, 101, 281-291.

33. Yang, S.; Wang, P.; Yang, X.; Shan, L.; Zhang, W.; Shao, X.; Niu, R., Degradation efficiencies of azo dye Acid Orange 7 by the interaction of heat, UV and anions with common oxidants: Persulfate, peroxymonosulfate and hydrogen peroxide. *J. Hazard. Mater*. **2010**, 179, (1), 552-558.

34. Garforth, A.; Fiddy, S.; Lin, Y. H.; Ghanbari-Siakhali, A.; Sharratt, P. N.; Dwyer, J., Catalytic degradation of high density polyethylene: An evaluation of mesoporous and microporous catalysts using thermal analysis. *Thermochim. Acta* **1997**, 294, (1), 65-69.

35. Hakkarainen, M.; Albertsson, A.C., Environmental Degradation of Polyethylene. In: Albertsson AC. (eds) Long Term Properties of Polyolefins. Advances in Polymer Science, vol 169. Springer, Berlin, Heidelberg.

36. Chen, W.; Fan, Z. L.; Gu, L.; Bao, X. H.; Wang, C. L., Enhanced capacitance of manganese oxide via confinement inside carbon nanotubes. *Chem. Commun*. **2010**, 46, (22), 3905-3907.

37. Thi Cam Ha, D.; Dang Thang, N.; Hoang, T.; Thuy Chinh, N.; Thi Thu Hien, T.; Viet Hung, L.; Van Huynh, N.; Xuan Bach, T.; Thi Phuong Thao, P.; Truong Giang, N.; Quang Trung, N., Plastic degradation by thermophilic Bacillus sp. BCBT21 isolated from composting agricultural residual in Vietnam. *Adv. Nat. Sci. Nanosci*. **2018**, 9, (1), 015014.

38. Ali, S. S.; Qazi, I. A.; Arshad, M.; Khan, Z.; Voice, T. C.; Mehmood, C. T., Photocatalytic degradation of low density polyethylene (LDPE) films using titania nanotubes. *Environ. Nanotech.* **2016**, 5, 44-53.

39. Tyler, D. R., Mechanistic Aspects of the effects of stress on the rates of photochemical degradation reactions in polymers. *J. Macromol. Sci. C* **2004**, 44, (4), 351-388.

40. Prieto-Rodríguez, L.; Oller, I.; Klamerth, N.; Agüera, A.; Rodríguez, E. M.; Malato, S., Application of solar AOPs and ozonation for elimination of micropollutants in municipal wastewater treatment plant effluents. *Water Res.* **2013**, 47, (4), 1521-1528.

Chapter 8. Conclusions and Perspectives

8.1 Conclusions

Advanced oxidation processes have demonstrated outstanding performances in wastewater treatment especially on recalcitrant organic pollutants. Highly reactive oxygen species (ROS) such as hydroxyl and sulfate radicals generated from the super oxidants by activation can effectively degrade toxic organic chemicals into harmless substances such as water and carbon dioxide. Among all the well-developed AOP approaches, sulfur radical based AOPs (SR-AOPs) have attracted more interests in recent years due to the robust oxidation capacity and high adaptability in a wider range of environment. A green AOP system initiated by metal free nanocarbon materials has been proved to have great potential on organic degradation. Nanocarbons such as graphene and carbon nanotubes are excellent catalysts to activate persulfate oxidants, persulfate (PS) and peroxymonosulfate (PMS), to generate ROS at the same time, while totally avoiding metal leaching. The superb catalytic activity of the nanocarbon materials can be attributed to their fast electron transfer ability from the catalyst surface to PMS/PS and absorbed water molecules for ROS formation. Numerous methods have been established to modify pristine nanocarbon materials in order to further boost the catalytic ability, including heteroatom doping, nanocarbon hydration and metal encapsulation. Through heteroatom doing such ash nitrogen and sulfur, the catalytic activity of pristine carbons can be largely promoted for PMS/PS activation by the increased active sites. In addition, a nonradical oxidation pathway was discovered and proved to be immune to radical quenching agents, thus offering an effective strategy for organic degradation even in harsh environments containing radical scavengers. Moreover, the catalytic ability of nanocarbons was further enhanced via transition metal encapsulation, in which the nano metal particles are perfectly warped by graphene layers, thus the metal leaching can be significantly avoided. Meanwhile, by taking the advantage of electron rich metal particles and the unique electroconductivity of

nanocarbons, abundant electrons can be efficiently transferred from metal to out layers for PMS activation. The application of nanocarbon-induced SR-ASPs on microplastics degradation has extended the purpose to a brand new field and provided a novel solution to alleviate the increasingly serious microplastics pollution. The comprehensive illustration of modified nanocarbon synthesis and the mechanism studies of persulfate oxidants activation are thoroughly investigated with repetitive experimental proofs and theoretical calculations. The detailed conclusions from the thesis are listed below.

8.1.1 Carbocatalytic activation of persulfate for removal of antibiotics in water solutions

- A facile method is reported for preparation of nitrogen doped reduced graphene oxide (N-rGO) using urea as a nitrogen precursor.
- The as-prepared metal-free N-rGO showed great potential for activating persulfate (PS) to produce reactive radicals for degradation of an antibiotic sulfachloropyridazine (SCP).
- The activation processes were studied by in situ electron paramagnetic resonance (EPR), which discovered the newly observed hydroxyl radicals from PS activation.

8.1.2 Nitrogen-doped bamboo-like carbon nanotubes with nickel encapsulation for persulfate activation to remove emerging contaminants with excellent catalytic stability

- Nitrogen-doped bamboo-like carbon nanotubes encapsulated with nickel nanoparticles (Ni@NCNTs) were feasibly fabricated by a one-pot pyrolysis route by using melamine and nickel salt as precursors.
- Ni@NCNTs were employed as both adsorbents and catalysts for activating persulfate to remove an emerging pollutant, antibiotic sulfachloropyridazine (SCP). The

characterization study and SCP oxidation reaction indicated that the nitrogen modification could enhance both adsorption capacity and catalytic ability of Ni@NCNTs.

- Electron paramagnetic resonance (EPR) and classical radical quenching tests discovered a simultaneous radical/non-radical mechanism in Ni@NCNTs/persulfate system, which proved such a system a promising alternative to metal oxides and other carbon catalysts.

8.1.3 Nickel in hierarchically structured nitrogen-doped graphene for robust and promoted degradation of antibiotics

- Nickel nanoparticles encapsulated in nitrogen-doped porous graphene (Ni@NPG) were successfully synthesized through a one-pot method and employed as a novel material for catalytic activation of persulfate (PS).
- Ni@NPG exhibits excellent adsorption and catalysis with 100% SCP removal from water in less than 30 min while, the great stability and reusability can be achieved with satisfactory organic degradation after four successive runs with negligible amount of metal leaching concentration.
- Electron paramagnetic resonance (EPR) and quenching experiments reveal the PS activation mechanism involved of generation of $SO_4^{\bullet-}$, $^{\bullet}OH$ and $^{\bullet}O_2^-$ without singlet oxygen. The synergistic effect of radical and nonradical pathway played crucial roles during the SCP oxidation process.

8.1.4 Magnetic Ni-Co alloy encapsulated N-doped carbon nanotubes for catalytic membrane degradation of emerging contaminants

- Nitrogen-doped carbon nanotubes encapsulated with Ni-Co alloy nanoparticles (NiCo@NCNTs) were readily synthesized by annealing Ni/Co salts with dicyandiamide.

- The synergistic effect of nitrogen doping and metal alloy encapsulation significantly enhanced the catalytic activity and stability of NCNTs in catalytic activation of peroxymonosulfate (PMS) for purification of an emerging pollutant, ibuprofen.
- Mechanistic investigation was performed using electron paramagnetic resonance and competitive radical screening tests, which indicated that radical ($^{\bullet}OH$ and $SO_4^{\bullet-}$) oxidation and nonradical pathway co-existed and played critical roles for catalytic degradation.
- The study provides a novel advanced oxidation system with catalytic membrane for wastewater remediation.

8.1.5 Catalytic degradation of cosmetic microplastics by hydrothermal carbocatalysis: A new approach with magnetic carbon nanosprings and sulfate radicals

- Spring-like carbon nanotubes were fabricated bearing high-level nitrogen dopants and encapsulated metal nanoparticles, demonstrating outstanding catalytic performance in activation of peroxymonosulfate (PMS) to generate sulfate radicals for microplastics degradation.
- The spiral architecture and highly graphitic degree guaranteed superb stability of the carbocatalysts in HT environment.
- in the carbon/thermal/PMS system, a 40 wt.% decomposition of microplastics was achieved due to the robust and magnetic carbon hybrids
- The toxicity test revealed that the organic intermediates from microplastics degradation were environmental-benign to the aquatic microorganisms, and can serve as a carbon source for algae cultivation.

8.1.6 Summarization of catalysts

Table 8.1 Summarization of catalysts

Chapter No.	Catalyst	Oxidant	Target pollutants	Active sites	Catalytic mechanism
3	N-rGO	PDS	SCP	1. Defective edges 2. Oxygen groups 3. N-doping in the sp^2 carbon matrix 4. Transition metal nanoparticles encapsulation. 5. Metal and nitrogen bonds in the carbon support.	1. Nonradical process: Conductive carbon matrix served as a charge shuttle between the adsorbed organic (electron donor) and PDS (electron acceptor). 2. The delocalized system of π-electrons is beneficial for facilitating redox processes. 3. The incorporated alien atoms can break the chemical inertness of nanocarbons by disrupting the electronic and spin culture of the hybridized carbon atoms. 4. Encapsulation of metal nanoparticles within carbon layers modulate the electrons states of the interacting carbon via charge transport to increase the electron density. 5. Metal nanoparticles can modify the electronic structure and reduce the local surface work function of carbon walls, promoting the electron transfer from the metal to carbon.
4	Ni@NCNT	PDS	SCP		
5	Ni@NPG	PDS	SCP		
6	NiCo@NCNT	PMS	IBP		
7	Mn@NCNT	PMS	MPs		

8.2 Perspectives

- Sulfate radical driven advanced oxidation processes have considerably potential on removing toxic organic contaminants in wastewater treatment by using oxidants such as PMS and PDS and metal free catalyst . However, the inherent production of sulfate related ions, ionic groups and unreacted radicals ($HSO_5^{\bullet-}$, $SO_3^{\bullet-}$, $HO_2^{\bullet}$, or $O_2^{\bullet-}$) might lead to mild secondary pollution, which deserves to be further evaluated. In addition, the toxicity study should also be proceeded on these ionic groups and radicals in order to prove the environmentally friendly nature of the SR-AOPs.

  To date, a series of organic contaminants have been tested by sulfate radical driven advanced oxidation processes, which include phenol, antibiotics, ibuprofen and microplastics. A larger variety of other organic contaminants should be tested in the future study to explore the extensive application of the SR-AOPs.
- The nanocarbon materials have been modified for achieving more robust catalytic performance in PMS/PDS activation reactions through various strategies such as heteroatom doping and transition metal encapsulation. However, a relatively high-energy input is required during the catalyst fabrication process, thus the development of a facile process with less complicated process and less energy input is highly desired.

- The nancarbon catalyst synthesis such as graphene and carbon nanotubes can only produced in a laboratory scale. Therefore, in order to popularize its application, it is important to develop an economical and efficient fabrication process of nanocarbons for an industrial scale production.
- The carbon nanotubes have been modified by metal encapsulation and shown a great improvement in catalytic activity. The metal leaching problem was largely avoided when

comparing with metal catalysts such as NiO and Fe_2O_3, yet the metal leaching concentration has not reduced to zero, which could bring potential risk to the environment.

- The advanced oxidation processes initiated by as-synthesized metal free nanocarbon materials have shown great potentials in wastewater remediation field. However, most of the experiments were done in the laboratory, indicating the results are confined by not only the lab-scale but also the lack of the real life situations. For applying our SR-AOPs systems in the real wastewater treatment condition in a large scale, it is necessary to explore the possible influences of actual complicated factors such as the presence of organism and different mineral salts.

Appendix

The copyright licenses for some references in Chapter 2 (literature review) are attached below:

1. Ref. 40 (Figure 2.1)
2. Ref. 23 (Figure 2.2)
3. Ref. 49 (Figure 2.3)
4. Ref. 31 (Figure 2.4)
5. Ref. 64 (Figure 2.5)
6. Ref. 79 (Figure 2.6)
7. Ref. 80 (Figure 2.7)
8. Ref. 88 (Figure 2.8)
9. Ref. 90 (Figure 2.9)
10. Ref. 90 (Figure 2.10)
11. Ref. 95 (Figure 2.11)
12. Ref. 101 (Figure 2.12)
13. Ref. 99 (Figure 2.13)
14. Ref. 32 (Figure 2.14)
15. Ref. 32 (Figure 2.15)
16. Ref. 35 (Figure 2.16)
17. Ref. 35 (Figure 2.17)
18. Ref. 118 (Figure 2.18)
19. Ref. 121 (Figure 2.19)
20. Ref. 139 (Figure 2.20)
21. Ref. 30 (Figure 2.21)

Copyright Clearance Center

Note: Copyright.com supplies permissions but not the copyrighted content itself.

1 PAYMENT 2 REVIEW 3 CONFIRMATION

Step 3: Order Confirmation

Thank you for your order! A confirmation for your order will be sent to your account email address. If you have questions about your order, you can call us 24 hrs/day, M-F at +1.855.239.3415 Toll Free, or write to us at info@copyright.com. This is not an invoice.

Confirmation Number: 11850629
Order Date: 09/12/2019

If you paid by credit card, your order will be finalized and your card will be charged within 24 hours. If you choose to be invoiced, you can change or cancel your order until the invoice is generated.

Payment Information

Jian Kang
kangjiansg@hotmail.com
+61 (4)51881962
Payment Method: n/a

Order Details

Physical chemistry chemical physics

Order detail ID:	72007933
Order License Id:	4666780742322
ISSN:	1463-9084
Publication Type:	e-Journal
Volume:	
Issue:	
Start page:	
Publisher:	ROYAL SOCIETY OF CHEMISTRY
Author/Editor:	Royal Society of Chemistry (Great Britain)

Permission Status: Granted
Permission type: Republish or display content
Type of use: Thesis/Dissertation

Requestor type	Not-for-profit entity
Format	Electronic
Portion	image/photo
Number of images/photos requested	1
The requesting person/organization	Jian Kang
Title or numeric reference of the portion(s)	fig 1
Title of the article or chapter the portion is from	Graphene and carbon nanotube composite electrodes for supercapacitors with ultra-high energy density
Editor of portion(s)	N/A
Author of portion(s)	N/A
Volume of serial or monograph	N/A
Page range of portion	42
Publication date of portion	10102019
Rights for	Main product
Duration of use	Current edition and up to 5 years
Creation of copies for the disabled	no
	no

With minor editing privileges	
For distribution to	Worldwide
In the following language(s)	Original language of publication
With incidental promotional use	no
Lifetime unit quantity of new product	Up to 499
Title	Synthesis of doped nanocarbon materials for catalytic decomposition of persistent organic pollutants
Institution name	n/a
Expected presentation date	Sep 2019

Note: This item will be invoiced or charged separately through CCC's **RightsLink** service. More info **$ 0.00**

This is not an invoice.

Total order items: 1

Order Total: 0.00 USD

Confirmation Number: 11850629

Special Rightsholder Terms & Conditions

The following terms & conditions apply to the specific publication under which they are listed

Physical chemistry chemical physics
Permission type: Republish or display content
Type of use: Thesis/Dissertation

TERMS AND CONDITIONS

The following terms are individual to this publisher:

None

Other Terms and Conditions:

STANDARD TERMS AND CONDITIONS

1. Description of Service; Defined Terms. This Republication License enables the User to obtain licenses for republication of one or more copyrighted works as described in detail on the relevant Order Confirmation (the "Work(s)"). Copyright Clearance Center, Inc. ("CCC") grants licenses through the Service on behalf of the rightsholder identified on the Order Confirmation (the "Rightsholder"). "Republication", as used herein, generally means the inclusion of a Work, in whole or in part, in a new work or works, also as described on the Order Confirmation. "User", as used herein, means the person or entity making such republication.

2. The terms set forth in the relevant Order Confirmation, and any terms set by the Rightsholder with respect to a particular Work, govern the terms of use of Works in connection with the Service. By using the Service, the person transacting for a republication license on behalf of the User represents and warrants that he/she/it (a) has been duly authorized by the User to accept, and hereby does accept, all such terms and conditions on behalf of User, and (b) shall inform User of all such terms and conditions. In the event such person is a "freelancer" or other third party independent of User and CCC, such party shall be deemed jointly a "User" for purposes of these terms and conditions. In any event, User shall be deemed to have accepted and agreed to all such terms and conditions if User republishes the Work in any fashion.

3. Scope of License; Limitations and Obligations.

3.1 All Works and all rights therein, including copyright rights, remain the sole and exclusive property of the Rightsholder. The license created by the exchange of an Order Confirmation (and/or any invoice) and payment by User of the full amount set forth on that document includes only those rights expressly set forth in the Order Confirmation and in these terms and conditions, and conveys no other rights in the Work(s) to User. All rights not expressly granted are hereby reserved.

3.2 General Payment Terms: You may pay by credit card or through an account with us payable at the end of the month. If you and we agree that you may establish a standing account with CCC, then the following terms apply: Remit Payment to: Copyright Clearance Center, 29118 Network Place, Chicago, IL 60673-1291. Payments Due: Invoices are payable upon their delivery to you (or upon our notice to you that they are available to you for downloading). After 30 days, outstanding amounts will be subject to a service charge of 1-1/2% per month or, if less, the maximum rate allowed by applicable law. Unless otherwise specifically set forth in the Order Confirmation or in a separate written agreement signed by CCC, invoices are due and payable on "net 30" terms. While User may exercise the rights licensed immediately upon issuance of the Order Confirmation, the license is automatically revoked and is null and void, as if it had never been issued, if complete payment for the license is not received on a timely basis either from User directly or through a payment agent, such as a credit card company.

3.3 Unless otherwise provided in the Order Confirmation, any grant of rights to User (i) is "one-time" (including the editions and product family specified in the license), (ii) is non-exclusive and non-transferable and (iii) is subject to any and all limitations and restrictions (such as, but not limited to, limitations on duration of use or circulation) included in the Order Confirmation or invoice and/or in these terms and conditions. Upon completion of the licensed use, User shall either secure a new permission for further use of the Work(s) or immediately cease any new use of the Work(s) and shall render inaccessible (such as by deleting or by removing or severing links or other locators) any further copies of the Work (except for copies printed on paper in accordance with this license and still in User's stock at the end of such period).

3.4 In the event that the material for which a republication license is sought includes third party materials (such as photographs, illustrations, graphs, inserts and similar materials) which are identified in such material as having been used by permission, User is responsible for identifying, and seeking separate licenses (under this Service or otherwise) for, any of such third party materials; without a separate license, such third party materials may not be used.

3.5 Use of proper copyright notice for a Work is required as a condition of any license granted under the Service. Unless otherwise provided in the Order Confirmation, a proper copyright notice will read substantially as follows: "Republished with permission of [Rightsholder's name], from [Work's title, author, volume, edition number and year of copyright]; permission conveyed through Copyright Clearance Center, Inc. " Such notice must be provided in a reasonably legible font size and must be placed either immediately adjacent to the Work as used (for example, as part of a by-line or footnote but not as a separate electronic link) or in the place where substantially all other credits or notices for the new work containing the republished Work are located. Failure to include the required notice results in loss to the Rightsholder and CCC, and the User shall be liable to pay liquidated damages for each such failure equal to twice the use fee specified in the Order Confirmation, in addition to the use fee itself and any other fees and charges specified.

3.6 User may only make alterations to the Work if and as expressly set forth in the Order Confirmation. No Work may be used in any way that is defamatory, violates the rights of third parties (including such third parties' rights of copyright, privacy, publicity, or other tangible or intangible property), or is otherwise illegal, sexually explicit or obscene. In addition, User may not conjoin a Work with any other material that may result in damage to the reputation of the Rightsholder. User agrees to inform CCC if it becomes aware of any infringement of any rights in a Work and to cooperate with any reasonable request of CCC or the Rightsholder in connection therewith.

4. Indemnity. User hereby indemnifies and agrees to defend the Rightsholder and CCC, and their respective employees and directors, against all claims, liability, damages, costs and expenses, including legal fees and expenses, arising out of any use of a Work beyond the scope of the rights granted herein, or any use of a Work which has been altered in any unauthorized way by User, including claims of defamation or infringement of rights of copyright, publicity, privacy or other tangible or intangible property.

5. Limitation of Liability. UNDER NO CIRCUMSTANCES WILL CCC OR THE RIGHTSHOLDER BE LIABLE FOR ANY DIRECT, INDIRECT, CONSEQUENTIAL OR INCIDENTAL DAMAGES (INCLUDING WITHOUT LIMITATION DAMAGES FOR LOSS OF BUSINESS PROFITS OR INFORMATION, OR FOR BUSINESS INTERRUPTION) ARISING OUT OF THE USE OR INABILITY TO USE A WORK, EVEN IF ONE OF THEM HAS BEEN ADVISED OF THE POSSIBILITY OF SUCH DAMAGES. In any event, the total liability of the Rightsholder and CCC (including their respective employees and directors) shall not exceed the total amount actually paid by User for this license. User assumes full liability for the actions and omissions of its principals, employees, agents, affiliates, successors and assigns.

6. Limited Warranties. THE WORK(S) AND RIGHT(S) ARE PROVIDED "AS IS". CCC HAS THE RIGHT TO GRANT TO USER THE RIGHTS GRANTED IN THE ORDER CONFIRMATION DOCUMENT. CCC AND THE RIGHTSHOLDER DISCLAIM ALL OTHER WARRANTIES RELATING TO THE WORK(S) AND RIGHT(S), EITHER EXPRESS OR IMPLIED, INCLUDING WITHOUT LIMITATION IMPLIED WARRANTIES OF MERCHANTABILITY OR FITNESS FOR A PARTICULAR PURPOSE. ADDITIONAL RIGHTS MAY BE REQUIRED TO USE ILLUSTRATIONS, GRAPHS, PHOTOGRAPHS, ABSTRACTS, INSERTS OR OTHER PORTIONS OF THE WORK (AS OPPOSED TO THE ENTIRE WORK) IN A MANNER CONTEMPLATED BY USER; USER

UNDERSTANDS AND AGREES THAT NEITHER CCC NOR THE RIGHTSHOLDER MAY HAVE SUCH ADDITIONAL RIGHTS TO GRANT.

7. Effect of Breach. Any failure by User to pay any amount when due, or any use by User of a Work beyond the scope of the license set forth in the Order Confirmation and/or these terms and conditions, shall be a material breach of the license created by the Order Confirmation and these terms and conditions. Any breach not cured within 30 days of written notice thereof shall result in immediate termination of such license without further notice. Any unauthorized (but licensable) use of a Work that is terminated immediately upon notice thereof may be liquidated by payment of the Rightsholder's ordinary license price therefor; any unauthorized (and unlicensable) use that is not terminated immediately for any reason (including, for example, because materials containing the Work cannot reasonably be recalled) will be subject to all remedies available at law or in equity, but in no event to a payment of less than three times the Rightsholder's ordinary license price for the most closely analogous licensable use plus Rightsholder's and/or CCC's costs and expenses incurred in collecting such payment.

8. **Miscellaneous.**

8.1 User acknowledges that CCC may, from time to time, make changes or additions to the Service or to these terms and conditions, and CCC reserves the right to send notice to the User by electronic mail or otherwise for the purposes of notifying User of such changes or additions; provided that any such changes or additions shall not apply to permissions already secured and paid for.

8.2 Use of User-related information collected through the Service is governed by CCC's privacy policy, available online here: http://www.copyright.com/content/cc3/en/tools/footer/privacypolicy.html.

8.3 The licensing transaction described in the Order Confirmation is personal to User. Therefore, User may not assign or transfer to any other person (whether a natural person or an organization of any kind) the license created by the Order Confirmation and these terms and conditions or any rights granted hereunder; provided, however, that User may assign such license in its entirety on written notice to CCC in the event of a transfer of all or substantially all of User's rights in the new material which includes the Work(s) licensed under this Service.

8.4 No amendment or waiver of any terms is binding unless set forth in writing and signed by the parties. The Rightsholder and CCC hereby object to any terms contained in any writing prepared by the User or its principals, employees, agents or affiliates and purporting to govern or otherwise relate to the licensing transaction described in the Order Confirmation, which terms are in any way inconsistent with any terms set forth in the Order Confirmation and/or in these terms and conditions or CCC's standard operating procedures, whether such writing is prepared prior to, simultaneously with or subsequent to the Order Confirmation, and whether such writing appears on a copy of the Order Confirmation or in a separate instrument.

8.5 The licensing transaction described in the Order Confirmation document shall be governed by and construed under the law of the State of New York, USA, without regard to the principles thereof of conflicts of law. Any case, controversy, suit, action, or proceeding arising out of, in connection with, or related to such licensing transaction shall be brought, at CCC's sole discretion, in any federal or state court located in the County of New York, State of New York, USA, or in any federal or state court whose geographical jurisdiction covers the location of the Rightsholder set forth in the Order Confirmation. The parties expressly submit to the personal jurisdiction and venue of each such federal or state court.If you have any comments or questions about the Service or Copyright Clearance Center, please contact us at 978-750-8400 or send an e-mail to info@copyright.com.

v 1.1

Close

Confirmation Number: 11850629

Citation Information

Order Detail ID: 72007933

Physical chemistry chemical physics by Royal Society of Chemistry (Great Britain) Reproduced with permission of ROYAL SOCIETY OF CHEMISTRY in the format Thesis/Dissertation via Copyright Clearance Center.

Close

ELSEVIER LICENSE
TERMS AND CONDITIONS

Sep 12, 2019

This Agreement between Jian Kang ("You") and Elsevier ("Elsevier") consists of your license details and the terms and conditions provided by Elsevier and Copyright Clearance Center.

License Number	4666770625740
License date	Sep 12, 2019
Licensed Content Publisher	Elsevier
Licensed Content Publication	Carbon
Licensed Content Title	Sulfur-doped porous carbons: Synthesis and applications
Licensed Content Author	Wojciech Kiciński,Mateusz Szala,Michał Bystrzejewski
Licensed Content Date	Mar 1, 2014
Licensed Content Volume	68
Licensed Content Issue	n/a
Licensed Content Pages	32
Start Page	1
End Page	32
Type of Use	reuse in a thesis/dissertation
Intended publisher of new work	other
Portion	figures/tables/illustrations
Number of figures/tables/illustrations	1
Format	electronic
Are you the author of this Elsevier article?	No
Will you be translating?	No
Original figure numbers	Figure 13
Title of your thesis/dissertation	Synthesis of doped nanocarbon materials for catalytic decomposition of persistent organic pollutants
Expected completion date	Sep 2019
Estimated size (number of pages)	300
Requestor Location	Jian Kang 4 Dalby Court Perth, WA 6102 Australia Attn:
Publisher Tax ID	GB 494 6272 12
Total	0.00 USD
Terms and Conditions	

INTRODUCTION

1. The publisher for this copyrighted material is Elsevier. By clicking "accept" in connection with completing this licensing transaction, you agree that the following terms and conditions apply to this transaction (along with the Billing and Payment terms and conditions established by Copyright Clearance Center, Inc. ("CCC"), at the time that you opened your Rightslink account and that are available at any time at http://myaccount.copyright.com).

GENERAL TERMS

2. Elsevier hereby grants you permission to reproduce the aforementioned material subject to the terms and conditions indicated.
3. Acknowledgement: If any part of the material to be used (for example, figures) has appeared in our publication with credit or acknowledgement to another source, permission must also be sought from that source. If such permission is not obtained then that material may not be included in your publication/copies. Suitable acknowledgement to the source must be made, either as a footnote or in a reference list at the end of your publication, as follows:
"Reprinted from Publication title, Vol /edition number, Author(s), Title of article / title of chapter, Pages No., Copyright (Year), with permission from Elsevier [OR APPLICABLE SOCIETY COPYRIGHT OWNER]." Also Lancet special credit - "Reprinted from The Lancet, Vol. number, Author(s), Title of article, Pages No., Copyright (Year), with permission from Elsevier."
4. Reproduction of this material is confined to the purpose and/or media for which permission is hereby given.

5. Altering/Modifying Material: Not Permitted. However figures and illustrations may be altered/adapted minimally to serve your work. Any other abbreviations, additions, deletions and/or any other alterations shall be made only with prior written authorization of Elsevier Ltd. (Please contact Elsevier at permissions@elsevier.com). No modifications can be made to any Lancet figures/tables and they must be reproduced in full.
6. If the permission fee for the requested use of our material is waived in this instance, please be advised that your future requests for Elsevier materials may attract a fee.
7. Reservation of Rights: Publisher reserves all rights not specifically granted in the combination of (i) the license details provided by you and accepted in the course of this licensing transaction, (ii) these terms and conditions and (iii) CCC's Billing and Payment terms and conditions.
8. License Contingent Upon Payment: While you may exercise the rights licensed immediately upon issuance of the license at the end of the licensing process for the transaction, provided that you have disclosed complete and accurate details of your proposed use, no license is finally effective unless and until full payment is received from you (either by publisher or by CCC) as provided in CCC's Billing and Payment terms and conditions. If full payment is not received on a timely basis, then any license preliminarily granted shall be deemed automatically revoked and shall be void as if never granted. Further, in the event that you breach any of these terms and conditions or any of CCC's Billing and Payment terms and conditions, the license is automatically revoked and shall be void as if never granted. Use of materials as described in a revoked license, as well as any use of the materials beyond the scope of an unrevoked license, may constitute copyright infringement and publisher reserves the right to take any and all action to protect its copyright in the materials.
9. Warranties: Publisher makes no representations or warranties with respect to the licensed material.
10. Indemnity: You hereby indemnify and agree to hold harmless publisher and CCC, and their respective officers, directors, employees and agents, from and against any and all claims arising out of your use of the licensed material other than as specifically authorized pursuant to this license.
11. No Transfer of License: This license is personal to you and may not be sublicensed, assigned, or transferred by you to any other person without publisher's written permission.
12. No Amendment Except in Writing: This license may not be amended except in a writing signed by both parties (or, in the case of publisher, by CCC on publisher's behalf).
13. Objection to Contrary Terms: Publisher hereby objects to any terms contained in any purchase order, acknowledgment, check endorsement or other writing prepared by you, which terms are inconsistent with these terms and conditions or CCC's Billing and Payment terms and conditions. These terms and conditions, together with CCC's Billing and Payment terms and conditions (which are incorporated herein), comprise the entire agreement between you and publisher (and CCC) concerning this licensing transaction. In the event of any conflict between your obligations established by these terms and conditions and those established by CCC's Billing and Payment terms and conditions, these terms and conditions shall control.
14. Revocation: Elsevier or Copyright Clearance Center may deny the permissions described in this License at their sole discretion, for any reason or no reason, with a full refund payable to you. Notice of such denial will be made using the contact information provided by you. Failure to receive such notice will not alter or invalidate the denial. In no event will Elsevier or Copyright Clearance Center be responsible or liable for any costs, expenses or damage incurred by you as a result of a denial of your permission request, other than a refund of the amount(s) paid by you to Elsevier and/or Copyright Clearance Center for denied permissions.

LIMITED LICENSE

The following terms and conditions apply only to specific license types:
15. **Translation**: This permission is granted for non-exclusive world **English** rights only unless your license was granted for translation rights. If you licensed translation rights you may only translate this content into the languages you requested. A professional translator must perform all translations and reproduce the content word for word preserving the integrity of the article.
16. **Posting licensed content on any Website**: The following terms and conditions apply as follows: Licensing material from an Elsevier journal: All content posted to the web site must maintain the copyright information line on the bottom of each image; A hyper-text must be included to the Homepage of the journal from which you are licensing at http://www.sciencedirect.com/science/journal/xxxxx or the Elsevier homepage for books at http://www.elsevier.com; Central Storage: This license does not include permission for a scanned version of the material to be stored in a central repository such as that provided by Heron/XanEdu.
Licensing material from an Elsevier book: A hyper-text link must be included to the Elsevier homepage at http://www.elsevier.com . All content posted to the web site must maintain the copyright information line on the bottom of each image.

Posting licensed content on Electronic reserve: In addition to the above the following clauses are applicable: The web site must be password-protected and made available only to bona fide students registered on a relevant course. This permission is granted for 1 year only. You may obtain a new license for future website posting.
17. **For journal authors:** the following clauses are applicable in addition to the above:
Preprints:

A preprint is an author's own write-up of research results and analysis, it has not been peer-reviewed, nor has it had any other value added to it by a publisher (such as formatting, copyright, technical enhancement etc.).
Authors can share their preprints anywhere at any time. Preprints should not be added to or enhanced in any way in order to appear more like, or to substitute for, the final versions of articles however authors can update their preprints on arXiv or RePEc with their Accepted Author Manuscript (see below).
If accepted for publication, we encourage authors to link from the preprint to their formal publication via its DOI. Millions of researchers have access to the formal publications on ScienceDirect, and so links will help users to find, access, cite and use the best available version. Please note that Cell Press, The Lancet and some society-owned have different preprint policies. Information on these policies is available on the journal homepage.
Accepted Author Manuscripts: An accepted author manuscript is the manuscript of an article that has been accepted for publication and which typically includes author-incorporated changes suggested during submission, peer review and editor-author communications.
Authors can share their accepted author manuscript:

- immediately
  - via their non-commercial person homepage or blog
  - by updating a preprint in arXiv or RePEc with the accepted manuscript
  - via their research institute or institutional repository for internal institutional uses or as part of an invitation-only research collaboration work-group
  - directly by providing copies to their students or to research collaborators for their personal use
  - for private scholarly sharing as part of an invitation-only work group on commercial sites with which Elsevier has an agreement
- After the embargo period
  - via non-commercial hosting platforms such as their institutional repository
  - via commercial sites with which Elsevier has an agreement

In all cases accepted manuscripts should:

- link to the formal publication via its DOI
- bear a CC-BY-NC-ND license - this is easy to do
- if aggregated with other manuscripts, for example in a repository or other site, be shared in alignment with our hosting policy not be added to or enhanced in any way to appear more like, or to substitute for, the published journal article.

Published journal article (JPA): A published journal article (PJA) is the definitive final record of published research that appears or will appear in the journal and embodies all value-adding publishing activities including peer review co-ordination, copy-editing, formatting, (if relevant) pagination and online enrichment.
Policies for sharing publishing journal articles differ for subscription and gold open access articles:
Subscription Articles: If you are an author, please share a link to your article rather than the full-text. Millions of researchers have access to the formal publications on ScienceDirect, and so links will help your users to find, access, cite, and use the best available version.
Theses and dissertations which contain embedded PJAs as part of the formal submission can be posted publicly by the awarding institution with DOI links back to the formal publications on ScienceDirect.
If you are affiliated with a library that subscribes to ScienceDirect you have additional private sharing rights for others' research accessed under that agreement. This includes use for classroom teaching and internal training at the institution (including use in course packs and courseware programs), and inclusion of the article for grant funding purposes.
Gold Open Access Articles: May be shared according to the author-selected end-user license and should contain a CrossMark logo, the end user license, and a DOI link to the formal publication on ScienceDirect.
Please refer to Elsevier's posting policy for further information.
18. **For book authors** the following clauses are applicable in addition to the above:
Authors are permitted to place a brief summary of their work online only. You are not allowed to download and post the published electronic version of your chapter, nor may you scan the printed edition to create an electronic version. **Posting to a repository:** Authors are permitted to post a summary of their chapter only in their institution's repository.
19. **Thesis/Dissertation**: If your license is for use in a thesis/dissertation your thesis may be submitted to your institution in either print or electronic form. Should your thesis be published commercially, please reapply for permission. These requirements include permission for the Library and Archives of Canada to supply single copies, on demand, of the complete thesis and include permission for Proquest/UMI to supply single copies, on demand, of the complete thesis. Should your thesis be published commercially, please reapply for permission. Theses and dissertations which contain embedded PJAs as part of the formal submission can be posted publicly by the awarding institution with DOI links back to the formal publications on ScienceDirect.

Elsevier Open Access Terms and Conditions
You can publish open access with Elsevier in hundreds of open access journals or in nearly 2000 established subscription journals that support open access publishing. Permitted third

party re-use of these open access articles is defined by the author's choice of Creative Commons user license. See our open access license policy for more information.

Terms & Conditions applicable to all Open Access articles published with Elsevier:

Any reuse of the article must not represent the author as endorsing the adaptation of the article nor should the article be modified in such a way as to damage the author's honour or reputation. If any changes have been made, such changes must be clearly indicated.

The author(s) must be appropriately credited and we ask that you include the end user license and a DOI link to the formal publication on ScienceDirect.

If any part of the material to be used (for example, figures) has appeared in our publication with credit or acknowledgement to another source it is the responsibility of the user to ensure their reuse complies with the terms and conditions determined by the rights holder.

Additional Terms & Conditions applicable to each Creative Commons user license:

CC BY: The CC-BY license allows users to copy, to create extracts, abstracts and new works from the Article, to alter and revise the Article and to make commercial use of the Article (including reuse and/or resale of the Article by commercial entities), provided the user gives appropriate credit (with a link to the formal publication through the relevant DOI), provides a link to the license, indicates if changes were made and the licensor is not represented as endorsing the use made of the work. The full details of the license are available at http://creativecommons.org/licenses/by/4.0.

CC BY NC SA: The CC BY-NC-SA license allows users to copy, to create extracts, abstracts and new works from the Article, to alter and revise the Article, provided this is not done for commercial purposes, and that the user gives appropriate credit (with a link to the formal publication through the relevant DOI), provides a link to the license, indicates if changes were made and the licensor is not represented as endorsing the use made of the work. Further, any new works must be made available on the same conditions. The full details of the license are available at http://creativecommons.org/licenses/by-nc-sa/4.0.

CC BY NC ND: The CC BY-NC-ND license allows users to copy and distribute the Article, provided this is not done for commercial purposes and further does not permit distribution of the Article if it is changed or edited in any way, and provided the user gives appropriate credit (with a link to the formal publication through the relevant DOI), provides a link to the license, and that the licensor is not represented as endorsing the use made of the work. The full details of the license are available at http://creativecommons.org/licenses/by-nc-nd/4.0.

Any commercial reuse of Open Access articles published with a CC BY NC SA or CC BY NC ND license requires permission from Elsevier and will be subject to a fee.

Commercial reuse includes:

- Associating advertising with the full text of the Article
- Charging fees for document delivery or access
- Article aggregation
- Systematic distribution via e-mail lists or share buttons

Posting or linking by commercial companies for use by customers of those companies.

20. **Other Conditions**:

v1.9

Questions? customercare@copyright.com or +1-855-239-3415 (toll free in the US) or +1-978-646-2777.

Title: Treatment of Saline Wastewater Contaminated with Hydrocarbons by the Photo-Fenton Process

Author: José Ermírio F. Moraes, Frank H. Quina, Cláudio Augusto O. Nascimento, et al

Publication: Environmental Science & Technology

Publisher: American Chemical Society

Date: Feb 1, 2004

PERMISSION/LICENSE IS GRANTED FOR YOUR ORDER AT NO CHARGE

This type of permission/license, instead of the standard Terms & Conditions, is sent to you because no fee is being charged for your order. Please note the following:

- Permission is granted for your request in both print and electronic formats, and translations.
- If figures and/or tables were requested, they may be adapted or used in part.
- Please print this page for your records and send a copy of it to your publisher/graduate school.
- Appropriate credit for the requested material should be given as follows: "Reprinted (adapted) with permission from (COMPLETE REFERENCE CITATION). Copyright (YEAR) American Chemical Society." Insert appropriate information in place of the capitalized words.
- One-time permission is granted only for the use specified in your request. No additional uses are granted (such as derivative works or other editions). For any other uses, please submit a new request.

If credit is given to another source for the material you requested, permission must be obtained from that source.

BACK CLOSE WINDOW

Title: Activation of persulfate (PS) and peroxymonosulfate (PMS) and application for the degradation of emerging contaminants

Author: Jianlong Wang,Shizong Wang

Publication: Chemical Engineering Journal

Publisher: Elsevier

Date: 15 February 2018

Order Completed

Thank you for your order.

This Agreement between Jian Kang ("You") and Elsevier ("Elsevier") consists of your license details and the terms and conditions provided by Elsevier and Copyright Clearance Center.

Your confirmation email will contain your order number for future reference.

printable details

License Number	4672231000217
License date	Sep 18, 2019
Licensed Content Publisher	Elsevier
Licensed Content Publication	Chemical Engineering Journal
Licensed Content Title	Activation of persulfate (PS) and peroxymonosulfate (PMS) and application for the degradation of emerging contaminants
Licensed Content Author	Jianlong Wang,Shizong Wang
Licensed Content Date	Feb 15, 2018
Licensed Content Volume	334
Licensed Content Issue	n/a
Licensed Content Pages	16
Type of Use	reuse in a thesis/dissertation
Portion	figures/tables/illustrations
Number of figures/tables/illustrations	1
Format	electronic
Are you the author of this Elsevier article?	No
Will you be translating?	No
Original figure numbers	Figure 4
Title of your thesis/dissertation	Synthesis of doped nanocarbon materials for catalytic decomposition of persistent organic pollutants
Expected completion date	Sep 2019
Estimated size (number of pages)	300
Requestor Location	Jian Kang 4 Dalby Court Perth, WA 6102 Australia Attn:
Publisher Tax ID	GB 494 6272 12
Total	0.00 USD

ORDER MORE CLOSE WINDOW

Title: Efficient heterogeneous activation of peroxymonosulfate by facilely prepared Co/Fe bimetallic oxides: Kinetics and mechanism

Author: Liwei Chen,Xu Zuo,Liang Zhou,Yang Huang,Shengjiong Yang,Tianming Cai,Dahu Ding

Publication: Chemical Engineering Journal

Publisher: Elsevier

Date: 1 August 2018

Order Completed

Thank you for your order.

This Agreement between Jian Kang ("You") and Elsevier ("Elsevier") consists of your license details and the terms and conditions provided by Elsevier and Copyright Clearance Center.

Your confirmation email will contain your order number for future reference.

printable details

License Number	4672250760853
License date	Sep 18, 2019
Licensed Content Publisher	Elsevier
Licensed Content Publication	Chemical Engineering Journal
Licensed Content Title	Efficient heterogeneous activation of peroxymonosulfate by facilely prepared Co/Fe bimetallic oxides: Kinetics and mechanism
Licensed Content Author	Liwei Chen,Xu Zuo,Liang Zhou,Yang Huang,Shengjiong Yang,Tianming Cai,Dahu Ding
Licensed Content Date	Aug 1, 2018
Licensed Content Volume	345
Licensed Content Issue	n/a
Licensed Content Pages	11
Type of Use	reuse in a thesis/dissertation
Portion	figures/tables/illustrations
Number of figures/tables/illustrations	1
Format	electronic
Are you the author of this Elsevier article?	No
Will you be translating?	No
Original figure numbers	Scheme 1
Title of your thesis/dissertation	Synthesis of doped nanocarbon materials for catalytic decomposition of persistent organic pollutants
Expected completion date	Sep 2019
Estimated size (number of pages)	300
Requestor Location	Jian Kang 4 Dalby Court Perth, WA 6102 Australia Attn:
Publisher Tax ID	GB 494 6272 12
Total	0.00 USD

ORDER MORE CLOSE WINDOW

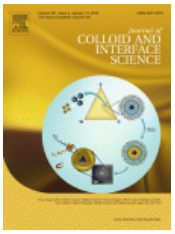

Title: Magnetic porous ferrospinel NiFe2O4: A novel ozonation catalyst with strong catalytic property for degradation of di-n-butyl phthalate and convenient separation from water

Author: Yueming Ren,Qing Dong,Jing Feng,Jun Ma,Qing Wen,Milin Zhang

Publication: Journal of Colloid and Interface Science

Publisher: Elsevier

Date: 15 September 2012

Order Completed

Thank you for your order.

This Agreement between Jian Kang ("You") and Elsevier ("Elsevier") consists of your license details and the terms and conditions provided by Elsevier and Copyright Clearance Center.

Your confirmation email will contain your order number for future reference.

printable details

License Number	4672251208502
License date	Sep 18, 2019
Licensed Content Publisher	Elsevier
Licensed Content Publication	Journal of Colloid and Interface Science
Licensed Content Title	Magnetic porous ferrospinel NiFe2O4: A novel ozonation catalyst with strong catalytic property for degradation of di-n-butyl phthalate and convenient separation from water
Licensed Content Author	Yueming Ren,Qing Dong,Jing Feng,Jun Ma,Qing Wen,Milin Zhang
Licensed Content Date	Sep 15, 2012
Licensed Content Volume	382
Licensed Content Issue	1
Licensed Content Pages	7
Type of Use	reuse in a thesis/dissertation
Portion	figures/tables/illustrations
Number of figures/tables/illustrations	1
Format	electronic
Are you the author of this Elsevier article?	No
Will you be translating?	No
Original figure numbers	Graphical abstract
Title of your thesis/dissertation	Synthesis of doped nanocarbon materials for catalytic decomposition of persistent organic pollutants
Expected completion date	Sep 2019
Estimated size (number of pages)	300
Requestor Location	Jian Kang 4 Dalby Court Perth, WA 6102 Australia Attn:
Publisher Tax ID	GB 494 6272 12
Total	0.00 USD

ORDER MORE CLOSE WINDOW

Title:	Reduced Graphene Oxide for Catalytic Oxidation of Aqueous Organic Pollutants
Author:	Hongqi Sun, Shizhen Liu, Guanliang Zhou, et al
Publication:	Applied Materials
Publisher:	American Chemical Society
Date:	Oct 1, 2012

PERMISSION/LICENSE IS GRANTED FOR YOUR ORDER AT NO CHARGE

This type of permission/license, instead of the standard Terms & Conditions, is sent to you because no fee is being charged for your order. Please note the following:

- Permission is granted for your request in both print and electronic formats, and translations.
- If figures and/or tables were requested, they may be adapted or used in part.
- Please print this page for your records and send a copy of it to your publisher/graduate school.
- Appropriate credit for the requested material should be given as follows: "Reprinted (adapted) with permission from (COMPLETE REFERENCE CITATION). Copyright (YEAR) American Chemical Society." Insert appropriate information in place of the capitalized words.
- One-time permission is granted only for the use specified in your request. No additional uses are granted (such as derivative works or other editions). For any other uses, please submit a new request.

If credit is given to another source for the material you requested, permission must be obtained from that source.

BACK CLOSE WINDOW

Title:	Nitrogen-Doped Graphene for Generation and Evolution of Reactive Radicals by Metal-Free Catalysis
Author:	Xiaoguang Duan, Zhimin Ao, Hongqi Sun, et al
Publication:	Applied Materials
Publisher:	American Chemical Society
Date:	Feb 1, 2015

PERMISSION/LICENSE IS GRANTED FOR YOUR ORDER AT NO CHARGE

This type of permission/license, instead of the standard Terms & Conditions, is sent to you because no fee is being charged for your order. Please note the following:

- Permission is granted for your request in both print and electronic formats, and translations.
- If figures and/or tables were requested, they may be adapted or used in part.
- Please print this page for your records and send a copy of it to your publisher/graduate school.
- Appropriate credit for the requested material should be given as follows: "Reprinted (adapted) with permission from (COMPLETE REFERENCE CITATION). Copyright (YEAR) American Chemical Society." Insert appropriate information in place of the capitalized words.
- One-time permission is granted only for the use specified in your request. No additional uses are granted (such as derivative works or other editions). For any other uses, please submit a new request.

If credit is given to another source for the material you requested, permission must be obtained from that source.

BACK CLOSE WINDOW

Title: Sulfur and Nitrogen Co-Doped Graphene for Metal-Free Catalytic Oxidation Reactions
Author: Shaobin Wang, Yuxian Wang, Hongqi Sun, et al
Publication: Small
Publisher: John Wiley and Sons
Date: Mar 18, 2015

Order Completed

Thank you for your order.

This Agreement between Jian Kang ("You") and John Wiley and Sons ("John Wiley and Sons") consists of your license details and the terms and conditions provided by John Wiley and Sons and Copyright Clearance Center.

Your confirmation email will contain your order number for future reference.

printable details

License Number	4672270791009
License date	Sep 18, 2019
Licensed Content Publisher	John Wiley and Sons
Licensed Content Publication	Small
Licensed Content Title	Sulfur and Nitrogen Co-Doped Graphene for Metal-Free Catalytic Oxidation Reactions
Licensed Content Author	Shaobin Wang, Yuxian Wang, Hongqi Sun, et al
Licensed Content Date	Mar 18, 2015
Licensed Content Volume	11
Licensed Content Issue	25
Licensed Content Pages	9
Type of use	Dissertation/Thesis
Requestor type	University/Academic
Format	Electronic
Portion	Figure/table
Number of figures/tables	1
Original Wiley figure/table number(s)	Figure 5
Will you be translating?	No
Title of your thesis / dissertation	Synthesis of doped nanocarbon materials for catalytic decomposition of persistent organic pollutants
Expected completion date	Sep 2019
Expected size (number of pages)	300
Requestor Location	Jian Kang 4 Dalby Court Perth, WA 6102 Australia Attn:
Publisher Tax ID	EU826007151
Total	0.00 USD

Would you like to purchase the full text of this article? If so, please continue on to the content ordering system located here: Purchase PDF

If you click on the buttons below or close this window, you will not be able to return to the content ordering system.

ORDER MORE CLOSE WINDOW

Title: Microplastics in freshwater systems: A review on occurrence, environmental effects, and methods for microplastics detection

Author: Jingyi Li,Huihui Liu,J. Paul Chen

Publication: Water Research

Publisher: Elsevier

Date: 15 June 2018

Order Completed

Thank you for your order.

This Agreement between Jian Kang ("You") and Elsevier ("Elsevier") consists of your license details and the terms and conditions provided by Elsevier and Copyright Clearance Center.

Your confirmation email will contain your order number for future reference.

printable details

License Number	4672271054547
License date	Sep 18, 2019
Licensed Content Publisher	Elsevier
Licensed Content Publication	Water Research
Licensed Content Title	Microplastics in freshwater systems: A review on occurrence, environmental effects, and methods for microplastics detection
Licensed Content Author	Jingyi Li,Huihui Liu,J. Paul Chen
Licensed Content Date	Jun 15, 2018
Licensed Content Volume	137
Licensed Content Issue	n/a
Licensed Content Pages	13
Type of Use	reuse in a thesis/dissertation
Portion	figures/tables/illustrations
Number of figures/tables/illustrations	1
Format	electronic
Are you the author of this Elsevier article?	No
Will you be translating?	No
Original figure numbers	Figure 3
Title of your thesis/dissertation	Synthesis of doped nanocarbon materials for catalytic decomposition of persistent organic pollutants
Expected completion date	Sep 2019
Estimated size (number of pages)	300
Requestor Location	Jian Kang 4 Dalby Court Perth, WA 6102 Australia Attn:
Publisher Tax ID	GB 494 6272 12
Total	0.00 USD

ORDER MORE CLOSE WINDOW

Title: Effects of microplastics on European flat oysters, Ostrea edulis and their associated benthic communities
Author: Dannielle Senga Green
Publication: Environmental Pollution
Publisher: Elsevier
Date: September 2016

Order Completed

Thank you for your order.

This Agreement between Jian Kang ("You") and Elsevier ("Elsevier") consists of your license details and the terms and conditions provided by Elsevier and Copyright Clearance Center.

Your confirmation email will contain your order number for future reference.

printable details

License Number	4672271483968
License date	Sep 18, 2019
Licensed Content Publisher	Elsevier
Licensed Content Publication	Environmental Pollution
Licensed Content Title	Effects of microplastics on European flat oysters, Ostrea edulis and their associated benthic communities
Licensed Content Author	Dannielle Senga Green
Licensed Content Date	Sep 1, 2016
Licensed Content Volume	216
Licensed Content Issue	n/a
Licensed Content Pages	9
Type of Use	reuse in a thesis/dissertation
Portion	figures/tables/illustrations
Number of figures/tables/illustrations	1
Format	electronic
Are you the author of this Elsevier article?	No
Will you be translating?	No
Original figure numbers	Graphical abstract
Title of your thesis/dissertation	Synthesis of doped nanocarbon materials for catalytic decomposition of persistent organic pollutants
Expected completion date	Sep 2019
Estimated size (number of pages)	300
Requestor Location	Jian Kang 4 Dalby Court Perth, WA 6102 Australia Attn:
Publisher Tax ID	GB 494 6272 12
Total	0.00 USD

ORDER MORE CLOSE WINDOW

Title:	Biodegradation of polyethylene microplastics by the marine fungus Zalerion maritimum
Author:	Ana Paço,Kátia Duarte,João P. da Costa,Patrícia S.M. Santos,R. Pereira,M.E. Pereira,Ana C. Freitas,Armando C. Duarte,Teresa A.P. Rocha-Santos
Publication:	Science of The Total Environment
Publisher:	Elsevier
Date:	15 May 2017

Order Completed

Thank you for your order.

This Agreement between Jian Kang ("You") and Elsevier ("Elsevier") consists of your license details and the terms and conditions provided by Elsevier and Copyright Clearance Center.

Your confirmation email will contain your order number for future reference.

printable details

License Number	4672280342402
License date	Sep 18, 2019
Licensed Content Publisher	Elsevier
Licensed Content Publication	Science of The Total Environment
Licensed Content Title	Biodegradation of polyethylene microplastics by the marine fungus Zalerion maritimum
Licensed Content Author	Ana Paço,Kátia Duarte,João P. da Costa,Patrícia S.M. Santos,R. Pereira,M.E. Pereira,Ana C. Freitas,Armando C. Duarte,Teresa A.P. Rocha-Santos
Licensed Content Date	May 15, 2017
Licensed Content Volume	586
Licensed Content Issue	n/a
Licensed Content Pages	6
Type of Use	reuse in a thesis/dissertation
Portion	figures/tables/illustrations
Number of figures/tables/illustrations	1
Format	electronic
Are you the author of this Elsevier article?	No
Will you be translating?	No
Original figure numbers	Graphical abstract
Title of your thesis/dissertation	Synthesis of doped nanocarbon materials for catalytic decomposition of persistent organic pollutants
Expected completion date	Sep 2019
Estimated size (number of pages)	300
Requestor Location	Jian Kang 4 Dalby Court Perth, WA 6102 Australia Attn:
Publisher Tax ID	GB 494 6272 12
Total	0.00 USD

ORDER MORE CLOSE WINDOW

Attribution statement

Published paper

1. "**Catalytic degradation of antibiotics by metal-free catalysis over nitrogen-doped graphene.** *Catalysis Today* 2019, in press"

Authors	**Conception and design**	**Experiments conduction & data acquisition**	**Data processing & analysis**	**interpretation & discussion**	**Manuscript writing, revision and finalisation**	**Final approval**
Li Zhou			✓			
	I acknowledge that these represent my contribution to the above result output. Sign:					
Xiaoguang Duan		✓		✓		
	I acknowledge that these represent my contribution to the above result output. Sign:					
Hongqi Sun	✓			✓		✓
	I acknowledge that these represent my contribution to the above result output. Sign:					
Shaobin Wang	✓	✓	✓	✓	✓	✓
	I acknowledge that these represent my contribution to the above result output. Sign:					

2. “**Catalytic degradation of cosmetic microplastics by hydrothermal carbocatalysis: A new approach with magnetic carbon nanosprings and sulfate radicals.** Cell Press Matter 2019,1, 745-758.”

Authors	**Conception and design**	**Experiments conduction & data acquisition**	**Data processing & analysis**	**interpretation & discussion**	**Manuscript writing, revision and finalisation**	**Final approval**
Li Zhou		✓				
	I acknowledge that these represent my contribution to the above result output. Sign:					
Xiaoguang Duan	✓			✓		
	I acknowledge that these represent my contribution to the above result output. Sign:					
Hongqi Sun	✓	✓	✓	✓	✓	✓
	I acknowledge that these represent my contribution to the above result output. Sign:					
Zhimin Ao		✓				
	I acknowledge that these represent my contribution to the above result output. Sign:					
Shaobin Wang	✓	✓	✓	✓	✓	✓
	I acknowledge that these represent my contribution to the above result output. Sign:					

3. "**Nitrogen-doped bamboo-like carbon nanotubes with Ni encapsulation for persulfate activation to remove emerging contaminants with excellent catalytic stability**. *Chemical Engineering Journal* 2018, 332, 398-408."

Authors	**Conceptio n / design**	**Experiments conduction & data acquisition**	**Data processing & analysis**	**interpretation & discussion**	**Manuscript writing, revision and finalisation**	**Final approval**
Xiaoguang Duan,		✓		✓		
	I acknowledge that these represent my contribution to the above result output. Sign:					
Chen Wang	✓	✓				
	I acknowledge that these represent my contribution to the above result output. Sign:					
Hongqi Sun	✓			✓	✓	✓
	I acknowledge that these represent my contribution to the above result output. Sign:					
Xiaoyao Tan		✓				
	I acknowledge that these represent my contribution to the above result output. Sign:					
Moses O. Tade					✓	
	I acknowledge that these represent my contribution to the above result output. Sign:					
Shaobin Wang	✓	✓	✓	✓	✓	✓
	I acknowledge that these represent my contribution to the above result output. Sign:					

4. **“Nickel in hierarchically structured nitrogen-doped graphene for robust and promoted degradation of antibiotics.** Journal of Cleaner Production 2019, 218, 202-211.”

Authors	**Conception and design**	**Experiments conduction & data acquisition**	**Data processing & analysis**	**interpretation & discussion**	**Manuscript writing, revision and finalisation**	**Final approval**
Huayang Zhang		✓				
	I acknowledge that these represent my contribution to the above result output. Sign:					
Xiaoguang Duan		✓	✓	✓		
	I acknowledge that these represent my contribution to the above result output. Sign:					
Hongqi Sun	✓	✓	✓	✓	✓	✓
	I acknowledge that these represent my contribution to the above result output. Sign:					
Xiaoyao Tan		✓				
	I acknowledge that these represent my contribution to the above result output. Sign:					
Shaobin Wang	✓	✓	✓	✓	✓	✓
	I acknowledge that these represent my contribution to the above result output. Sign:					

5. **"Magnetic Ni-Co alloy encapsulated N-doped carbon nanotubes for catalytic membrane degradation of emerging contaminants.** Chemical Engineering Journal 2019, 362, 251-261"

Authors	**Conception and design**	**Experiments conduction & data acquisition**	**Data processing & analysis**	**interpretation & discussion**	**Manuscript writing, revision and finalisation**	**Final approval**
Huayang Zhang		✓				
	I acknowledge that these represent my contribution to the above result output. Sign:					
Xiaoguang Duan	✓		✓		✓	
	I acknowledge that these represent my contribution to the above result output. Sign:					
Hongqi Sun						
	I acknowledge that these represent my contribution to the above result output. Sign:					
Xiaoyao Tan		✓				
	I acknowledge that these represent my contribution to the above result output. Sign:					
Shaomin Liu	✓	✓	✓	✓	✓	✓
	I acknowledge that these represent my contribution to the above result output. Sign:					
Shaobin Wang	✓	✓	✓	✓	✓	✓
	I acknowledge that these represent my contribution to the above result output. Sign:					